Ronald Millett
AUTEUR DE LA THÈSE / AUTHOR OF THESIS

Ph.D. (Electrical Engineering)
GRADE / DEGREE

School of Information Technology and Engineering
FACULTÉ, ÉCOLE, DÉPARTEMENT / FACULTY, SCHOOL, DEPARTMENT

Modeling, Fabrication, and Measurement of Laterally-coupled Distributed Feedback Lasers
TITRE DE LA THÈSE / TITLE OF THESIS

Henry Schriemer
DIRECTEUR (DIRECTRICE) DE LA THÈSE / THESIS SUPERVISOR

Trevor Hall
CO-DIRECTEUR (CO-DIRECTRICE) DE LA THÈSE / THESIS CO-SUPERVISOR

EXAMINATEURS (EXAMINATRICES) DE LA THÈSE / THESIS EXAMINERS

Daneil Cassody (McMaster University)

Gary Tarr (Carleton University)

Pierre Berini

Karin Hinzer

Gary W. Slater
Le Doyen de la Faculté des études supérieures et postdoctorales / Dean of the Faculty of Graduate and Postdoctoral Studies

MODELING, FABRICATION, AND MEASUREMENT OF LATERALLY-COUPLED DISTRIBUTED FEEDBACK LASERS

by

Ronald R. Millett

A thesis submitted in partial fulfillment of the
requirements for the degree of

Doctorate of Philosophy

Faculty of Engineering
University of Ottawa

Library and Archives
Canada

Published Heritage
Branch

395 Wellington Street
Ottawa ON K1A 0N4
Canada

Bibliothèque et
Archives Canada

Direction du
Patrimoine de l'édition

395, rue Wellington
Ottawa ON K1A 0N4
Canada

Your file Votre référence
ISBN: 978-0-494-61396-2
Our file Notre référence
ISBN: 978-0-494-61396-2

NOTICE:

The author has granted a non-exclusive license allowing Library and Archives Canada to reproduce, publish, archive, preserve, conserve, communicate to the public by telecommunication or on the Internet, loan, distribute and sell theses worldwide, for commercial or non-commercial purposes, in microform, paper, electronic and/or any other formats.

The author retains copyright ownership and moral rights in this thesis. Neither the thesis nor substantial extracts from it may be printed or otherwise reproduced without the author's permission.

AVIS:

L'auteur a accordé une licence non exclusive permettant à la Bibliothèque et Archives Canada de reproduire, publier, archiver, sauvegarder, conserver, transmettre au public par télécommunication ou par l'Internet, prêter, distribuer et vendre des thèses partout dans le monde, à des fins commerciales ou autres, sur support microforme, papier, électronique et/ou autres formats.

L'auteur conserve la propriété du droit d'auteur et des droits moraux qui protège cette thèse. Ni la thèse ni des extraits substantiels de celle-ci ne doivent être imprimés ou autrement reproduits sans son autorisation.

In compliance with the Canadian Privacy Act some supporting forms may have been removed from this thesis.

While these forms may be included in the document page count, their removal does not represent any loss of content from the thesis.

Conformément à la loi canadienne sur la protection de la vie privée, quelques formulaires secondaires ont été enlevés de cette thèse.

Bien que ces formulaires aient inclus dans la pagination, il n'y aura aucun contenu manquant.

Canada

ABSTRACT

This thesis describes the modeling, design, fabrication, experiment, and measurement analysis of a 1310 nm laterally-coupled distributed feedback (LC-DFB) laser diode with higher order gratings. In LC-DFB lasers, a grating is etched directly out of the waveguide ridge, eliminating regrowth steps. We propose the use of stepper lithography for LC-DFB laser fabrication, a technique more suitable for high-volume manufacture than traditional approaches, such as electron-beam lithography. We also propose the use of higher order gratings, requiring larger grating periods than first-order gratings, to improve manufacturing tolerances.

Simulations using Streifer's modified coupled-mode approach were used to explore the laser design space. This thesis extends the original formulation to a two-dimensional cross-section to accurately model the LC-DFB lasers. The effective coupling coefficient, κ_{eff}, calculated using this approach varied considerably from the generally used simple coupling coefficient, κ_p, found when neglecting Streifer correction terms. Our model determined that larger duty cycles (> 0.5), and greater ridge width contrasts produce higher $|\kappa_{eff}|$ values. The inclusion of a λ/4 phase-shift tends to degrade higher order grating performance. Non-rectangular grating shapes, such as triangular and sinusoidal, often have stronger coupling, particularly at higher grating orders, and are potentially simpler to fabricate.

The fabricated lasers had excellent side-mode suppression ratios of > 50 dB. The efficiencies and threshold currents of the LC-DFB lasers are comparable to the Fabry-Perot lasers, indicating that the higher order grating losses are not prohibitive. The single-mode yield was compromised by weaker than expected gratings due to rounding during fabrication, and cross-wafer variations, however, yields of ~50% on the best design variations are very promising, particularly for a first fabrication run. The overall performance indicates that with some design improvements, guided by our model, this

laser has commercial potential. The experimentally determined κ_{eff} matched well with the simulated values, within fabrication and experimental variations.

PUBLICATIONS

The following publications are on work directly covered in this thesis:

[1] **R. Millett**, K. Hinzer, A. Benhsaien, T.J. Hall, and H. Schriemer, "Enhancing Coupling Coefficients by Shaping Laterally-Coupled Gratings," submitted to *Nanotechnology*, August 2009.

[2] A. Assadihaghi, **R. Millett**, "Threshold current reduction in third-order laterally-coupled DFB lasers," *To be presented at the 2nd Annual CMC Microsystems and Nanoelectronics Research Conference,* Ottawa, ON, October 13-14, 2009.

[3] **R. Millett**, Henry Schriemer, Karin Hinzer, Kais Dridi and Trevor Hall, "Fabrication-Tolerant 1310 nm Laterally-Coupled Distributed Feedback Lasers with High Sidemode Suppression Ratios," *Proc. SPIE*, accepted 21 March by *Photonics North 2009*, Quebec City, Canada, 24-27 May 2009.

[4] **R. Millett**, H. Schriemer, T. Hall, and K. Hinzer, "Effects of Grating Order and Tooth Rounding in Laterally-Coupled Distributed Feedback Lasers," *J. Opt. Quantum Electron.*, 10.1007/s11082-009-9293-2 , April 2009.

[5] **R. Millett**, K. Hinzer, T. Hall, M. Poirier, and H. Schriemer, "Monolithically-Integrated 4x4 SOA Switch Fabricated Using Quantum Well Intermixing," *Photonics West*, San Jose, CA, Jan. 24-29, 2009.

[6] **R. Millett**, A. Benhsaien, K. Hinzer, T. Hall, and H. Schriemer, "Simulation of Fourth-Order Laterally-Coupled Gratings," *COMSOL Conference 2008*, Boston, MA, October 2008.

[7] **R. Millett**, K. Hinzer, T. Hall, and H. Schriemer, "Grating Orders, Duty Cycles, and Cavity Lengths for Second-Order Laterally-Coupled Distributed Feedback Lasers," *1st Annual CMC Microsystems and Nanoelectronics Research Conference*, Ottawa, ON, October 15, 2008 (winner of Gold Leaf Award for best student paper).

[8] **R. Millett**, K. Hinzer, T. Hall, and H. Schriemer, "Simulation Analysis of Higher Order Laterally-Coupled Distributed Feedback Lasers," *IEEE J. Quantum Electron.*, vol. 44, pp. 1145-1151, December 2008.

[9] **R. Millett**, H. Schriemer, T. Hall, and K. Hinzer, "Properties of Laterally-Coupled Distributed Feedback Lasers with Higher Order Gratings," *8th International Conference on the Numerical Simulation of Optoelectronic Devices*, University of Nottingham, Nottingham, UK, Sept. 1-5, 2008.

[10] **R. Millett**, H. Schriemer, and K. Hinzer, "Laterally-Coupled Grating with Non-Rectangular Tooth Shape for Improved Coupling Coefficients," U.S. Prov. Patent filed Aug. 28, 2008.

[11] **R. Millett**, K. Hinzer, T. Hall, and H. Schriemer, "Fabrication-Tolerant Higher Order Laterally-Coupled Distributed Feedback Lasers," *Photonics North*, Montreal, PQ, June 2-4, 2008.

[12] **R. Millett**, H. Awad, M. Poirier, V.I. Tolstikhin, T. Hall, K. Hinzer, and H. Schriemer, "Design and Fabrication of a λ/4 Phase-Shifted 1310 nm Laterally-Coupled Distributed-Feedback Laser," *Conference on Lasers and Electro-Optics*, San Jose, CA, May 4-9, 2008.

The following publications were produced during my Ph.D. studies but are not directly related to the thesis topic:

[13] A. Assadihaghi, H. Teimoori, **R. Millett**, A. Benhsaien, V. Tolstikhin, K. Hinzer, and T. Hall, "O-band Semiconductor Optical Amplifier Design for CWDM Applications," *1st Annual CMC Microsystems and Nanoelectronics Research Conference*, Ottawa, ON, October 15, 2008.

[14] **R. Millett**, J. Ramsey, P. Bock, J. Nkanta, H. Schriemer, T. Hall, and S. Bidnyk, "Synthesis of planar reflective gratings for silicon interconnects," *Advances in Optical Technologies: Special Issue on Silicon Photonics*, vol. 2008, June 2008.

[15] S. Bidnyk, P. Bock, T. Hall, **R. Millett**, and H. Schriemer, "Polarization compensators in silicon-on-insulator reflective interconnects," *Photonics North*, Montreal, PQ, June 2-4, 2008.

[16] **R. Millett**, T. Hall, K. Hinzer, V. Tolstikhin, K. Pimenov, Y. Logvin, and H. Schriemer, "Monolithically Integrated InGaAsP/InP 1x2 SOA Optical Switch," *Photonics North*, Ottawa, ON, June 4-7, 2007.

[17] **R. Millett**, J. Wheeldon, T. Hall, and H. Schriemer, "Towards Modelling Semiconductor Heterojunctions," *COMSOL Conference 2006*, Boston, MA, October 2006.

"There is no greater mystery to me than that of light traveling through darkness."

- Alexander Volkov

TABLE OF CONTENTS

LIST OF FIGURES

LIST OF TABLES

ACKNOWLEDGMENTS

Like all theses, this Ph.D. thesis is not the result of solitary effort. I've been very fortunate to have supervising professors who have provided me with unwavering support during my studies. Professor Henry Schriemer has been a valuable mentor since the earliest days of my graduate-level studies. Professor Trevor Hall has given me the support and encouragement I've needed to pursue my thesis topic. Professor Karin Hinzer has been unfailingly generous in her time, knowledge, and enthusiasm during the course of this project.

It has been a pleasure studying at the Centre for Research in Photonics and at the University of Ottawa. I would like to especially thank my colleagues Jeff Wheeldon, for setting up and administering our computational workstation, Julie Nkanta for developing the laser test setup, Hazem Awad for helping to lay out the mask for this project, and A. 'Ben' Benhsaien for his continuation of this work. A special thanks to Kais Dridi, who gathered many of the experimental results for these lasers. I am grateful to Maxime Poirier, formerly of CMC Microsystems, for his knowledge and patience during the course of this project. Valery Tolstikhin of OneChip Photonics has provided valuable assistance during the course of my studies. I also wish to acknowledge those organizations that have provided funding and support for the research contained in this thesis. This includes the University of Ottawa, Canadian Foundation for Innovation (CFI), Natural Sciences and Engineering Research Council (NSERC), CMC Microsystems, OneChip Photonics, the Canada Research Chairs Program, the Ontario Research Fund, Ontario Graduate Scholarship Program, and the Ontario Centres of Excellence (OCE).

Finally, it is my pleasure to say thank you to my entire family, who have always been there when I've needed them. A special thanks to my wife, Holly. Her love and encouragement have never failed to lift me up; especially during those times when I've been 'spinning my wheels'.

CHAPTER 1 - INTRODUCTION

1.1 Motivation

The laser, once considered an invention in search of an application, has become an indispensable piece of modern technology. One of the most important applications of the laser has been in optical communications. Fiber-optic networks have spanned the globe, multiplying the demand for reliable, high-performance, mass-produced lasers. It is widely expected that optical networks are moving towards dense wavelength-division multiplexing (DWDM) architectures with wavelength channels separated by 100 GHz or less. These DWDM applications demand laser sources with temperature and wavelength stability beyond that of a standard Fabry-Perot (FP) laser diode.

Distributed feedback lasers provide temperature stability and spectral purity through the use of a wavelength selective grating. While they have superior characteristics compared to FP laser diodes, the addition of a periodic grating structure means that DFB lasers also require more complex processing. In a standard DFB laser process, epitaxial layers are grown, a grating is defined and etched using holographic techniques, and the upper layers are grown above the grating. A waveguide ridge is then defined and etched. In contrast, the FP laser requires only a single growth and etch step.

The additional processing steps required for a DFB laser tends to lower manufacturing throughput, making DFB lasers less attractive compared to FP laser diodes. Laterally-coupled distributed feedback (LC-DFB) lasers eliminate the regrowth steps described above for DFB lasers by patterning the grating directly out of the waveguide ridge. The optical mode will then be evanescently coupled to the grating on either side of the ridge, hence the term 'laterally-coupled'. Various examples of LC-DFB lasers have been demonstrated over the past twenty years (see Chapter 2), but most rely on e-beam lithography to meet the stringent specifications required for the grating. E-beam lithography is slower and more expensive technique compared to standard optical lithography, eliminating one of the prime motivations for using LC-DFB lasers: a greater manufacturing throughput.

1.2 Objective

The objective of this thesis is to demonstrate the design and fabrication of LC-DFB lasers with higher order gratings. Stepper lithography and inductively-coupled plasma etching will be the target technology for fabricating these lasers. Stepper lithography is well-suited for fabricating lasers in a manufacturing environment. Although stepper lithography machines with resolutions of 100 nm do exist, the 5x i-line machine available at the Canadian Photonics Fabrication Centre (CPFC) is limited to resolutions of 365 nm or higher. This is above the limit for first-order gratings within the 1310 nm range, but just within reach of third-order gratings. By moving to higher order gratings, we can use larger grating periods and thus accept less stringent manufacturing tolerances compared to first-order gratings. The simulation of laterally-coupled higher order gratings requires a full two-dimensional treatment including radiating partial waves. The development of this model and its application to finding high performance, fabrication-tolerant grating geometries is one of the major contributions of this thesis. The experimental results are used to confirm and further develop our LC-DFB laser design.

1.3 Thesis Organization

In Chapter 2, other LC-DFB laser designs are reviewed, including a summary of the performance and manufacturing techniques of all such lasers to date. A brief description of our LC-DFB laser is given. Chapter 3 describes the design of the epitaxial growth structure used in our LC-DFB laser. In Chapter 4, a summary of common DFB modeling techniques is presented, and the modified coupled-mode theory used in this thesis is derived. Chapter 5 is a thorough examination of the effects of the grating geometry on the LC-DFB laser performance. The grating geometry parameters include the grating order, shape, duty cycle, grating height and grating width. Chapter 6 is a description of the three-dimensional modeling of the LC-DFB laser, including the cavity length considerations, phase-shifts, and facet reflectivities. Chapter 7 presents the experimental results obtained from the LC-DFB laser diodes that were tested. They include LI curves, spectra, IV curves, other results. A comparison between the experimental results and the expected theoretical simulations is made. In Appendix A, a description is given of the highly flexible LC-DFB mask layout with DW-2000 software using the concept of 'p-cells'. In Appendix B, a monolithically integrated 4x4 optical switch design is described. This design, to be fabricated using quantum well intermixing, is an example of a complementary device that could be integrated with the lasers described in this thesis.

CHAPTER 2 - REVIEW OF LATERALLY-COUPLED DISTRIBUTED FEEDBACK LASERS

2.1 A Brief History of the Laser

The development of the laser (Light Amplification by Stimulated Emission of Radiation) is one of the great scientific and engineering achievements of the 20th century. Stimulated emission was first described by Einstein in his 1916 derivation of Planck's law of radiation [1]. However, it was not until the 1950s that the theoretical possibility of lasers was proved with the development of the maser (Microwave Amplification by Stimulated Emission of Radiation). While von Neumann had formulated the basics of a laser as early as 1953 [2], the first fully-developed laser theory was the result of the Nobel prize-winning efforts of Townes [3], Basov and Prokhorov. In 1960, Theodore Maiman was the first to demonstrate a laser experimentally using a ruby crystal [4]. If it were not for the development of semiconductor lasers, however, lasers would likely have remained laboratory tools, instead of the ubiquitous components that they are today, to be found in DVD players, scanners, fiber-optic networks, and countless other devices. A comprehensive history of the semiconductor laser is a topic that is too extensive to treat here, instead, the reader is referred to excellent surveys such as those by Holonyak, Rediker, and others [5]-[8]. Some milestones include the first semiconductor lasers developed by Hall [9], Nathan [10], Quist [11], and Holonyak [12], the first semiconductor heterojunction lasers by Hayashi [13][14], Kressel [15], and Alferov [16], the first quantum-well lasers [17],[18], and the first quantum-dot devices [19]. This thesis focuses on a particular class of lasers known as distributed feedback (DFB) lasers.

2.2 Distributed Feedback Laser Advantages

The earliest semiconductor lasers were of a Fabry-Perot (FP) design. FP lasers provide optical feedback through reflection at the end facets of the laser cavity. FP lasers were made particularly simple to fabricate as the cleaved facets of semiconductor material provide an interface between air and the semiconductor that is naturally partially-reflective. The Fabry-Perot cavity, however, will support numerous longitudinal modes, each with different frequencies. The gain and spontaneous emission spectra for bulk materials are several nanometers in width, providing enough optical gain to support many such modes, resulting in a relatively broad emission spectrum, an example of which is shown in Figure 1a. Distributed feedback lasers use a wavelength selective grating to greatly improve the spectral purity of the laser output, as demonstrated in Figure 1b. In many applications the FP laser provides acceptable performance, however, for applications with stringent wavelength and linewidth requirements, FP lasers are often inadequate. Modern high-speed fiber-optic telecommunications networks in particular require lasers with frequency selectivity for two reasons: dispersion and wavelength division multiplexing.

Dispersion causes optical pulses to spread out in time as they travel down the length of fiber. A bit stream consisting of many such pulses will begin to smear together as they travel down a sufficiently long dispersive fiber, causing an unacceptable bit error rate. This pulse spreading is due to the frequencies that comprise the pulse traveling at different group velocities. Thus, having a more coherent transmitter (i.e. a laser source with a narrower linewidth) will result in less pulse spreading due to dispersion. A typical silica fiber-optic cable has a dispersion of 17 ps/nm at 1550 nm, the wavelength of minimum optical attenuation. A bit rate of 500 Mb/s over 100 km, for example, will require a spectral width of < 0.15 nm from the laser source to limit interpulse mixing to < 10% of the bit period. A typical FP laser with a cavity length of 400 μm has a spacing between adjacent longitudinal modes of 0.8 nm, so additional filtering (with an attendant loss of optical power) or excellent dispersion compensation would be required to make

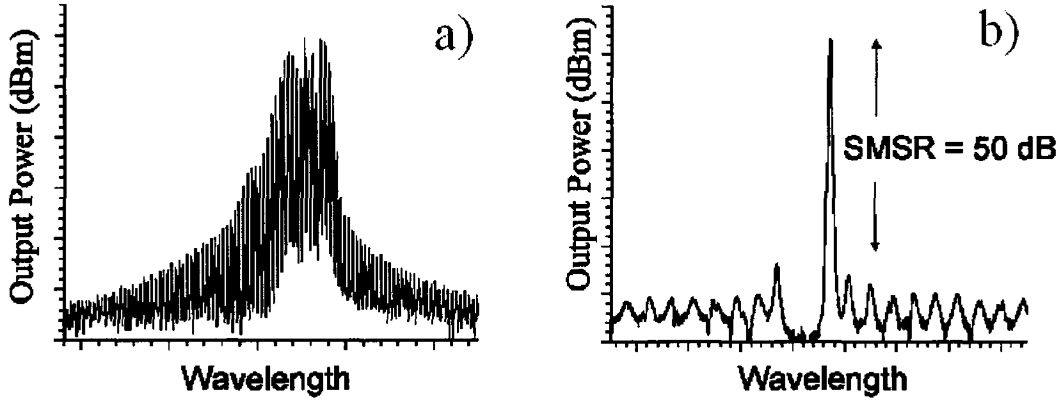

Figure 1. **Examples of a) Fabry-Perot and b) distributed feedback laser spectra**

FP lasers suitable for this application [20]. Current fiber-optic networks operating at speeds of 10-40 Gb/s have an even stricter requirements for the laser linewidth.

While there are numerous methods to compensate for dispersion, wavelength division multiplexing (WDM) provides an even stronger incentive to develop stable, coherent transmitters. The bandwidth of a standard optical fiber can be greatly increased if multiple signals, each assigned to a different wavelength, are combined (i.e. multiplexed) together and transmitted simultaneously. Since light of different wavelengths can propagate without interference, hundreds of signals can be combined into a single fiber in dense wavelength division multiplexing (DWDM) schemes. The ITU-T G.694.1 standard developed in 2002 calls for 100 GHz channel spacing around 1550 nm, corresponding to a wavelength separation of ~0.8 nm. Current state-of-the-art DWDM systems have channel spacings as low as 25 GHz. Clearly the multimode FP lasers described above, with longitudinal modes separated by 0.8 nm, are inadequate for these DWDM applications. The temperature stability of DFB lasers is also an important benefit. The temperature dependence of a Fabry-Perot laser is dominated by the temperature coefficient of the peak gain wavelength, which his approximately $d\lambda_p / dT$ = 0.5 nm/K for long-wavelength InGaAsP/InP double-heterostructure lasers. In DFB or DBR lasers, the temperature dependence is dominated by the temperature coefficient of the refractive index, which is approximately $dn/dT = 0.1\ \mathrm{K}^{-1}$ [21]. This results in a much greater wavelength stability over temperature for DFB lasers compared to FP lasers [22].

2.3 Fundamentals of Bragg Gratings

The wavelength selectivity of periodic structures was first described by the father and son team of W.H. and W.L. Bragg in their Nobel prize-winning examination of the x-ray diffraction of crystal structures [23]. An intuitive picture of Bragg gratings can be painted using Huygen's principle. In Huygen's principle, the cumulative effect of a diffractive material can be considered to be the summation of a series of point sources. Assume a plane wave, of wavelength λ, is traveling through free-space. It is incident on a grating structure with period, Λ, at an angle, θ_i, and reflecting with an angle, θ_d. In Figure 2, this advancing plane wave is represented by a ray perpendicular to the advancing wavefront. Due to the periodicity of the grating, every ray separated by one period will experience the same reflection angle. Looking at two adjacent rays separated by a single period, from Figure 2, the first ray travels a total distance of L_{ABC}, and the second ray travels a total distance of $L_{A'B'C'}$ before reaching the same final wavefront. To have constructive interference, the peaks and valleys of every periodically spaced ray should have the same phase at the output wavefront. As the plane wave has a phase dependence of

$$\varphi = \frac{2\pi n L}{\lambda}, \tag{2.1}$$

where n is the refractive index of the medium, and L is the distance traveled, the phases of the two rays will be equal and constructively interfere when

$$\frac{2\pi n}{\lambda}\left[L_{ABC}\right] = \frac{2\pi n}{\lambda}\left[L_{A'B'C'}\right] + 2\pi M \tag{2.2}$$

where M is an integer. It is not the absolute value of the lengths L_{ABC} and $L_{A'B'C'}$ that is of importance, but the relative difference in the two path lengths, $L_{ABC} - L_{A'B'C'}$. This path length difference can be determined geometrically from Figure 2. The difference in the incident beam path is given by $L_{x'B'}$, while the difference in the reflected beam path is given by L_{Bx}. The length of the *x'B'* path is determined from the horizontally-hatched right-angle triangle in Figure 2, while the length of the *Bx* path is found from the vertically-hatched right-angle triangle. Both triangles have a hypotenuse equal to the period length, Λ. Substituting these values from (2.2) results in

$$\left(L_{ABC} - L_{A'B'C'}\right) = \left(L_{Bx} - L_{x'B'}\right) = \Lambda\left(\sin\theta_d - \sin\theta_i\right) = \frac{M\lambda}{n} \tag{2.3}$$

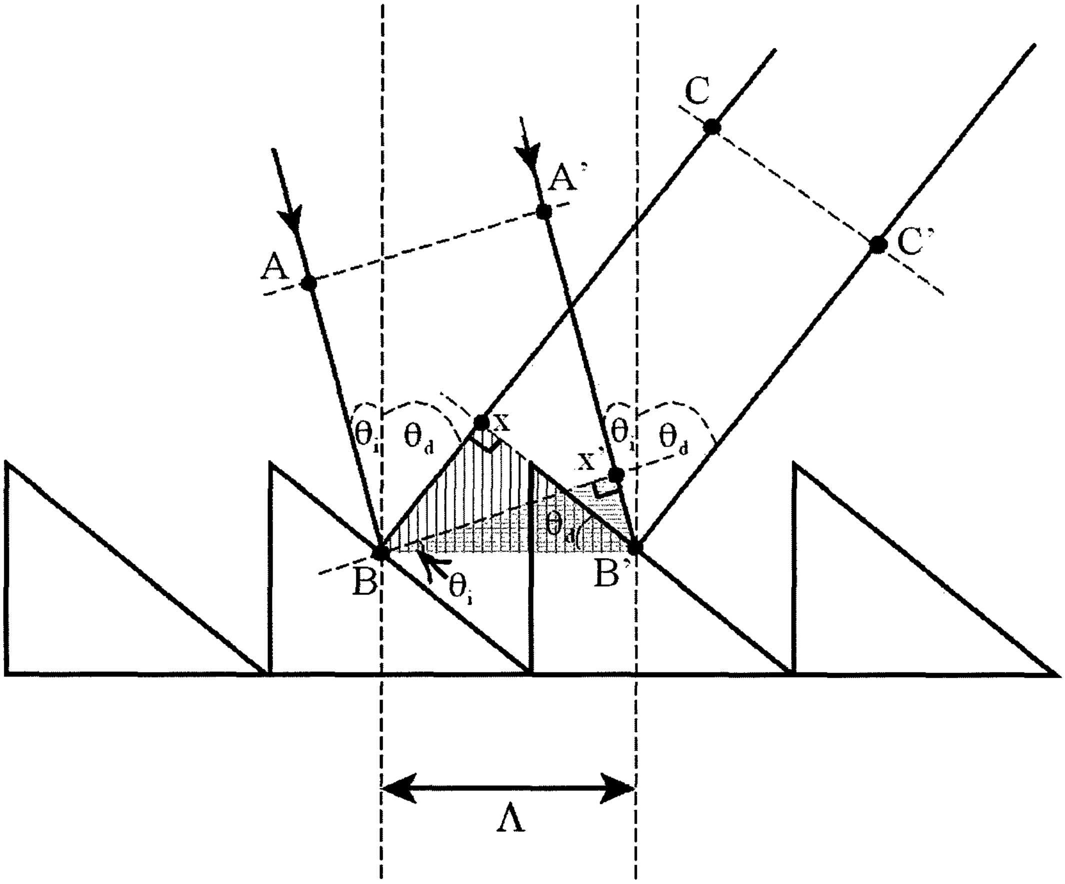

Figure 2. **Diffraction of light from a blazed grating**

where M is a positive or negative integer known as the order of diffraction. Since it must be an integer in order for constructive interference to occur, only particular values of wavelength, λ, will satisfy the constructive interference condition. This will result in these particular wavelengths being reflected more strongly from this grating.

The benefits of embedding such a periodic grating in a laser cavity are that it allows greater control over the laser wavelength and will have narrower linewidth compared to FP lasers, as shown in Figure 1. In Figure 3, we have an example of a periodic Bragg grating embedded in a semiconductor material through a periodic modulation of the refractive index between two values, n_1 and n_2 in the grating region. It is desired to have light reflected backwards to the direction of propagation to achieve a feedback effect. We again look at the interference between two light rays separated by a grating period and beginning along the same wavefront (at points A and A') and ending at the same wavefront (at points C and C'). The $A'B'C'$ path is now longer than the ABC path by the

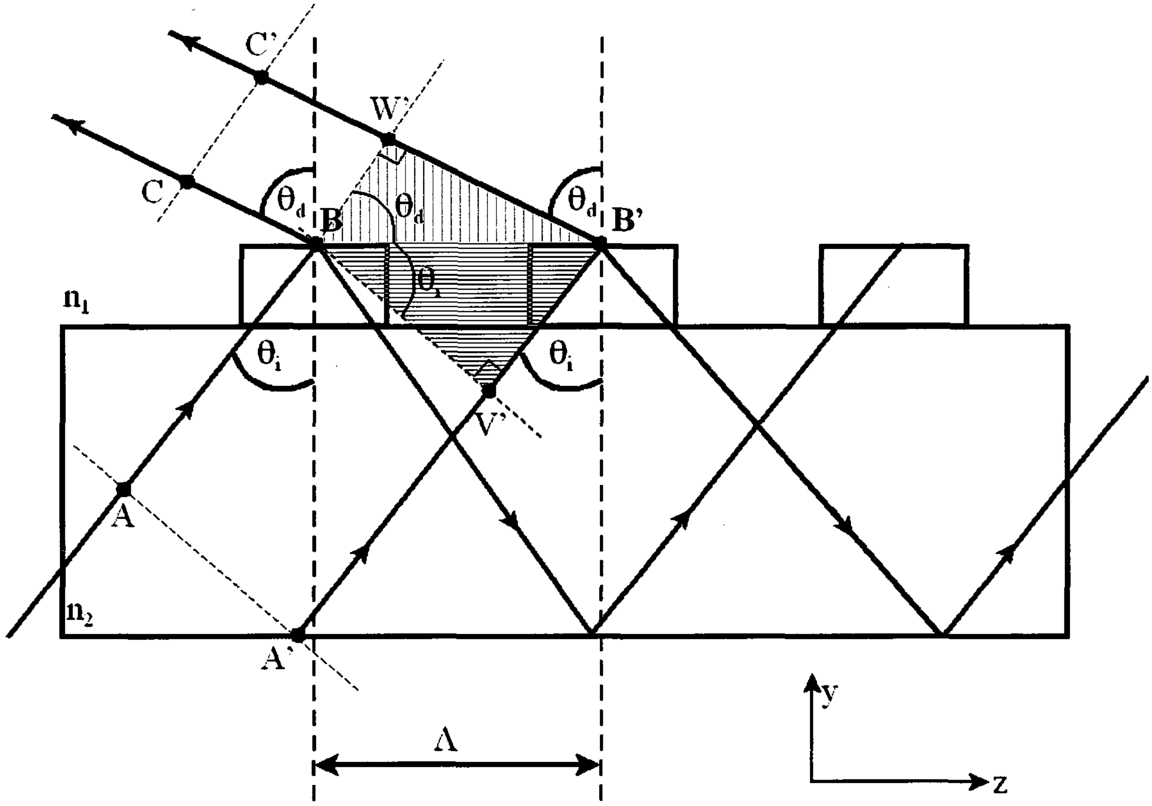

Figure 3. **Plane wave diffraction in a waveguide Bragg grating.**

length of the paths *V'B'* and *B'W'*. The constructive interference condition is

$$\frac{n}{\lambda}\left[L_{A'B'C'} - L_{ABC}\right] = \frac{n_2 L_{V'B'}}{\lambda} + \frac{n_1 L_{B'W'}}{\lambda} = M, \tag{2.4}$$

where we now have different refractive indices for each path and *M* is once again a positive or negative integer defined as the diffraction order. The path lengths are determined geometrically from the two right-angle triangles, horizontally-hatched for the *V'B'* path and vertically-hatched for the *B'W'* path, that have hypotenuses that are one period in length. Substituting these lengths into (2.4) results in

$$\frac{n_1 \Lambda \sin\theta_d}{\lambda} + \frac{n_2 \Lambda \sin\theta_i}{\lambda} = M. \tag{2.5}$$

Since the laser cavity is an optical waveguide that should confine light, additional restrictions are placed on the angle of incidence, θ_i, to permit total internal reflection at the interface between the two refractive indices. From Snell's law, we can derive a minimum angle of incidence, known as the critical angle, θ_c, given by

$$\sin\theta_i \geq \sin\theta_c = \frac{n_1}{n_2} \tag{2.6}$$

where it is assumed that $n_2 > n_1$. Substituting this condition into (2.5) gives

$$\sin\theta_d \geq \left(\frac{M\lambda}{\Lambda n_1} - 1\right) = \left(\frac{2M}{p} - 1\right), \tag{2.7}$$

where *p* is the grating order, not to be confused with the diffraction order *M*, defined as

$$p = \frac{2\Lambda n_1}{\lambda} \approx \frac{2\Lambda n_{eff}}{\lambda}. \tag{2.8}$$

In (2.8) we assume that the difference between the two refractive indices that comprise the grating is negligibly different, such that $n_1 \approx n_2 \approx n_{eff}$, where n_{eff} is the effective index of the unperturbed waveguide. This assumption is appropriate for LC-DFB lasers that are only evanescently coupling the optical mode to the grating region. As a result, the effective index is nearly identical in both grating regions.

For a distributed feedback laser, we wish to have incident light travel along the longitudinal (*z*-) direction and diffract directly backwards along the direction of propagation. These conditions are satisfied when $\theta_d = \theta_i = \pi/2$. Substituting this condition into (2.7), such that $\sin\theta_d = 1$, and using the equality results in a constructive interference condition of

$$\frac{M}{p} = 1 \Rightarrow p = M. \tag{2.9}$$

We will see constructive interference when *p* is equal to *M*, in other words, we consider *p* to be a positive or negative integer like *M*. If we wish to provide feedback for light of wavelength λ_B, then from the definition of *p* in (2.8) we should select a grating with a period of

$$\Lambda = \frac{M\lambda_B}{2n_{eff}}. \tag{2.10}$$

Since *M* can be any positive or negative integer, the grating period as defined by (2.10) will have multiple solutions. Since negative period lengths are unphysical, we need only consider the positive diffraction orders. When *p* is set equal to 1, then (2.7) will allow only two possible solutions (using the equality condition). The first solution is for when *M*=0, resulting in $\sin\theta_d = -1$, or $\theta_d = -\pi/2$. In this case, we have a feed-forward effect, and the light experiencing zero-order diffraction continues along the direction of propagation. The second solution is for M=1, resulting in $\sin\theta_d = 1$, or $\theta_d = \pi/2$. In this case, we have a feedback effect, and the light coupled into the first diffraction order is reflected backwards from the direction of propagation. Diffraction orders greater than 1 do not provide any physical diffraction angles for this p=1, or first-order, grating.

From (2.10), we see that we can have larger, and therefore easier to fabricate, grating periods by setting p equal to larger orders, i.e. $p > 1$. The trade-off for this is that additional diffraction orders now contribute in potentially unwanted ways. In a second-order grating where we set p=2, in addition to the feed-forward solution of (2.7) when M=0 and a feedback solution when M=2, we have an additional diffraction angle when M=1. This results in a diffraction of $\sin\theta_d = 0$, or $\theta_d = 0$. This means that for a second-order grating where p=2, light coupled into the first diffraction order, where M=1, will be reflected perpendicular to the direction of propagation. This light will tend to radiate away from the laser cavity and result in additional optical losses. It can also be exploited to produce surface-emitting laser designs [24]. The result is similar for a third-order grating with p=3, except there are now two solutions in addition to the feed-forward and feedback case, when M=1 and M=2. These solutions will result in light radiating at angles of $\theta_d = \pm\sin^{-1}(1/3)$. These radiating diffraction orders will exist when $p > 1$, resulting in light radiating away from the waveguide, increasing the optical losses. In this thesis, we will see in Chapter 5 and 6 how these higher order grating losses can be minimized by adjustment of the grating geometry. As a result of using higher order gratings, we can exploit standard optical lithography processes to allow high-volume manufacturing of these LC-DFB lasers.

2.4 Manufacturing Distributed Feedback Lasers

The earliest reported work on distributed feedback lasers was done by Kogelnik and Shank [25], [26]. The periodic index variations in this early work were created using unstable gelatin films. Early work by Nakamura *et al.* used ion milling [27] and chemical etching [28], while Scifres, Burnham and Streifer fabricated heterojunction DFB lasers using ion milling on ultraviolet-exposed photoresist [29]. Room-temperature devices were reported by Casey, Somekh and Ilegems in 1975 [30]. The extension of room-temperature DFB lasers into telecommunications wavelengths was achieved with the use of InP/InGaAsP materials by Uematsu, Okuda and Kinoshita [31], and Utaka *et al.* [32].

A typical DFB manufacturing process is described by Carroll *et al.* [20], and shown in Figure 4. The process begins at step 1 with a semiconductor wafer, often chosen to be InP for lasers operating in telecommunications wavelengths (1300 - 1600 nm). High-quality crystalline semiconductor wafers can be grown using the Czochralski method. Next, in step 2, the desired epitaxial layers are grown above the semiconductor substrate, through techniques such as molecular beam epitaxy (MBE) or metal-organic chemical vapour deposition (MOCVD). These layers will provide optical and electrical confinement in the active layer. The optical confinement is due to larger refractive indices in and around the active layer, while electrical confinement is provided by doped heterostructures surrounding the active layer. The active region can consist of bulk material, quantum-wells, or quantum dots. More details on the design of the epitaxial growth structure will be given in Chapter 3. Once the lower epitaxial layers are grown, the grating is defined in a resist. This is often done by exposing a photoresist to a periodic standing wave pattern generated by an ultraviolet laser source. Another alternative technique is to use electron-beam (e-beam) lithography, which uses special electro-sensitive resists. E-beam lithography has a high resolution, allowing more precise grating structures, such as first-order gratings, and phase-shifted gratings. However, e-beam lithography is a serial exposure technique that is a relatively slow, expensive fabrication method compared to optical lithography. Once the grating has been defined

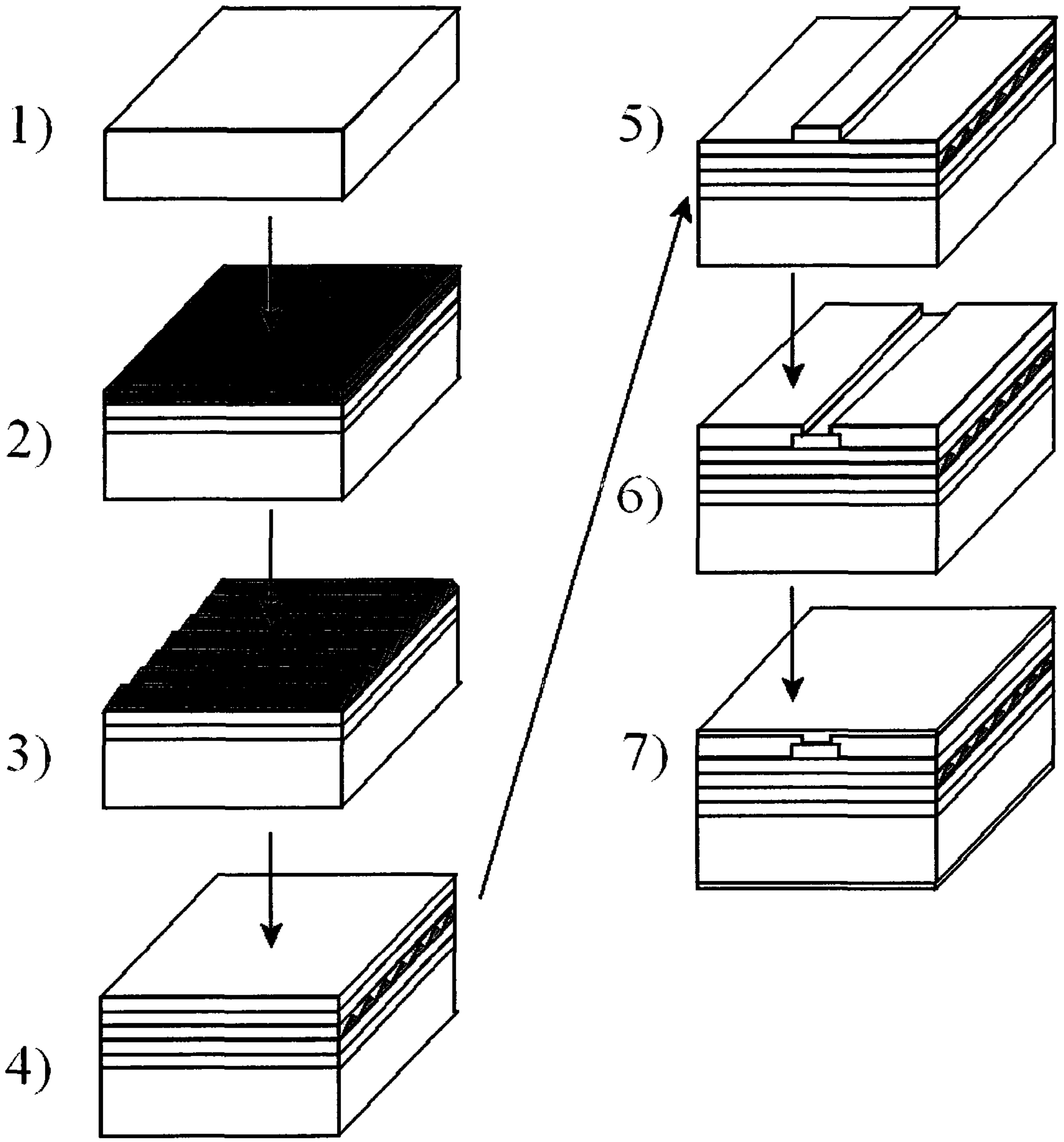

Figure 4. **Example of a standard DFB fabrication process, 1) as-grown InP wafer, 2) growth of lower layers, 3) patterning of grating, 4) growth of upper layers (regrowth), 5) patterning of waveguide ridge, 6) dielectric deposition and via etch, 7) formation of top and bottom metal contacts.**

in the photoresist, it can be etched onto the semiconductor material, shown as step 3 in Figure 4. The grating is then overgrown with the upper layers of the laser diode in step 4. In step 5, transverse optical confinement structures, such as a waveguide ridge or buried heterostructure, can be created using standard photolithographic techniques like contact lithography. Insulating dielectric layers are then grown above the heterostructure, with vias etched into the areas where electrical injection is desired in step 6. Ohmic contacts are formed above and below the device in step 7, typically using evaporation and/or electroplating, providing the n- and p-contacts. The substrate is often thinned to reduce the resistance of the device before applying the n-contact.

E-beam lithography allows a high degree of control over the grating parameters compared to using ultraviolet standing waves when fabricating DFB gratings. The slow speed and expense of e-beam lithography, however, are major drawbacks. E-beam has generally been used in a complementary fashion with optical lithography, with e-beam providing the one- off masks and reticles that are then used by optical lithography for high-volume manufacturing. We can get more control over grating parameters than ultraviolet, and a higher throughput than e-beam, by using stepper lithography for grating fabrication. In stepper lithography small repeatable sections of a wafer, with fine resolution features, are optically exposed in a step-and-repeat fashion. The mask features are projected a distance from the mask and de-magnified, usually by a factor of 4x or 5x, to allow fine resolution mask features. For instance, to produce 0.1 μm features on the wafer using 5x stepper lithography, the mask will actually have a feature size of 0.5 μm. This has the additional benefit of making any dirt or particles on the mask proportionally smaller on the wafer. Stepper lithography offers a compromise between speed and precision during fabrication. A stepper lithography system was demonstrated in 1977 by the GCA Corporation, and has steadily improved in both resolution and stepper tile size in the past thirty years. An outline of the history of stepper lithography can be found in [33]. In i-line stepper lithography, developed in the mid-1980s, the light source is a mercury lamp filtered for the i-line of the spectrum, at a wavelength of 365 nm. This allows a resolution of 365 nm, a value that is near the 600 nm period length of 1310 nm DFB lasers, making the use of i-line stepper lithography attractive for these devices.

2.5 Laterally-Coupled Distributed Feedback Laser Review

The previous description of the fabrication of a standard DFB laser in Section 2.2 reveals a fabrication inefficiency: the requirement for two separate epitaxial layer growth steps, one before and one after the creation of the DFB grating. This additional regrowth requirement will reduce the manufacturing throughput and introduces the potential of damage to the surface of the wafer while being handled between growths.

Corrugated-ridge, or laterally-coupled gratings for DFB lasers eliminate this regrowth step. In laterally-coupled distributed feedback (LC-DFB) lasers, the fabrication steps, shown in Figure 5, are the same as for the standard DFB laser shown in Figure 4, except now in step 3 the grating is patterned out of the upper layers of the epitaxial layer structure, thus providing both optical confinement and a feedback grating in a single fabrication step. LC-DFB lasers were first fabricated by Miller *et al.* of the University of Illinois in 1991 using e-beam lithography [34]. Despite its drawbacks mentioned above, e-beam lithography has remained the most popular choice for the fabrication of LC-DFB lasers [34]-[46]. The reason for this is the stringent grating specifications. They must have deep enough sidewalls to create strong coupling to the evanescent field of the optical mode, finely-spaced enough to reflect the correct Bragg wavelength, and sufficiently smooth and vertical to minimize scattering losses.

Miller's original design demonstrated the feasibility of LC-DFB lasers, but had a poor side-mode suppression ratio (SMSR). The SMSR is the ratio between the lasing peak and the next highest peak in the output spectrum of the laser, shown as 50 dB in Figure 1. The facets of this laser did not have anti-reflection coatings, causing Fabry-Perot modes that degraded the laser performance. The threshold current was also somewhat large for this design, with a value of > 100 mA.

Wong *et al.* of the Massachusetts Institute of Technology described the possibility of creating first-order sidewall gratings using x-ray lithography in 1993 [35]. The gratings

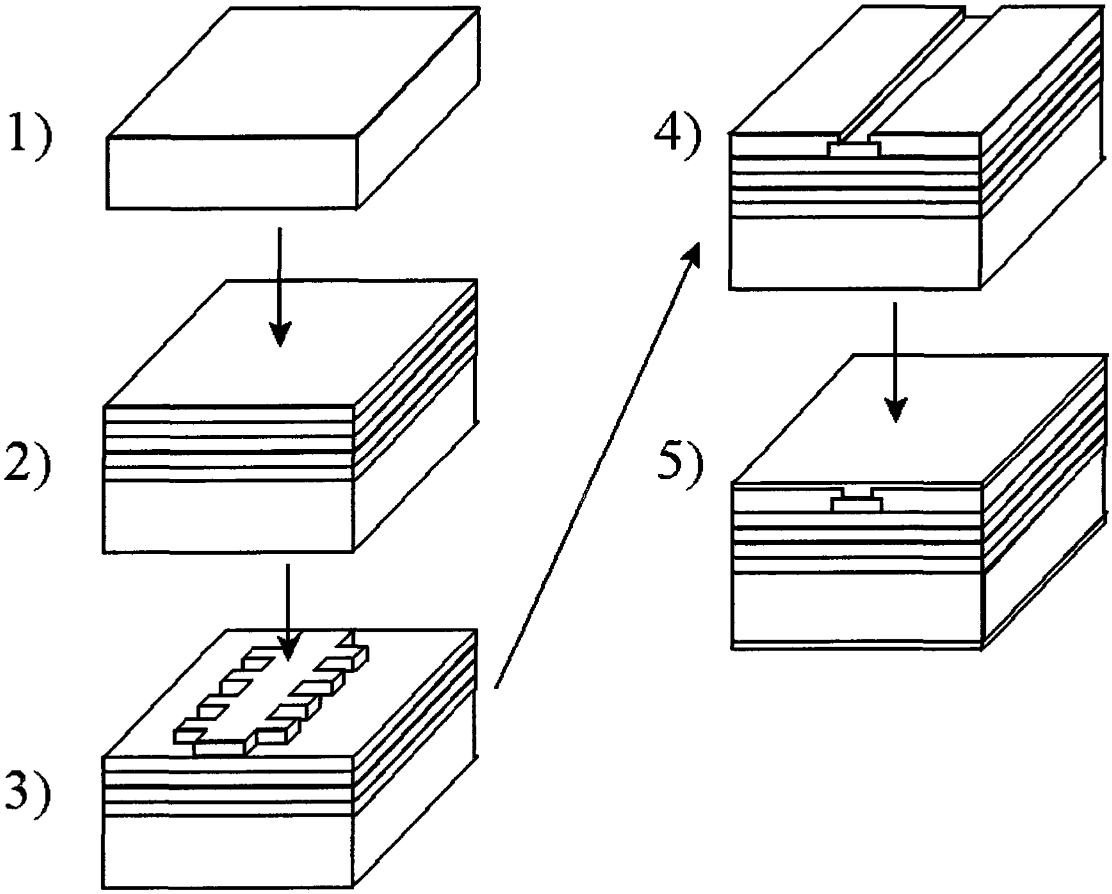

Figure 5. **Example of laterally-coupled distributed feedback laser fabrication. 1) As-grown InP wafer, 2) growth of all epitaxial layers, 3) patterning of grating, 4) dielectric deposition and via etch, 5) formation of top and bottom metal contacts**

were created in two separate steps: a chemical etch to define the ridge, then x-ray lithography to etch out the grating. The results appeared promising, but no demonstration of lasers was ever published by this group. R.D. Martin *et al.* of the University of Delaware, Jet Propulsion Laboratory, and Cornell University demonstrated a LC-DFB laser on InGaAs-GaAs-AlGaAs in 1994 [36]. The threshold current was 11 mA with an SMSR of 30 dB for a wavelength of 937 nm. E-beam lithography and chemically-assisted ion beam etching (CAIBE) were used to fabricate the grating. Further published work from this group includes similar results from Tiberio *et al.* [37] and more details on the continuous-wave performance of the LC-DFB laser, including measurement of the coupling coefficient, by Martin *et al.* in 1995 [38].

Watanabe *et al.* of Pioneer Electronic Corp. and the University of Tokyo demonstrated LC-DFB lasers using a MQW active region fabricated using a wet-dry hybrid etching process in 1998 [39]. They were able to achieve threshold currents of 18.5 mA and SMSR values of > 40 dB for as-cleaved devices of various cavity lengths. They used e-beam lithography to define the grating, followed by reactive-ion etching (RIE) and then wet etching. The wet etching step removed any layer material remaining from the dry etch, smoothing the device structure and improving the precision of fabrication compared to using only dry etching. Further work published by this group include a 1300 nm LC-DFB laser with a threshold current of 17 mA and SMSR of > 45 dB [40].

J.T. Hastings *et al.* of the Massachusetts Institute of Technology fabricated apodized sidewall gratings [41]. Apodized gratings modulate the periodic waveguide with a lower-frequency sinusoid or a Gaussian to produce filters with lower cross-talk. Applied to DFB lasers, these apodized gratings promise a better SMSR. The gratings that were fabricated were tested as filters, and demonstrated an enhanced suppression of side-modes compared to uniform gratings. The apodized gratings, however, had poorer TE mode performance, with a higher transmission minimum in the stopband. The gratings were manufactured using a technique known as spatial-phase-locked electron beam lithography. This technique accurately positions the electron beam using a grid patterned on the substrate using interference lithography. This resulted in a mean stitching error of +/- 0.6 nm, a high degree of accuracy compared to the grating period of ~225 nm. A patent relating to the apodized grating structure was granted in 2002 [42].

Müller *et al.* of Nanoplus Nanosystems, the University of Würtzburg, and Alcatel Corp. presented results on wide-range tunable LC-DFB lasers in 2001 [43]. The grating is not defined from etched semiconductor material, but from laterally-positioned Cr metal that is evaporated on the semiconductor, and then lifted off in the regions where there are gaps between the grating teeth. This Cr grating demonstrated a tuning range of 25 nm using a two-section electrode. A threshold current of 32 mA and SMSR of > 30 dB was achieved. This design was extended to quantum dot active regions in 2002 [44], where the tuning range was extended to 30 nm with a threshold current of 13 mA and similar SMSR values (> 30 dB). The latest version of this laser with a quantum dot active region demonstrated a 45 dB SMSR for temperatures up to 85 °C [45].

Also in 2001, Wiedmann *et al.* of the Tokyo Institute of Technology and Hanyang University in Korea demonstrated a laterally-coupled DFB/DBR laser [46]. At one of the DFB region is the output facet, at the other end is a highly-reflective DBR grating region. Second-, third-, and fifth-order gratings were tested. The higher order gratings had a lower expected coupling coefficient, but fabrication difficulties decreased the coupling coefficient of the lower (first and second) order gratings. The DBR region focuses nearly all of the light out of a single facet producing a higher single-ended output power. They were able to achieve a 33 dB SMSR at a bias current of ~30 mA for a 220 μm long laser cavity. The threshold current for this 1550 nm laser was 12.4 mA.

Bach *et al.* of the University of Würzburg and Alcatel created an LC-DBR laser using focused ion beam lithography (FIB) [47]. Using FIB, Ga^+ ions were implanted on either side of the ridge waveguide. The bandgap of the implanted regions shifted after rapid thermal annealing due to quantum well intermixing. The crystal quality of the InP was also changed in the implanted regions, resulting in a strongly increased HF etch rate, and allowed the formation of an index grating. Threshold currents as low as 8 mA, SMSR values of > 40 dB and continuous wave efficiencies of 0.37 W/A were measured for a 600 μm long device. In 2004, this device design was used in a 22 GHz modulation scheme [48] .

Schreiner *et al.* of the University of Stuttgart and Alcatel created tunable LC-DFB lasers using a separate active tunable DBR region and an uncorrugated gain region [49]. Each region has a separate driving current, and the device will behave as a DFB laser when the corrugated region is biased to provide gain, or as a DBR laser when the uncorrugated region is biased to provide gain. In the DFB mode, the device showed SMSR values of

~30 dB. The threshold current is not clearly stated, as it depends on two separate current sources, but it is approximately 30 mA. This device demonstrated tunability over a range of wavelengths between 1590.8 nm and 1595.2 nm.

In 2003 B. Reid *et al.* of Bookham Technology presented an LC-DFB with third-order gratings fabricated using stepper lithography [50]. Their work describes a fabrication process similar to that used for the LC-DFB lasers in this thesis. Threshold currents of ~80 mA were required for these lasers. SMSR values of over 55 dB, linewidths < 1 MHz, and optical output powers higher than 100 mW were achieved. The LI characteristic demonstrated a kink that the authors believed indicated a stronger grating than expected. They speculated that this stronger grating trapped more light in the cavity, inducing spatial hole burning as the power increased. This shows the importance of proper grating optimization in LC-DFB laser design and is a motivator for work described in this thesis. A patent for a weakly-guided LC-DFB laser was granted to B. Reid in 2003 [51]

A quantum well LC-DFB laser was described by Das *et al.* of Osaka University in 2004 [52]. They used a standard manufacturing technique, e-beam lithography with RIE, but also incorporated a $\lambda/4$ phase shift to improve performance. They achieved an SMSR of 46 dB and a threshold current of 15 mA at a wavelength of 967.8 nm.

In 2005, Wang *et al.* of Tsinghua University fabricated deep-etched gratings for LC-DFB lasers using holographic exposure with inductively-coupled plasma RIE [53]. A second-order grating with a duty cycle of 0.3 was used for this laser. This is not an optimal point for fabrication, as will be demonstrated in our analysis of Section 5.1. The threshold current was 34 mA with an SMSR of > 45 dB.

Laterally-coupled gratings can also be used for non-telecom wavelengths. In 2005, Golka *et al.* presented a GaAs/GaAlAs quantum cascade laser for long wavelengths (10.7 μm), in the mid-infrared range [54]. For this wavelength, the necessary period was 1.72

μm, and simple contact lithography was sufficient to define the grating. The quantum cascade laser had to be driven in a low-temperature (78K), pulsed regime (5kHz repetition rate) to achieve lasing; an SMSR of 20 dB was observed under these conditions.

In 2006, a dual-wavelength source was created by Pozzi *et al.* of Università degli Studi di Milano by etching gratings with different periods on either side of the ridge [55]. The grating period difference was 0.07 nm, for wavelengths of 1346.32 nm and 1346.47 nm. Low threshold currents were claimed but not explicitly stated. The SMSR reported was > 30 dB. Photomixing of the output using a fast photodetector and RF spectrum analyzer demonstrated the generation of millimeter-wave signals at 22.5 GHz.

Most recently, Laakso *et al.* of the Tampere University of Technology in Finland have demonstrated LC-DFB lasers with higher order gratings created using a nano-imprinting process [56]. Their 980 nm lasers had up to 50 dB SMSR, with a threshold current of 30 mA and a slope efficiency of 0.34W/A for a 570 μm long LC-DFB with a third-order grating, when operated at a temperature of 10°C.

Table 1 summarizes the performance of the LC-DFB lasers that have been fabricated thus far. The lasers listed in Table 1, with the exception of Miller, have SMSR values of 15-55 dBs. To avoid inter-channel interference in WDM systems, however, it is desirable to have SMSR values of > 30 dB [57]. Threshold current values range from 11 to 100 mA, lower threshold currents will reduce the power consumption of the laser. Most of the laser designs have been designed to operate at telecommunications wavelengths of around 1.3 or 1.5 μm, and have been fabricated using e-beam lithography. Clearly, there is considerable scope for improvement in LC-DFB laser design.

Laser	Threshold current (mA)	Side-mode suppression ratio (dB)	Fabrication technique	Wavelength (nm)	Reference
Miller 1991	100	High (FP modes occurred)	E-beam	1049.8-1064	[34]
Tiberio 1994	11	30	E-beam /CAIBE	937	[37]
Watanabe 1998	18.5	40	Wet-dry hybrid / E-beam	1570	[39]
Chen 2000	17	45	E-beam	1300	[40]
Schreiner 2001	30	> 30	E-beam	1589-1595	[49]
Wiedmann 2001	12.4	33	E-beam	1550	[46]
Muller 2002	13	> 35	E-beam	980-1010	[44]
Reid 2003	~80	55	Stepper	1470-1490	[50]
Bach 2004	70	40	Focused ion beam	1560-1570	[48]
Das 2004	46	15	E-beam (lambda/4 shifted)	967.8	[52]
Wang 2005	34	45	Holographic	1545	[53]
Golka 2005	590	20	Contact UV	10 700 (mid-IR)	[54]
Pozzi 2006		30	E-beam	1346	[55]
Gerschutz 2008	17	45	E-beam	1300	[45]
Viheriälä 2009	30	50	Nano-imprinting	980	[56]

Table 1. Summary of reported LC-DFB laser specifications

2.6 This Work

The laterally-coupled DFB laser described in this work is shown in a cutaway view in Figure 6. The goal was to create an LC-DFB laser that could be fabricated using i-line stepper lithography. The epitaxial layer structure, described in more detail in Chapter 3, is made of InP/InGaAsP material grown on an n-doped InP wafer.

The waveguide ridge is patterned using 5x i-line lithography, a lithographic technique that has a minimum resolution of 365 nm. For the target wavelength of 1310 nm, first- and second-order gratings would require grating periods of ~200 nm and ~400 nm, respectively, too fine for i-line stepper lithography. However, third-order gratings, with a period of ~600 nm, are just possible. The LC-DFB lasers described here use third- and fourth-order gratings. The use of higher order gratings requires modifications to the modeling and design techniques generally used for first-order DFB lasers. The radiation from the lower diffraction orders must be taken into account to properly to design a DFB laser with higher order gratings.

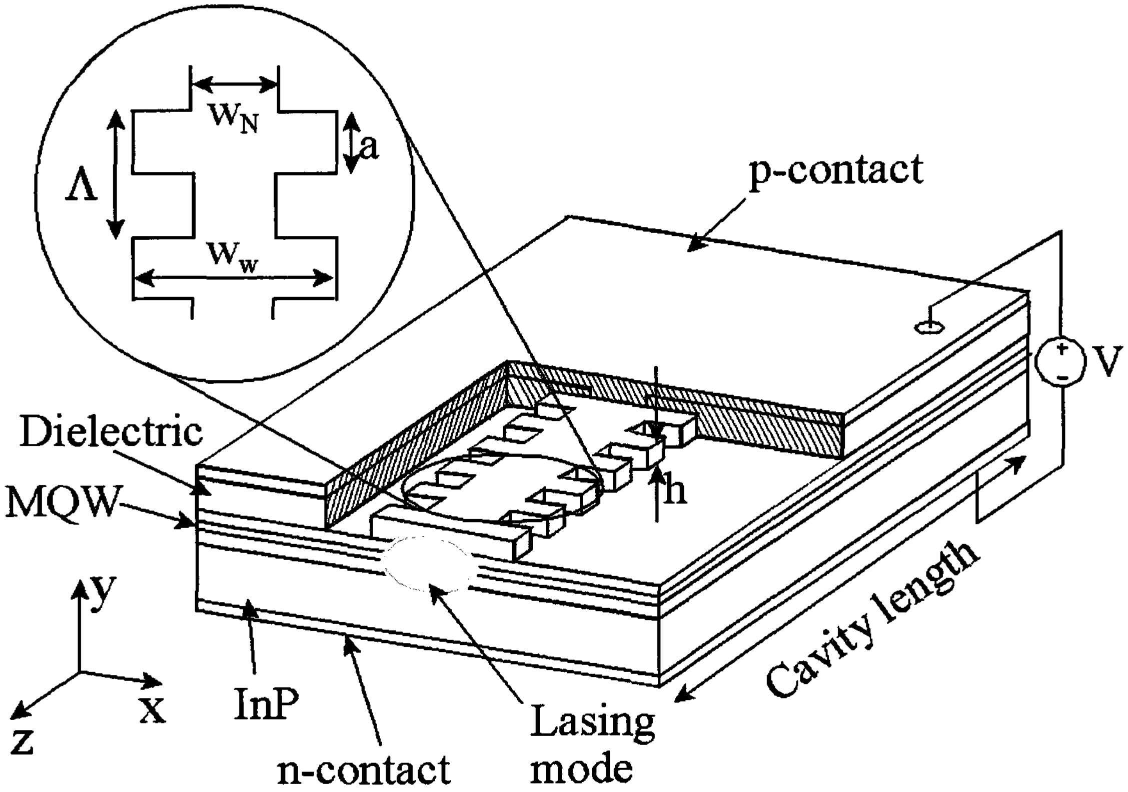

Figure 6. Cutaway schematic of the LC-DFB laser described herein

CHAPTER 3 - DESIGN OF EPITAXIAL GROWTH STRUCTURE

The epitaxial growth structure of our LC-DFB laser must provide optical gain around a wavelength of 1310 nm, efficiently inject carriers into the active region, and provide optical mode confinement. The goal of the epitaxial layer design was to simultaneously achieve these goals along with a i) low threshold current, ii) low electrical resistance, and iii) high efficiency across a broad temperature range. The growth structure was designed in two parts: the active region and the surrounding double heterostructure epitaxial layers.

3.1 Multi-Quantum-Well Active Region

The active region of the device will ideally provide optical gain with a minimum amount of current density, and have a well-defined output polarization. These requirements can be met with the use of a strained multi-quantum-well (MQW) region. Quantum well regions have a lower threshold current density than similar bulk regions. This is due not only to the smaller size of quantum well active regions compared to bulk regions, but also due to different distributions of carrier states with energy as the dimensions are reduced to quantum sizes. In semiconductor crystals carriers are not distributed uniformly, but according to Fermi statistics and the number of states available for a given energy. Figure 7 shows such a density of states for bulk material, $\rho_{3D}(E)$, and quantum well material, at different subband levels, $\rho_{2D}(E)$. The quantum well density of states follows a staircase pattern with an envelope defined by the bulk density of states, which has a parabolic profile. With generally fewer states available for a given energy, carriers will tend to fill up the lower energy states for quantum wells more quickly than for bulk materials as carrier injection increases. This will result in the population inversion condition for optical gain being realized for smaller carrier densities for quantum well materials compared to bulk materials. Quantum dot active regions hold promise for even lower threshold devices, having a delta-shaped density of states characteristic, but present state-of-the-art quantum dots remain difficult to fabricate

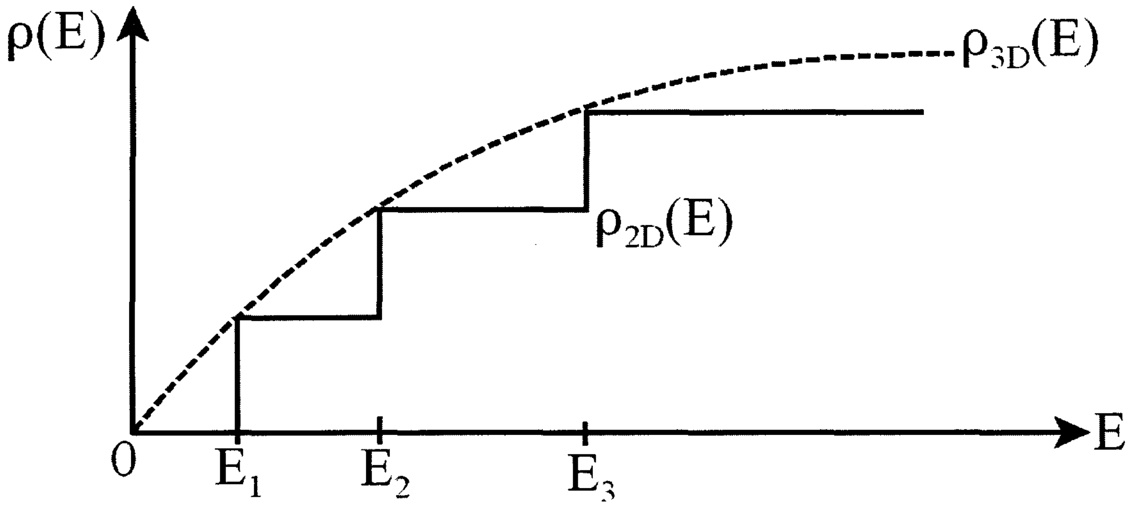

Figure 7. **Density of states for bulk material, ρ_{3D} (dashed line), and quantum well material, ρ_{2D} (solid line), *vs.* energy**

reliably compared to quantum wells, particularly in a mass-manufacturing environment. In contrast, advances in epitaxial layer growth techniques have made the fabrication of high-quality quantum well layers routine.

The periodic crystal lattice of semiconductor materials such as InP and InGaAsP produce electronic bandstructures, with free electrons in the conduction band and free holes in the valence band. While in reality there are many electronic bands, we use the approximation of Kane's model to simplify the bandstructure. In this approximation, the conduction band and six valence bands are taken into account: a light hole, heavy hole, and a doubly-degenerate spin-orbit split-off band, as shown in the energy-momentum diagram of Figure 8. The spin-orbit split-off bands are due to the splitting in energy levels depending on the spin (up or down) of an electron. All other bands are neglected. Another common approach is Luttinger-Kohn's model, where the same bands are solved, but also taking into account the interaction of these bands with all other bands using perturbation theory.

In direct bandgap semiconductors such as InP and InGaAsP, the extrema of the conduction band (the Γ-valley) and valence bands (at E=0) are aligned in the energy-momentum diagram, as pictured in Figure 8. This means that during radiative recombination an electron can drop from the conduction band to the valence bands directly, without the mediation of a phonon. Without energy wasted on heat-producing phonons, active semiconductor devices are much more efficient when direct bandgap materials are used. The energy separation between the valence bands and the conduction band are determined by the properties of the materials used. In this work, $In_{1-x}Ga_xAs_yP_{1-y}$ is used for the quantum well and barrier layers. The molar concentrations of Ga and As, x and and y, are chosen to achieve the desired transition energy (wavelength). The transition energies are determined from the energy band diagram using the stationary Schrödinger's equation,

$$\left[-\frac{\hbar^2}{2m}\nabla^2+V(y)\right]\Psi(x,y,z)=E\Psi(x,y,z) \tag{3.1}$$

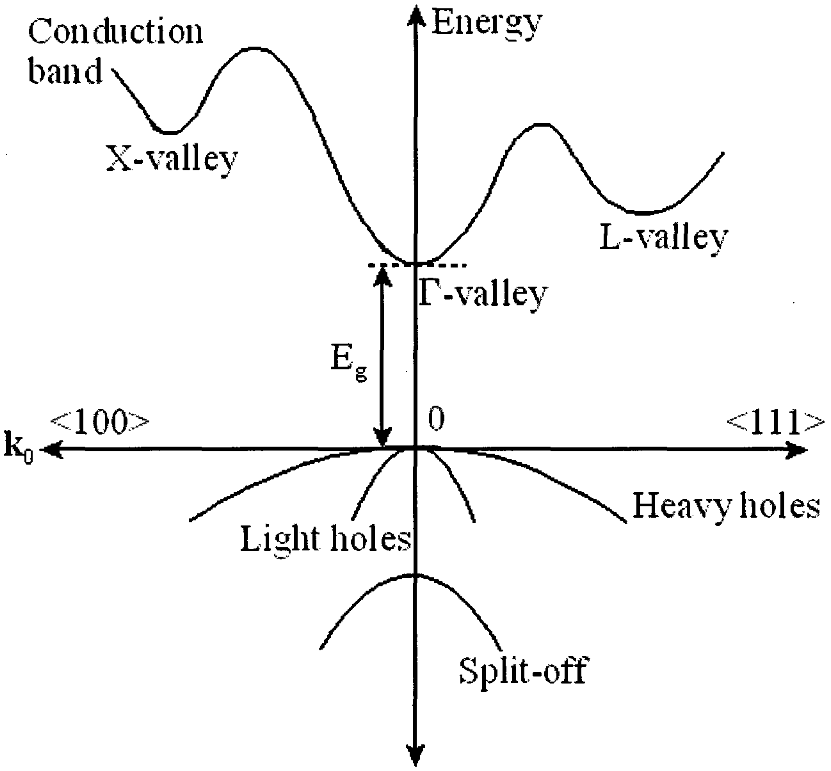

Figure 8. Band structure of a semiconductor crystal according to Kane's model

where $\Psi(x,y,z)$ is the wavefunction, E is the energy eigenvalue associated with the wavefunction, $\hbar$ is the reduced Planck's constant, m is the mass of the particle, and V is the potential energy experienced by the particle. For carriers in a semiconductor material, the mass is replaced by an effective mass, m^*, due to the influence of the periodic potential of the surrounding crystal structure. The effective masses for electrons, light holes, and heavy holes are denoted m_e^*, m_{lh}^*, and m_{hh}^*, respectively.

Since carriers in a quantum well experience confinement in the plane (here denoted x-z) the wavefunction takes the form of the free-electron wavefunction in these unbounded spatial directions:

$$\Psi(x,y,z) = \frac{e^{ik_x x + ik_z z}}{\sqrt{A}} \varphi_n(y) \tag{3.2}$$

In this equation, A is a normalization constant, $k_{x,z}$, is the wavenumber in the x-,z-direction, and $\varphi_n(y)$ is the normalized wavefunction in the y-direction corresponding to the n^{th} eigenvalue, E_n. The potential energy, V, is determined by the energy band diagram, and for epitaxially grown layers can be considered to have the form of a square well, with a potential energy difference of V_0 between the well and barrier layers. The value of V_0 is related to the difference in bandgap between the quantum well and barrier materials, with the bandgap discontinuity split between the conduction and valence band quantum wells. An example of a square quantum well of InGaAsP/InP material is shown in Figure 9.

The square quantum well is a classic problem in quantum mechanics, also known as the finite barrier model. It has even wavefunction solutions (where n=0,2,4,...) of the form:

$$\varphi_n = \begin{cases} C_1 e^{-\alpha_n(|y|-L/2)} & |y| \geq L/2 \\ C_2 \cos k_n y & |y| < L/2 \end{cases} \tag{3.3}$$

where $C_{1,2}$ are normalization constants, L is the thickness of the quantum well,

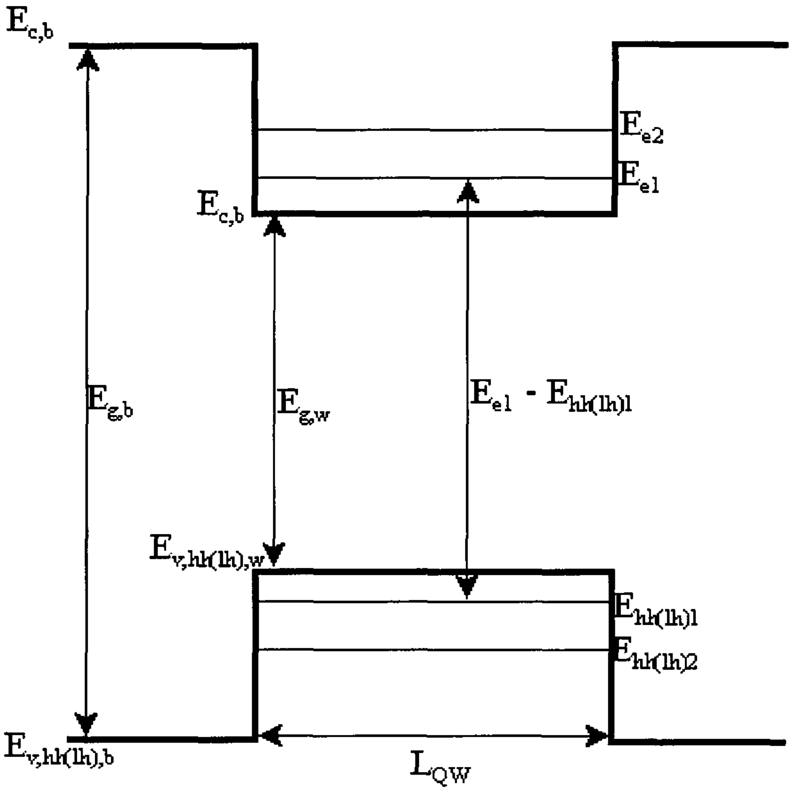

Figure 9. **Ground-state transition energies of an InGaAsP/InP quantum well**

$$k_n = \frac{\sqrt{2m_w^* E_n}}{\hbar} \tag{3.4}$$

is the wave number, and

$$\alpha_n = \frac{\sqrt{2m_b^* (V_0 - E_n)}}{\hbar} \tag{3.5}$$

is the attenuation coefficient. Schrödinger's equation also admits an odd solution (n=1,3,5,...) , with the wavefunction described by a sine rather than cosine function within the well. However, since we are concerned with the ground-state transitions where the energy is lowest, we will be solving for even wavefunctions where n=0. In the above equation the effective particle masses in the well and barrier regions are denoted by m_w^* and m_b^*, respectively. By applying the boundary conditions of continuity at the interface between the well and barrier regions of the wavefunction and its derivative divided by the effective mass, a combined equation for k_n and α_n can be obtained,

$$\alpha_n = \frac{m_b^* k_n}{m_w^*} \tan\left(k_n \frac{L}{2}\right) \tag{3.6}$$

Substituting (3.4) and (3.5) into (3.6) gives an eigenequation for the wavefunction energy levels, E_n.

In Kane's model, there are three possible transitions for an electron in the conduction band to recombine with a hole, producing additional energy that may produce stimulated emission (or spontaneous emission, phonons, etc.): conduction band to light-hole (C-LH), conduction band to heavy-hole (C-HH), and conduction band to spin-orbit split-off band (C-SS). The transition to the light hole and heavy hole bands are the most important, being the lowest energy radiative transitions. Since carriers injected into the quantum well will tend to relax into the lowest energy states, the lowest energy transitions will be the most probable. When the light inducing stimulated emission is TM polarized, the C-LH transition will be favoured, while the C-HH transition is favoured for TE polarization, as can be seen by a detailed calculation of the momentum matrix elements for TE and TM polarized light that will not be discussed here. TE polarized light has a higher gain than TM polarized light for materials such as InGaAsP when they are unstrained, resulting in light-hole and heavy-hole bands that are degenerate. The reader is referred to [22] for more details of this polarization dependency.

The light hole/heavy hole band degeneracy can be lifted by using strained layers. A strain is produced in epitaxially grown materials when adjacent layers have mismatched lattice constants. Strain will break the symmetry of the crystal lattice, resulting in generally different shifts for each of the conduction and valence bands. The strain must be kept relatively small (a few percent) to avoid defects in the lattice that can act as traps, producing undesirable carrier recombination. When a quantum well is fabricated using a tensile strained layer, the light hole band is shifted upwards in energy and the C-LH transition is favoured, causing TM polarized light to experience higher gain, as explained in more detail below. For sufficient tensile strain, TM polarized light will have greater gain than TE polarized light. For semiconductor optical amplifiers (SOAs), a low polarization dependent gain (PDG) is desirable, so quantum wells (or bulk materials) with enough tensile strain to have nearly equal amounts of gain for TE and TM polarizations are often used.

Lasers have opposite requirements - for a stable, coherent output the polarization state must be well-defined. The propagation constants of TE and TM polarized light will generally differ in ridge waveguides, leading to a broader output spectrum if both polarizations experience enough gain to support lasing modes. To avoid this, TE polarization is favoured by using compressively strained quantum wells. Applying a compressive strain shifts the heavy hole band upward, favouring the C-HH transition and selectively providing gain to TE polarized light. To minimize possible dislocations due to the compressive strain, the barrier layers are slightly tensile strained.

To calculate the effect of strain on the energy levels of a quantum well, the approach of Chuang is used [58]. The in-plane strain, ε, of a quantum well grown in the y-direction is defined as

$$\varepsilon = \varepsilon_{xx} = \varepsilon_{zz} = \frac{a_0 - a(x_w, y_w)}{a_0} \tag{3.7}$$

where a_0 is the lattice constant of the substrate material and $a(m,n)$ is the lattice constant of the material with the molar fractions x_w and y_w. ε is positive for a tensile strain and negative for a compressive strain. We assume that the strain is constant in the quantum well layers. This will generally be correct, assuming that we satisfy the stability condition for the net strain of a MQW structure. If the net strain along the MQW structure, ε^*, given by

$$\varepsilon^* = \frac{\varepsilon_{QW} L_{QW} + \varepsilon_b L_b}{L_{QW} + L_b} \tag{3.8}$$

is < 0.5%, where $\varepsilon_{QW(b)}$ is the QW (barrier) strain, and $L_{QW(b)}$ is the QW (barrier) thickness, it has been demonstrated experimentally and theoretically that there will be no misfit dislocations in the layer that will cause local strain defects [59]. We will ensure that the net strain satisfies this condition in the final MQW design.

Along the y-direction the strain, ε_{yy}, is

$$\varepsilon_{yy} = -2\frac{\sigma}{1-\sigma} = -2\frac{C_{12}}{C_{11}}\varepsilon \tag{3.9}$$

where σ is Poisson's ratio, and C_{11}, C_{12} are elastic stiffness coefficients. The amount of conduction band shift is:

$$\delta E_c = a_c\left(\varepsilon_{xx} + \varepsilon_{yy} + \varepsilon_{zz}\right) = 2a_c\left(1 - \frac{C_{12}}{C_{11}}\right) \tag{3.10}$$

where a_c is the conduction band hydrostatic deformation potential. The heavy-hole band band will be shifted by

$$\delta E_{HH} = -P_\varepsilon - Q_\varepsilon \tag{3.11}$$

where

$$P_\varepsilon = -a_v\left(\varepsilon_{xx} + \varepsilon_{yy} + \varepsilon_{zz}\right) = -2a_v\left(1 - \frac{C_{12}}{C_{11}}\right)\varepsilon \tag{3.12}$$

and

$$Q_\varepsilon = -\frac{b}{2}\left(\varepsilon_{xx} + \varepsilon_{yy} + \varepsilon_{zz}\right) = -b\left(1 + 2\frac{C_{12}}{C_{11}}\right)\varepsilon. \tag{3.13}$$

a_v is the valence band hydrostatic deformation potential and b is the shear deformation potential of the quaternary material. The light-hole band is shifted by

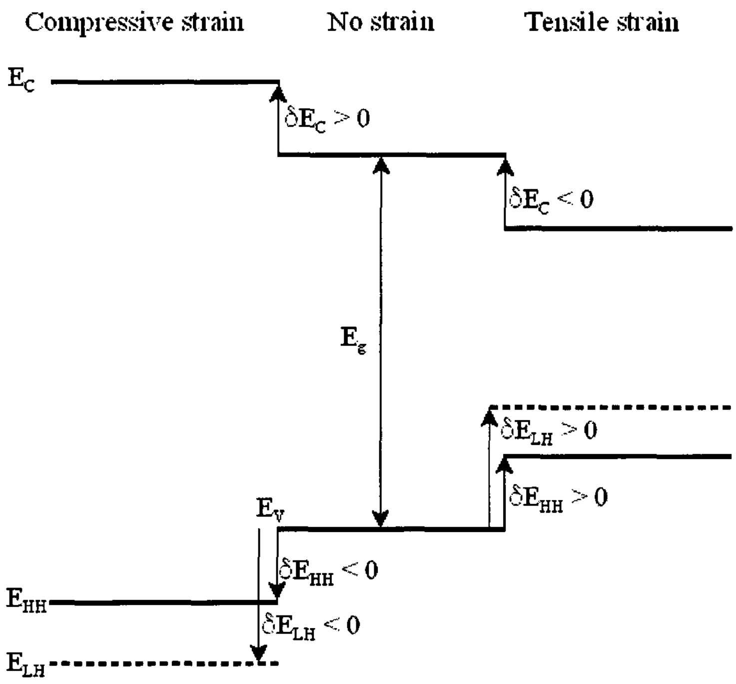

Figure 10. Band structure shifts due to strain (adapted from [58]).

$$\delta E_{LH} = -P_{\varepsilon} + \frac{1}{2}\left(Q_{\varepsilon} - \Delta_0 + \sqrt{\Delta_0^2 + 2\Delta_0 Q_{\varepsilon} + 9Q_{\varepsilon}^2}\right) \tag{3.14}$$

where Δ_0 is the spin-orbit splitting energy.

The effect of these band edge shifts is illustrated in Figure 10. For a tensile strain, the conduction band is shifted downwards, while the light-hole band is shifted above the heavy-hole band. For a compressive strain, the conduction band is shifted upwards, and the heavy-hole band is shifted above the light-hole band. As mentioned above, we will consider a compressively-strained QW structure to provide a TE polarized output. The transition energy of a compressively strained material is found by first obtaining the bandgaps of the QW and materials, neglecting strain effects. We use the formula of Chuang, [22]:

$$E_g = 1.35 + 0.668x_{w(b)} - 1.068y_{w(b)} + 0.758x_{w(b)}^2 + 0.078y_{w(b)}^2 - 0.069x_{w(b)}y_{w(b)} \\ -0.322x_{w(b)}^2 y_{w(b)} + 0.03x_{w(b)}y_{w(b)}^2, \tag{3.15}$$

where $x_{w(b)}$ is the Ga mole concentration, and $y_{w(b)}$ the As mole concentration, of the well(barrier) material. The strain effects are now taken into account, with the conduction band and heavy-hole band shifting the bandgap by an amount calculated in (3.10) and (3.11). The strain parameters used in these equations – ε, $a_{c,v}$, b, $C_{11,12}$, and Δ_0, as well as the absolute valence band potentials and effective carrier masses of the quaternary material, are found through linear interpolation of the binary material values. An example of this calculation is shown for the lattice constant, a, in Figure 11. The lattice constant determines the strain in the material according to (3.7). Quaternary materials with lattice constants below the line shown for the InP lattice constant, a_0, in the Figure will have a compressive strain, those above are tensile-strained. These values are used to construct two finite-barrier quantum wells – one for the conduction band electrons and one for holes in the heavy-hole band. The lowest energy level of each of these wells (E_{e1} and E_{hh1}, referring to Figure 9) is found from the numerical solution of (3.4)-(3.6). The total C-HH transition energy is the difference in these energy levels, including the strain-shifted bandgap, or $E_{e1} - E_{hh1}$, referring to Figure 9. The design of the MQW region for this laser is based on the previous strain analysis. The goal is to find a quantum well composition and thickness that will give a compressively strained structure with a ground-state transition energy corresponding to a wavelength of 1290 nm. Although the target gain peak is 1310 nm, a shorter wavelength is chosen for this analysis, and for the target photoluminescence as there will be greater heating when electrically pumped than when optically pumped, causing bandgap shrinkage [60].

The amount of strain is fixed at 0.9% (compressive) within the quantum well and 0.1% (tensile) within the barrier regions. This amount of compressive strain is sufficient to provide a significant amount of polarization-dependent gain, but not so large that dislocations will occur in the lattice, producing unwanted traps for the carriers. This amount of compressive strain has also shown low threshold currents and temperature

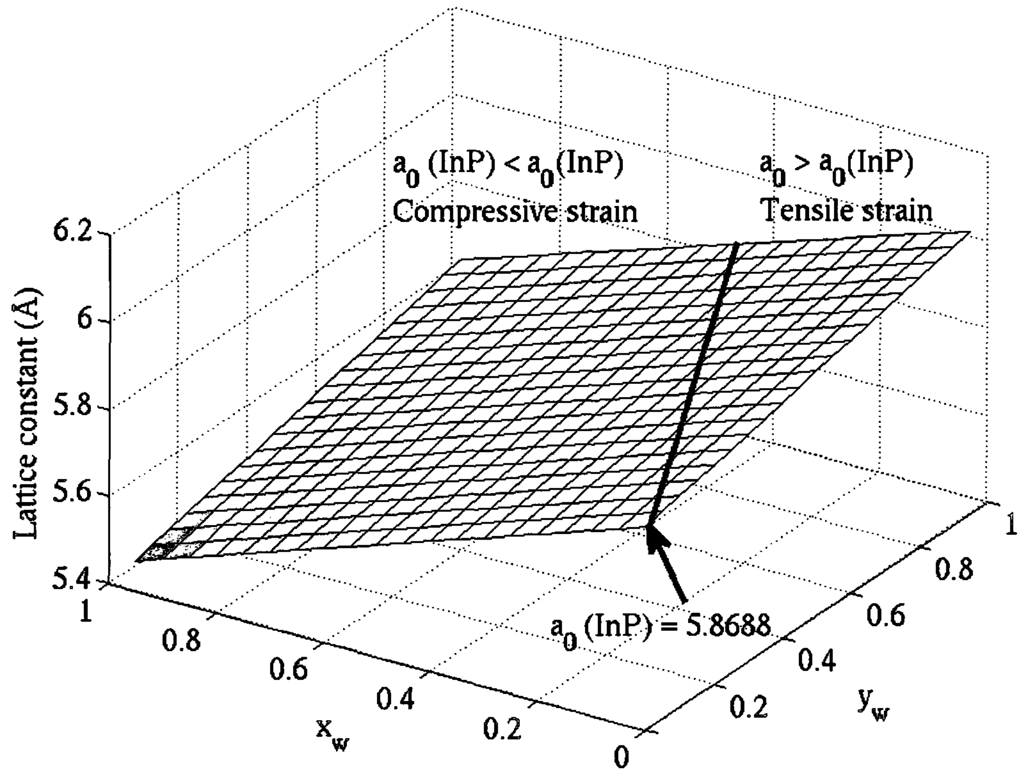

Figure 11. **Lattice constant, a_0, of quaternary $In_{1-x}Ga_xAs_yP_{1-y}$ material as a function of Ga mole concentration (x_w) and As mole concentration (y_w), showing regions of compressive and tensile strain when grown on an InP substrate.**

dependence. This will be confirmed in the final design using (3.8). The As concentration and bandgap for a compressive strain of 0.9% is shown in Figure 12. For these strain values, the Ga mole concentration in the QW is limited to $x_w < 0.35$, since greater x_w values would require $y_w > 1$, an unphysical value, to maintain 0.9% compressive strain. Since we are targeting a transition energy value of 0.96 eV, the bandgap of the quantum well material cannot exceed this value. This further restricts the value of $x_w > 0.05$, so the total range of the Ga mole concentration is $0.05 < x_w < 0.35$.

Restricting ourselves to quantum well and barrier material compositions that have 0.9% compressive and 0.1% tensile strains, respectively, we can find the quantum well thicknesses, L_{QW}, that result in our desired 0.96 eV C-HH transition energy. The contour map of solutions in Figure 13 describes these thicknesses (in nm) for different well (x_w)

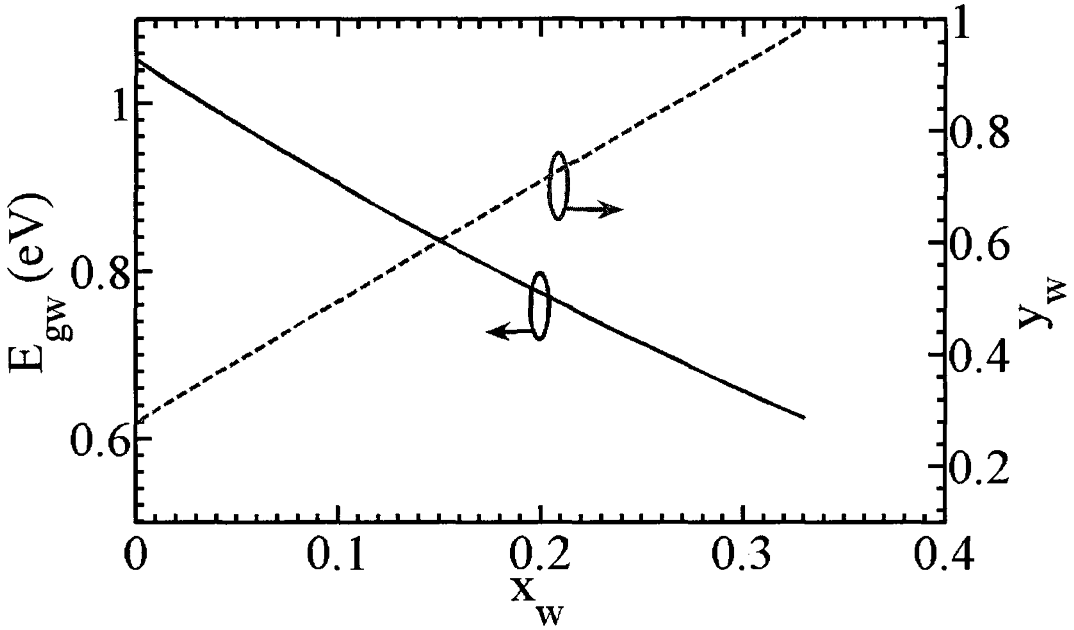

Figure 12. Bandgap energies and As mole concentrations of 0.9% compressively-strained InGaAsP *vs.* Ga mole concentration

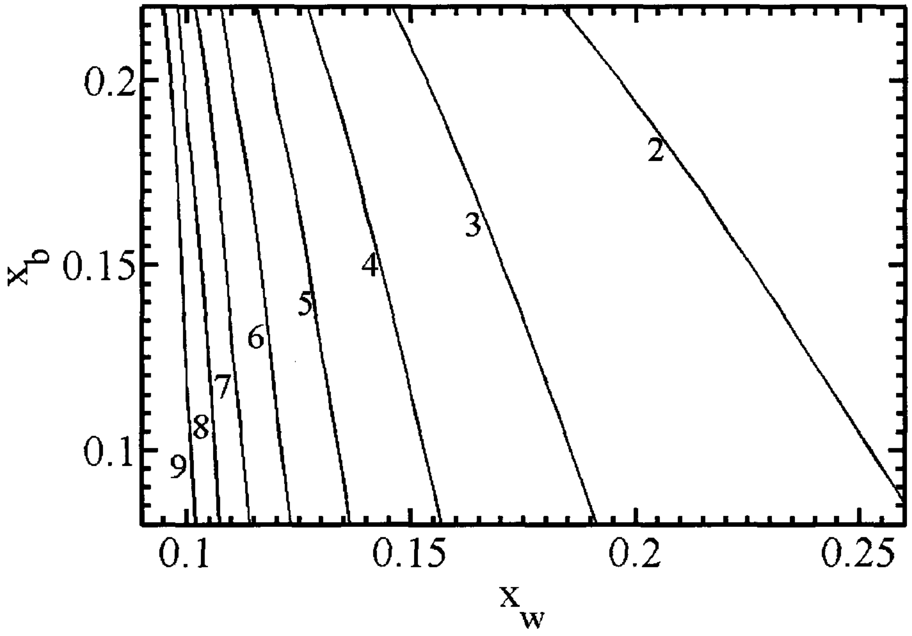

Figure 13. QW thicknesses (in nm) for a C-HH transition energy of 0.96 eV with different Ga mole concentrations in the well (x_w) and barrier material (x_b).

and barrier (x_b) material compositions. For each of these Ga molar compositions, $x_{w,b}$, the As molar composition, $y_{w,b}$, is selected so as to maintain the desired strain values. The quantum well thicknesses are more sensitive to x_w than to x_b, and they increase rapidly as $x_w \rightarrow 0.05$. The value of L_{QW} should not be too small – this will make it difficult to fabricate, and carriers will have a lower probability of being captured in the well. A quantum well that is too large will increase the amount of applied current required to reach the threshold current density. The analysis results of Figure 13 reveal that there are wide range of quantum well thicknesses that are available to reach our target transition energy of 0.96 eV and compressive strain of 0.9%. Numerous theoretical and experimental studies have been performed to optimize the well thickness of strained InGaAsP MQW structures, most targeted for the 1.55 µm wavelength. A good review of these works can be found in [61] and [62]. Most relevant to this structure is a review by Matsumoto *et al.* for compressively-strained 1.3 µm wavelength lasers in InGaAsP [63]. They found the lowest threshold current densities for quantum wells between 6-10 nm in thickness, when the barrier layers were 10 nm in thickness. As the net strain, given by (3.8) increases as L_{QW} increases, we select the lower end of this thickness range, or 6 nm. When using 10 nm thick barrier layers, this results in a net strain of 0.275% and a total MQW stack thickness of 90 nm, well within the critical thickness limits of < 0.5% for 100 nm thick MQW stacks. Thus, the final design of the MQW active region is chosen to be 6 nm 0.9% compressively strained of $In_{0.89}Ga_{0.11}As_{0.52}P_{0.48}$ separated by 10 nm barrier layers of 0.1% tensile strained $In_{0.79}Ga_{0.21}As_{0.42}P_{0.58}$. In reality, as will be described later in this Chapter, it is the PL spectrum, and not the exact material compositions, which are used when fabricating the epitaxial structure, but these compositions will provide a guidline for the PL spectrum and for further modeling using LAS2D software.

3.2 Double Heterostructure

The design of the double heterostructure was performed with the aid of LAS2D laser simulation software [64], using the active region determined in Section 3.1. LAS2D models the two-dimensional optoelectronic properties of Fabry-Perot (FP) laser structures. Although LAS2D is intended to accurately model only FP lasers, its results can be used to optimize the epitaxial layer structure of the LC-DFB lasers considered here. Both FP and LC-DFB lasers will have the same 2D cross-section, with the difference being that the ridge width of the LC-DFB laser will vary with the grating period in the longitudinal direction. This analysis will assume that this variation in ridge width will have a minimal impact on the efficient injection of carriers, i.e. that at an arbitrary point in the laser cavity, a 2D cross-section will provide good efficiency and gain for both DFB and FP lasers. LAS2D will also be used to provide an accurate three-dimensional model of the LC-DFB laser, described in more detail in Chapter 6. For the moment, however, the simple default FP laser model provided by LAS2D is sufficient, as long as we keep in mind that when using the laser characteristics generated to optimize the layer structure, they are relatively, but not absolutely, correct.

While LAS2D provides comprehensive details of the carrier and photon densities in the two-dimensional laser cross-section for a range of applied biases, there are three global metrics that are of the most interest when optimizing the epitaxial layer design: the current threshold, efficiency, and dynamic electrical resistance. These three characteristics are calculated by LAS2D for a FP laser, but it can be assumed that a DFB laser using the same cross-section will have similar relative characteristics, i.e. an epitaxial layer structure designed to have a low FP laser current threshold will also exhibit a relatively low current threshold if it is used for a DFB laser. We make this assumption based on the idea that the DFB grating provides only a minor perturbation to the fundamental mode shape and carrier injection profile in the transverse cross-section. Lateral current-spreading, where carriers are injected away from the centre of the waveguide mode, can cause a reduction in the efficiency of the laser, particularly when wide ridges are used. Thus, the wider of the anticipated grating ridge widths of 3 μm was used for the laser cross-section, as it will exhibit more of the undesirable lateral current spreading that should be minimized. The list of the LAS2D simulation parameters are summarized in Table 2. For further information on these parameters, the reader should

LAS2D parameter	Description	Value
Λ	Laser wavelength guess	1310 nm
L	Length of laser cavity	500 μm
T	Temperature (for non-isothermal model)	298 K
$\lvert R_{f,r} \rvert$	Front, rear facet intensity reflectivity	0.4
α_{scat}	Optical scattering loss	2.0 cm^{-1}
d_degf	Ground state degeneracy of donors (for ionization calculations)	2.0
Ed	Energy of donor level	0.01 eV
exp_un	Temperature dependency of electron mobility models	-0.5
exp_up	Temperature dependency of hole mobility models	-3
w_{cont}	Width of metal contact on top of ridge	1.5 μm
dxmin	Minimum mesh density	0.02 μm
dxmax	Maximum mesh density	0.1-0.5 μm
B0	Spontaneous radiative recombination constant	1x10^{-10} cm^{-3}
exp_rad	Temperature dependency of radiative recombination rate	-1.5
cn,cp	CHCC, CHSH Auger recombination constants	1x10^{-30} cm^{6}/s
alfn	Free carrier absorption parameter due to electrons in the quantum wells	3x10^{-18} cm^{-2}
alfp	Free carrier absorption parameter due to holes in the quantum wells	7x10^{-18} cm^{-2}
alfvb	Intervalence band absorption parameter due to holes in the quantum wells	5x10^{-18} cm^{-2}
t_augern, t_augerp	Temperature dependency of CHCC,CHSH Auger recombination rate	350 K
t_alfn, t_alfp	Temperature dependency of electron, hole free carrier absorption	325 K
t_alfvb	Temperature dependency of intervalence band absorption	325 K
gain model	Selects gain model used	Asada [66]
fgain	Scaling factor for calculated gain	1.00
fap	Scaling factor for free-carrier and intervalence band absorption	1.00
fup	Scaling factor for hole mobility	1.00
tau_in	Intraband relaxation time	0.1 ps
exp_tin	Temperature dependence of intraband relaxation time	-2.0

Table 2. LAS2D parameters

refer to the LAS2D manual [65]. Ideally, there would be multiple Fabry-Perot laser test structures using the same epitaxy as our DFB laser that would allow us to fine-tune the simulation parameters. However, for these simulations, we use the standard default values for the InGaAsP material system.

The optimization of a double heterostructure is a large multi-dimensional problem. For each layer, the thickness, doping level, and composition can be separately optimized, and each change in these parameters will have an effect on all other layers. For a seven layer structure, for example, there will be 21 degrees of freedom, not including additional parameters such as the ridge width and metal contact width. This problem can be simplified, however, since not every layer is equally important to the overall performance. The laser characteristics are very sensitive to only a few critical layers. A rough optimization of non-critical layers, and then a rigorous optimization of the critical layers will suffice to provide an acceptable epitaxial layer structure in a reasonable amount of time.

The most critical layers in the design are those of the active region, either a single layer for a bulk material or multiple well and barrier layers in the case of a MQW design. The composition and thickness of these layers is dictated by the wavelength requirements of the laser, as outlined above in Section 3.1. The quantum wells will be nominally undoped, although in practice some diffusion of Zn (the p-dopant) into the active region is common. The next most critical layers are those that are closest to the active region. The composition and doping of the p-doped layer just above the undoped MQW stack (referred to as layer 7 in Table 1) is one such critical layer. There are two reasons for this. First, this layer directly influences the concentration of holes injected into the MQW region. The hole concentration is a limiting factor on the MQW gain due to the much lower mobility of holes compared to electrons. Second, this is the p-doped layer with the highest optical confinement since it is the closest to the MQW region, i.e. the centre of the fundamental optical mode. Optical absorption in p-doped layers will tend to be greater than n-doped layers due to inter-valence band absorption, which is proportional to the local hole concentration. This also makes the the p-doped InP layer just above layer 7 (composing the bottom part of the ridge, or layer 8 referring to Table 3 at the end of this chapter) an important factor in the performance of the laser.

LAS2D simulations were run with different thicknesses, compositions, and doping levels of layer 7. Figure 14 shows the dependence of the threshold current, maximum efficiency, and dynamic resistance of the laser on these characteristics of layer 7. The threshold current, maximum efficiency, and resistance all drop as the thickness of this layer is reduced, according to Figure 14a. It is not desirable to have this layer be too thin, however, since it will result in more asymmetrical mode profiles. Asymmetrical mode profiles will result in greater coupling loss to an optical fiber, since fibers possess circular symmetery. The thickness of this layer was set at 0.15 microns, a value that shows a moderate resistance and threshold while maintaining a low mode asymmetry. The effect of the doping of this layer is shown in Figure 14b. The dynamic resistance has a minimal value at a doping level of 5×10^{17} cm^{-3}, while the threshold current shows a minimal decrease with lower doping, it is not particularly sensitive to the doping in this range of values. The doping level of 5×10^{17} cm^{-3} that minimized the dynamic resistance was chosen.

The effect of the material composition of layer 7 is shown in Figure 14c. There is a range of optimal values around y=0.15-0.3 where the threshold and resistance are low and there is a high tolerance for variation. This region of preferable values is where the bandgap of the material is large enough to encourage carriers to flow across the lower heterojunction into the MQW region, but not so large that carriers from the p-doped InP material in layer 8 do not see a significant drop in the bandgap at the upper heterojunction. An As concentration of y=0.156 was chosen, corresponding to a Ga concentration of x=0.071 for a material that is lattice-matched to InP.

It is common practice to insert a highly p-doped InGaAs and InGaAsP layer at the top of the growth structure to facilitate the electrical connection, producing a better ohmic p-

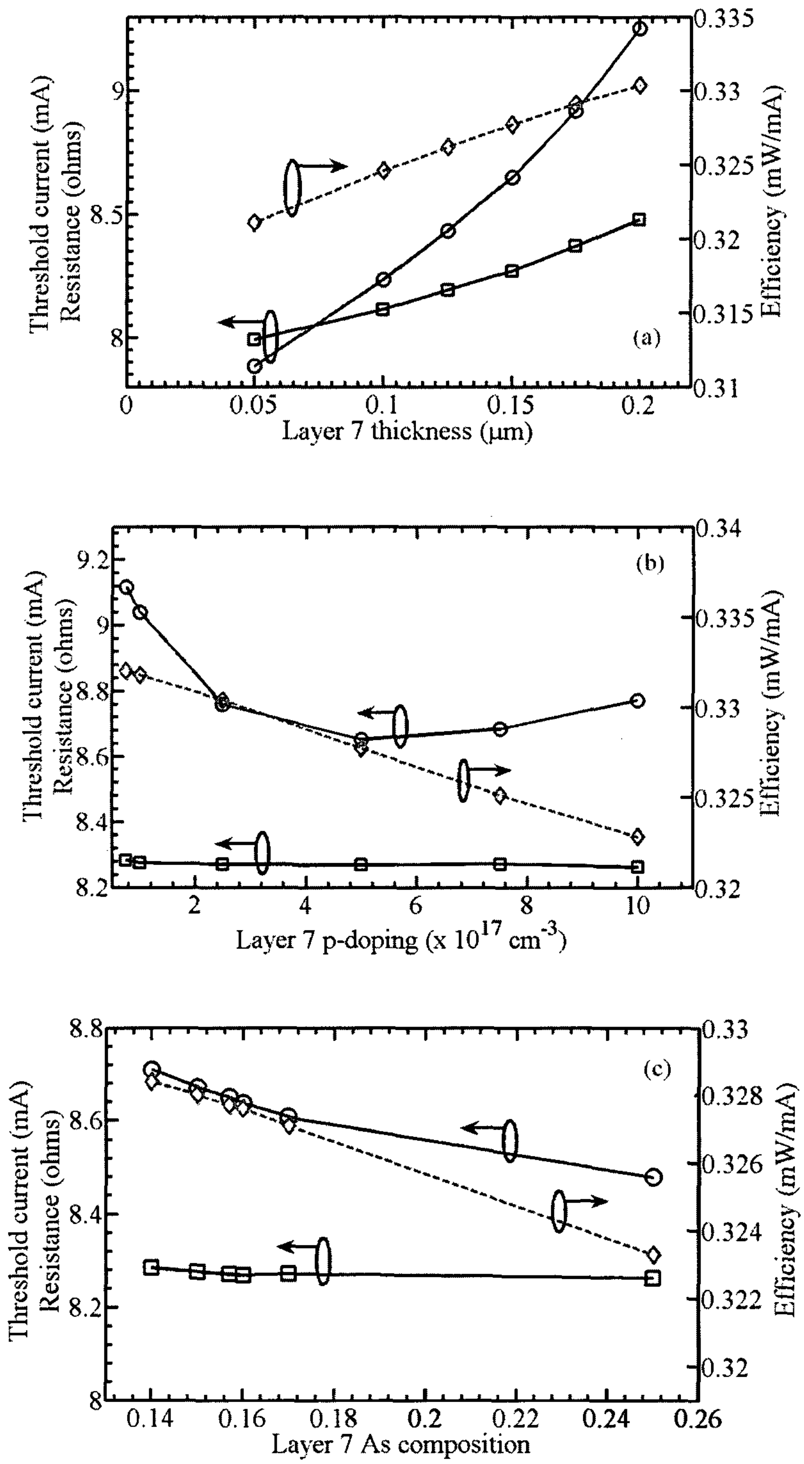

Figure 14. Threshold current (black line with square markers), electrical resistance (blue line with circle markers), and maximum efficiency (green dashed line with diamond markers) vs. a) thickness, b) doping, and c) composition of layer 7, for nominal values of 0.15 μm thickness, 5 x 10^{17} cm^{-3} p-doping, and a composition of 0.156.

contact. Finite-element analysis of the ridge waveguide cross-section (more details of which can be found in Chapter 4) using this epitaxial growth structure revealed a problem with this upper InGaAs layer. The refractive index of InGaAs, according to LAS2D, is 3.78, compared to an active region index of 3.448. Thus, even though this layer may be only tenths of a micron thick, it can shift the mode profile upwards to produce a local maximum, as shown in Figure 15. This can be mitigated by increasing the height of the ridge, or decreasing the InGaAs thickness. Etching of smooth and vertical sidewalls becomes more difficult as the depth increases. For the dry-etching method used here, it is desirable to keep the etch depth < 0.5 μm to remain within reasonable fabrication

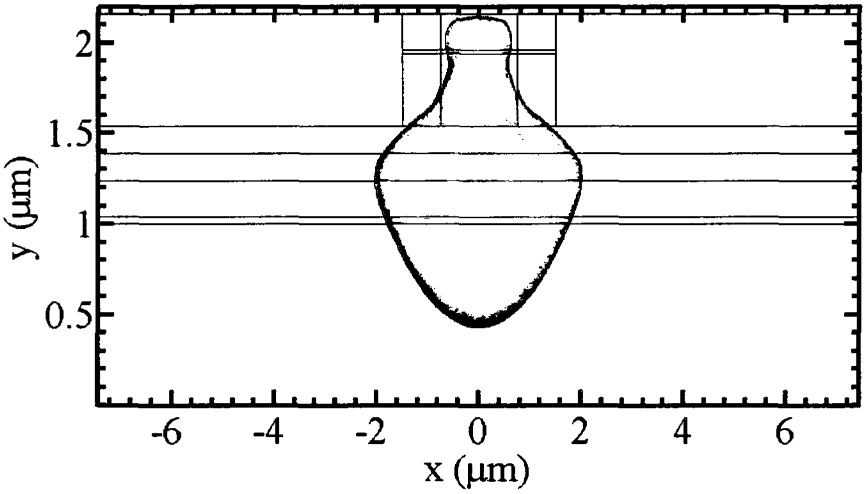

Figure 15. **Mode distortion with a 0.2 μm thick InGaAs layer, logarithmic plot of $|E_x|$, with 20 dB extents.**

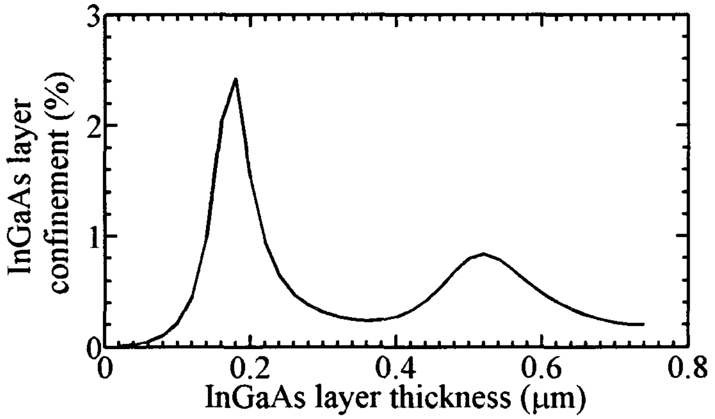

Figure 16. ***Confinement in InGaAs layer vs. layer thickness***

tolerances. Therefore, the optical confinement in the InGaAs layer was improved by reducing the thickness of this layer. Figure 16 shows the change in confinement of the optical mode in the InGaAs layer as the thickness of the InGaAs layer is changed. Clearly there is significant mode field distortion near the peak value of ~0.2 μm, where there is 2.5% confinement in the layer. Note that there are some resonance effects, i.e. there are peaks at particular InGaAs layer thicknesses rather than a simple increasing/decreasing relationship. The value chosen for this design was 50 nm, a thickness that allows only 0.03% confinement in the InGaAs layer while still providing an improved electrical connection. The penalty for this reduced thickness (compared to typical values of 200 nm) may be that the contact will be less ohmic, i.e. that more carriers will recombine, reducing the overall efficiency of the laser. However, this is a less severe penalty than having a significant amount of the optical mode overlapping with a highly lossy p-doped layer.

LAS2D is also capable of non-isothermal simulations that account for heat generated via Joule heating (H_J), recombination (H_R) , and optical absorption (H_O) processes. The heat generation terms for these processes are,

$$\begin{aligned} H_J &= \frac{|\mathbf{J}_n|^2}{q\mu_n n} + \frac{|\mathbf{J}_p|^2}{q\mu_p p} \\ H_R &= R_{NR}\left\{\left(F_n - F_p\right) + qT\left(P_p - P_n\right)\right\} \\ H_O &= \alpha_i S I(x,y)\left(F_n - F_p\right), \end{aligned} \tag{3.16}$$

Where $\mathbf{J}_{n(p)}$ are the electron (hole) current densities, $\mu_{n(p)}$ are the electron (hole) mobilities, n is the electron and p the hole carrier concentration, R_{NR} is the total non-radiative recombination rate (considered to be the sum of the Shockley-Read-Hall and Auger recombination rates), T is the local temperature, $F_{n,p}$ is the electron (hole) Fermi level, $P_{n,p}$ is the electron (hole) thermoelectric power, α_i is the internal optical absorption, S is the photon density, and $I(x,y)$ is the optical field intensity.

When a laser is operated at higher temperatures its performance will generally be degraded. At a temperature of 358K (84.85 °C), the maximum efficiency was 0.3 W/A, the threshold current was 10.8 mW, and the dynamic resistance was 9.5 Ω, worse than those calculated for the 298 K ambient temperature case above. The performance degradation is due to two main reasons. First, at higher temperatures, the carriers will have a higher average energy, and are less likely to be confined to the active region. Second, the radiative recombination terms will also tend to become larger as the temperature increases. For instance, the largest Auger recombination term in the T=298 K simulation was 2.4 x 10^{25} cm^{-3}/s, while for the T=358 K simulation, R_{aug}=6.2 x 10^{25} cm^{-3}/s.

The local temperature, as revealed by Figure 17, for an ambient temperature of 358 K and a bias current of 60 mA, has a maximum in the p-doped layers that comprise the ridge. It is the Joule heating term that is the significant factor in this additional heating. The Joule heat generation term, H_J is proportional to the electron and hole current densities and inversely proportional to the electron and hole carrier densities. The maximum hole current density of 6000 A/cm^2, as calculated by LAS2D, is near the p-contact, and is larger than the maximum electron current density of $4000A/cm^2$. The effect of the larger hole current density on the Joule heating is further magnified by the lower value of the hole mobility, μ_p, compared to the electron mobility, μ_n. In InP, the mobility of electrons is $\mu_n = 5370$ cm^2/Vs, compared to a mobility of $\mu_p = 150$ cm^2/Vs at T=300K. For comparable values of electron and hole carrier concentration and current, p-doped regions will experience 35 times as much Joule heating as n-doped regions. For this reason, the region near the p-contact will experience the greatest amount of heating at higher bias currents, and consequently have the largest local temperature. This is a general result that has also been reported in other laser diode models [67].

The final epitaxial layer composition is revealed in Table 3. During growth, the composition of the various quaternary layers is not measured directly, but instead through

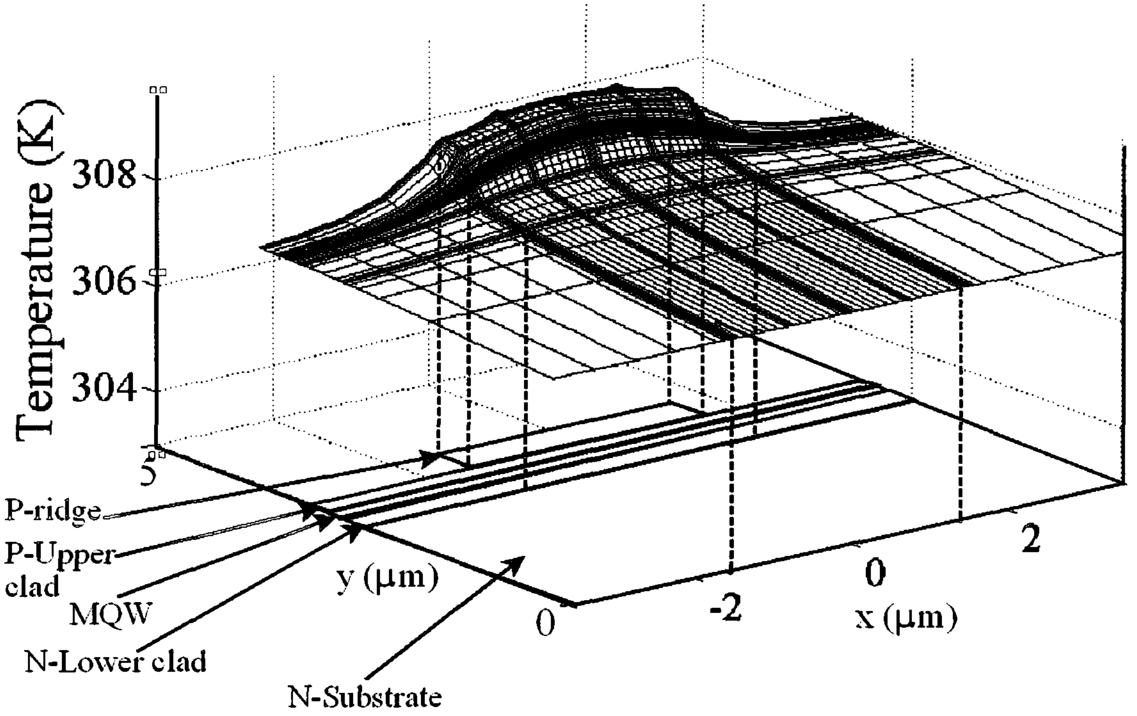

Figure 17. **Temperature distribution of laser with an applied current of 62 mA at an ambient temperature of 298 K.**

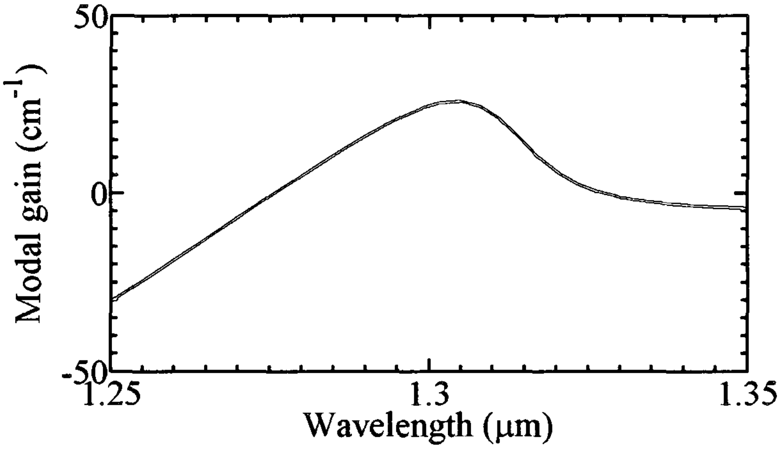

Figure 18. **Modal gain *vs.* wavelength for epitaxial structure with 21 mA of applied current**

photoluminescence measurements. Thus, although the composition of the layers is determined through the mole fractions of the group III and V materials, it is the photoluminescence peaks of each material composition in the layer strucuture that are of interest to the crystal grower. According to LAS2D, this structure exhibited a FP laser threshold current of 8.3 mA, maximum efficiency of 0.33 mW/mA, and dynamic resistance of 8.7 Ω at a temperature of 298 K. The proper design of this heterostructure is confirmed by the gain curve of Figure 18, generated by LAS2D, which demonstrates a modal gain centered at approximately 1310 nm, the target Bragg wavelength, when this heterostructure (in a FP configuration) is forward-biased with 21 mA of current.

Layer No.	Composition	PL peak (nm)		Nominal strain		Thickness (nm)	Doping level (cm^{-3})	Refractive index (I=50 mA)	Description
				(%)	(T.S./C.S.)				
10	$Ga_{0.47}In_{0.53}As$	1660		U.S.		50	Zn: $N_A = 1x10^{19}$	3.782	P-contact
9	$Ga_{0.21}In_{0.79}As_{0.42}P_{0.58}$	1150		U.S.		20	Zn: $N_A = 1.3x10^{18}$	3.403	Ridge
8	InP	919		U.S.		400	Zn: $N_A = 5x10^{18}$	3.207	Ridge
7	$Ga_{0.07}In_{0.93}As_{0.16}P_{0.84}$	1000		U.S.		150	Zn: $N_A = 5x10^{17}$	3.274	Upper clad
6	$Ga_{0.21}In_{0.79}As_{0.42}P_{0.58}$	1150		0.1	T.S.	60	u.d. ($N_D < 3x10^{15}$)	3.403	MQW active region
5	$Ga_{0.21}In_{0.79}As_{0.42}P_{0.58}$ (b)	1290	(1150)	0.1	T.S.	10	u.d. ($N_D < 3x10^{15}$)	3.403	
	$Ga_{0.11}In_{0.89}As_{0.52}P_{0.48}$ (w)		(1390)	**0.90**	C.S.	6	u.d. ($N_D < 3x10^{15}$)	3.448	
4	$Ga_{0.21}In_{0.79}As_{0.42}P_{0.58}$	1150		0.1	T.S.	20	u.d. ($N_D < 3x10^{15}$)	3.403	
3	$Ga_{0.07}In_{0.93}As_{0.16}P_{0.84}$	1000		U.S.		200	**Si:** $N_D = 5x10^{17}$	3.274	Lower clad
2	InP	919		U.S.		40	**Si:** $N_D = 8x10^{17}$	3.207	Buffer
1	InP	919		U.S.		1000	**Si:** $N_D = 1x10^{18}$	3.207	Buffer
0	InP	919		U.S.		n/a	**Si:** $N_D = 4x10^{18}$	3.207	Substrate

Table 3. LC-DFB epitaxial layer structure

*** PL: photoluminescence, TS: tensile strain, CS : compressive strain, u.d. : undoped**

CHAPTER 4 – LATERALLY-COUPLED DISTRIBUTED FEEDBACK LASER MODELING

4.1 Distributed Feedback Laser Modeling Techniques

There are four major approaches to the modeling of distributed feedback lasers: coupled-mode theory, transmission-line modeling, Green's function analysis, and the transfer-matrix method. These models will be described in more detail in this chapter. The divisions between these models are not clear-cut; more than one of these numerical methods have been combined in a single model; for instance, using Green's function analysis to find the modified coupled-mode coefficients [68]. However, a knowledge of the basics of these models will be sufficient to understand nearly all DFB modeling variants.

The common starting point for all of these techniques is Maxwell's equations,

$$\nabla \times \mathbf{E} = -\frac{\partial}{\partial t}\mathbf{B} \tag{4.1}$$

$$\nabla \times \mathbf{H} = \mathbf{J} + \frac{\partial}{\partial t}\mathbf{D} \tag{4.2}$$

$$\nabla \cdot \mathbf{D} = \rho \tag{4.3}$$

$$\nabla \cdot \mathbf{B} = 0 \tag{4.4}$$

where **E** is the electric field vector (V/m), **H** is the magnetic field vector, **D** is the electric displacement flux density (C/m^2), **B** is the magnetic flux density (Wb/m^2), **J** is the current density (A/m^2), and ρ is the charge density (C/m^3). The semiconductor material may be considered to be isotropic:

$$\mathbf{D} = \varepsilon \mathbf{E} \tag{4.5}$$

$$\mathbf{B} = \mu \mathbf{H} \tag{4.6}$$

where ε is the permittivity and μ the permeability of the semiconductor medium. For this analysis, we use a static model, so the time dependencies vanish. From Maxwell's equations, the Helmholtz wave equation is obtained,

$$\nabla^2 \mathbf{E}(x,y,z) + k_0^2 n_0^2(x,y,z) = 0 \tag{4.7}$$

$n_0(x,y,z)$ is the three-dimensional refractive index profile, which in this case for a DFB laser will be periodic along the laser cavity within the grating region, and k_0 is the vacuum wave number, given by

$$k_0 = \frac{2\pi}{\lambda}, \tag{4.8}$$

where λ is the wavelength of light. The goal of the different modeling methods outlined below is to solve the Helmholtz equation for $\mathbf{E}(x,y,z)$ given a three-dimensional refractive index profile.

4.1.1 Coupled-Mode Theory

Coupled-mode theory was the earliest method applied to the modeling of distributed feedback lasers, by Kogelnik and Shank in 1972 [26]. In coupled-mode analysis, the second-order wave equation for a periodic structure is formulated as two coupled first-order equations, expressed in matrix form as [22]:

$$\frac{d}{dz}\begin{bmatrix} A(z) \\ B(z) \end{bmatrix} = j\begin{bmatrix} (\delta + j\alpha) & \kappa_{ab} \\ \kappa_{ba} & -(\delta + j\alpha) \end{bmatrix}\begin{bmatrix} A(z) \\ B(z) \end{bmatrix}, \tag{4.9}$$

where δ is the detuning of the propagation frequency from the Bragg frequency, $\delta = \beta - \beta_0$, α is the modal gain/loss, and $\kappa_{ab(ba)}$ is the coupling coefficient in the forward (reverse) direction. The Bragg frequency detuning represents the deviation from the ideal Bragg frequency of the grating due to the details of the longitudinal laser cavity such as the cavity length and facet reflectivities. The longitudinal fields, $A(z)$ and $B(z)$, are the slowly-varying amplitudes of the electric field:

$$E_x(x,y,z) = A(z)e^{j\beta z}U(x,y) + B(z)e^{-j\beta z}U(x,y) \tag{4.10}$$

where $U(x,y)$ is the transverse mode profile, $A(z)$ is the forward-propagating field amplitude, and $B(z)$ is the backward-propagating field amplitude. Coupled-mode theory is well-suited to modeling uniform grating sections. It can also treat certain grating non-uniformities, such as phase-shifts, by incorporating them between uniform sections [69].

4.1.2 Transfer Matrix Method

The transfer matrix method (TMM) is a general purpose technique that divides a computational domain into discrete sections, with known relations between fields at the boundaries of the sections. The overall field can be obtained by a series of matrix multiplications for each of the sections. To apply this analysis to a DFB laser, the electric field is again assumed to have the slowly-varying form of (4.10). The periodic grating is now expressed in terms of alternating regions with an effective refractive index $n_{eff,a}$ and $n_{eff,b}$, as illustrated in Figure 19. At the interface between each of these regions, there is a discontinuity in the propagation constants and modal fields of the local normal modes. The forward- and backward-propagating fundamental mode in region a, $A_a(z)$ and $B_a(z)$, can be expressed in terms of the forward- and backward-propagating fundamental mode in region b, $A_b(z)$ and $B_b(z)$, through the matrix equation [70]:

$$\begin{bmatrix} A_a \\ B_a \end{bmatrix} = \begin{bmatrix} 1/t_{ab} & r_{ab}/t_{ab} \\ r_{ab}/t_{ab} & 1/t_{ab} \end{bmatrix} \begin{bmatrix} A_b \\ B_b \end{bmatrix} \tag{4.11}$$

where

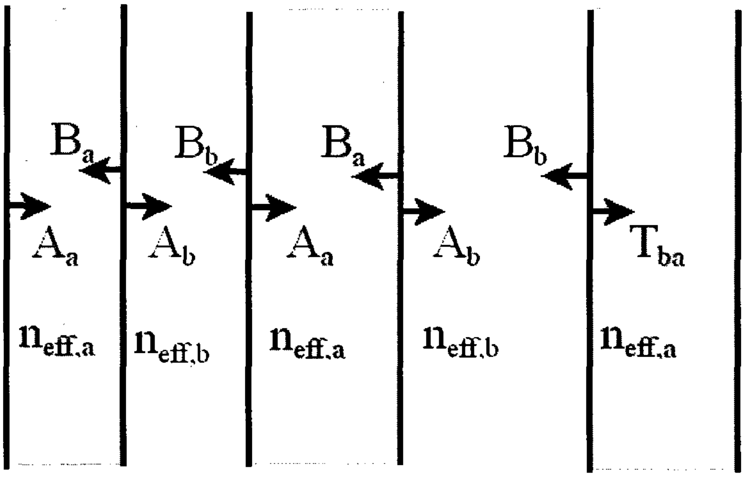

Figure 19. **Illustration of the transfer matrix method (TMM) with two alternating media of different sizes**

$$t_{ab} = \frac{2n_{eff,a}}{n_{eff,a} + n_{eff,b}} \frac{1}{\chi_{ab}} \qquad (4.12)$$
$$r_{ab} = \frac{n_{eff,a} - n_{eff,b}}{n_{eff,a} + n_{eff,b}}$$

The coefficients r_{ab} and t_{ab} are related to the reflection and transmission coefficients, R and T, by [22]

$$R = |r_{ab}|^2 \text{ and } T = \frac{n_{eff,b}}{n_{eff,a}} |t_{ab}|^2 \qquad (4.13)$$

where it has been assumed that the mode is propagating perpendicular to the layered material described by the transfer matrix. From (4.13) we see that $R + T = 1$, as would be expected from the principle of conservation of energy.

The χ_{ab} term is the overlap in the modal fields, $\phi_{a,b}$, between the two sections:

$$\chi_{ab} = \frac{\int \phi_a \phi_b dxdy}{\int \phi_a^2 dxdy} \tag{4.14}$$

The transfer matrix method can be used to provide accurate solutions of not only periodic dielectric gratings, but also structures with large discontinuities (e.g. phase shifts) and aperiodic structures. It has been applied in to the case of a second-order grating by Rozzi *et al.* in a rigorous analysis that included all radiation modes [71]. The difficulty with this type of analysis is that it requires a complete knowledge of the guided and radiation modes when it is applied to higher order gratings. Rozzi *et al.* used the effective index method to reduce the two-dimensional waveguide cross-section to one dimension, making the problem much more tractable. The laterally-coupled gratings considered here require a strictly two-dimensional treatment, making the full analysis used by Rozzi *et al.* much more difficult to realize. A complete solution of all the guided and radiation modes of a two-dimensional waveguide is a computationally-intensive problem.

In his comparison between TMM and coupled-mode analysis, Makino demonstrated that the two methods were equivalent when applied to uniform gratings [70]. The benefit of TMM is that it is more easily applied to aperiodic structures than coupled-mode theory, which is based on a Fourier series expansion of the periodic corrugation. However, TMM must discretize non-rectangular grating shapes into many sections to properly define them; by contrast, CMT requires only a change in the Fourier coefficient.

4.1.3 Transmission Line Laser Model

The transmission line laser model (TLLM), originally developed by Lowery [72], is closely related to TMM, except instead of transfer matrices, scattering (or S) matrices are used in each section. The derivation of S matrices is a well-known problem in microwave circuits, and many solution algorithms can be adapted for the transmission line laser model (TLLM). The application of TLLM to DFB lasers was also first performed by Lowery [73]. The main contrast with TMM is that the calculations are all done in the time domain, enabling dynamic studies of DFB lasers. This is particularly useful for studying the transient operation of lasers as they are switched on or off, for instance during direct modulation.

To apply the transmission line model to the problem of a DFB laser, the laser cavity is divided into a series of discrete sections with alternating low and high impedances, as shown in Figure 20. Each section spans a half-period of the DFB laser. Within each section, the S matrices are used to calculate the incident and reflected forward-traveling, $A^{r,i}(n)$, and backward-traveling, $B^{i,r}(n)$ fields. While all fields in Figure 20 are depicted for a single time step, the fields are in fact calculated based on the adjacent fields as calculated during the previous time step. Thus, at time step *k*, the forward- and backward- traveling waves within the n^{th} section are calculated from the incident waves of the (*k*-1) time step by the matrix equation

$$\begin{bmatrix} A^r(n) \\ B^r(n) \end{bmatrix}_k = \begin{bmatrix} S_{11}(n) & S_{12}(n) \\ S_{21}(n) & S_{22}(n) \end{bmatrix} \begin{bmatrix} A^i(n) \\ B^i(n) \end{bmatrix}_{k-1} \tag{4.15}$$

where the 2x2 matrix contains the scattering parameters of the n^{th} discrete section, represented by S(*n*) in Figure 20. There are two types of interfaces in the transmission line DFB laser model: low-to-high impedence, and high-to-low impedence. In a low-to-high impedence transition, such as between sections *n* and *n*+1 in Figure 20, the fields are calculated by the matrix equation

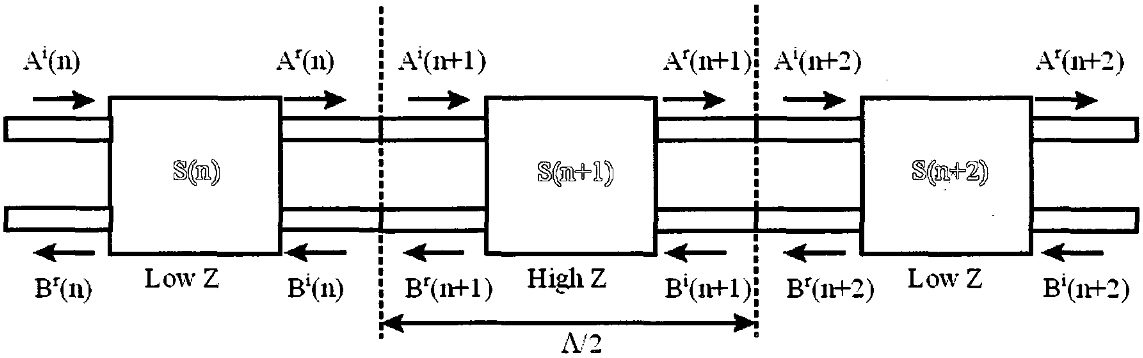

Figure 20. **Transmission line laser model representation of a DFB laser for three sections**

$$\begin{bmatrix} A^i(n+1) \\ B^i(n) \end{bmatrix}_k = \begin{bmatrix} 1+\kappa\Lambda/2 & -\kappa\Lambda/2 \\ \kappa\Lambda/2 & 1-\kappa\Lambda/2 \end{bmatrix} \begin{bmatrix} A^r(n) \\ B^r(n+1) \end{bmatrix}_{k-1} \tag{4.16}$$

where the fields in the right-most matrix, $A^r(n)$ and $B^r(n+1)$, are those calculated in the previous time iteration, and κ is the coupling coefficient. Similarly, for a high-to-low impedence transition, the matrix equation is given as

$$\begin{bmatrix} A^i(n+2) \\ B^i(n+1) \end{bmatrix}_k = \begin{bmatrix} 1-\kappa\Lambda/2 & \kappa\Lambda/2 \\ -\kappa\Lambda/2 & 1+\kappa\Lambda/2 \end{bmatrix} \begin{bmatrix} A^r(n+1) \\ B^r(n+2) \end{bmatrix}_{k-1} \tag{4.17}$$

The advantages and disadvantages of the TLLM are similar to TMM. It is well-suited to one-dimensional cross-sections and first-order gratings, and is the basis for the commercial software VPIphotonics [74], which has been in turn used in other DFB laser studies [75], [76]. However, the higher order laterally-coupled gratings considered here would require significantly more computational effort, as a two-dimensional analysis including radiating diffraction orders is required.

4.1.4 Green's Function Method

The Green's function method is a general technique that is used in the solution of non-homogeneous partial differential equations. Consider a partial differential equation of the form

$$Lu(x) = f(x) \tag{4.18}$$

Where $u(x)$ is the function to be solved, $f(x)$ is a source term, and L is a linear differential operator. Instead of considering $f(x)$ as a continuous source function, we approximate it as a series of discrete point sources, acting at the points $x = \chi_1, \chi_2, \ldots \chi_n$, where x is within a desired solution interval of $0 \le x \le l$. The Green's function, $G(x;\chi_i)$, is defined as the solution of (4.18) due to a unit point source at $x = \chi_i$. The solution due to the discrete function at that point is $G(x;\chi_i)f(\chi_i)$. To obtain the total solution, the point functions can be summed up:

$$u(x)=\sum_{i=1}^{n}G(x;\chi_i)f(\chi_i). \tag{4.19}$$

The validity of this approximation becomes better as we sample the continuous function *f*(*x*) with more points. In the limit where $n\rightarrow\infty$, we replace the summation with an integral, as

$$u(x)=\int_0^l G(x;\chi)f(\chi)d\chi \tag{4.20}$$

This integral over the solution domain (in this case $0\leq x\leq l$) is essentially the impulse-response of the partial differential equation (the Green's function), weighted by the source term.

The most difficult step of this method is usually obtaining the Green's function itself. Except for special cases, the Green's function for most partial differential equations must be evaluated numerically [77]. Shams-Zadeh-Amiri *et al.* describe in detail the solution of the Green's function for a higher order grating using a transfer matrix method [68]. This solution resulted in the modified coupled-mode equations, described below, demonstrating the equivalence of the Green's function and modified coupled-mode analysis.

Freeze *et. al.* have developed a recursive Green's function method that is capable of modeling many general periodic structures, including DFB waveguides. This method can also be extended to complex-coupled gratings [78]. In Section 7.7 of this thesis, we use a Green's function solution for the amplified spontaneous emission (ASE) in the DFB laser to determine the coupling coefficients of the grating using the ASE spectrum, based on the approach of Wenzel [79].

4.1.5 Summary

While DFB lasers have been extensively modeled using the methods above, the use of laterally-coupled higher order gratings is a particularly demanding case. Higher order gratings have been simulated for a one-dimensional cross-section with all of these techniques. The equivalence of these techniques has been established in a number of studies, for example, [68], [70], and [80]. There is potential for extending all of these analyses to two dimensions, however, most require knowledge of the radiation modes of the lateral cross-section.

In modified coupled-mode theory, the original equations given in (4.9) for first-order gratings have been modified to account for partial wave radiation loss by Streifer *et al.*, [81], [82]. My thesis will present the extension of this theory to a two-dimensional cross-section. This theory will account for the radiating diffraction orders of higher order gratings, without requiring the solution of all radiation modes. One drawback of this modified coupled-mode theory is that it is derived for scalar fields, in our case the TE mode. In one-dimensional waveguides the analytical solutions for the fields can be divided into transverse electric (TE) and transverse magnetic (TM) modes. In two-dimensional waveguides, the field solutions will always have a minor field component. For rectangular waveguides such as those examined here, this minor field component is negligible compared to the major field component, and we can refer to the solutions as being quasi-TE or quasi-TM fields. This allows us to extend these equations to the two-dimensional case without requiring a fully-vectorial formulation.

4.2 Modified Coupled-Mode Theory

Since the original formulation of modified-coupled mode theory assumed a one-dimensional cross-section, in this thesis we extend the cross-section to two dimensions, more accurately describing the laterally-coupled grating. We will consider only consider quasi-TE modes, since the 0.9% compressively strained quantum wells will selectively provide gain to TE polarized light. This laser is not designed to be operated at high powers, and at moderate values of bias current, the laser should be mainly TE-polarized.

Modified coupled-mode theory begins with the Helmholtz wave equation, which must be satisfied by the TE-polarized electric field, E_x:

$$\nabla^2 E_x(x,y,z) + k_0^2 n^2(x,y,z) E_x(x,y,z) = 0, \tag{4.21}$$

where $n(x,y,z)$ is the three-dimensional refractive index profile and k_0 is the vacuum wave number.

Since $n^2(x,y,z)$ is periodic in the z-direction for a uniform grating, it can be expressed as a Fourier series:

$$n^2(x,y,z) = \hat{n}_0^2(x,y) + \sum_{\substack{q=-\infty \\ q\neq 0}}^{\infty} A_q(x,y)\exp\left(j2\pi qz/\Lambda\right). \tag{4.22}$$

In (4.22), the q=0 term has been removed from the Fourier summation, and expressed separately as $\hat{n}_0^2$, i.e. the refractive index profile in the transverse direction that has been averaged over a single grating period. The value of $\hat{n}_0^2$ is complex, $\hat{n}_0 = n_0(x,y) - j\hat{\alpha}(x,y)$, where n_0 is the real, and α is the imaginary portion of the refractive index. Λ is the grating period, and $A_q(x,y)$ is the two-dimensional Fourier coefficient of the grating. While a Fourier transform of the periodic portion of the refractive index would be more accurate for gratings of limited length, the Fourier series (which assumes an infinite grating length) provides a good approximation, since a single grating period is much smaller compared to the cavity length for all practical DFB lasers. For instance, our 1310 nm lasers have a period length of 600 nm, orders of magnitude less than the typical laser lengths of ~500 μm. Substitution of (4.22) into the wave equation results in

$$\nabla^2 E_x(x,y,z) + k_0^2 \hat{n}_0^2 E_x(x,y,z) + k_0^2 E_x(x,y,z) \sum_{\substack{q=-\infty \\ q\neq 0}}^{\infty} A_q(x,y) exp\left(j2\pi qz / \Lambda\right) = 0. \quad (4.23)$$

For a DFB laser with an N^{th} order grating with a period of Λ, according to (2.10), the propagation constant of the TE mode, $\beta_0 = 2\pi n_{eff} / \lambda$, should satisfy the Bragg condition:

$$\beta_0 = N\pi / \Lambda \qquad N = 1,2,3,\ldots \; . \qquad (4.24)$$

The electric field in a periodic medium can also be expressed as an infinite summation of partial waves, according to the Floquet-Bloch theorem, as

$$E_x(x,y,z) = \sum_{m=-\infty}^{\infty} E_x^{(m)}(x,y,z) \exp\left(j\beta_m z\right), \qquad (4.25)$$

where $E_x^{(m)}$ is the m^{th} partial wave field component (m denoting field order); and β_m, the propagation constant of an m^{th} order partial wave, is defined with respect to β_0, the Bragg frequency of the grating given in (4.24), as

$$\beta_m = \beta_0 + \frac{2\pi m}{\Lambda}. \qquad (4.26)$$

The mode field is assumed to consist of a series of standing waves in the z-direction, with the lowest order mode, m=0, being the mode that would exist in the waveguide in the absence of a grating. Inserting (4.25) into the wave equation (4.23), yields, for an arbitrary value of m:

$$\begin{aligned} &\nabla^2 E_x^{(m)}(x,y,z) + \left(k_0^2 \hat{n}_0^2(x,y) - \beta_m^2\right) E_x^{(m)}(x,y,z) \\ &= -2j\beta_m \frac{\partial E_x^{(m)}(x,y,z)}{\partial z} - k_0^2 \sum_{\substack{q=-\infty \\ q\neq 0}}^{\infty} A_q(x,y) E_x^{(m-q)}(x,y,z) \end{aligned} \qquad (4.27)$$

For a particular partial wave, of order $p=-N$, $\beta_p=-\beta_0$, corresponding to the contradirectionally propagating fundamental mode. These forward- and backward-propagating waves, $E_x^{(0)}(x,y,z)$ and $E_x^{(p)}(x,y,z)$, may thus be expressed in terms of the transverse fundamental mode profile, $\varepsilon_0(x,y)$, as

$$E_x^{(0)}(x,y,z)=A\left(z\right)\varepsilon_0(x,y), \qquad E_x^{(p)}(x,y,z)=B\left(z\right)\varepsilon_0(x,y). \tag{4.28}$$

This defines the forward and backward longitudinal mode components, *A*(*z*) and *B*(*z*), respectively. Substituting (4.28) for *m*=0 and *m*=*p* into (4.27), and using the slowly-varying approximation that neglects the near-vanishing $\partial^2/\partial z^2$ longitudinal mode terms, yields two coupled equations:

$$\begin{aligned}&\frac{\partial^2\varepsilon_0(x,y)}{\partial x^2}A\left(z\right)+\frac{\partial^2\varepsilon_0(x,y)}{\partial y^2}A\left(z\right)+\left[k_0^2\hat{n}_0^2(x,y)-\beta_0^2\right]A\left(z\right)\varepsilon_0(x,y)\\&=-2j\beta_0\frac{dA}{dz}\varepsilon_0(x,y)-k_0^2A_{-p}\left(x,y\right)B\left(z\right)\varepsilon_0\left(x,y\right)-k_0^2\sum_{\substack{q=-\infty\\q\neq0,-p}}^{\infty}A_q(x,y)E_x^{(-q)}\left(x,y,z\right)\end{aligned} \tag{4.29}$$

and

$$\begin{aligned}&\frac{\partial^2\varepsilon_0(x,y)}{\partial x^2}B\left(z\right)+\frac{\partial^2\varepsilon_0(x,y)}{\partial y^2}B\left(z\right)+\left[k_0^2\hat{n}_0^2(x,y)-\beta_0^2\right]B\left(z\right)\varepsilon_0(x,y)\\&=2j\beta_0\frac{dB}{dz}\varepsilon_0(x,y)-k_0^2A_p\left(x,y\right)A\left(z\right)\varepsilon_0\left(x,y\right)-k_0^2\sum_{\substack{q=-\infty\\q\neq0,p}}^{\infty}A_q(x,y)E_x^{(p-q)}\left(x,y,z\right)\end{aligned} \tag{4.30}$$

where the coupled terms of the summation have been placed on the right-hand sides of (4.29) and (4.30). If we assume that the fundamental mode field, $\varepsilon_0(x,y)$, is negligibly perturbed by the higher order terms of the Fourier expansion and the imaginary part of the refractive index, then $\varepsilon_0(x,y)$ satisfies the homogeneous forms of (4.29) and (4.30), as

$$\frac{\partial^2 \varepsilon_0(x,y)}{\partial x^2}+\frac{\partial^2 \varepsilon_0(x,y)}{\partial y^2}+\left(k_0^2 n_0^2(x,y)-\beta^2\right)\varepsilon_0(x,y)=0. \tag{4.31}$$

We can simplify the expression for $\hat{n}_0^2$ in terms of its real and imaginary parts, n_0 and $\hat{\alpha}$, if we assume that $\hat{n}_0^2=\left(n_0^2-2jn_0\hat{\alpha}-\hat{\alpha}^2\right)\approx n_0^2-2jn_0\hat{\alpha}$. Substitution of (4.31) into the coupled equations, (4.29) and (4.30), results in

$$\begin{aligned}&2j\beta_0\frac{dA}{dz}\varepsilon_0(x,y)+\left[-2jk_0n_0(x,y)\hat{\alpha}(x,y)+\left(\beta^2-\beta_0^2\right)\right]A(z)\varepsilon_0(x,y)\\&=-k_0^2A_{-p}(x,y)B(z)\varepsilon_0(x,y)-k_0^2\sum_{\substack{q=-\infty\\q\neq 0,-p}}^{\infty}A_q(x,y)E_x^{(-p)}(x,y,z)\end{aligned} \tag{4.32}$$

and

$$\begin{aligned}&-2j\beta_0\frac{dB}{dz}\varepsilon_0(x,y)+\left[-2jk_0n_0(x,y)\hat{\alpha}(x,y)+\left(\beta^2-\beta_0^2\right)\right]B(z)\varepsilon_0(x,y)\\&=-k_0^2A_{p}(x,y)A(z)\varepsilon_0(x,y)-k_0^2\sum_{\substack{q=-\infty\\q\neq 0,p}}^{\infty}A_q(x,y)E_x^{(p-q)}(x,y,z).\end{aligned} \tag{4.33}$$

These equations can be expressed in terms of the optical power by multiplying them by $\varepsilon_0(x,y)$ and integrating over the transverse cross-section from $(-\infty<x<\infty)$ and $(-\infty<y<\infty)$, yielding

$$\begin{aligned}&\frac{dA}{dz}+(-\alpha-j\delta)A(z)\\&=j\kappa_{-p}B(z)+\frac{jk_0^2}{2\beta_0P}\sum_{\substack{q=-\infty\\q\neq 0,-p}}^{\infty}\int_{-\infty}^{\infty}\int_{-\infty}^{\infty}A_q(x,y)\varepsilon_0(x,y)E_x^{(-q)}(x,y,z)\,dxdy,\end{aligned} \tag{4.34}$$

and

$$\begin{aligned}&-\frac{dB}{dz}+(-\alpha-j\delta)B(z)\\&=j\kappa_{p}A(z)+\frac{jk_0^2}{2\beta_0P}\sum_{\substack{q=-\infty\\q\neq 0,p}}^{\infty}\int_{-\infty}^{\infty}\int_{-\infty}^{\infty}A_q(x,y)\varepsilon_0(x,y)E_x^{(p-q)}(x,y,z)\,dxdy,\end{aligned} \tag{4.35}$$

where the total power is

$$P = \int_{-\infty}^{\infty}\int_{-\infty}^{\infty} \varepsilon_0^2(x,y)dxdy. \tag{4.36}$$

The modal gain (when positive) or loss (when negative), is given by

$$\alpha = \frac{k_0^2}{2\beta_0 P}\int_{-\infty}^{\infty}\int_{-\infty}^{\infty} n_0(x,y)\tilde{\alpha}(x,y)\varepsilon_0^2(x,y)dxdy. \tag{4.37}$$

Note that the remaining integration in (4.34) and (4.35) is effectively only over the two-dimensional grating region since the Fourier coefficients vanish outside that range. $\delta = \left(\beta^2 - \beta_0^2\right)/\left(2\beta_0\right) \approx \beta - \beta_0$ is the Bragg frequency detuning, and the coupling coefficient between the two contradirectionally propagating modes is

$$\kappa_p = \frac{k_0^2}{2\beta_0 P}\int_{-\infty}^{\infty}\int_{-\infty}^{\infty} A_p(x,y)\varepsilon_0^2(x,y)dxdy. \tag{4.38}$$

It should be noted that (4.38) for κ_p is the standard equation used to calculate the coupling coefficient of first-order rectangular gratings, as evaluated by Choi *et al.* for various LC-DFB geometries [83].

The partial wave fields, $E_x^{(m)}$, are determined by (4.27), the right-hand side of which incorporates the m^{th} partial wave dependence on all other partial waves. It has been shown that a first-order approximation to the rightmost term, where only the contributions of the lowest order modes, $E_x^{(0)}$ and $E_x^{(p)}$, are considered, gives an acceptable estimation in the one-dimensional case [82]. If we also assume that the *z*-derivative terms in (4.27) are negligible compared to the others, consistent with the slowly-varying approximation, and that the modal gain/loss can be neglected for partial waves other than the fundamental modes, then, using (4.28), (4.27) reduces to

$$\begin{aligned}\frac{\partial^2 E_x^{(m)}(x,y,z)}{\partial x^2}+\frac{\partial^2 E_x^{(m)}(x,y,z)}{\partial y^2}+\left[k_0^2 n_0^2(x,y)-\beta_m^2\right]E_x^{(m)}(x,y,z)\\ =-k_0^2\left[A_m(x,y)A(z)+A_{m-p}B(z)\right]\varepsilon_0(x,y).\end{aligned} \tag{4.39}$$

(4.39) has a solution of the form

$$E_x^{(m)}(x,y,z)=A(z)\,\varepsilon_m^{(0)}(x,y)+B(z)\,\varepsilon_m^{(p)}(x,y) \qquad m\neq 0,p, \tag{4.40}$$

where $\varepsilon_m^{(0)}(x,y)$ and $\varepsilon_m^{(p)}(x,y)$ both satisfy

$$\begin{aligned}&\frac{d^2\varepsilon_m^{(i)}(x,y)}{dx^2}+\frac{d^2\varepsilon_m^{(i)}(x,y)}{dy^2}+\left[k_0^2 n_0^2(x,y)-\beta_m^2\right]\varepsilon_m^{(i)}(x,y)\\ &=-k_0^2 A_{m-i}(x,y)\varepsilon_0(x,y) \qquad\qquad m\neq i, i=0,p.\end{aligned} \tag{4.41}$$

The solutions for $\varepsilon_m^{(i)}(x,y)$ may then be substituted into (4.34) and (4.35) to obtain the modified coupled-mode equations, yielding

$$\begin{aligned}\frac{dA}{dz}+(-\alpha-j\delta-j\zeta_1)A=j\left(\kappa_p^*+\zeta_2\right)B\\ -\frac{dB}{dz}+(-\alpha-j\delta-j\zeta_3)B=j\left(\kappa_p+\zeta_4\right)A\end{aligned} \tag{4.42}$$

where $\zeta_{1,\ldots,4}$ are the Streifer correction terms that account for partial-wave coupling. These terms are calculated, using the partial wave solutions obtained from (4.41), as

$$\begin{aligned}
\zeta_1 &= \sum_{\substack{q=-\infty \\ q\neq 0,-p}}^{\infty} \eta_{q,-q}^{(0)} \\
\zeta_2 &= \sum_{\substack{q=-\infty \\ q\neq 0,-p}}^{\infty} \eta_{q,-q}^{(p)} \\
\zeta_3 &= \sum_{\substack{q=-\infty \\ q\neq 0,p}}^{\infty} \eta_{q,p-q}^{(p)} \\
\zeta_4 &= \sum_{\substack{q=-\infty \\ q\neq 0,p}}^{\infty} \eta_{q,p-q}^{(0)}
\end{aligned} \tag{4.43}$$

where

$$\eta_{r,s}^{(i)} \frac{k_0^2}{2\beta_0 P} \iint_G A_r(x,y)\varepsilon_0(x,y)\varepsilon_s^{(i)}(x,y)dxdy. \tag{4.44}$$

The Streifer correction terms have a physical interpretation that is worthwhile to consider for a better understanding of modified coupled-mode analysis results. The ζ_1 term represents the reaction of all partial waves, radiating and non-radiating, generated by the forward-propagating wave on the forward-propagating wave itself. Similarly, the ζ_3 term represents the reaction of all partial waves generated by the backward-propagating wave on the backward-propagating wave itself. For all gratings, these terms will be equal, $\zeta_1 = \zeta_3$ [82]. The real parts of $\zeta_{1,3}$ may be positive or negative, and will affect the deviation from the Bragg frequency. The imaginary portions of $\zeta_{1,3}$ represent the additional radiation loss in the transverse direction due to the partial waves, and hence are always positive. These terms will cause the threshold gain required for higher order gratings to be greater than for first-order gratings, because the latter ideally have $\zeta_{1,\ldots,4} = 0$, and thus no radiation loss in the transverse direction. The ζ_2 term is due to the reaction of all partial waves generated by the backward-propagating mode on the forward-propagating mode, and vice versa for the ζ_4 term. For gratings with grating teeth that are symmetrical in the +*z* and –*z* directions, such as most of the gratings considered (see Figure 21 below), $\zeta_2 = \zeta_4$. The ζ_2 and ζ_4 terms represent additional indirect coupling between the forward- and backward-propagating modes through the partial waves. They act as corrections to the coupling coefficient, and therefore an effective coupling coefficient, taking into account partial wave effects, can be defined as [84]:

$$\kappa_{eff} = \sqrt{\left(\kappa_p + \zeta_2\right)\left(\kappa_{-p} + \zeta_4\right)} = \left|\kappa_{eff}\right| e^{j\phi\left(\kappa_{eff}\right)} \tag{4.45}$$

This effective coupling coefficient is generally a complex value, with the real portion denoting the degree of index coupling of the grating, and the imaginary portion the degree of gain/loss coupling of the grating.

4.3 Grating Fourier Coefficients

The Fourier coefficients, $A_q(x,y)$, are determined by the shape of the grating. Following the analysis of Streifer [81], we express an arbitrary squared refractive index profile within a grating region of period Λ as

$$n^2(x,y,z) = \sum_{q=-\infty}^{\infty} \begin{bmatrix} n_1^2 \left\{U\left(z - w_1(x,y) - q\Lambda\right) - U\left(z - w_2(x,y)\right) - q\Lambda\right\} \\ +n_2^2 \left\{U\left(z - w_2(x,y) - q\Lambda\right) - U\left(z - w_1(x,y) - \left(q+1\right)\Lambda\right)\right\} \end{bmatrix} \tag{4.46}$$

where U is the Heaviside step function, and w_1 and w_2 are arbitrary functions used to define the leading and trailing edges of the grating shape. This function can be used to determine any grating tooth shape, not only rectangular. The step function is used to define the abrupt change in refractive index at the interface between n_1 and n_2 materials, as shown in Figure 21, and does not fix the grating shape as rectangular. We begin by assuming variation of the grating in only in the the yz-plane. Variations of the grating in the horizontal direction can be expressed according to our coordinate system by a simple change of variable, from y to x. The average refractive index (i.e. q=0), is

$$n_0^2(y) = \left\{ n_1^2 \left(w_2(y) - w_1(y) \right) + n_2^2 \left(\Lambda + w_1(y) - w_2(y) \right) \right\} / \Lambda \tag{4.47}$$

To obtain the Fourier series in the *z*-direction, the standard Fourier series formula for the Heaviside step function is used:

$$A_q(x,y) = \begin{cases} \dfrac{1}{\Lambda} \displaystyle\int_{-\Lambda/2}^{\Lambda/2} n^2(x,y,z) \exp\left(-j2\pi qz/\Lambda\right) dz & \\ = \dfrac{\left(n_2^2 - n_1^2\right)}{j2\pi q} \left\{ \exp\left(-j2\pi q w_2(y)/\Lambda\right) - \exp\left(-j2\pi q w_1(y)/\Lambda\right) \right\}, & (x,y) \in G \\ 0, & else \end{cases} \tag{4.48}$$

where *G* is the two-dimensional grating region. The functions, $w_1(y)$ and $w_2(y)$ define the leading and trailing edge of the grating shape over one period. n_1 and n_2 refer to the refractive indices of the high-index semiconductor and low-index dielectric material, respectively, and Λ is the period of the grating. Figure 21 shows the four varieties of grating shapes to be considered here: sinusoidal, blazed, rectangular, and trapezoidal.

4.3.1 Sinusoidal Gratings

For sinusoidal gratings, shown in Figure 21a, the shape functions are given by,

$$w_1 = \frac{\Lambda}{2\pi} \cos^{-1}\left(\frac{2}{g}(y - g/2) \right) \text{ and } w_2 = -\frac{\Lambda}{2\pi} \cos^{-1}\left(\frac{2}{g}(y - g/2) \right) \tag{4.49}$$

where *g* is the grating height. Note that, in this particular case, $w_1 = -w_2$ due to the symmetry of the grating. These shape functions result in an average refractive index, determined from (4.47), of

$$n_0^2(y) = \frac{n_1^2}{\pi} \cos^{-1}\left(\frac{2}{g}(y - g/2) \right) + n_2^2 \left(1 - \frac{1}{\pi} \cos^{-1}\left(\frac{2}{g}(y - g/2) \right) \right) \tag{4.50}$$

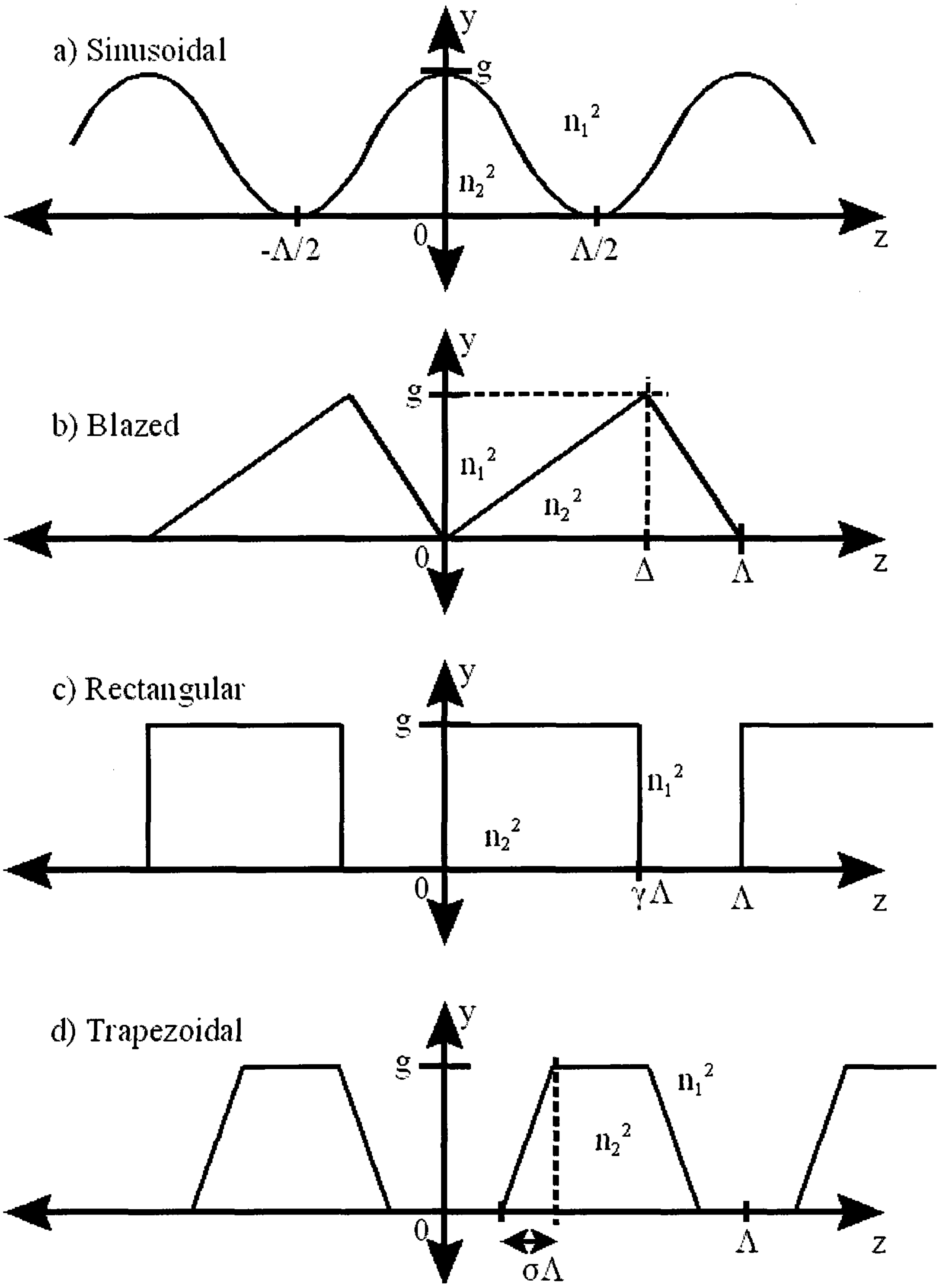

Figure 21. **a) Sinusoidal, b) blazed, c) rectangular, and d) trapezoidal grating dimensions**

within the grating region. This term reduces to n_1^2 in the limit where $y \rightarrow g$ and to n_2^2 in the limit where $y \rightarrow 0$, a useful check for the accuracy of the expression. Substituting (4.49) into (4.48) gives the Fourier coefficients for a sinusoidal grating:

$$A_q(y) = -\frac{\left(n_2^2 - n_1^2\right)}{\pi q}\left\{\sin\left[q\cos^{-1}\left(\frac{2}{g}(y - g/2)\right)\right]\right\} \tag{4.51}$$

4.3.2 Blazed Gratings

For a blazed grating, shown in Figure 21b, the grating shape functions are:

$$w_1(y) = -\frac{(\Lambda - \Delta)}{g}y \text{ and } w_2(y) = \frac{\Delta}{g}y \tag{4.52}$$

where Δ is the blazed grating shape parameter. The average refractive index, $n_0^2(y)$ is

$$n_0^2(y) = n_1^2\left(\frac{y}{g}\right) + n_2^2\left(1 - \frac{y}{g}\right) \tag{4.53}$$

within the grating region. Note that this is independent of the blazed grating shape parameter, Δ. The Fourier coefficients of the blazed grating are

$$A_{q,blazed}(y) = \frac{\left(n_2^2 - n_1^2\right)}{j2\pi q}\left\{\exp\left(-j2\pi q\left(\frac{\Delta}{g\Lambda}\right)y\right) - \exp\left(-j2\pi q\left(\frac{\Lambda - \Delta}{g\Lambda}\right)y\right)\right\} \tag{4.54}$$

This cannot be simplified to a sine function since blazed gratings are generally asymmetric. For symmetrical blazed gratings, i.e. triangular gratings as we will refer to them in Chapter 5, $\Delta = \frac{1}{2}\Lambda$, $w_1 = -w_2$, and the Fourier coefficients can then be simplified to a sine function, as

$$A_{q,\Delta}(y) = -\frac{\left(n_2^2 - n_1^2\right)}{\pi q}\sin\left(\pi q\left(\frac{y}{g}\right)\right). \tag{4.55}$$

4.3.3 Rectangular Gratings

The simplest grating shape is rectangular, as rectangular gratings have spatially-independent Fourier coefficients (except for the dependence on G, the grating region). For a rectangular grating with a duty cycle of γ, as shown in Figure 21c, the shape functions are

$$w_1 = -\left(\Lambda - \gamma\Lambda\right)/2 \text{ and } w_2 = \left(\Lambda - \gamma\Lambda\right)/2 = -w_1. \tag{4.56}$$

These equations give an average squared refractive index of

$$n_0^2 = n_1^2\left(1-\gamma\right) + n_2^2\left(\gamma\right) \tag{4.57}$$

and Fourier coefficients of

$$A_{q,\Pi} = -\frac{\left(n_2^2 - n_1^2\right)}{\pi q}\sin\left(\pi q\gamma\right). \tag{4.58}$$

4.3.4 Trapezoidal Gratings

The gradual transition from a triangular to a rectangular grating can be studied using a trapezoidal grating shape, pictured in Figure 21d. The grating shape is assumed to be a combination of the rectangular grating and triangular grating shapes. For simplicity, we assume the grating is symmetrical, with the shape functions:

$$w_1(y) = -\frac{\Lambda}{4} + \sigma\Lambda\left(\frac{1}{2} - \frac{x}{g}\right) \text{ and } w_2(y) = \frac{\Lambda}{4} - \sigma\Lambda\left(\frac{1}{2} - \frac{x}{g}\right) \tag{4.59}$$

The σ parameter controls the portion of a grating period that is angled, as shown in Figure 21d. When $\sigma = 0$, the grating is rectangular in shape with a duty cycle of 0.5.

When $\sigma = 1/2$, the grating has a symmetrical triangular shape. In between these values, the grating is trapezoidal in shape. The average squared refractive index is

$$n_0^2(y) = n_1^2\left(\frac{1}{2} - \sigma\left(1 - \frac{2y}{g}\right)\right) + n_2^2\left(\frac{1}{2} + \sigma\left(1 - \frac{2y}{g}\right)\right) \tag{4.60}$$

and the Fourier coefficients are defined by

$$A_{q,trap}(y) = -\frac{\left(n_2^2 - n_1^2\right)}{\pi q}\sin\left[\pi q\left(\frac{1}{2} - \sigma\left(1 - \frac{2y}{g}\right)\right)\right]. \tag{4.61}$$

4.4 Modified Coupled-Mode Numerical Simulation

The first step in the modeling of LC-DFB lasers using modified coupled-mode theory is to solve (4.38), (4.41), and (4.43) for the modified coupled-mode coefficients, i.e. κ_p and ζ_{1-4}. This section describes in detail the procedure to determine these coefficients for a given LC-DFB cross-section. First, the fundamental quasi-TE mode solution for the waveguide is found using finite-element analysis. This solution is used in (4.38) to calculate κ_p; the fundamental mode field is also substituted into (4.41) when solving for the partial wave fields. These partial wave fields, also solved using finite-element analysis, are then used in (4.43) and (4.44) to find the Streifer correction terms, ζ_{1-4}.

4.4.1 Fundamental Quasi-TE Mode Solution

The fundamental quasi-TE mode solution, $\varepsilon_0(x, y)$, is calculated from the homogeneous wave equation (4.31). The modal solutions are obtained using the RF Module of COMSOL Multiphysics software [85]. This finite-element analysis software may be used to find the modal solutions of arbitrarily shaped waveguides. The solutions are fully vectorial, so all spatial components of the **E** and **H** fields are solved. Since the Streifer terms are formulated from the scalar wave equation, only the scalar E_x field is utilized in further calculations.

The average squared refractive indices used in the grating region are given by the formulae of Section 4.3, for example, (4.57) for a rectangular grating. An average refractive index is also used in the MQW region, instead of individually specifying the indices of each quantum well and barrier layer. The average index in the MQW active region, n_{MQW}, is

$$n_{MQW} = \frac{N_{QW} n_{QW} L_{QW} + (N_{QW}+1) n_b L_b}{N_{QW} L_{QW} + (N_{QW}+1) L_b} \tag{4.62}$$

where N_{QW} is the number of quantum wells, $L_{QW(b)}$ is the thickness of the quantum well (barrier) layer, and $n_{QW(b)}$ is the refractive index of the individual quantum well (barrier) layers. This average refractive index greatly minimizes the number of mesh elements required by eliminating the nanometer-scale quantum wells, and has a negligible impact on the fundamental mode solution. An example of a quasi-TE mode solution is shown in Figure 22.

One of the difficulties that arise during finite-element solution using COMSOL Multiphysics is that of spurious mode solutions. The standard boundary conditions that are used in COMSOL are perfect electric conductors (PECs). While the computational boundaries may be set wide enough so that these boundaries do not interfere with the desired fundamental mode solution, they can generate artificial resonances that often result in numerous unphysical higher order mode solutions. While with a standard simulation the fundamental mode solution can be manually inspected to ensure it has been properly solved, we prefer an automated solution for the large number of mode solutions that will be obtained. To algorithmically extract the fundamental quasi-TE mode solution from the many spurious solutions generated by COMSOL, I performed

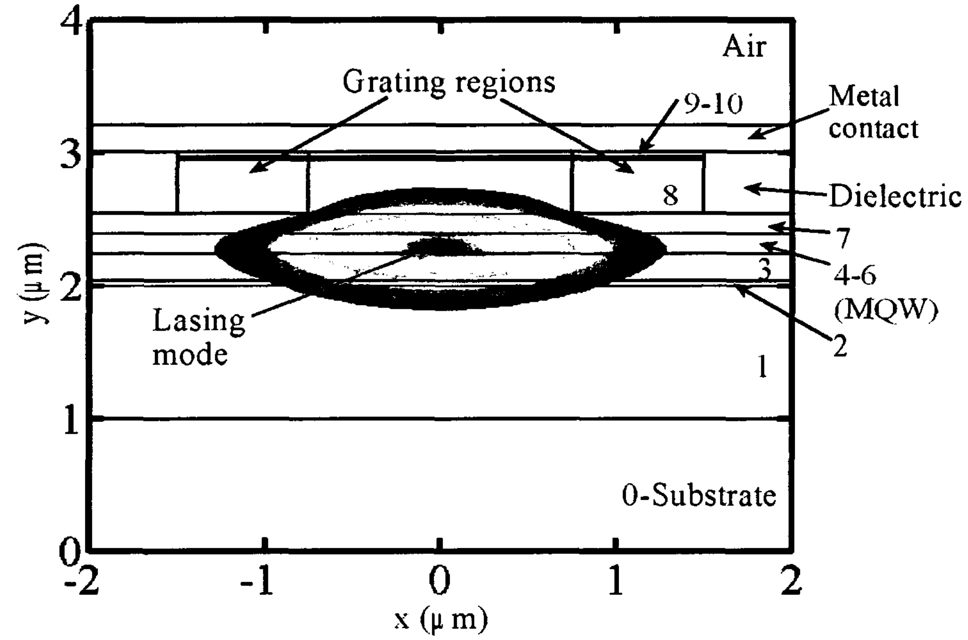

Figure 22. **Fundamental quasi-TE mode solution of LC-DFB laser. Refer to Table 3 for details of each layer number.**

modal overlaps of the $|E_x(x,y)|$ fields with a two-dimensional Gaussian function. The fundamental quasi-TE mode solution will have a significantly higher overlap value compared to all other solutions. The reason for this is that the single peak in the vertical and horizontal directions of the fundamental mode solutions, closely matches the form of a Gaussian (with different sigma values in the x- and y-directions), which also has a single peak in the horizontal and vertical direction, particularly compared to multiple peaks in higher order solutions. I found this method to be a simple yet fast way to find the quasi-TE mode fields (or quasi-TM mode fields if the $|H_x(x,y)|$ field is used) given the large array of spurious solutions that can be generated by COMSOL. The drawback is that this approach is somewhat dependent on the choice of the Gaussian test mode parameters - manual inspection is still sometimes required, particularly if widely-varying ridge geometries are simulated.

The computational window required to determine the fundamental quasi-TE mode is smaller than for the partial wave solutions, since the mode is not radiating. The window of 14 μm x 10 μm, in the x- and y-directions, respectively, was selected to be sufficiently large so that there is negligible interaction of the mode field with the PEC boundaries. The finite-element mesh was adaptively refined to maximize the mesh density in the areas of the highest mode intensity. The effective index eigenvalue and quasi-TE mode eigenfunction are used in (4.38) to generate κ_p, the coupling coefficient between the two contradirectionally propagating fundamental modes. In a first-order grating, κ_p can be considered to be the total coupling coefficient, since there is no coupling to radiating partial waves. Previous analyses of the coupling coefficient of higher order LC-DFB lasers have considered only the κ_p term in the calculation of the coupling coefficient [55], [86], [87]. Our calculations demonstrate that the effective coupling coefficient, κ_{eff}, as defined by (4.45), can vary significantly from κ_p.

4.4.2 Partial Wave Solutions

Once the fundamental quasi-TE mode for the LC-DFB waveguide has been obtained, (4.41), (4.43), and (4.44) are used to find the Streifer coefficients. The calculation of the Streifer coefficients requires the solution of the partial waves, $\varepsilon_m^{(i)}(x,y)$ from (4.41). This two-dimensional problem is solved using COMSOL Multiphysics, using the Helmholtz wave equation application mode [85]. The problem is simpler than the mode-solving problem of Section 4.4.1 because it is not an eigenvalue problem; instead, the propagation constant is a known quantity given by (4.26).

The partial wave problem, however, does present an additional difficulty compared to the mode-solving problem. For partial wave orders $0 < m < N$-1, the partial wave will be radiative. For higher order gratings, this results in N-1 radiating partial wave solutions. This presents difficulties when simple Dirichlet or Neumann boundary conditions are used. If a significant portion of the radiating field is reflected from these boundaries, spurious resonances will occur, resulting in incorrect solutions. The size of the computational window could be increased until there is a negligible field at the boundary, but this requires an impractically large amount of computational memory and prohibitively long simulation times. Instead, absorbing boundary conditions are used for computing the partial waves. Figure 23 illustrates the difference in the solutions obtained when absorbing boundary conditions are used. The spurious resonances that are apparent in Figure 23a, with simple Dirichlet boundaries, are eliminated by the absorbing boundary conditions, as shown in Figure 23b.

The absorbing boundary has a conductivity that increases in only one direction, i.e. in the x-direction for the left and right boundaries and in the y-direction at the bottom boundary (the highly-reflective layer of metal and air above the ridge makes the use of an absorbing boundary at the top unnecessary). The unitless extinction coefficient, σ, in the x-direction is given by,

$$\sigma = \sigma_{\max}\left(\left(x - x_0\right)/W\right)^2 \tag{4.63}$$

where W is the width of the absorbing layer, x_0 is the x-coordinate at the edge of the boundary layer, and $\sigma_{\max}$ is the maximum extinction coefficient that occurs at the outer edge of the absorbing boundary. A value of W=1 μm was chosen to maintain a reasonable sized computational area, and the change in ζ_1 as the value of $\sigma_{\max}$ was varied was determined. It was found that the real and imaginary parts of ζ_1 both reach a stable plateau for a range of values near $\sigma_{\max} = 10$. This value of $\sigma_{\max}$ is used for all subsequent calculations.

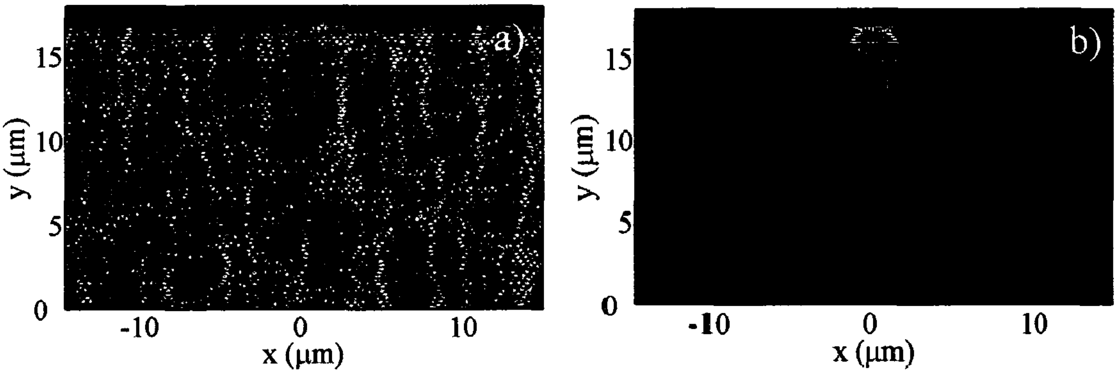

Figure 23. Radiating partial wave of order m=0.7 for a third-order grating with a duty cycle of 0.7 a) without absorbing boundary conditions and b) with absorbing boundary conditions

In a similar fashion, the computational window size and density of the adaptive mesh were chosen to be sufficiently large to achieve convergence of the coupled-mode coefficients. The size of the computational window is 30 μm in width, with a substrate thickness of 15 μm and a top air layer of 1 μm. The mesh is adaptively refined for each fundamental mode and partial wave solution. The reader is referred to COMSOL documentation for more details on the adaptive mesh refinement algoritm used [85]. The effect of adaptive refinement is to increase the density of the mesh in the regions of the highest field intensity. Typical fundamental mode solutions used 100 000 mesh elements and typical partial wave solutions used 200 000 mesh elements. Figure 24 shows a representative adaptive mesh used for a a) fundamental TE mode and b) first-order partial wave solution. It is apparent from comparison of the meshes that the partial wave solutions require a dense mesh over a much larger spatial extent than the fundamental mode solution mesh. The infinite summations of (4.43) must be truncated to allow the Streifer coefficients to be numerically evaluated. Fortunately, the terms, as they are weighted by the Fourier coefficient term, decrease in value away from the major partial wave orders near q=0, and higher order partial wave orders can be safely neglected. We found that the coupling coefficient converged to within 0.1% of the asymptotically converged solution when using only partial wave orders from $-9 \le m \le 7$. These are the partial wave orders used in the subsequent simulations.

All modified coupling coefficients for a given two-dimensional cross-section can be generated in approximately 30 minutes using a 2.66 GHz dual quad-core computer with 24G of RAM using a Linux operating system. Only ζ_1 and ζ_2 are calculated for rectangular gratings since, as mentioned above, $\zeta_1 = \zeta_3$ and $\zeta_2 = \zeta_4$ due to the symmetry of the grating.

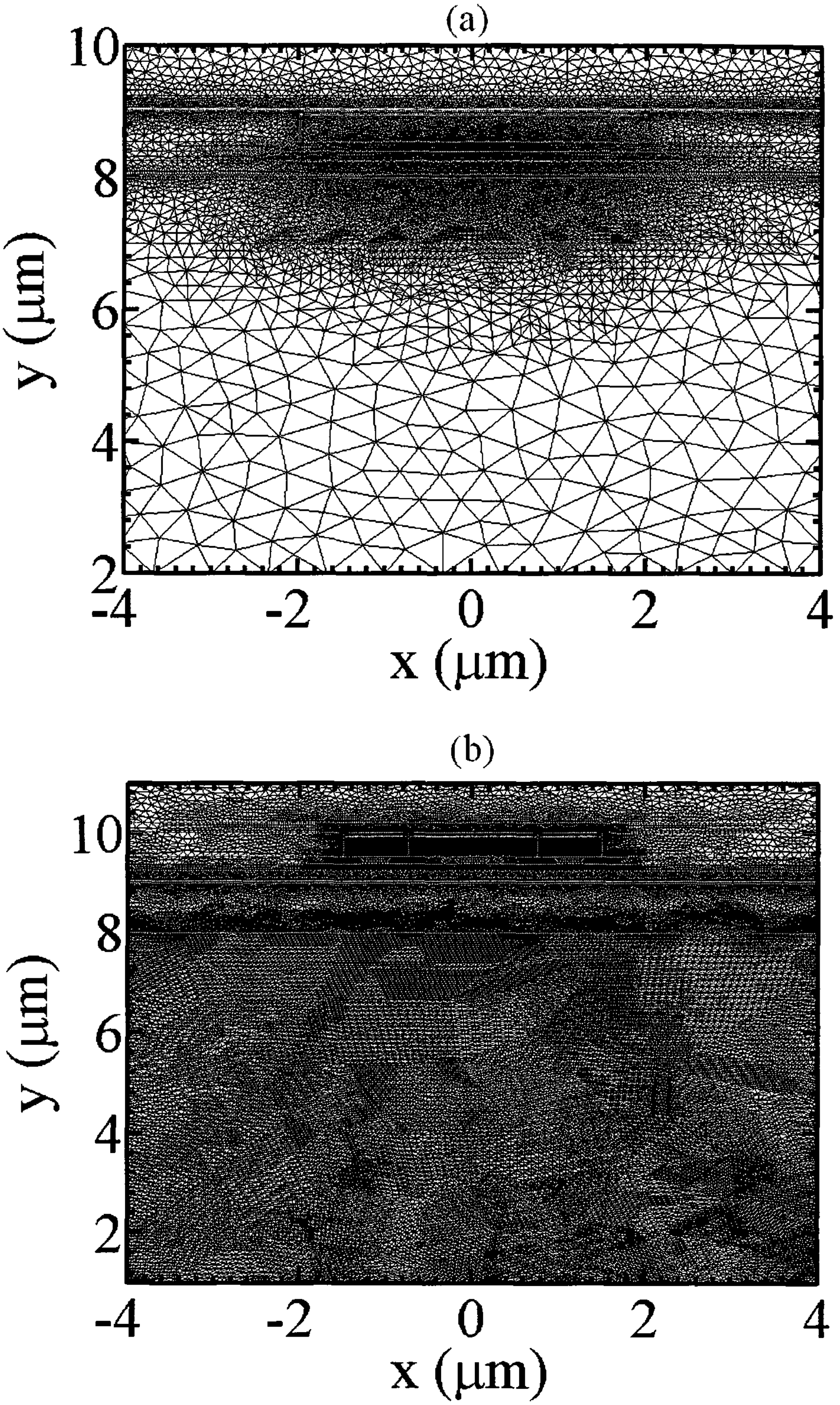

Figure 24. Adaptive mesh for the a) fundamental quasi-TE mode and b) first-order partial wave solution.

4.5 Simplified Laterally-Coupled Distributed Feedback Threshold Solutions

The simplified longitudinal mode solutions are found from the modified coupled-mode equations given in (4.42). For the simplified solutions, it is assumed that the threshold gain, α, and Bragg frequency detuning, δ, are independent of position. This assumption is reasonable near threshold where the carrier distribution, and hence gain, should be relatively uniform. As we will see in Chapter 6, this assumption can fail as we operate the laser at higher bias currents. These two eigenvalues, α and δ, must be solved along with the two eigenfunctions, A and B, the forward- and backward-propagating longitudinal modes, respectively, from (4.42). The facet reflectivities, r_1 and r_2, are assumed to be known quantities, resulting in a two-point boundary value problem.

To solve (4.42) for A and B, we use a technique known as the shooting method [88]. With the shooting method, we begin at the left facet, with reflectivity r_1. The value of $B(z=0)$, the counter-propagating field at the left facet, is arbitrarily chosen. It can be shown that the eigenvalues are independent of the chosen value of $B(z=0)$. The value of $A(z=0)$ is obtained through the boundary condition $A(z=0)=r_1B(z=0)$. Values for α and δ are assumed, and the longitudinal fields for the assumed eigenvalues are found by integrating the left facet fields according to (4.42) to find $A(z=L)$ and $B(z=L)$, the values of the fields at the right facet. These fields are compared to the boundary condition $B(z=L)=r_2A(z=L)$, resulting in an error function of the form,

$$\varepsilon = A(z=L)-r_2B(z=L) \tag{4.64}$$

For a solution (i.e. the α and δ eigenvalues) to be found, both the real and imaginary portions of this error function must equal zero

$$\begin{aligned}\Re\{\varepsilon(\alpha,\delta)\}&=0\\ \Im\{\varepsilon(\alpha,\delta)\}&=0\end{aligned} \tag{4.65}$$

The shooting method adjusts the eigenvalues used based on the error condition (4.65) after each iteration until a convergent solution has been found. Two further algorithms are required to obtain these solutions: 1) a numerical integrator to evaluate $A(z=L)$ and $B(z=L)$ given $A(z=0)$, $B(z=0)$, α, and δ, and 2) a root-finding algorithm to determine what α and δ eigenvalues satisfy the error condition (4.65). We will use a 4th-order Runge-Kutta integrator and a Newton-Raphson root-finder for these two algorithms.

4.5.1 4th-order Runge-Kutta Numerical Integration

To find the field amplitudes at the right facet, $A(z=L)$ and $B(z=L)$, from (4.42), a 4th-order Runge-Kutta (RK4) integrator is used. This method applies to coupled first-order differential equations of the general form

$$\frac{dy_i(z)}{dz}=f_i(z,y_0,y_1,\ldots,y_{N-1}) \qquad i=0,\ldots,N-1, \tag{4.66}$$

where y_i are the coupled eigenfunctions (in our case A and B), and z is the dependent variable. The RK4 solver is implemented by dividing the computational domain into discrete slices of length h along the longitudinal (z-) direction. The first values, $y_i^{(1)}$ are assumed to be known from the boundary conditions, and all subsequent values of the eigenfunctions, $y_i^{(n+1)}$, are obtained from the values in the previous slice, $y_i^{(n)}$, using,

$$
\begin{aligned}
k_1 &= hf\left(z^{(n)}, y_i^{(n)}\right),\\
k_2 &= hf\left(z^{(n)} + h/2, y_i^{(n)} + k_1/2\right),\\
k_3 &= hf\left(z^{(n)} + h/2, y_i^{(n)} + k_2/2\right),\\
k_4 &= hf\left(z^{(n)} + h, y_i^{(n)} + k_3\right)
\end{aligned}
$$

and

$$y_i^{(n+1)} = y_i^{(n)} + \frac{k_1}{6} + \frac{k_2}{3} + \frac{k_3}{3} + \frac{k_4}{6}. \tag{4.67}$$

The RK4 method is a much more robust but slower solver compared to those based on other techniques such as Burlisch-Stoer and predictor-corrector methods [88]. It is possible that these other methods would also be suitable for this problem, but it was decided to trade off computational efficiency for a reliable solution algorithm in this case. The algorithm is applied to (4.42) by setting $y_1^{(n)} = A^{(n)}$ and $y_2^{(n)} = B^{(n)}$, so that

$$f\left(z^{(n)}, A^{(n)}, B^{(n)}, \alpha, \delta\right) = \left(\alpha + j\delta + j\zeta_1\right)A^{(n)} + j\left(\kappa_p^* + \zeta_2\right)B^{(n)} \tag{4.68}$$

It is straightforward to include an arbitrary phase-shift in the RK4 solver. At the point where the phase-shift occurs, the phase of the A and B fields are correspondingly shifted. For instance, a λ/4 phase-shift between the slices n and n+1, the A and B fields will be given by,

$$
\begin{aligned}
A^{(n+1)} &= A^{(n)} e^{i\pi/2}\\
B^{(n+1)} &= B^{(n)} e^{-i\pi/2}
\end{aligned}
\tag{4.69}
$$

where the negative shift for the B field is due to the negative propagation constant relative to A.

4.5.2 Newton-Raphson Root-Finding Algorithm

The Newton-Raphson algorithm is an iterative technique that relies on the partial derivative of a function to make successively improving approximations of the root for the next iteration [88]. It converges rapidly, but only if a good initial guess is provided. A general multidimensional root-finding problem consists of N functions to be zeroed, with each having N dependent variables:

$$F_i(x_1, x_2, \ldots, x_N) = 0 \qquad i = 1, 2, \ldots, N. \tag{4.70}$$

In our case we have simply two functions, $\Re\{\varepsilon\}$ and $\Im\{\varepsilon\}$, given by (4.64), and two dependent variables, α and δ. The general case can be expressed in matrix notation, i.e. **F**(**x**)=0, where **F** is a vector of the functions to be zeroed and **x** is a vector dependent variables. Expanding **F** in the neighborhood of **x** using a Taylor series results in,

$$F_i(\mathbf{x}+\delta\mathbf{x}) = F_i(\mathbf{x}) + \sum_{j=1}^{N} \frac{\partial F_i}{\partial x_j}\delta x_j + O\left(\delta\mathbf{x}^2\right) \tag{4.71}$$

where $O(\delta\mathbf{x}^2)$ denotes second-order terms of the Taylor series expansion that are ignored. The matrix of partial derivatives in (4.71) is known as the Jacobian matrix, **J**, with elements given by:

$$J_{ij} = \frac{\partial F_i}{\partial x_j}. \tag{4.72}$$

Using the Jacobian matrix, **J**, the first-order Taylor expansion is expressed in matrix notation as:

$$\mathbf{F}(\mathbf{x}+\delta\mathbf{x}) = \mathbf{F}(\mathbf{x}) + \mathbf{J}\cdot\delta\mathbf{x} + O\left(\delta\mathbf{x}^2\right). \tag{4.73}$$

The Newton-Raphson (NR) technique begins by taking an initial guess, solving for **F**(**x**) and **J**, and then calculating the $\delta\mathbf{x}$, based on these values, that is most likely to lead to a root. This $\delta\mathbf{x}$ is added to the current guess to give an improved guess for the next iteration, $\delta\mathbf{x}_{new} = \mathbf{x}_{old} + \delta\mathbf{x}$. To calculate the best-guess value of $\delta\mathbf{x}$, we neglect the higher order terms of the Taylor expansion and set $\mathbf{F}(\mathbf{x}+\delta\mathbf{x})=0$ to obtain

$$\mathbf{J} \cdot \delta\mathbf{x} = -\mathbf{F}. \tag{4.74}$$

This is the matrix equation that must be solved for each iteration of the Newton-Raphson method to find $\delta\mathbf{x}$, and hence $\delta\mathbf{x}_{\text{new}}$.

This method assumes that **J** is a known quantity. The error function we are using is not analytical, so the Jacobian must be calculated numerically. A finite difference method is employed to calculate the Jacobian matrix:

$$J_{ij} = \frac{F_i(x_j + hx_j) - F_i(x_j)}{hx_j} \tag{4.75}$$

where h is a very small step size operator. In our case, h was set to the square root of 'eps', a Matlab variable that returns the lowest available numerical precision. This gave a value of h=1.4901 x 10^{-8} on a standard Windows desktop PC.

The NR root-finding algorithm is applied to this problem by using the vectors

$$\mathbf{x} = \begin{bmatrix} \delta \\ \alpha \end{bmatrix} \text{ and } \mathbf{F} = \begin{bmatrix} \Re\{\varepsilon\} \\ \Im\{\varepsilon\} \end{bmatrix}. \tag{4.76}$$

4.5.3 Implementation

The shooting method relies on a root-finding algorithm to successively determine the solution that matches the boundary conditions. The NR root-finding algorithm is well-suited to determining a single root when given a good initial starting point. Unfortunately, multi-dimensional root-finding of multiple non-linear equations is not a trivial problem. Press *et al.* go so far as to say that, "there are *no* good, general methods for solving systems of more than one nonlinear equation. Furthermore, … there *never will be* any good, general methods…" [88]. In our case we have two functions, the real and imaginary parts of the error function. The intersection of the zero contours of these functions will give the roots. These contours will consist of an unknown number of disjoint curves. As an example, Figure 25 shows the zero contours of the error function for a third-order phase-shifted grating with a duty cycle of 0.6 and length of 500 μm. The contours in Figure 25 are plotted versus the normalized gain, αL, and normalized Bragg deviation, δL. The contours have multiple intersection points, and the NR root-finding algorithm will converge on only one of these possible solutions.

To find all roots in the two-dimensional space within a reasonable amount of time, a two step algorithm is used. First, a rough pass over the entire solution space is performed. Step sizes of $\Delta(\alpha L)=0.2$ and $\Delta(\delta L)=0.5$ were found to be sufficient. From this low-resolution picture of the solution space, all local minima are bracketed. Each of these local minima are then used as initial guesses for the two-dimensional NR root-finding algorithm. It often happens that two distinct local minima converge to the same solution; in this case the repeat solution is simply discarded.

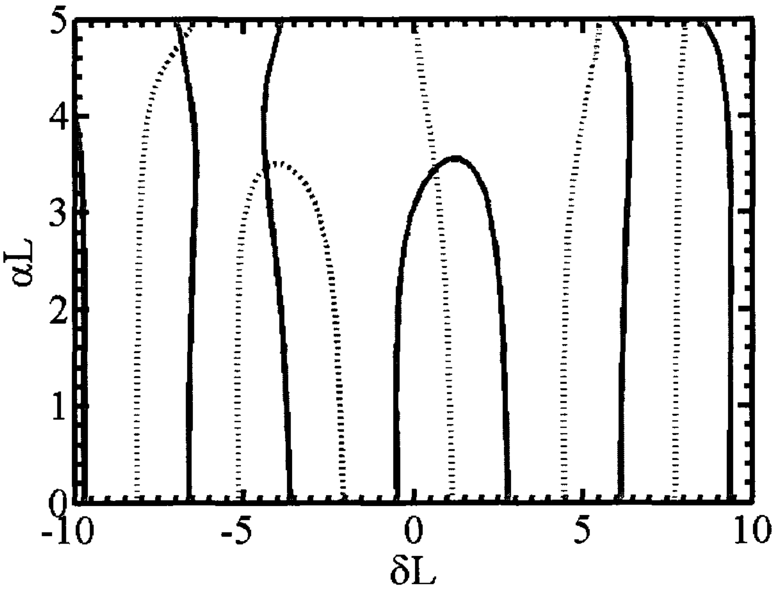

Figure 25. **Zero contours of the real part of the error function (solid lines) and the imaginary part of the error function (dotted lines) for a phase-shifted third-order 500 μm long grating with a duty cycle of 0.6. Intersection points indicate eigenvalue solutions.**

The algorithm was implemented using MATLAB. Convergence typically occurs within three iterations, taking only a few seconds, with the most computationally-intensive portion of this calculation being the initial search for root intervals. For a typical search area of $\delta L \in [-10,10]$ and $\alpha L \in [0,5]$ the complete root-finding routine takes only approximately 30 seconds on a standard desktop PC.

The critical parameters that can be obtained from this analysis are the longitudinal mode with the lowest normalized threshold gain, $(\alpha L)_{\min}$, and the difference between this gain and the normalized threshold gain of the next mode with the next lowest (αL). This is referred to as the normalized gain difference, or NGD. A good LC-DFB laser design will have a relatively low $(\alpha L)_{\min}$ and a relatively high NGD. Typically, values of NGD > 0.2 are considered desirable [89]. Another critical consideration when selecting a cavity length is the optical field flatness. This can be quantified with the flatness parameter, F:

$$F = \frac{1}{L}\int_{0}^{L}\left[I(z)/I_{av} - 1\right]^{2} dz \tag{4.77}$$

where the intensity, I, is given by $I = |A(z)|^2 + |B(z)|^2$, and I_{av} is the average intensity in the laser cavity. F will decrease as the optical field becomes more uniform within the laser cavity. The carrier distributions tend to approximately follow the optical field intensity, I. If I is highly non-uniform, the carrier distributions will be non-uniform, leading to longitudinal spatial hole burning (LSHB). A large degree of LSHB produces a number of detrimental effects in DFB lasers, including frequency shifts, nonlinear LI characteristics, and a longer settling time after a change in current due to the time constant of the spatial hole burning. To minimize LSHB, a flatness criterion of $F < 0.05$ is used, based on the work of Fernandes [90].

4.6 Comparison with Other Models

The simulations by Zhong *et al.* [91] provide a useful comparison for our model. Their simulation of a second-order distributed feedback laser includes the calculation of the modified coupled-mode characteristics and the simplified longitudinal mode solutions based on a 2D cross-section. The gratings examined by Zhong *et al.* in this particular paper are not laterally-coupled, but are instead within a thin 30 nm layer near the active layer. However, the solution procedure for the two treatments is similar. Although their exact solution algorithm is not explained in detail, they did use a modified coupled-mode analysis on a two-dimensional cross-section, with the partial-wave fields calculated using a finite-difference solver. The goal is to replicate their results using the solution algorithm that was outlined in Sections 4.4 and 4.5.

The placement of the gratings leads to a radiating partial wave that is quite different from those calculated for the LC-DFB lasers shown in Figure 23b). The radiating partial wave field, shown in Figure 26, agrees well with the result shown by Zhong *et al.*, although an

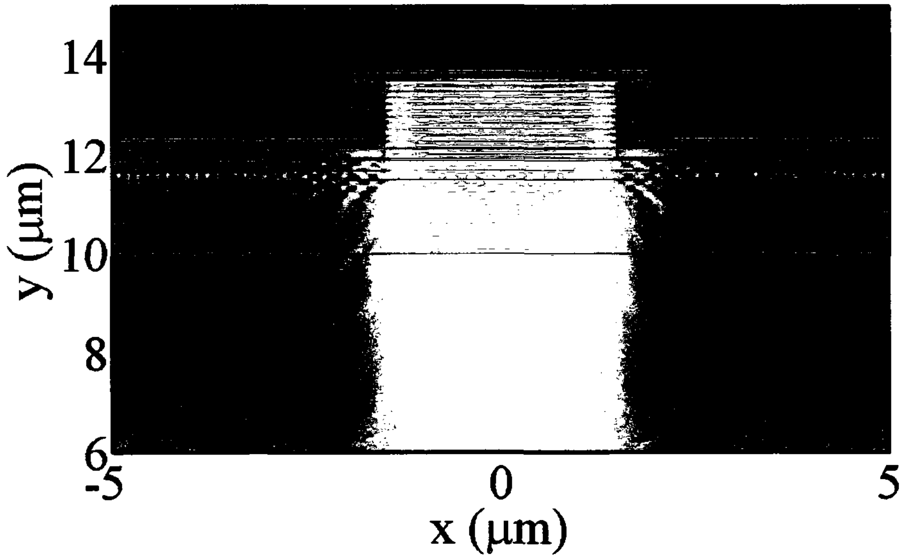

Figure 26. **First-order radiating partial wave calculated for the DFB laser of Zhong *et al.***

exact comparison is impossible since their figure does not include an intensity scale. From this figure, we see that there are strong resonances within the waveguide ridge, mainly in the y-direction. Depending on the height of the ridge, these resonances will be stronger or weaker, resulting in a periodic effective coupling coefficient dependence on the ridge height that also occurs for laterally-coupled gratings, as we will see in Chapter 5.

A numerical comparison can be performed by calculating κ_{eff} for a range of duty cycles from 0 to 1. The solid lines of Figure 27 are points calculated by our program, the circle markers denote points calculated by Zhong *et al.*; the maximum deviation between the two sets of values is 4%. The Zhong paper did not include the refractive index they used for the MQW active region, and the height of the ridge was oddly specified in terms of the radiating partial wave wavelength (which was only approximately stated), so some deviations between the two results are not unexpected. Figure 27 shows quite close agreement, however, for both the real and imaginary parts of κ_{eff} over the entire range of duty cycles.

The longitudinal mode solutions were compared by calculating the solutions for a 0.5 and 1 mm laser cavity at a duty cycle of 0.6. A comparison of the solutions calculated by

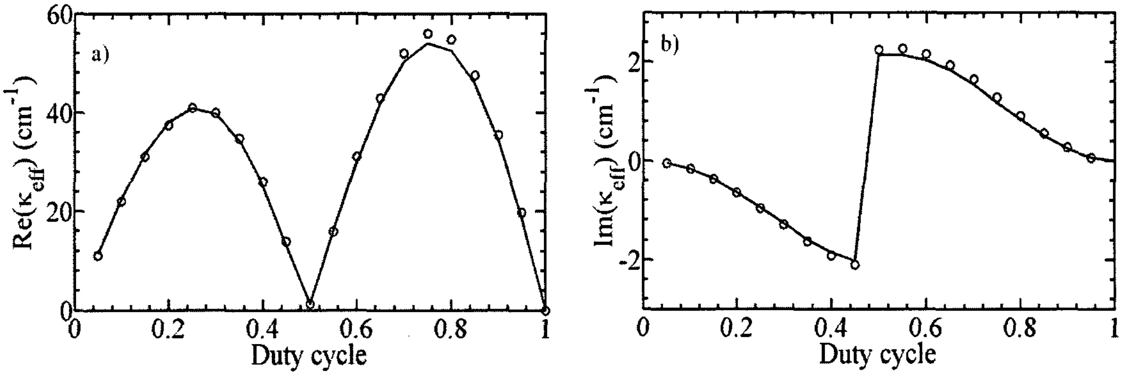

Figure 27. **Comparison of a) real and b) imaginary parts of the effective coupling coefficient calculated for the DFB laser of Zhong *et al.*. Solid lines are our calculated results, circle markers are points calculated by Zhong *et al.***

Zhong *et al.* and those calculated using our model is shown in Table 4. There is a deviation of < 0.1% in the longitudinal mode solutions when using the NR root-finding routine described above. The results of this model were also checked against the effective coupling coefficient calculations of Zhong *et al.* for laterally-coupled gratings [92], and the longitudinal mode solutions of Kinoshita [93]. This model also showed a good agreement within 10% of the results of both of these papers.

Cavity length	**L=0.5 mm**		**L=1 mm**	
	δL	αL	δL	αL
This work	2.944, -3.136	1.296, 1.458	4.109, -4.283	0.649, 1.012
Zhong *et al.*	2.942, -3.134	1.294, 1.456	4.108, -4.282	0.649, 1.012

Table 4. Comparison of this model and results of Zhong *et al.* [91]

CHAPTER 5 – ANALYSIS OF LATERALLY-COUPLED GRATING PARAMETERS

The main motivation for the development of these LC-DFB lasers is to achieve improved manufacturability using stepper lithography, as described in Chapter 2. It anticipated that LC-DFB lasers manufactured using stepper lithography will have a higher potential throughput compared to traditional DFB laser manufacturing due to the elimination of a regrowth step. However, if the design is highly sensitive to normal process variations, the resulting poor yield may cancel out the benefits of this higher throughput. It is important, therefore, to consider those grating parameters that may be reasonably expected to experience process variations, and to ensure that we choose a design that is not only high-performance, but also fabrication-tolerant. In this chapter, we will consider five grating parameters: the grating order, shape, duty cycle, grating height, and ridge width. In addition, the effect of the metal contact composition will be considered.

The gratings are compared through the modified coupled-mode coefficients, calculated using the numerical methods and theory of Chapter 4. In particular, the effective coupling coefficient, κ_{eff}, given by (4.45), provides a useful parameter for the comparison of different gratings that have the partial wave correction terms included. The magnitude, $|\kappa_{eff}| = \sqrt{\Im\{\kappa_{eff}\}^2 + \Re\{\kappa_{eff}\}^2}$ - where $\Im\{\kappa_{eff}\}$ is the imaginary portion of κ_{eff}, and $\Re\{\kappa_{eff}\}$ the real portion of κ_{eff} - is a measure of the strength of the grating. The phase of κ_{eff}, $\phi(\kappa_{eff}) = \tan^{-1}\left(\Im\{\kappa_{eff}\}/\Re\{\kappa_{eff}\}\right)$, is a measure of the longitudinal mode discrimination of the grating. The inverse tan function is evaluated to be between $-\pi/2$ and $\pi/2$ radians, resulting in phase jumps when the phase is rotated more than π radians.

5.1 Duty Cycle

One of the most critical grating design parameters is the duty cycle, also referred to as the mark-to-space ratio. Referring to Figure 6, the duty cycle, γ, is given by $\gamma = a / \Lambda$, where a is the length of the wide ridge and Λ is the grating period. The Fourier coefficients of the rectangular grating, A_q, are determined by the duty cycle and refractive index contrast of the grating, as seen in (4.58). The refractive index contrast can be somewhat adjusted, but is largely dependent on the requirements of the epitaxial growth structure, described in Chapter 3. The duty cycle is a geometrical parameter whose variation provides for considerable adjustment of A_q, despite some caveats that will be described below.

In Figure 28, we see the variation in the effective coupling coefficient with duty cycle for grating orders from first to fourth. The effective coupling coefficient, κ_{eff}, generally

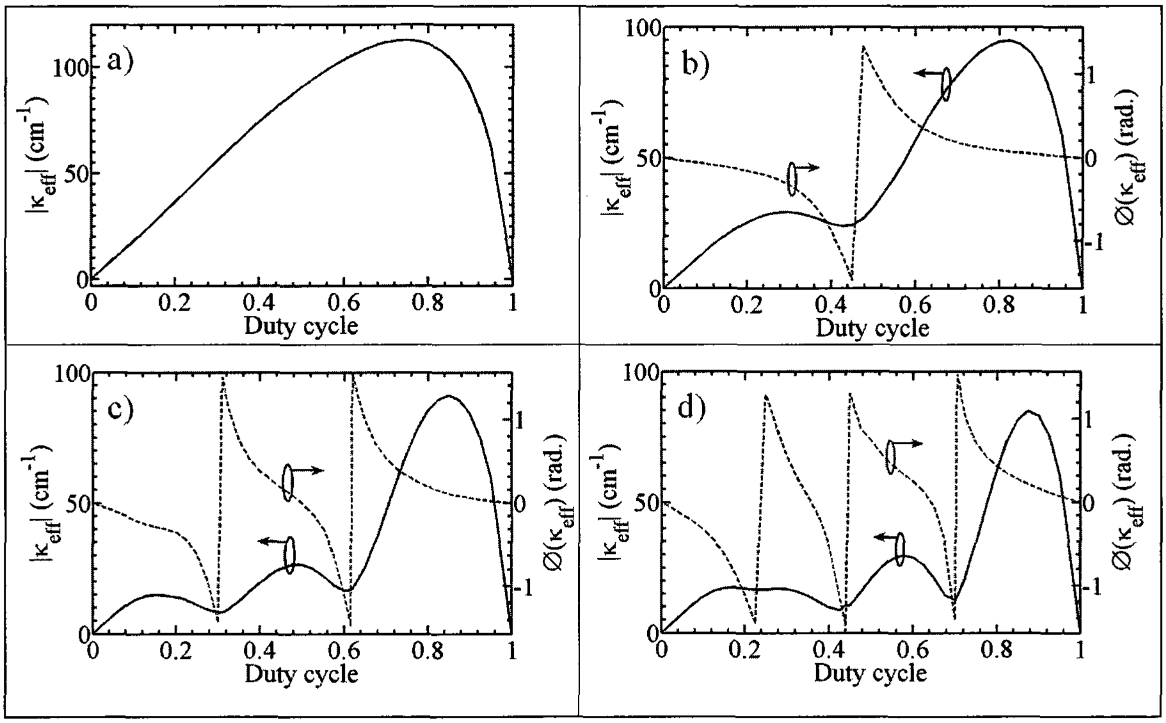

Figure 28. Effective coupling coefficient *vs.* duty cycle for a) first-order, b) second-order, c) third-order, and d) fourth-order gratings for a ridge width of $W_N/W_W = 1.5/3$ (μm).

grows with γ for all grating orders. As the duty cycle increases, the average refractive index in the grating region will also increase. This increases the optical confinement in the grating region, resulting in a larger κ_p value. As the duty cycle approaches 1, the grating begins to disappear, as will likewise the coupling. This overall trend is modulated by the peaks and valleys that occur in the Fourier coefficient, A_q, with the duty cycle. The number of these peaks and valleys will increase as the grating order increases. Not only do the number of peaks and valleys in $|\kappa_{eff}|$ increase as the grating order increases, but so do the number of phase jumps in κ_{eff}. The phase jumps indicate a wrapping of the phase, so more phase jumps indicates that the phase is changing more rapidly over the range of duty cycles.

These graphs reveal desirable points of stability for LC-DFB laser design. If κ_{eff} is tolerant to small changes in grating geometry, this results in a reliable laser and one that is tolerant to processing variations, producing a superior manufacturing yield. These points of stability correspond to the extrema of $|\kappa_{eff}|$ seen in Figure 28. For the first-order grating, the coupling coefficient is purely real, and $|\kappa_{eff}|$ has a single peak at a duty cycle of $\gamma = 0.78$. The second-order grating has two peaks of $|\kappa_{eff}|$ = 29.2 and 94.4 cm^{-1} at duty cycles of γ=0.3 and 0.8, the third-order grating has three peaks of $|\kappa_{eff}|$ = 15.2, 26.6, and 90.8 cm^{-1} at duty cycles of γ=0.15, 0.5, and 0.85, and the fourth-order grating has four peaks at duty cycles of γ=0.15, 0.3, 0.6, and 0.9 where $|\kappa_{eff}|$= 17.3, 16.3, 29.8, and 85.0 cm^{-1}, respectively.

The phase of κ_{eff} is zero for a first-order grating, and will jump π radians N -1 times for an N^{th} order grating. These jumps occur at γ=0.5 for the second-order grating, at γ=0.3 and 0.6 for the third-order grating, and at γ=0.25, 0.425, and 0.7 for the fourth-order grating. When the phase of κ_{eff} goes to zero, the longitudinal mode discrimination will be zero, and the lasing mode will be unstable, as will be seen in Chapter 6. These zero-crossings occur at gratings of third-order and higher, for example, at $\gamma = 0.5$ for the third-order grating, and at $\gamma = 0.35$ and 0.65 for the fourth-order grating.

The value of κ_{eff} can differ significantly from the simple coupling coefficient, κ_p, that neglects the radiating partial waves. For instance, at a duty cycle of 0.7, we calculate that a third-order grating has a simple coupling coefficient with a magnitude of $|\kappa_p| = 13.1$ cm^{-1}, while the calculated effective coupling coefficient has a magnitude over three times as large, of $|\kappa_{eff}|$=47.2 cm^{-1}. This demonstrates the importance of including radiating partial wave effects in calculations of higher order gratings.

The duty cycle that can be chosen will be limited by the resolution of the lithographic patterning process. A first-order grating with a Bragg wavelength of 1310 nm and γ=0.5 requires feature sizes of 100 nm, where the minimum feature size is $(1-\gamma)\Lambda$ for duty cycles > 0.5. This grating has a $|\kappa_{eff}|$=90.6 cm^{-1}. A third-order grating with the same Bragg wavelength of 1310 nm and γ=0.5 requires feature sizes of 300 nm, but has a $|\kappa_{eff}|$=26.1 cm^{-1}. The choice of higher duty cycles can improve the grating strength, but will require smaller feature sizes. This will be examined in more detail in the following section.

The ζ_1 *vs.* duty cycle characteristic, shown in Figure 29, is also important to consider. The imaginary parts of the ζ_1 terms, as mentioned above, represent the light radiating away into unwanted diffraction orders. Large imaginary terms will result in higher threshold gains as more light is lost. The first-order gratings do not experience this loss, and are not shown here, as ζ_1=0 for all duty cycles. Second-order gratings have a maximum $\Im\{\zeta_1\}$ of 27 cm^{-1} at γ=0.525, third-order gratings have a maximum $\Im\{\zeta_1\}$ of

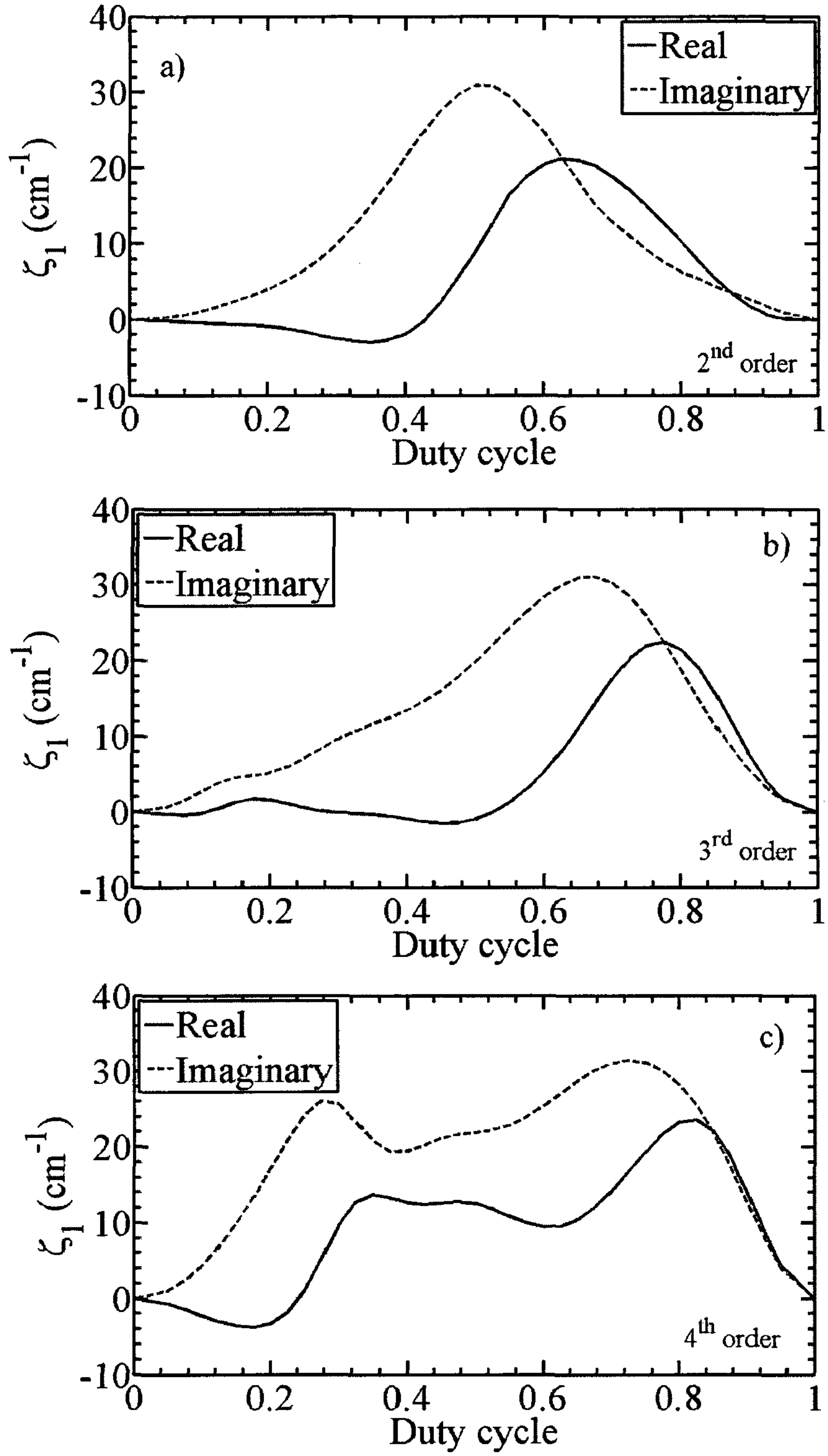

Figure 29. **Real (solid lines) and imaginary (dashed lines) portions of ζ_1 for second-, third-, and fourth-order gratings *vs.* duty cycle for W_N/W_W=1.5/3 (μm).**

31.1 cm^{-1} at γ=0.675, and fourth-order gratings have a maximum $\Im\{\zeta_1\}$ of 31.4 cm^{-1} at γ=0.725. There is relatively little difference in the maximum $\Im\{\zeta_1\}$ across the different grating orders, but for fourth-order gratings the maximum occurs at a γ value that is closer to the $|\kappa_{eff}|$ peak. It is difficult to draw general conclusions about the grating performance based purely on the ζ_1 values. We will instead use the longitudinal mode solutions, calculated in Chapter 6, as they will include the effect that these correction terms have on the grating performance.

5.2 Grating Order

First-order gratings are the standard choice for the majority of DFB laser designs. The reason for this is that higher order gratings will always have some light from the fundamental mode coupling into radiating diffraction orders, increasing the optical loss. It is now a standard process to use holography to define a sinusoidal first-order Bragg grating from the ultraviolet exposure of photoresist. Defining a first-order grating for a LC-DFB laser, however, is not as simple. As mentioned earlier, the typical grating period for a 1.3 μm DFB laser is approximately 200 nm. This requires feature sizes of 100 nm or less to define a first-order grating. The 5x i-line stepper available at CPFC, described in Chapter 2, has a minimum feature size of 365 nm, restricting it to gratings of at least third-order.

The previous analysis of the effect of the duty cycle showed that the magnitude of the coupling coefficient can be increased at higher duty cycles for all grating orders. When will it make sense to use a higher order grating with a higher duty cycle, rather than simply a lower order grating? We can answer this with the $|\kappa_{eff}|$ *vs.* minimum feature size characteristic shown in Figure 30. In this analysis, the minimum feature size is the gap between the grating teeth since duty cycles > 0.5 will have a greater $|\kappa_{eff}|$, as shown in Figure 28. This gap size is $(1-\gamma)\Lambda$ for a particular duty cycle. For a given feature size, and for all grating orders, the maximum $|\kappa_{eff}|$ associated with any duty cycle with a resolution less than or equal to the minimum feature size is selected. For example, although the duty cycle associated with a minimum feature size of 240 nm for a third-order grating is γ=0.6, the value of $|\kappa_{eff}|$ used is for γ=0.5, since it is greater and the minimum feature size for γ=0.5 is less. At minimum resolutions of $<$ 100 nm (the range where first-order gratings can be defined), it is always better to define a first-order grating to achieve the largest $|\kappa_{eff}|$. For larger minimum resolutions, a surprising result emerges: the best grating (i.e. the strongest) to fabricate for a given feature size is not necessarily the one with the lowest grating order. For feature sizes of 100 to 150 nm, it is the *third*-order and not the second-order grating with the largest $|\kappa_{eff}|$. For feature sizes of $>$ 150 nm, it is actually the *fourth*-order grating that has the largest coupling coefficient. Why does this happen? To illustrate the answer, let's look at feature sizes of 180 and 300 nm. At 180 nm, a maximum duty cycle of 0.55, 0.7, and 0.775, for second-, third-, and fourth-order gratings, respectively, can be achieved (first-order gratings cannot be defined at this minimum feature size), with $|\kappa_{eff}|$=42 cm^{-1}, 47.8 cm^{-1}, and 49 cm^{-1} for second-, third- and fourth-order gratings, respectively. The fourth-order grating is closer to its $|\kappa_{eff}|$ peak at this feature size than the other grating orders, allowing for a stronger grating. At a feature size of 300 nm, the best grating that can be fabricated of third-order is a γ=0.5 duty cycle one with $|\kappa_{eff}|$=26.6 cm^{-1}. The fourth-order grating can have a duty cycle of up to γ=0.625, but can achieve an even better $|\kappa_{eff}|$=29.8 cm^{-1} when a duty cycle of γ=0.575 is used. From Figure 28, we see that the local maximum at γ=0.5 for the third-order grating is smaller than the one at γ=0.575 for the fourth-order grating, due to the greater grating confinement at higher duty cycles. This difference of ~10% is not a excessive, but it could be useful when attempting to maximize the performance for a given minimum feature size limitation.

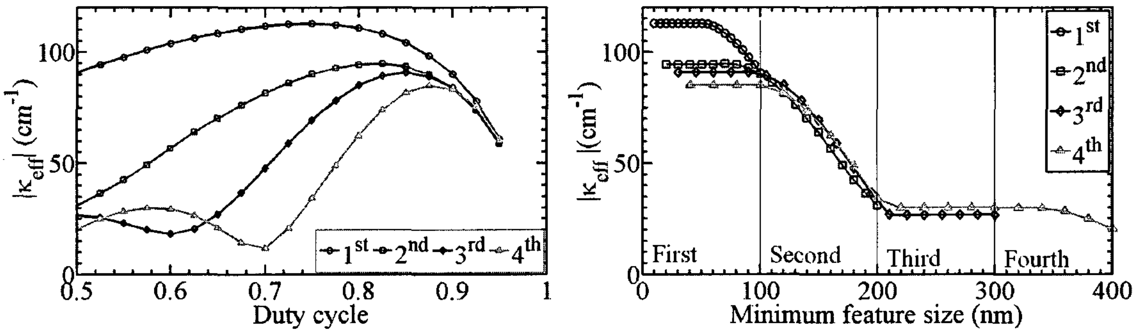

(a) (b)

Figure 30. a) Magnitude of effective coupling coefficient for higher duty cycles, b) maximum $|\kappa_{eff}|$ possible for a given minimum feature size, for first- through fourth-order gratings

Since it is clear that the 5x i-line stepper lithography resolution limit of > 300 nm available at CPFC forces us to use higher order gratings, it is helpful to determine what penalty must be paid when using higher order gratings in a DFB laser. The greater optical loss encapsulated in the $\zeta_{1,3}$ terms means that the threshold gain will be larger for a higher order grating than for a comparable first-order grating. This will increase the threshold current required and lower the laser efficiency. One benefit that a DFB laser with a higher order grating has over a standard first-order grating is that the higher order grating laser will have greater longitudinal mode discrimination at threshold, due to a degree of loss coupling. Using higher order gratings, in general, eliminates the two degenerate longitudinal modes at threshold that reduce the single-mode yield of the DFB laser. This will be more apparent in Chapter 6, where we analyze the longitudinal mode solutions for these grating geometries.

5.3 Grating Height

The height of the ridge, and hence of the laterally-coupled grating, is to some degree limited by the fabrication process used. To etch gratings with smooth, vertical sidewalls, it is desirable to have a shallower etch compared to traditional FP ridge heights of ~1 – 1.5 μm. The nominal grating height for this design is 0.5 μm, corresponding to a RIE depth that produces a quality grating etch and has good optoelectronic characteristics, as described in Chapter 3. We will investigate grating heights as low as 0.36 μm. For grating heights less than this value, the additional losses due to the proximity of the optical mode to the metal contact and InGaAs layer become unacceptable. We examine the effects of ridge height by increasing the thickness of layer 8, referring to the epitaxial growth structure of Table 3.

We wish to compare the simple coupling coefficient, κ_p, with the effective coupling coefficient, κ_{eff}. κ_p will generally increase as the grating height increases. This is due to the larger overlap of the fundamental mode with the grating region as the grating height increases. As the ridge height gets larger, and the high-index InGaAs layer moves farther away from the mode, the confinement in the grating region will slowly begin to diminish, causing a reduction in κ_p. This grating height dependence is validated in Figure 31 for a third-order grating with a duty cycle of 0.7. At this duty cycle the Streifer terms are particularly strong and the differences between κ_p and κ_{eff} are emphasized.

There is a pronounced difference between the behaviour of κ_p and that of κ_{eff} for higher order gratings, as shown in Figure 32 for a third-order grating with a duty cycle of 0.7.

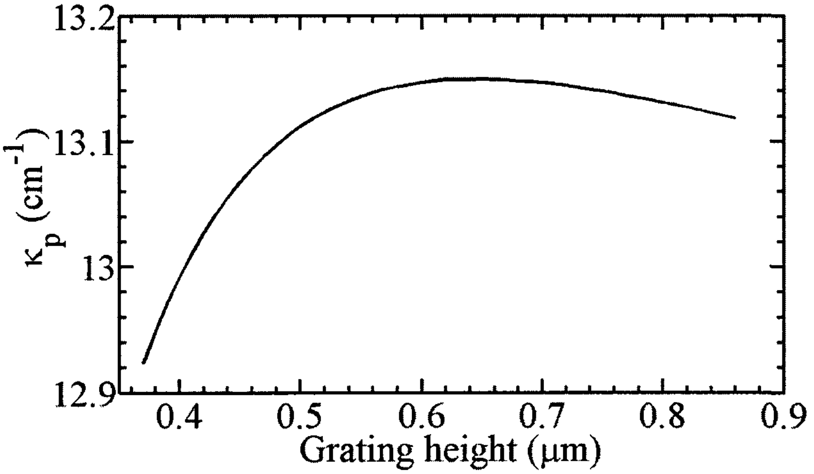

Figure 31. **Coupling coefficient of a third-order grating with a duty cycle of 0.7 *vs.* grating height for ridge widths of W_N/W_W = 1.5/3 (μm).**

Instead of a single broad peak in the coupling strength, κ_{eff} exhibits a periodic dependence on the grating height. The addition of the partial wave correction increases the coupling coefficient significantly, from values near $\kappa_p = 13$ cm^{-1} as observed in Figure 31 to a value at the nominal grating height of 0.47 μm of $\kappa_{eff} = 48.1\angle 0.58$ cm^{-1}. The magnitude of κ_{eff} reaches a maximum value of 49.1 cm^{-1} at a grating height of 0.49 μm. The next maximum occurs at a height of 0.75 μm where $|\kappa_{eff}| = 48.3$ cm^{-1}.

The periodic dependence of κ_{eff} on grating height arises from the radiating partial waves that are included in the calculation of the Streifer correction terms. The grating region, which sits upon epitaxial layers of differing compositions, has above it a Au/Pt/Ti metal contact. The radiating waves will experience partial reflection at each of these interfaces, forming a standing wave in the vertical direction, as shown in the detailed view of Figure 33. This effectively creates a series of vertical cavities. The grating height sets the resonance strength, yielding the periodic dependence seen in Figure 32. A smaller variation in κ_{eff} with grating height is seen for duty cycles and grating orders where the correction terms are less significant. For cases where there is a large swing in the effective coupling coefficient with height, such as that illustrated in Figure 32 for a duty cycle of 0.7, it is difficult to find a point that would be best for maximizing the

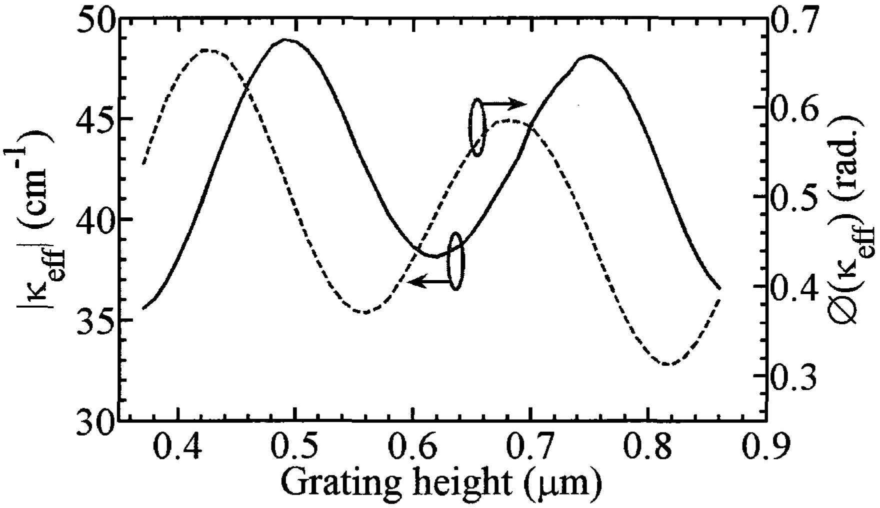

Figure 32. **Effective coupling coefficient of a third-order grating with a duty cycle of 0.7 *vs.* grating height for ridge widths of $W_N/W_W = 1.5/3$ (μm).**

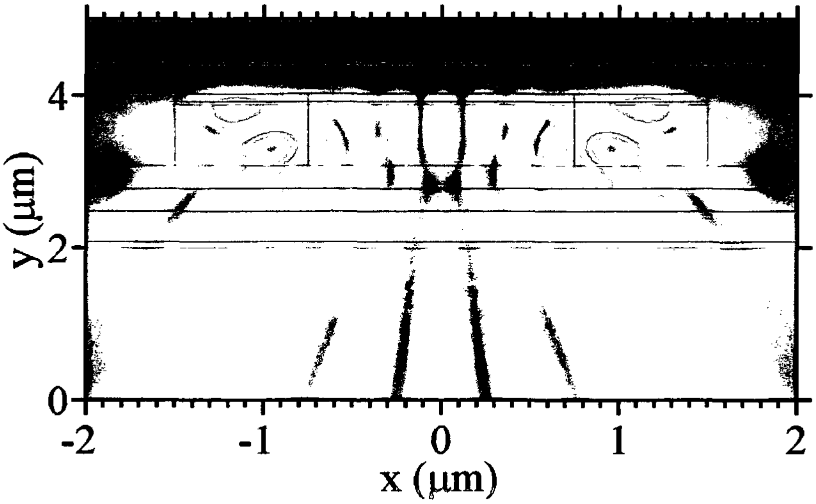

Figure 33. **Radiating partial-wave for a third-order grating**

manufacturing tolerance. The extrema of $|\kappa_{eff}|$, representing a stable amount of index-coupling, do not coincide with the extrema of $\phi(\kappa_{eff})$, representing a stable amount of loss coupling. It may be possible to improve both the real and imaginary portions of κ_{eff} by varying multiple layer thicknesses. Much like the design of anti-reflection coatings, however, optimizing the thicknesses of the layers for the best κ_{eff} will require detailed numerical calculations, since, unlike most other grating parameters, there is no obvious intuitive relationship.

The periodicity with grating height is also manifested in the simple longitudinal mode solutions of the modified coupled-mode equations. The minimal values of $(\alpha L)_{\min}$ do not coincide with the maximal values of NGD, as observed in Figure 34. A tradeoff must be made between a low threshold gain and having a large longitudinal mode discrimination. The $(\alpha L)_{\min}$ has local minima of 1.83 and 1.80 for the unshifted grating at grating heights of 0.52 μm and 0.78 μm, respectively, while the NGD has a maximum NGD of 1.38 at a grating height of 0.44 μm. Grating heights near 0.5 μm will provide a good balance of low threshold gain and high mode discrimination.

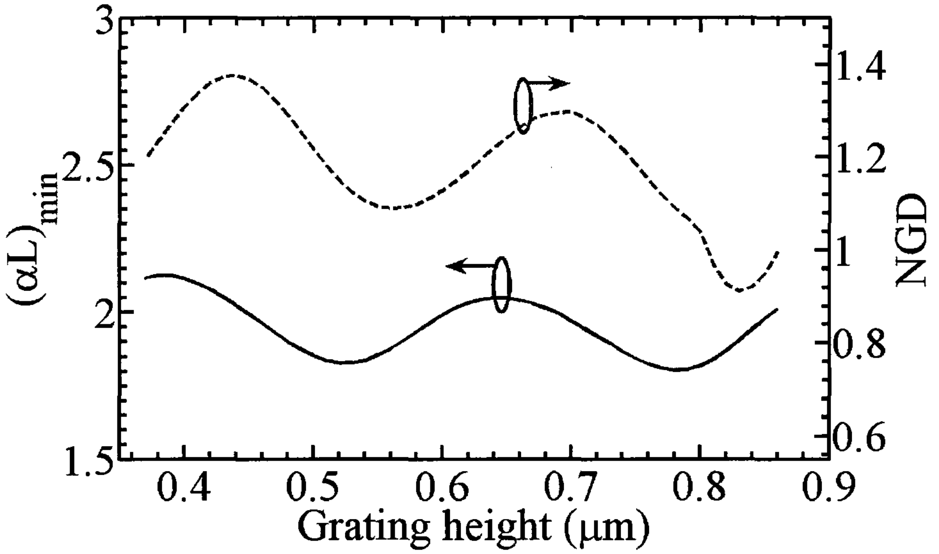

Figure 34. $(\alpha L)_{\min}$ **and NGD *vs.* grating height for a third-order grating with a duty cycle of 0.7 and ridge widths of W_N/W_w = 1.5/3 (μm)**

It should be noted that the electrical properties of the laser impose additional constraints on ridge height, and that these additional constraints may be in conflict with the purely optical considerations shown here. At greater ridge heights, the electrical resistance will increase, lowering the efficiency of the laser. This effect could be examined in more detail using LAS2D simulations. As mentioned above, large grating heights can also exhibit greater undercutting during fabrication, reducing coupling strength.

5.4 Ridge Width

In his study on the effect of ridge width on the coupling coefficients of laterally-coupled gratings, Choi found that the coupling coefficient will generally decrease as the narrow ridge width is increased [83]. Our results for higher order gratings confirm this decrease in the magnitude of the effective coupling coefficient. However, instead of a linear decrease in the value of $|\kappa_{eff}|$, subtle resonance peaks are visible, and there are more pronounced resonances in the phase of κ_{eff}, as shown in Figure 36. The resonance peaks

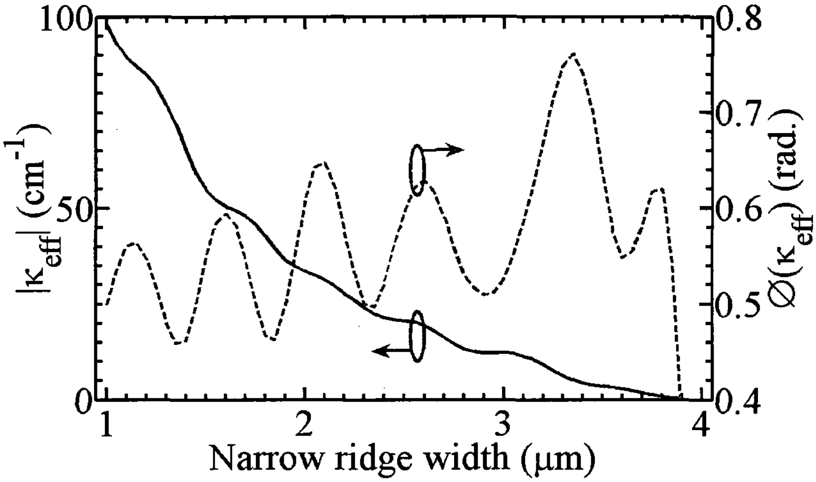

Figure 35. **Effective coupling coefficient *vs.* narrow ridge width for a wide ridge width of 4 μm, a third-order grating, and a duty cycle of 0.7**

are less pronounced than those due to the ridge height of Figure 32 for two reasons. First partial wave reflection from the side walls of the grating will not be as strong as that from the metal contact layer, as the refractive index contrasts are smaller. Second, the larger grating area as the width increases causes the magnitude of the κ_p terms to decrease faster compared to the resonance effects.

Subtle resonances are also observed for the dependence of $|\kappa_{eff}|$ and $\phi(\kappa_{eff})$ on the wide ridge width, W_W. In this case, shown in Figure 35, the value of κ_{eff} saturates as W_W becomes larger, with minimal change for $W_W > 3$ μm. The resonances of $|\kappa_{eff}|$ are no longer monotonic, unlike for the variation with W_N shown in Figure 35. This indicates that the partial wave resonances have a more dominant effect with W_W variation than W_N variation. The reason for this is that the simple coupling coefficient, κ_p begins to saturate in magnitude beyond $W_W > 3$ μm, and larger wide ridge widths have minimal impact. However, the partial wave resonances are still quite sensitive to the changes in W_W beyond this point, resulting in the stronger resonances in $|\kappa_{eff}|$ in Figure 36 compared to Figure 35, where the value of κ_p is sensitive to the whole range of W_N values used, damping out the partial wave resonaces.

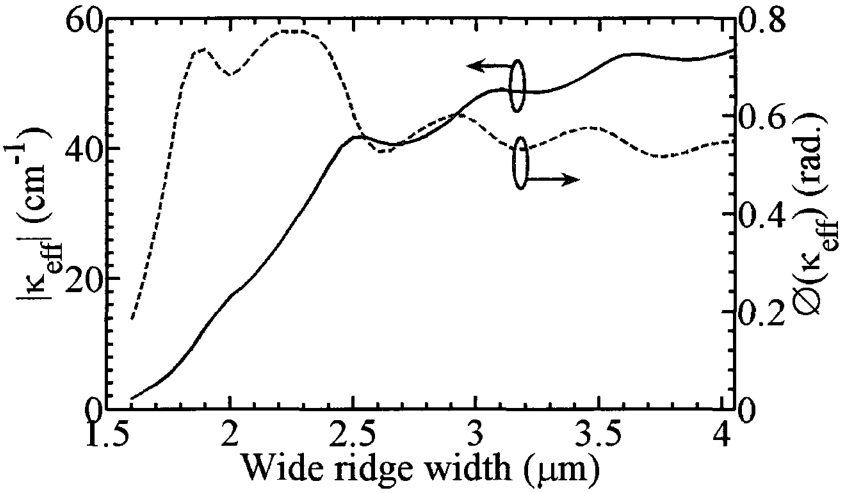

Figure 36. Effective coupling coefficient vs. wide ridge width for a narrow ridge width of 1.5 μm, a third-order grating, and a duty cycle of 0.7.

In choosing W_N and W_W, it is not sufficient to look at only the general trends to maximize $|\kappa_{eff}|$ of increasing W_W and decreasing W_N, given by Figure 35 and 35. The values of W_N and W_W are also constrained, as with the grating height, by electrical considerations. W_N must be wide enough to allow a dielectric via to be etched above the ridge to allow the formation of a p-contact. A value of 1.5 μm is a typical minimum ridge width required to obtain a proper dielectric via etch. In practice, as will be seen later, W_N was closer to 1.75 μm in the fabricated gratings. Very small values of W_N will also lead to a higher electrical resistance since the injected current must pass through the smaller metal contact surface area. The effect of larger electrical resistance is increased undesirable heating in the laser diode, further degrading the laser performance as fewer hot carriers are captured in the quantum wells. This also causes a shift in the operating wavelength because the material gain peak is red-shifted. The value of W_W is less constrained compared to W_N, but, as observed in Figure 35, increasing W_W leads to a minimal increase in $|\kappa_{eff}|$ beyond $W_W > 3$ μm. Very large W_W values could also cause lateral carrier leakage and an uneven distribution of carriers along the laser cavity as many more carriers could be injected in the wide ridge cross-sections than the narrow ridge cross-sections. The unevenness of the carrier distribution can be reduced by removing the InGaAs layer in the area beyond the metal contact, in particular above the grating teeth, reducing the carrier injection into these regions. This comes at the cost of an additional manufacturing step and a more complex mask. Larger W_W values will also tend to spread out the fundamental mode. Mode spreading will lead to greater mode asymmetry, increasing the coupling losses of the output waveguide to circularly symmetric optical fiber.

5.5 Grating Shape

In theory, the shape of the grating period can be arbitrary, but since we are fabricating gratings with periods near the resolution limit of i-line stepper lithography, only simple grating shapes that require little more resolution than the grating period itself should be used. The use of laterally-coupled gratings provides greater control over the grating shape than previous holographic methods, and this may potentially be exploited to improve the grating coupling. Four grating shapes will be examined in this Chapter: sinusoidal, triangular, rectangular, and trapezoidal. In Chapter 7, the influence of imperfections introduced during fabrication on the grating shape will be studied, particularly grating rounding.

Streifer *et al.* have performed a direct comparison between sinusoidal, triangular, and rectangular grating shapes for the one-dimensional case, considering only the simple coupling coefficient, κ_p. This investigation showed a significantly higher coupling coefficient for rectangular gratings compared to all other grating shapes [86]. The effect of different blazing angles, grating heights, and blazed grating shapes on the power radiated by a second-order grating was also studied by Streifer *et al.* [87]. Trapezoidal and rectangular grating shapes have been examined by P. Correc [94] and Cho *et al.* [95]. They also concluded that rectangular gratings provided the best coupling coefficient. This is perhaps what would intuitively be expected, since the abrupt interfaces of rectangular gratings are superior to other shapes for reflecting light directly backwards. We reveal, however, that when a more complete calculation of the coupling coefficient is performed that includes the Streifer correction terms that have been neglected in all previous analyses, non-rectangular grating shapes will often have a larger effective coupling coefficient than similar rectangular gratings for higher grating orders. This surprising result will be discussed in more detail below. In addition, we look at not only different vertically-varying grating shapes, as has been done with all previous analyses, but also horizontally-varying grating shapes. These grating shapes have not, to our knowledge, previously been analyzed.

As described in Section 4.3, the grating shape determines the Fourier coefficients, A_q , and the average refractive index, n_0, which is essentially the Fourier coefficient for q=0. Except for the special case of rectangular gratings, these two parameters will vary in the transverse direction within the grating region. Using the A_q and n_0 values derived in Section 4.3, the effective coupling coefficient was determined for sinusoidal, triangular, rectangular and trapezoidal grating shapes, for variation in the horizontal (x-) and vertical (y-) direction.

5.5.1. Vertical Shape Variation

An example of vertically-varying a) sinusoidal, b) triangular, and c) trapezoidal grating shapes are shown in Figure 37. Vertically-varying gratings, i.e. surface gratings, have been previously studied in the context of holographic fabrication techniques, but are more difficult to realize using standard etching techniques than horizontally-varying shapes. Multiple timed etches would be required, and even then, it would be difficult to define the vertically-varying grating shapes exactly. It is worth analyzing vertically-varying shapes to not only be generally applicable to holographically defined gratings but also since these shapes can be used to describe process variations that may occur during LC-DFB fabrication, such as undercutting of the ridge.

To provide a comparison point between different grating shapes, we plot in Figure 38 $|\kappa_{eff}|$ *vs.* the grating height for a third-order grating. As with Figure 32, the grating height is increased by thickening layer 8, referring to Table 3. Similar to the horizontal shape

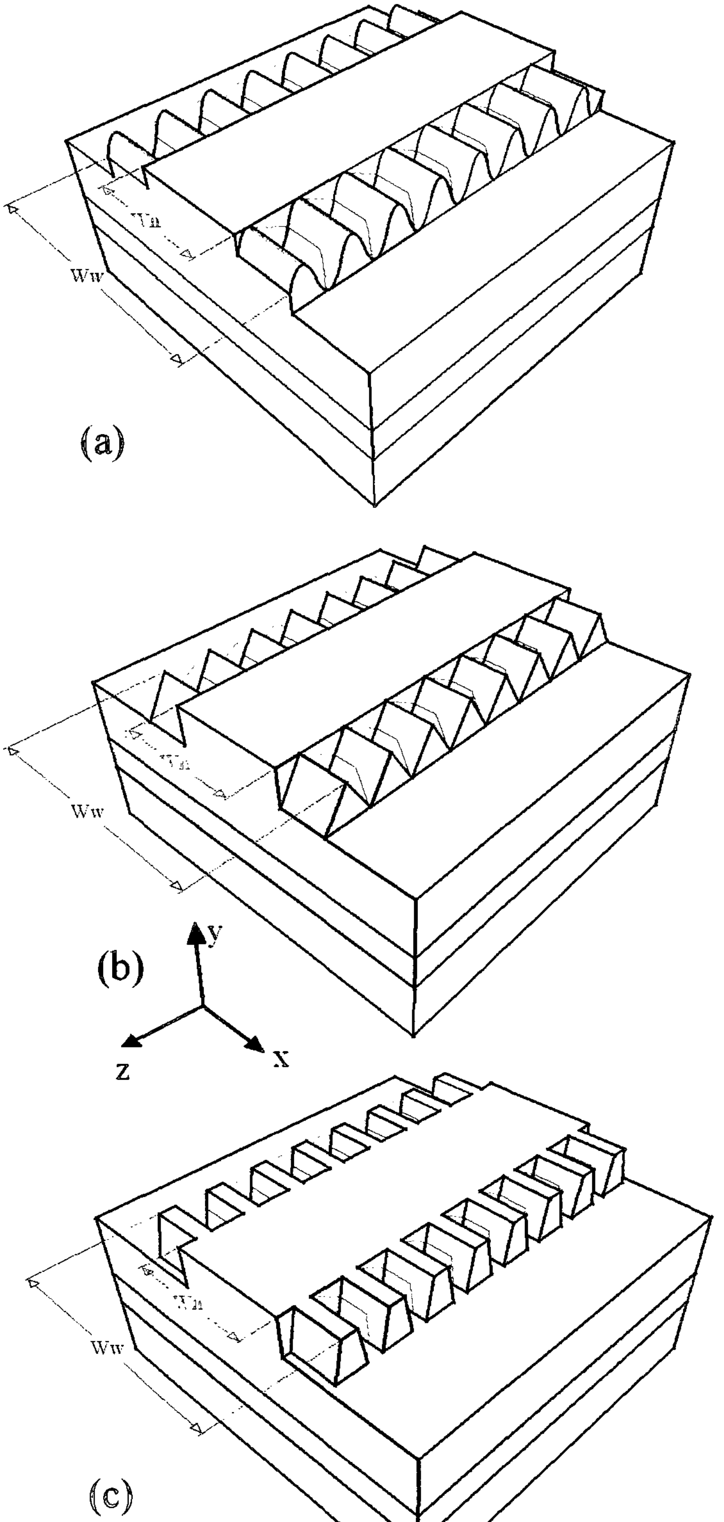

Figure 37. Vertically-varying a) sinusoidal, b) triangular, and c) trapezoidal laterally-coupled grating shapes

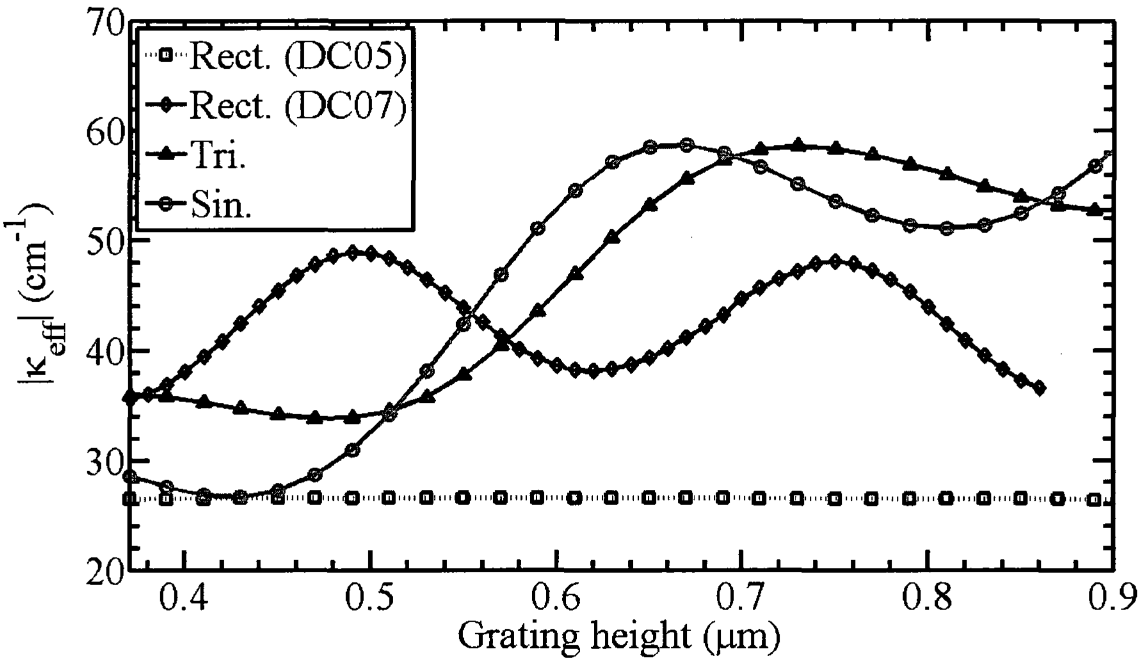

Figure 38. **Comparison of grating strength, $|\kappa_{eff}|$, for rectangular (with γ =0.5 and 0.7), symmetrical vertically blazed, and vertically sinusoidal gratings, for a third-order grating with W_N/W_W = 1.5/3 (μm).**

variation above, the rectangular grating shapes do not generally have the largest coupling coefficients. We have included not only rectangular gratings with duty cycles of γ=0.5, but also rectangular gratings with duty cycles of γ=0.7. As seen from Figure 28, higher duty cycle rectangular gratings generally have larger effective coupling coefficients. At smaller grating heights, such as the height of 0.47 μm used for our LC-DFB lasers, the rectangular grating with a duty cycle of 0.7 has the best coupling coefficient. The triangular and sinsusoidal gratings, however, have a higher coupling coefficient than the rectangular grating with γ=0.5, as might be expected from the previous section. As the grating height increases beyond 0.6 μm, however, the sinusoidal and triangular grating shapes out-perform both the half duty-cycle and the rectangular grating with the higher duty cycle of γ=0.7. This result is particularly interesting since most ridges in lasers are higher than the value of 0.47 used in this design. For the values of > 1 μm that are more common ridge heights, the sinusoidal or triangular grating shapes would provide a significantly better coupling coefficient than the rectangular grating of any duty cycle.

Another useful application of the vertical shape variation analysis is to determine the tolerances for the undercut of the ridge for our lateral coupling structures. It often occurs during wet etching that the bottom of the ridge will experience a greater etch than the upper part. This results in a sloped sidewall, as shown in an example of a ridge waveguide in Figure 39. To examine the potential for undercutting to weaken the grating coupling, a trapezoidal grating with varying angles of undercut was studied, similar to the horizontally- varying trapezoidal grating examined in the previous section. The result, shown in Figure 40, shows a degradation of the coupling coefficient as the grating deviates from vertical sidewalls. The negative angles represent undercut and the positive

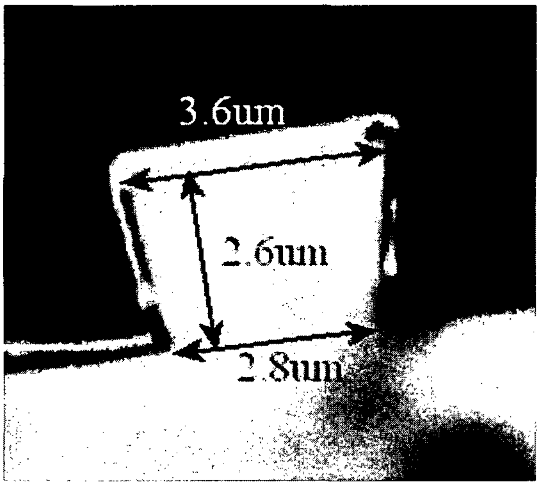

Figure 39. **Example of an undercut waveguide ridge**

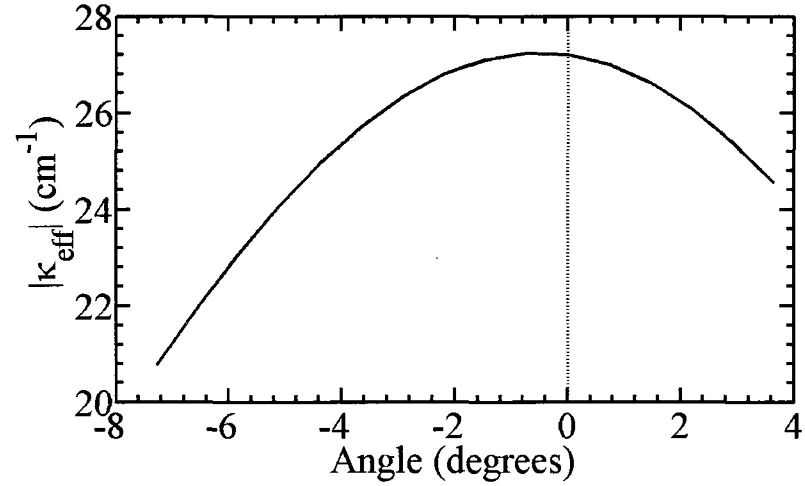

Figure 40. **Effective coupling coefficient *vs.* vertical tooth angle. The dashed line represents perfectly vertical tooth angle.**

angles represent trapezoidal grating tooth shapes. The coupling strength of the grating, $|\kappa_{eff}|$, will stay within 10% of the optimal value if the undercut is kept to less than 3 degrees.

5.5.2. Horizontal Shape Variation

Horizontally-varying a) sinusoidal, b) triangular, and c) trapezoidal laterally-coupled grating shapes are shown in Figure 41. Rectangular gratings, with no variation in the horizontal direction, will remain unchanged from the schematic shown in Figure 6. I propose the use of horizontal shape variation in the design of LC-DFB lasers because it is considerably simpler to manufacture than vertical shape variation. While vertical shape variations would require sophisticated etching techniques, such as multiple timed etches, horizontal shape variations could be fabricated using standard lithographic and etching techniques. In the following analysis we see which horizontal shape variations will provide acceptable coupling coefficients for LC-DFB lasers.

The performance of different grating shapes is compared by calculating the variation of $|\kappa_{eff}|$ *vs.* the narrow ridge width, W_N, for rectangular, sinusoidal, and triangular grating shapes, where κ_{eff} is calculated from (4.45). The exact grating shapes are shown in Figure 21. For this calculation, a duty cycle of γ=0.5 was used for the rectangular grating, and the triangular grating was assumed to be symmetrical so that $\Delta = \Lambda / 2$. This calculation was done for first-order gratings, shown in Figure 42a, second-order gratings in Figure 42b, and third-order gratings in Figure 42c. For first-order gratings, the rectangular grating has nearly the same coupling coefficient compared to the sinusoidal grating shape with both higher than triangular-shaped gratings. The Streifer correction terms go to zero for a first-order grating, so there are no oscillations with W_N and the imaginary part of κ_{eff} is zero. Second-order gratings with rectangular gratings have $\kappa_p = 0$, as calculated from (4.38). The value of κ_{eff} is due to the $\zeta_{2,4}$ correction terms,

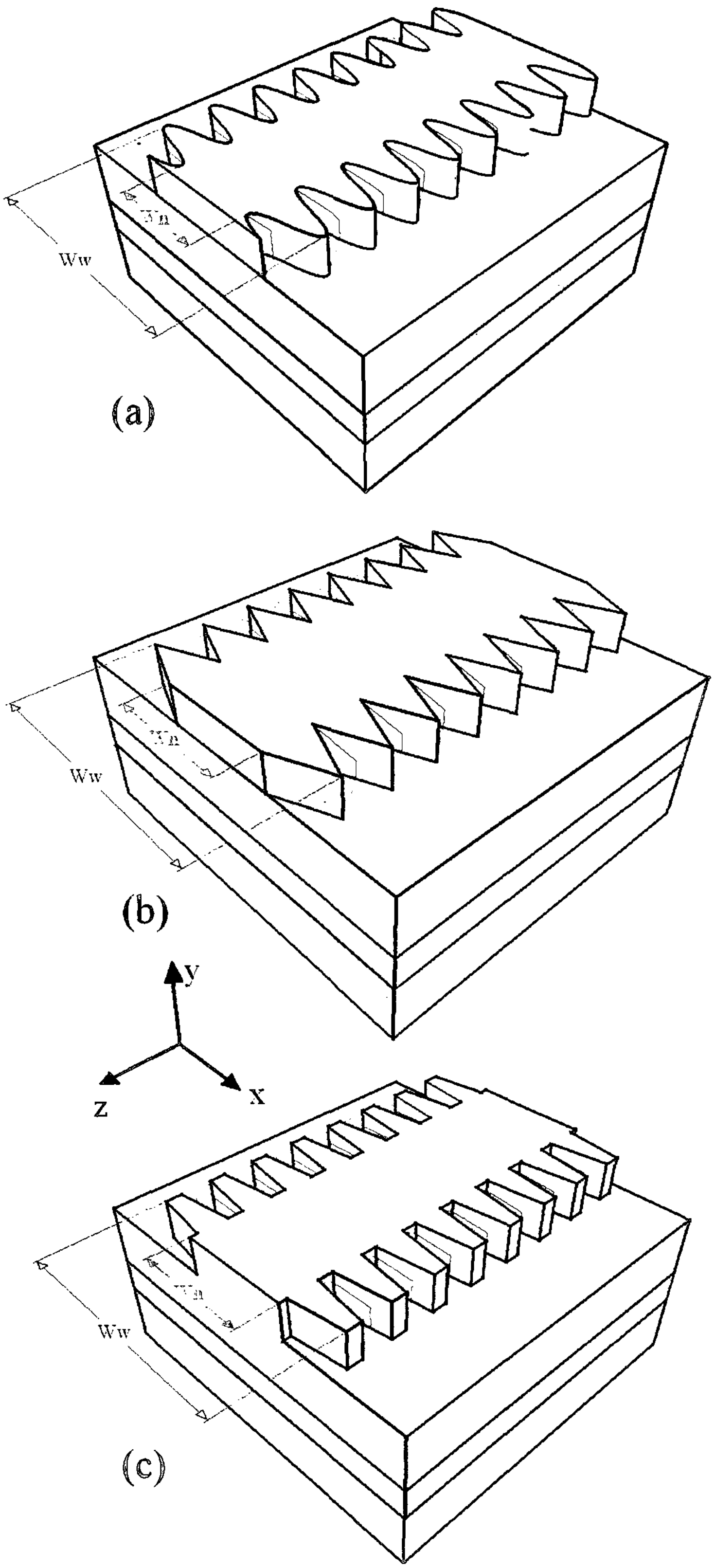

Figure 41. Horizontally-varying a) sinusoidal, b) triangular, and c) trapezoidal laterally-coupled grating shapes

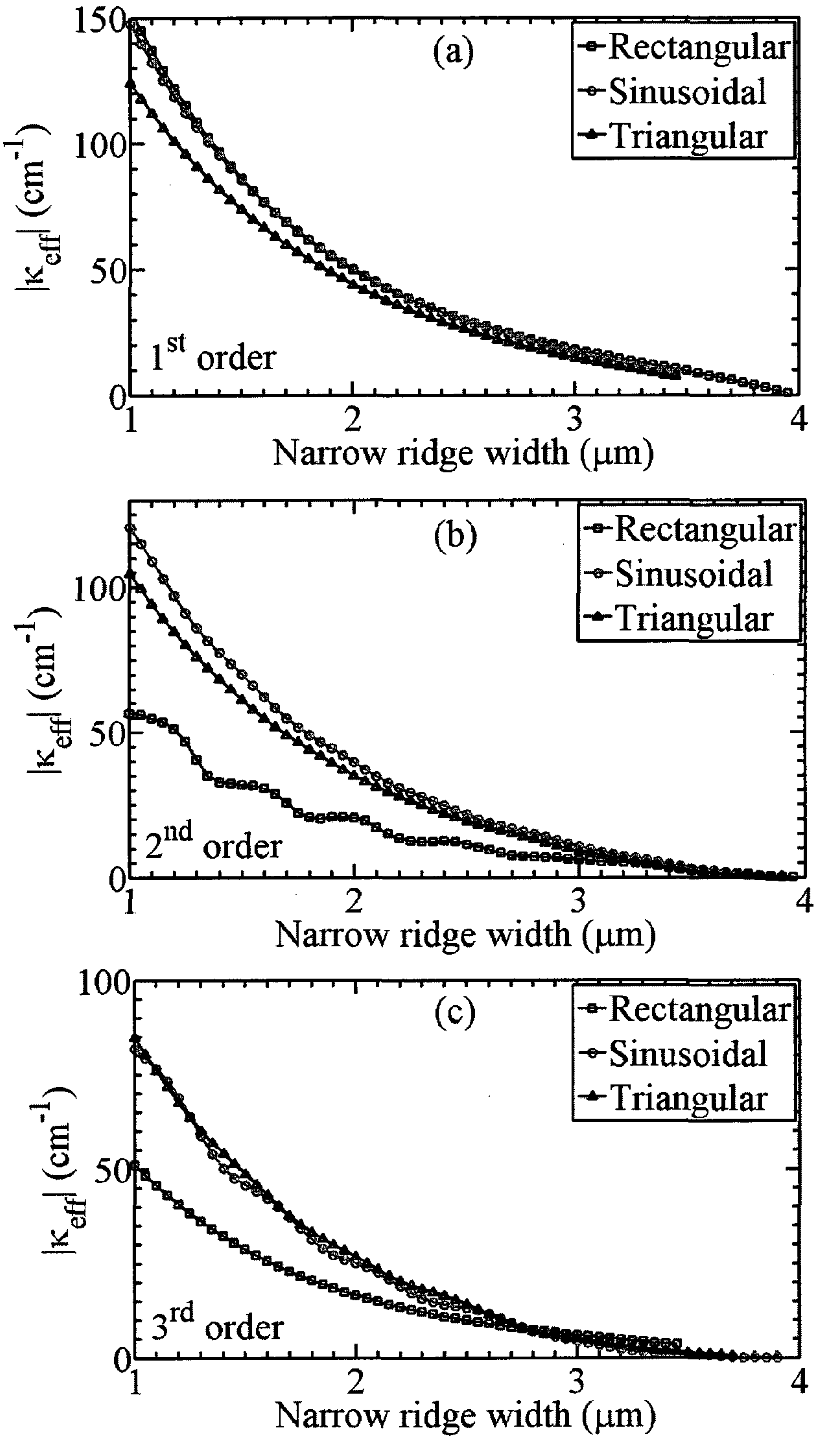

Figure 42. Magnitude of coupling coefficient *vs.* narrow ridge width for a a) first-, b) second-, and c) third-order grating with W_W=4 μm and rectangular (γ=0.5), sinusoidal, and triangular (Δ=Λ/2) grating shapes.

and significant oscillations in the value of $|\kappa_{eff}|$ result, as observed in Figure 42b. The sinusoidal and triangular gratings, with $\kappa_p \neq 0$, have nearly double the $|\kappa_{eff}|$ value at small narrow ridge widths of ~1 μm. The sinusoidal gratings exhibit a higher κ_{eff} compared to the triangular gratings over the entire range of W_N values.

The third-order case, shown in Figure 42c, again shows significantly higher κ_{eff} for the sinusoidal and triangular gratings compared to rectangular gratings. The coupling for third-order gratings is smaller than the second- or first-order gratings for the same grating shape. The sinusoidal grating no longer provides better coupling than the triangular grating for all W_N values, as was the case for first- and second-order gratings. Instead, the coupling is nearly identical for both sinusoidal and triangular gratings, with one or the other being greater depending on the value of W_N used. Based on the results of Figure 42, the sinusoidal grating provides the best coupling coefficient over the widest range of grating orders. We will see in Chapter 7 that the grating tooth edges tend to be rounded during fabrication. This means that the rounded edges of the sinusoidal grating could potentially be easier to fabricate than the sharp edges of rectangular or triangular gratings.

The increased optical confinement in sinusoidal and triangular gratings compared to rectangular gratings with γ=0.5 plays a role in the results of Figure 42. When W_N/W_W = 1.5/4 (μm), the optical confinement in the grating region of the rectangular grating is 0.43%, compared to 0.72% and 0.98%, for sinusoidal and triangular gratings, respectively. These confinement values are the ratio of the optical power contained in the grating regions to the total fundamental mode power, and would suggest nearly double the coupling coefficient for sinusoidal and triangular gratings compared to rectangular gratings. However, the grating confinement is not the only factor impacting the coupling coefficient, as Figure 43 demonstrates. The electric field will drop off in the grating region, away from the centre of the mode, for all grating shapes. The coupling coefficient, κ_p, for third-order gratings, according to (4.38), is proportional to the electric

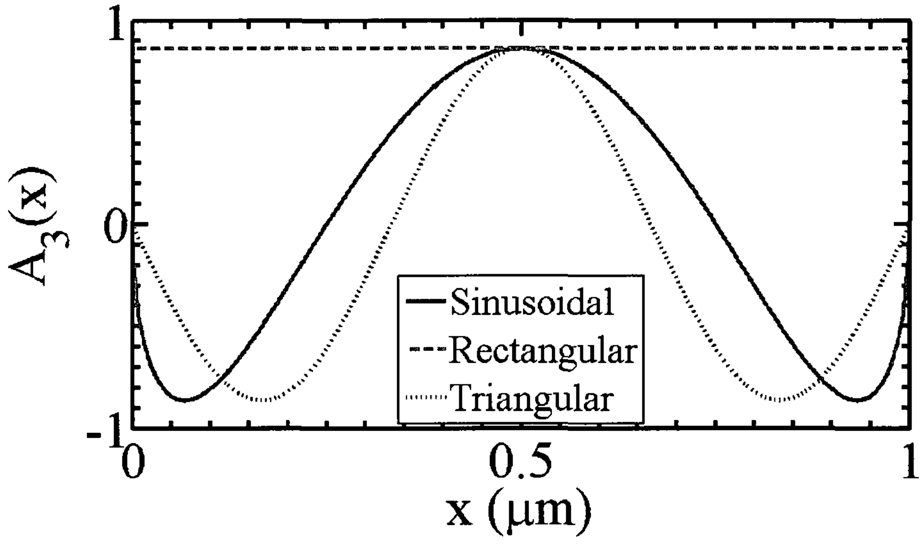

Figure 43. **Third-order Fourier coefficient of horizontally-varying rectangular (duty cycle=0.5), sinusoidal, and triangular gratings, for third-order gratings with W_N/W_W = 1.5/3 (μm).**

field, multiplied by the third-order Fourier coefficient, A_3, integrated over the grating region. While A_3 is constant for the rectangular grating everywhere in the grating region, the coefficients for sinusoidal and triangular gratings are vary from positive to negative. If the electric field were flat, the coupling coefficient would vanish since the sinusoidal and triangular grating Fourier coefficients average out to zero over the length of the grating. Since we have an exponentially decaying field in the grating region, however, the portion of the Fourier coefficient nearest the grating has the greatest influence on the coupling coefficient. The integral will be weighted towards the part of the grating closest to the central ridge, and therefore non-zero. The sinusoidal Fourier coefficient varies more rapidly in the region of the central ridge than the triangular grating, resulting in a higher coupling coefficient for the sinusoidal grating compared to the triangular grating than the confinement factors would suggest. In addition, due to the zero-average Fourier coefficients shown in Figure 43, rectangular gratings would have a higher coupling coefficient compared to the other grating shapes if they had similar grating confinement factors.

The trapezoidal grating has a shape intermediate between that of the rectangular and triangular gratings. It can be used to understand the greater coupling seen in the triangular grating compared to the half duty cycle rectangular grating. By varying the σ parameter between 0 (the rectangular grating case) and 0.5 (the triangular grating case) the transition between the two grating forms can be observed. The effective coupling coefficient *vs.* the σ parameter is plotted for first-, second-, third- and fourth-order gratings in Figure 44a, b, c, and d, respectively. The simple coupling coefficient, κ_p, for the first-order grating, calculated from (4.38), shows that the highest coupling coefficient is not the rectangular grating, where $\kappa_p = 81.6\ \text{cm}^{-1}$, but occurs for a trapezoidal grating with σ=0.26, where κ_p =94.4 cm^{-1}. For second-order and higher gratings, the effective coupling coefficient is now complex, with both a phase and magnitude. The phase decreases steadily in the second-order grating case, shown in Figure 44b, while there is a jump in the phase of κ_{eff} for the third-order grating at σ=0.18, and fourth-order grating at σ=0.24, as observed in Figure 44c and d. This phase jump point corresponds to the lowest value of $|\kappa_{eff}|$. Below this point, the κ_p values are negative, due to the sign of the

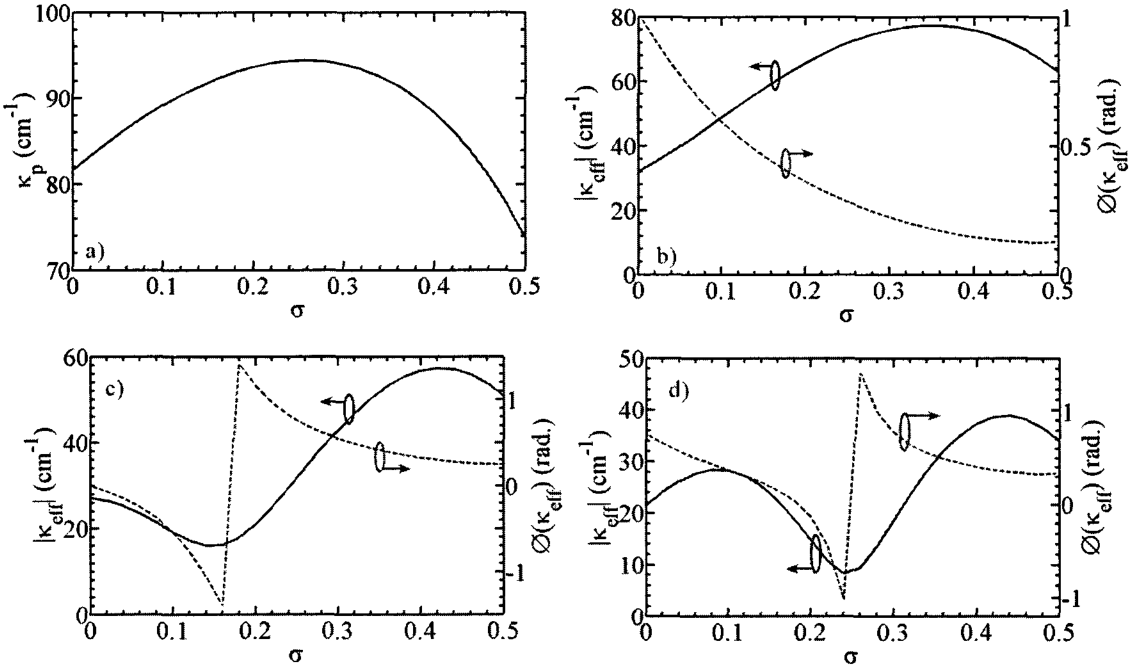

Figure 44. Effective coupling coefficient for trapezoidal grating shapes from rectangular (σ=0) to triangular (σ=0.5) for a a) first-, b) second-, c) third-, and d) fourth-order grating and W_N/W_W = 1.5/4 (μm).

Fourier coefficients. The $\zeta_{2,4}$ terms, calculated from (4.43), are positive, resulting in a lower overall coupling coefficient. As σ increases, κ_p goes from being positive to negative. Beyond this point, both κ_p and $\zeta_{2,4}$ are the same sign, and they produce a larger overall κ_{eff}. As with the first-order grating, the maximum $|\kappa_{eff}|$ values do not occur in the limit of the rectangular (or triangular) grating, but instead for trapezoidal shapes. The maximum value is $|\kappa_{eff}|$=77.3 cm^{-1} when σ=0.34 for the second-order grating, $|\kappa_{eff}|$=57.3 cm^{-1} when σ=0.42 for the third-order grating, $|\kappa_{eff}|$=38.8 cm^{-1} when σ=0.44 for the fourth-order grating. The magnitude of the maximum coupling coefficient decreases as the grating order increases, and the optimal σ value also increases. The same result, however, is found for all grating orders: the highest coupling coefficient is trapezoidal in shape. The results for different horizontally-varying grating shapes demonstrate that for laterally-coupled gratings, non-rectangular gratings often provide better coupling than standard γ=0.5 rectangular gratings. The additional confinement in the active region and addition of the partial wave terms produces κ_{eff} values that are larger than might intuitively be expected from non-rectangular grating shapes. This could be exploited to create more manufacturable laterally-coupled gratings with greater grating strength.

5.6 Effect of Metal Contacts

The composition of the metal contacts is an important feature of this design as the 0.5 μm high ridge is shallower than the 1 - 1.5 μm ridge height that is typically used in FP lasers. With the shallower ridge, the optical mode will have greater overlap with the metal contacts, resulting in higher waveguide losses through absorption. This section will describe some of the important considerations when selecting the metal contacts.

A simple gold (Au) contact has relatively low loss since it is highly reflective at a wavelength of 1310 nm, where it has a complex refractive index of 0.31 - j9.0 [96]. Although the attenuation coefficient is large, the small value of the real part of the refractive index ensures that relatively little of the optical mode will be confined in an Au region. Pure gold contacts, however, are often insufficient for an acceptable ohmic contact, due to two major disadvantages: poor adhesion to semiconductor materials, and the rapid diffusion of Au into the semiconductor after annealing [97]. The standard solution to these difficulties is to add a thin titanium (Ti) layer above the semiconductor material to improve metal adhesion, and a thin platinum (Pt) layer above the Ti and below the Au layer to prevent diffusion.

Smith *et al.* investigated the effect of the thicknesses of these metal layers on FP lasers and found that the addition of Ti layers can increase the absorption loss by up to a factor of 5 for shallow ridges [97], underscoring the importance of considering the composition of the metal contacts on the laser performance. Our analysis of the effect of metal contacts will consider two factors: 1) waveguide absorption, and 2) modified coupled-mode coefficients. The waveguide gain/loss coefficient, α, was defined earlier in (4.37). From the coupled-mode equations of (4.9) we see that in a waveguide with no distributed feedback, the differential equation for a forward-travelling wave becomes

$$\frac{dA(z)}{dz} = (\alpha + j\delta)A(z). \tag{5.1}$$

This admits an exponential solution for $A(z)$ of the form

$$A(z) = e^{j(-j\alpha+\delta)z} = e^{j\delta z}e^{\alpha z}. \tag{5.2}$$

From (5.2) we see that the amplitude of the optical mode decreases as we travel along the z-direction when α is negative, and increases as we travel along the z-direction when α is positive. In this section we consider only the portion of this coefficient due to the waveguide cross-section, excluding the MQW active region. The loss coefficient is defined as the magnitude of the negative portion of α, and is therefore a positive value. We calculate the loss coefficient from the fundamental quasi-TE mode solution, as determined using the solution procedure outlined in Section 4.4.1. The imaginary portion of the propagation constant, β, is equal to half the loss coefficient. We use complex refractive indices for Ti and Pt at 1310 nm of 3.65 - j4.27 and 4.25 - j6.62, respectively [98], [99].

The decrease in the waveguide loss as the thickness of either the Ti or the Pt layer is decreased (the other layer kept constant at 18 nm) is shown in Figure 45. The Ti layer has a slightly greater effect on the loss coefficient than the Pt layer, as it sits directly on top of the ridge. Without the Ti and Pt layers, the absorption loss is considerably less, approximately 14 cm^{-1}. The Ti/Pt layers do not increase the absorption loss by a factor of five since the height of the ridge is 500 nm here, rather than 400 nm in the study by Smith *et al.*, resulting in the optical mode centre being farther from the metal contact layers. Figure 45 demonstrates the advantages of minimizing the thickness of the Ti and Pt layers to improve the absorption coefficient. The thickness of the Au contact was found to have a negligible impact on the loss coefficient.

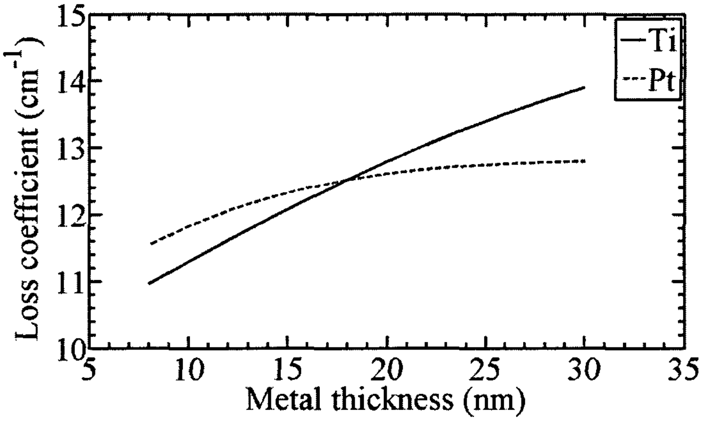

Figure 45. **Loss coefficient *vs.* Ti and Pt metal thickness for nominal thicknesses of 18/18/200 nm for Ti/Pt/Au, respectively.**

The composition of the metal contact will also affect the effective coupling coefficient and other modified coupled-mode coefficients. The radiating partial waves, in particular, will experience more or less absorption depending on the makeup of the metal contact. Figure 46 shows how the effective coupling coefficient *vs.* duty cycle characteristic changes depending on whether a simple Au contact is used or an Au/Pt/Ti contact is used. There is a maximum penalty of 18% in the magnitude of the effective coupling coefficient when using the Au/Pt/Ti contact, at a duty cycle of 0.6. This change is due entirely to the Streifer terms, as the simple coupling coefficient, κ_p, is negligibly affected by the composition of the metal contact. While the optical field experiences a greater absorption loss when using the Au/Pt/Ti contact compared to an Au contact, the thin Pt and Ti layers have almost no effect on the shape of the optical field, and thus on the confinement in the grating region.

Compared to the pure Au contact, the Au/Pt/Ti contact improves adhesion of the metal to the semiconductor while reducing metal diffusion into the semiconductor material during annealing. These improvements come at the cost of an increased absorption loss and a slightly poorer effective coupling coefficient at higher duty cycles. A slight improvement in the loss coefficient can be obtained if the Pt and Ti metal layers are made thinner, but

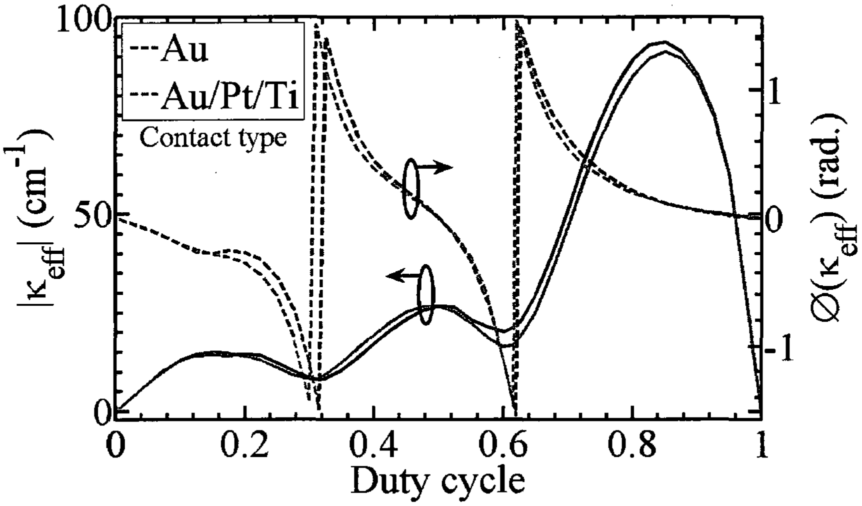

Figure 46. **Effective coupling coefficient *vs.* duty cycle for a third-order grating with Au contacts (black lines) and Au/Pt/Ti contacts (red lines)**

the thickness of the Au contact was found to have a negligible impact on the absorption coefficient.

The height of the grating can also play a role in minimizing the loss coefficient. The variation of the loss coefficient with grating height is shown in Figure 47 for a grating with a duty cycle of 0.5 and W_N / W_W = 1.5/4 (μm). The loss coefficient is slightly lower for this duty cycle than for a duty cycle of 0.6 since the modal field is less confined in the upper grating where the metal contacts are present when the duty cycle is smaller. We see that loss coefficient steadily decreases as the grating height increases. This decrease in the loss coefficient is due to the increasing distance of the centre of the modal field from the absorptive metal contacts as the grating height increases. While the mode shape remains essentially the same for all these grating heights, the evanescent portion of the mode in the metal contact region increases with smaller grating heights. The loss coefficient of 25 cm^{-1} at the nominal grating height of 0.47 μm is nearly half the loss coefficient of 46 cm^{-1} at a grating height of 0.35 μm, but the loss could be lowered yet further if the grating height is made larger. The loss coefficient will be below 8 cm^{-1}, for example, when the grating height is greater than 0.8 μm. Figure 47 demonstrates that if the fabrication technique allows for deeper gratings, the loss coefficient can be reduced.

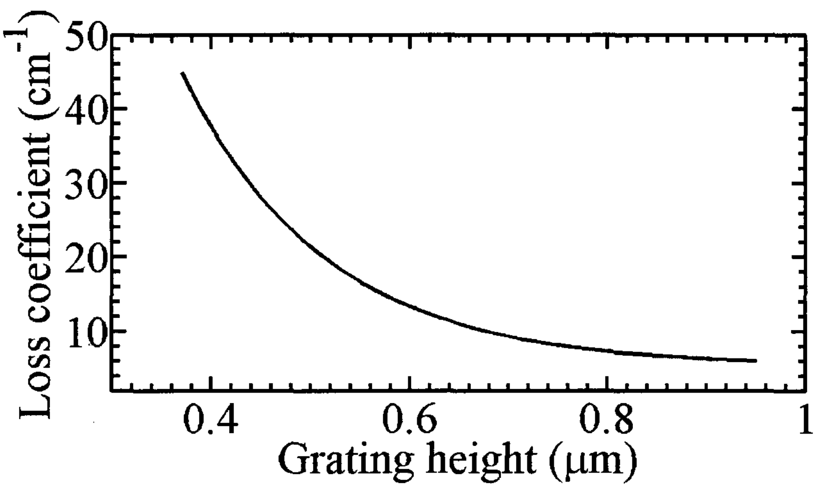

Figure 47. **Loss coefficient *vs.* grating height for grating with a duty cycle of 0.5 and W_N/W_W = 1.5/4 (μm).**

The effect of the duty cycle on the loss coefficient, shown in Figure 48, demonstrates a noticeable increase in the loss coefficient for duty cycles of > 0.8. Although it appears exponential on this scale, the loss coefficient will be fixed at the value of an equivalent FP laser when the duty cycle is 1. The greater loss coefficient is due to the increased mode overlap with the lossy upper waveguide layers and metal contacts at higher duty cycles. The reason for this increased confinement is that as the duty cycle increases, the average refractive index in the grating region, given by (4.57), will increase. This mode sees an increased refractive index in the upper layers, thus the upper evanescent portion of the mode is shifted upward, resulting in higher confinement in the upper waveguide layers. This increased loss coefficient will increase the minimum threshold gain somewhat for these higher duty cycles. An increase in the loss coefficient of an extra 1 cm^{-1} will require an additional normalized threshold gain of $\alpha L = 0.05$ for a 500 μm long laser. The loss coefficient for duty cycles < 0.8, however, remains relatively flat at around 25 cm^{-1}.

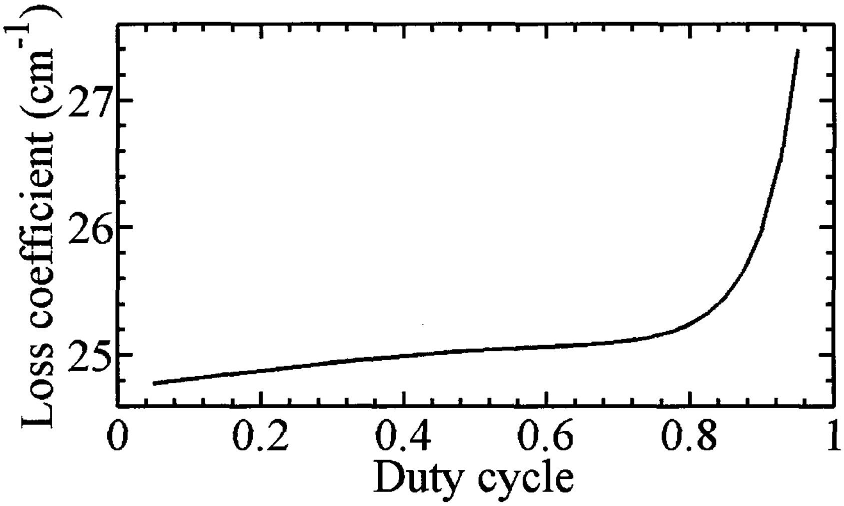

Figure 48. **Loss coefficient *vs.* duty cycle for a third-order grating with $W_N/W_W = 1.5/4$ (μm).**

5.7 Summary

Since the grating geometry determines the modified coupled-mode coefficients, it has been necessary to consider what grating geometries result in a high performance fabrication-tolerant LC-DFB laser design. Higher duty cycles such as 0.7-0.8 resulted in a higher effective coupling coefficient as the confinement in the grating region increased, as shown in Figure 28. The peaks and valleys of $|\kappa_{eff}|$ shown in this Figure provided good duty cycle values for stability and fabrication tolerance. From Figure 32, we saw that the effective coupling coefficient has a periodic dependence on the grating height due to resonances in the partial wave terms. The magnitude and phase of κ_{eff} are out of phase, which made it difficult to find a single point with optimal stability. The coupling coefficient dependence on the grating width also showed these resonances, but they were more subtle compared to those due to the ridge height as a result of a smaller index contrast in the x-direction and a greater increase in κ_p compared to the resonance effects when the ridge width was increased. The magnitude of the effective coupling coefficient, $|\kappa_{eff}|$, decreases as the narrow ridge width, W_N, was increased, with the wide ridge width, W_W, kept constant, as seen in Figure 35. If W_W was increased while keeping W_N constant, $|\kappa_{eff}|$ increased, as seen in Figure 36. The grating geometry must also take into account electrical and fabrication considerations, since too wide a ridge increases the lateral current spreading and the size of the optical mode, while too narrow a ridge increases electrical resistance and are more difficult to fabricate. Due to fabrication limitations, the duty cycle cannot be arbitrarily large or small. The grating height is shallower than a typical laser design to allow for a better definition of the grating using stepper lithography. This also lowers the electrical resistance, but increases the lossy effects of the metal contacts, as shown in Figure 47. Our vertically-varying grating shape analysis not only demonstrated the potential for stronger coupling using non-rectangular gratings, but also provided a tolerance analysis for the undercut of the waveguide ridges. Our analysis of non-rectangular grating shapes in the horizontal direction in Figure 42 also showed that they can provide stronger coupling than standard rectangular gratings. These non-rectangular shapes are also potentially easier to fabricate than rectangular gratings, particularly those with higher duty cycles. We saw that the composition of the metal contacts had a negligible impact on the simple coupling coefficient, κ_p, but in Figure 46 we observed a significant impact on the modified coupled-mode coefficients of 20% or more depending on whether a simple Au or Au/Ti/Pt contact was used. Metal contact composition was also demonstrated in Figure 45 to have a strong impact on the waveguide loss for these shallow waveguides. The duty cycle will have a minimal influence on the waveguide loss, as long as it is less than 0.8. At higher duty cycles > 0.8, the waveguide loss increases.

CHAPTER 6 – THREE-DIMENSIONAL LATERALLY-COUPLED DISTRIBUTED FEEDBACK LASER MODELING

6.1 Simple Longitudinal Mode Solutions

The solution of the modified coupled-mode equations in the simple case of invariant α and δ eigenvalues was described in Section 4.5. This solution method was applied to determine the properties of the longitudinal mode solutions as they relate to the grating parameters discussed in Chapter 5. In this section, we apply the simple longitudinal mode solutions to determine the effect of three-dimensional variations, specifically the cavity length, the addition of a λ/4 phase-shift, and the facet reflectivity of the LC-DFB laser.

6.1.1. Cavity Length

It has been noted in Chapter 5 that the inclusion of the Streifer terms has a significant impact on the effective coupling coefficient, particularly for certain duty cycles, and it is expected that this will translate into a significant impact on the longitudinal mode solutions as well. To see the effect of cavity length on the mode solutions, the modified coupled-mode equations are first obtained from the grating geometry, as in Chapter 5. The longitudinal mode solutions are then found for a range of fixed cavity lengths, using the solution method of Section 4.5. There are many longitudinal mode solutions for each cavity length, but those with the lowest threshold gains, α, are of the most interest, since they will begin lasing first at the threshold current. Figure 49 shows the longitudinal mode solutions of a third-order grating with γ=0.7 in terms of the normalized threshold gain αL, and normalized wavelength detuning, δL, of these

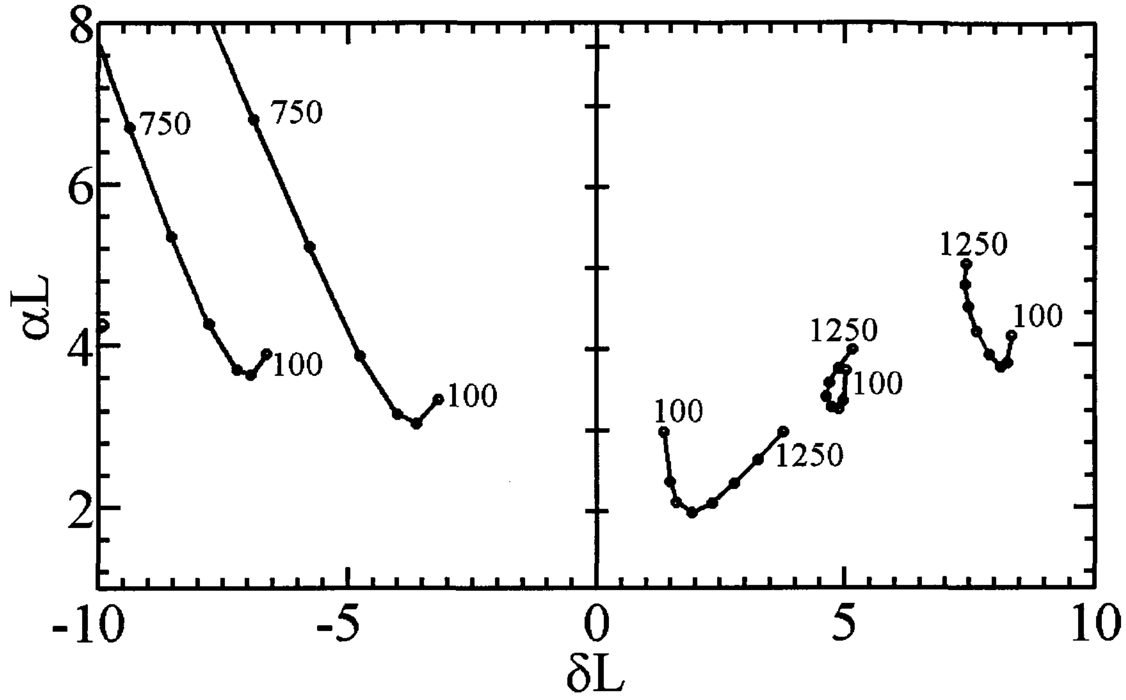

Figure 49. **Longitudinal mode solutions of a third-order grating with a 1.5/3 μm ridge width, duty cycle of 0.8 and cavity lengths of 100, 200, 300, 400, 500, 750, 1000 and 1250 μm, as indicated by the circular markers.**

solutions as the cavity lengths vary from 100 to 1250 μm. The normalized form of these two eigenvalues is used since they provide a better comparison among different cavity lengths. For instance, a longer cavity length may have a lower α, but it will require a higher carrier injection to reach this gain value than a shorter cavity. The normalized value, αL, will better reflect this than the α value alone.

The longitudinal mode solutions of a first-order grating will be symmetrical around the Bragg frequency ($\delta L = 0$). This means that for a given threshold gain, there will be two modes that will begin simultaneously lasing. In practice, fabrication variations will usually cause a single longitudinal mode to begin lasing first, but this adds a degree of unpredictability to the lasing wavelength. However, in this case, we see from Figure 49 that the solutions are not symmetrical around the Bragg frequency as they are for first-order gratings, but instead favour the shorter-wavelength solutions, where $\delta L > 0$. This permits greater certainty in the lasing wavelength for these lasers compared to those with first-order gratings.

It is also apparent from Figure 49 that there is, for each longitudinal mode solution, a cavity length for which the normalized threshold gain is minimized. Shorter cavities would give lower αL values if α was invariant. However, the greater feedback of longer cavities will tend to decrease α, since this will reduce the mirror losses. The optimal cavity length balances these two factors. Of particular importance is the longitudinal mode with the smallest threshold gain, $(\alpha L)_{\min}$. In Figure 49 this mode is the one with the lowest positive frequency deviation, $(\delta L)_{\min}$.

We now extend the longitudinal mode analysis to the entire range of duty cycles from 0 to 1 in 0.025 increments, and cavity lengths from 0 to 1200 μm in 50 μm increments, for a total of 897 points. This analysis was performed for grating orders from first-order to fourth-order. For each duty cycle and cavity length, the longitudinal mode solutions are found according to the method in Section 4.5, and the mode with the lowest normalized threshold gain, $(\alpha L)_{\min}$, is found, along with the corresponding $(\delta L)_{\min}$. This comprehensive analysis provides a wealth of information for the design of LC-DFB lasers with higher order gratings, and reveals many critical prevailing trends. The contours of $(\alpha L)_{\min}$ are shown in Figure 50, and those of $(\delta L)_{\min}$ in Figure 51. Larger effective coupling coefficients will yield smaller $(\alpha L)_{\min}$ values, as is evident by comparison with the $|\kappa_{eff}|$ vs. duty cycle characteristics shown in Figure 28. The minima of the $(\alpha L)_{min}$ represent desirable fabrication points, where the threshold gain, and hence the threshold current, is minimal. For all grating orders, the lowest threshold gains occur at higher duty cycles in the range of γ=~0.8. The lowest threshold gains are: $(\alpha L)_{\min}$=0.88 at γ=0.75 and L = 400 μm for the first-order grating, $(\alpha L)_{\min}$=1.03 at γ=0.85 and L = 450 μm for the second-order grating, $(\alpha L)_{\min}$=1.07 at γ=0.875 and L = 450 μm for the third- order grating, and $(\alpha L)_{\min}$=1.15 at γ=0.9 and L = 500 μm for the fourth-order grating. Higher grating orders require larger duty cycles and longer lengths

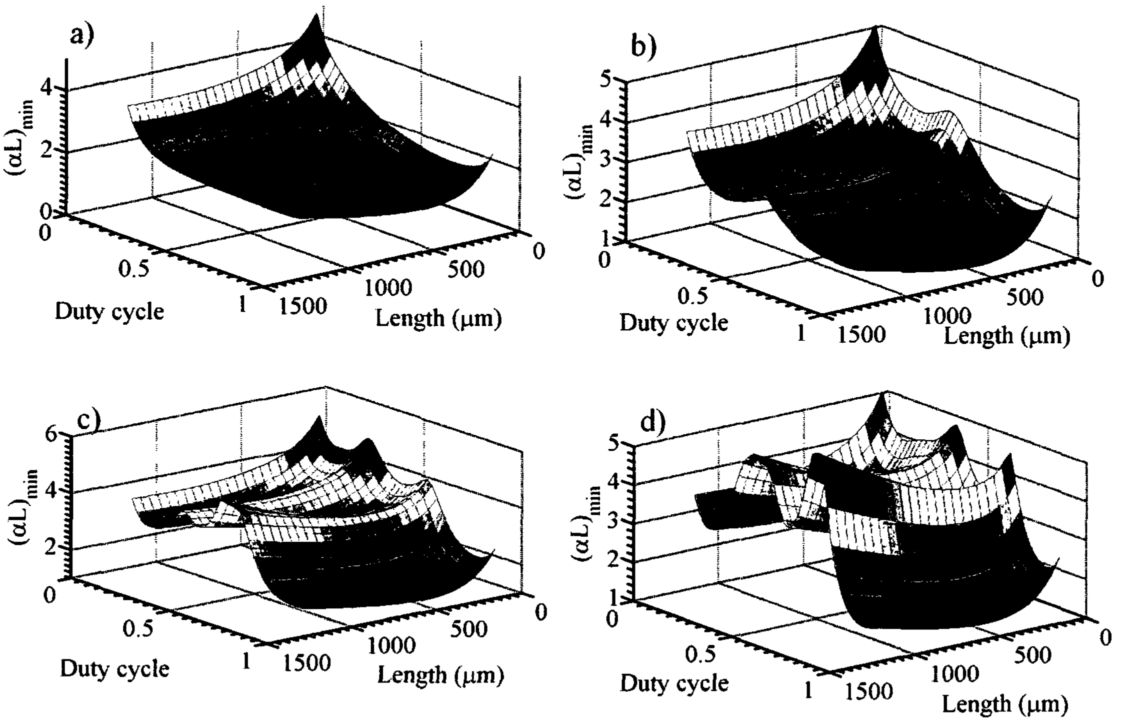

Figure 50. Surface plots of the normalized minimum threshold gain, $(\alpha L)_{\min}$, *vs.* duty cycle and cavity length for a) first- b) second-, c) third-, and d) fourth-order gratings

to reach the minimum threshold gain, and will have higher $(\alpha L)_{\min}$ values compared to first-order gratings. Higher order gratings also exhibit much more variation in $(\alpha L)_{\min}$ *vs.* duty cycle, making them less fabrication–tolerant than first-order gratings that have a much flatter characteristic.

The wavelength detuning, $(\delta L)_{\min}$, of the minimum threshold gain mode, is plotted in Figure 51 for the same range of duty cycles and cavity lengths as in Figure 50. The wavelength detuning of the minimum threshold gain mode will ideally be as close to the Bragg wavelength as possible, i.e. $(\delta L)_{\min} = 0$. Although not shown in Figure 51a, the first-order grating actually has two degenerate longitudinal mode solutions with the same threshold gain, one on either side of the Bragg wavelength, $\pm\delta L$. This symmetry is broken in the higher order gratings. For second-order gratings, $(\delta L)_{\min}$ smoothly transitions from negative values when $\gamma < 0.48$ to positive values when $\gamma > 0.48$. In

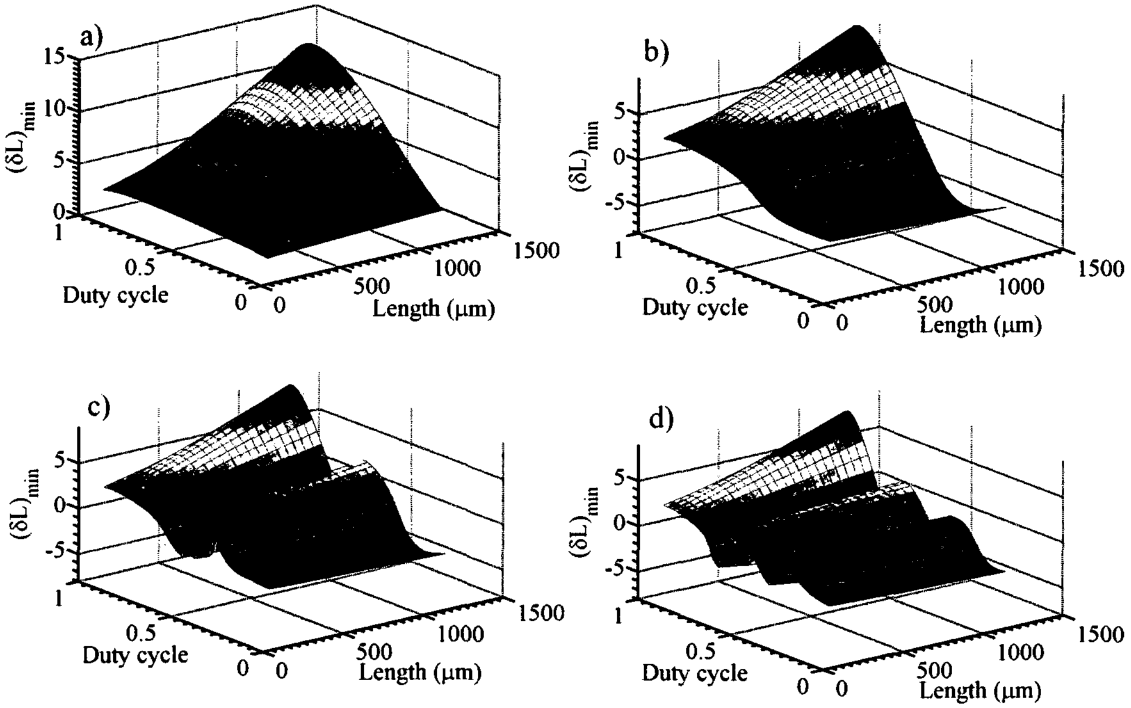

Figure 51. Surface plots of the normalized wavelength detuning of minimum threshold gain mode, $(\delta L)_{\min}$, vs. duty cycle and cavity length for a) first-, b) second-, c) third-, and d) fourth-order gratings

third-order and higher gratings, however, abrupt changes in the sign of $(\delta L)_{\min}$ appear. These jumps occur at duty cycles where the NGD goes to zero, and represent points of unstable wavelength detuning to be avoided. For third-order gratings, this jump occurs at γ=0.5, and for fourth-order gratings at γ=0.35 and 0.65. For all grating orders, larger lengths lead to a greater variation in $(\delta L)_{\min}$ but the form of the characteristic *vs.* the duty cycle remains the same.

We now look at not only the minimum threshold gain longitudinal mode solutions but also those with higher threshold gains in order to calculate the normalized gain difference. Out of the multiple solutions obtained for each duty cycle and cavity length, such as those demonstrated in Figure 49, the two lowest normalized threshold gain solutions are selected. The difference between these two threshold gains is the normalized gain difference, or NGD, as described earlier in Section 4.5. The result of

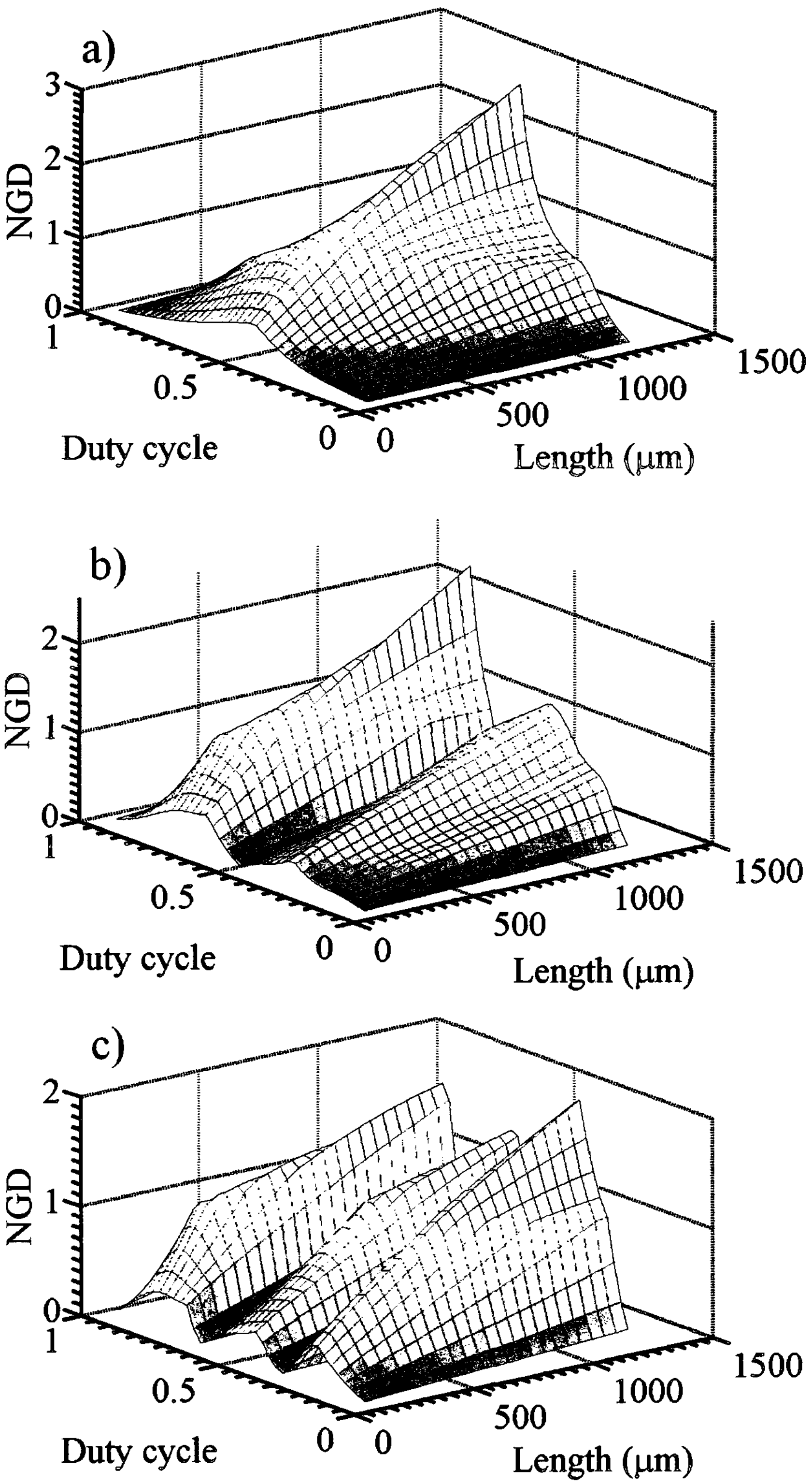

Figure 52. **Surface plots of the normalized gain difference *vs.* duty cycle and cavity length for a) second-, b) third-, and c) fourth-order gratings**

these calculations is shown in Figure 52, for a) second-order, b) third-order, and c) third-order gratings, over the full range of duty cycles and cavity lengths used for Figure 50 and Figure 51. Larger NGD values are desirable since they signify a strong, single longitudinal mode near threshold, making the lasing wavelength more predictable. The jumps in the sign of $(\delta L)_{\min}$ are reflected in the normalized gain difference plots of the third-, and fourth-order gratings shown in Figure 52b and c. The NGD is zero everywhere for the first-order grating, so it is not shown in Figure 52. The NGD grows for all grating orders as the cavity length grows longer. The maxima of the NGD curves reflect, at fixed lengths, points of maximum phase angle in κ_{eff}. When the imaginary portion of κ_{eff}, and hence $\phi(\kappa_{eff})$, goes to zero, the NGD also goes to zero since there will be two degenerate longitudinal modes. As the phase increases, the tilt in the longitudinal mode solutions increases, increasing the NGD. Thus, to obtain a large NGD, it is necessary to have a large $\phi(\kappa_{eff})$ for these lasers, although this occurs at points of minimal $|\kappa_{eff}|$ (and hence maximal $(\alpha L)_{\min}$), as seen in Figure 28. This results in a tradeoff between having a low $(\alpha L)_{\min}$ and a high NGD.

While first-order gratings, as observed above, will always have lower threshold gains compared to higher order gratings, the difference between them can be minimized. In Figure 53, the ratio of threshold gains between first- and third-order gratings, $\alpha_{th,1}/\alpha_{th,3}$ for different cavity lengths and duty cycles is plotted. The performance of the third-order grating approaches that of the first-order one as the duty cycle increases, since the minimum threshold gain of the third-order grating falls more sharply with duty cycle than the first-order grating for duty cycles > 0.5, as shown in Figure 50. $\alpha_{th,1}/\alpha_{th,3}$ is also greater for smaller cavity lengths and minimal at cavity lengths of ~300 to 600 μm as the third-order grating minimum threshold gain falls more sharply than the first-order grating in this range of cavity lengths, as seen in Figure 50. To improve the performance of higher order gratings compared to first-order gratings in LC-DFB lasers, the cavity length should be made shorter and the duty cycle larger. This will improve the relative

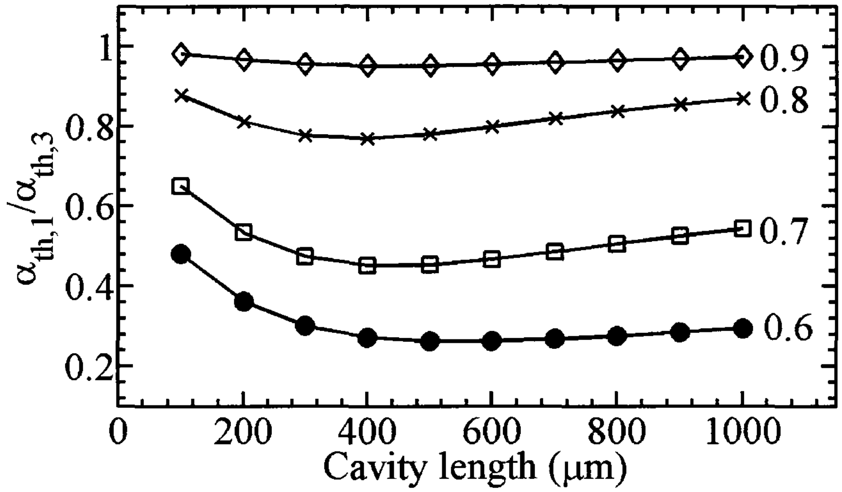

Figure 53. **Ratio of first-order to third-order threshold gains *vs.* cavity length for duty cycles of 0.6, 0.7, 0.8 and 0.9.**

performance of similar third-order and first-order lasers, but to obtain the best absolute performance, the surface plots of Figure 50-51 should be used. For instance, the gratings with a duty cycle of 0.9 have the best relative performance, but will also require a higher $(\alpha L)_{\min}$ than lower duty cycle designs.

The flatness of the longitudinal optical mode field, F, was defined earlier in (4.77). The more flat, or constant, the amplitude of the optical mode is over the cavity length, the smaller the effect of longitudinal spatial hole burning. This effect is minimized when the flatness criterion of $F < 0.05$ is satisfied. There will be, in general, multiple cavity lengths that satisfy the flatness criterion for a given grating geometry. A common rule of thumb used for standard first-order DFB lasers is that $\kappa_p L$ products of ~1.5 will result in a good uniform longitudinal mode profile for unshifted gratings, while for λ/4 phase-shifted gratings $\kappa_p L$ products of ~1.25 will produce the flattest profile [20]. To see if this holds for higher order gratings, the optical field of different $|\kappa_{eff}|L$ products is plotted for duty cycles of 0.5, 0.7 and 0.8 in Figure 54. The length scale is in arbitrary units, normalized to a total length of 100 units, since the total length of the laser cavity will be different for each of the optical fields shown. For example, a laser with a duty cycle of 0.5 will have

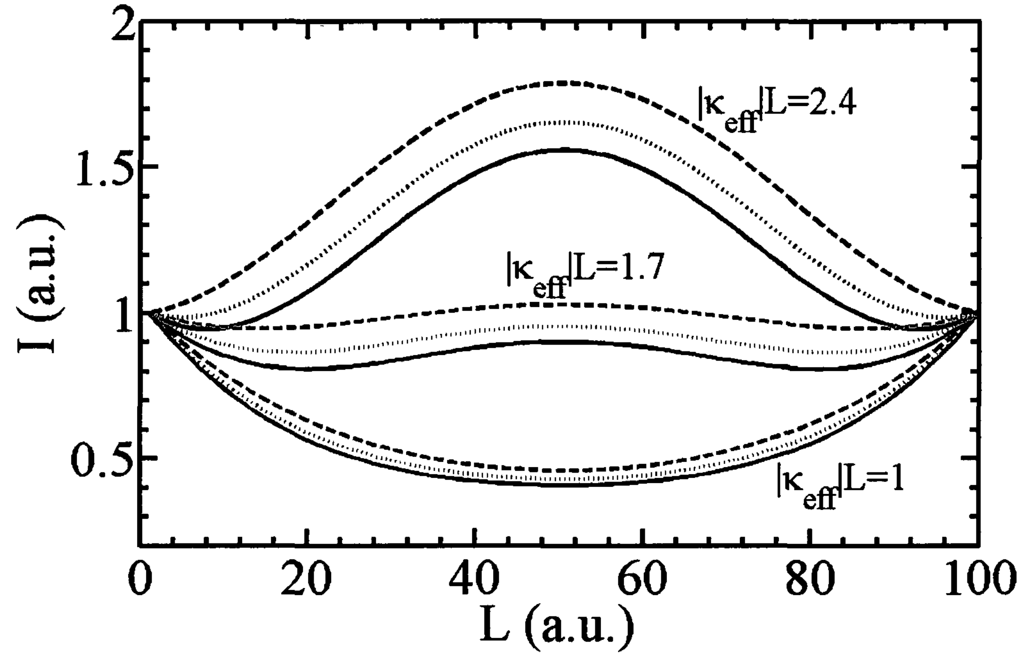

Figure 54. Longitudinal intensity profile along the laser cavity (normalized to 100 units in length) for $|\kappa_{eff}|L$ products of 1, 1.7 and 2.4 and duty cycles of 0.5 (solid lines), 0.7 (dashed lines), and 0.8 (dotted line).

cavity lengths of 376, 640, and 903 μm for $|\kappa_{eff}|L$ products of 1.0, 1.7, and 2.4, respectively. For $|\kappa_{eff}|L = 1$, the optical mode is largest near the facets, with γ=0.5 showing the most non-uniformity and γ=0.7 the least. When $|\kappa_{eff}|L$=1.7, the mode profiles are the flattest, with the γ=0.7 curve once again exhibiting the least non-uniformity and the γ=0.5 curve the most. The $|\kappa_{eff}|L$ =2.4 longitudinal mode intensity distribution is greatest in the middle of the laser cavity, with the γ=0.5 curve again exhibiting the least non-uniformity and the γ=0.7 curve the most. The γ=0.8 curve had moderate non-uniformity for all three $|\kappa_{eff}|L$ products shown here.

The smallest cavity lengths satisfying the flatness criterion for the whole range of duty cycles from 0 to 1, is shown in Figure 55 for first- through fourth-order gratings. The lengths satisfying the flatness criterion have a similar shape to the contours of the

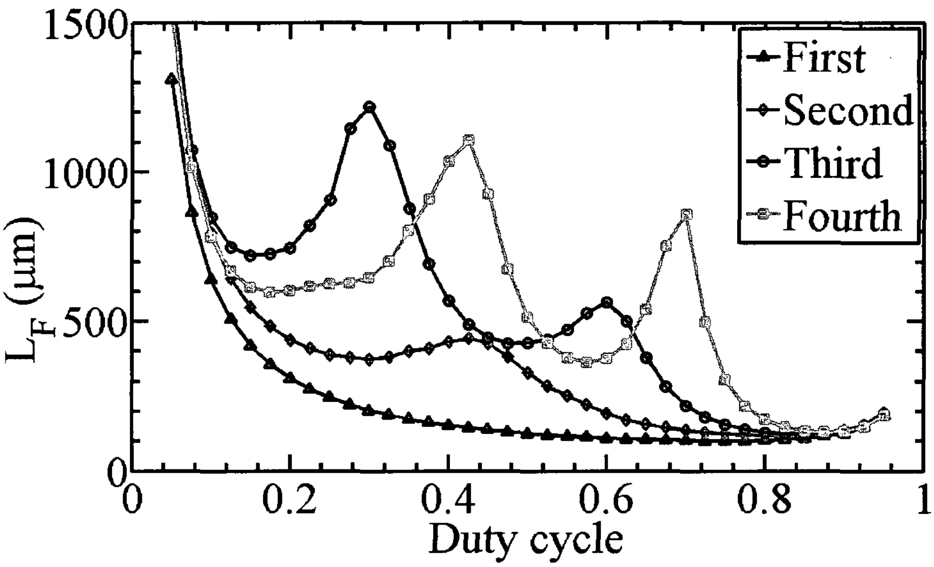

Figure 55. **Minimum flatness length *vs.* duty cycle for first- through fourth-order gratings with W_N/W_W= 1.5/3 (μm).**

normalized minimum threshold gain in Figure 50. At small duty cycles, longer cavities are required to satisfy the flatness criteria for all grating orders, while the duty cycles that permit the smallest cavity lengths while satisfying the flatness criterion are near the minimum threshold gain values of around 0.8. The minimum threshold gain values obtained from Figure 50 are outside the boundaries satisfying the flatness criterion for all grating orders. This implies a trade-off between a low threshold laser and one with lower spatial hole burning. If the application of the laser is a low-power design where having a low threshold is more critical, the flatness criterion may be relaxed somewhat to obtain a lower threshold current. On the other hand, if good high-power performance is desired, the threshold current may have to be larger than the best possible value to satisfy the flatness criterion.

The large variation between the different grating orders and duty cycles can be simplified by considering only the $|\kappa_{eff}|L$ product. The flatness *vs.* $|\kappa_{eff}|L$ characteristic shown in Figure 56 for gratings with a duty cycle of 0.8 does not change significantly with the grating order, with third-order gratings having only a slightly wider range of acceptable

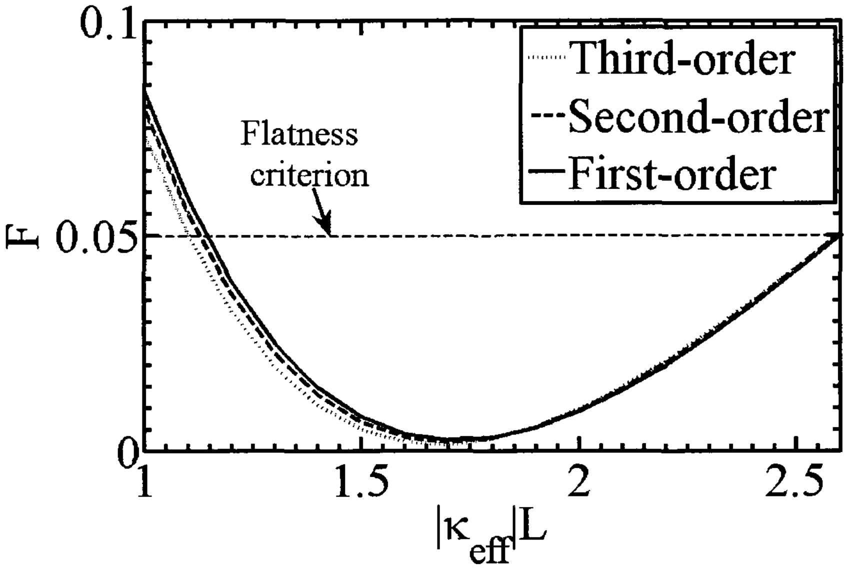

Figure 56. **Flatness, F, vs. $|\kappa_{eff}|L$ for first-, second-, and third-order gratings with a duty cycle of 0.8 and W_N/W_W = 1.5/3 (μm).**

$|\kappa_{eff}|L$ values satisfying the flatness criterion. From these results, it can be generally stated that the flatness criterion will be satisfied for $1.2 < |\kappa_{eff}|L < 2.6$. Minimum flatness values approaching zero are achieved when $|\kappa_{eff}|L = 1.7$. For a third-order grating with γ=0.5, the flatness is minimized when L=640 μm, with a range of $450 < L < 980$ μm satisfying the flatness criterion. For higher duty cycles, the length can potentially be decreased. For instance, when γ=0.8, the minimal value is L_F=200 μm, and a range of $140 < L < 300$ μm is acceptable.

Other grating parameters can also be analyzed for their affect on the flatness of the optical field. The W_N values and cavity lengths satisfying the flatness criterion are shown shaded in blue in Figure 57. As the narrow ridge width increases, the length of the cavity length required to satisfy the flatness criterion becomes larger. For values of $W_N > 3$ μm cavity lengths > 1200 μm are required to satisfy the flatness criterion. There are a range of cavity lengths that satisfy the flatness criterion for each W_N within this range of values. Generally the shorter cavity length of this range will be preferred since shorter cavity lengths will require lower threshold gain and can be operated at higher speeds. However,

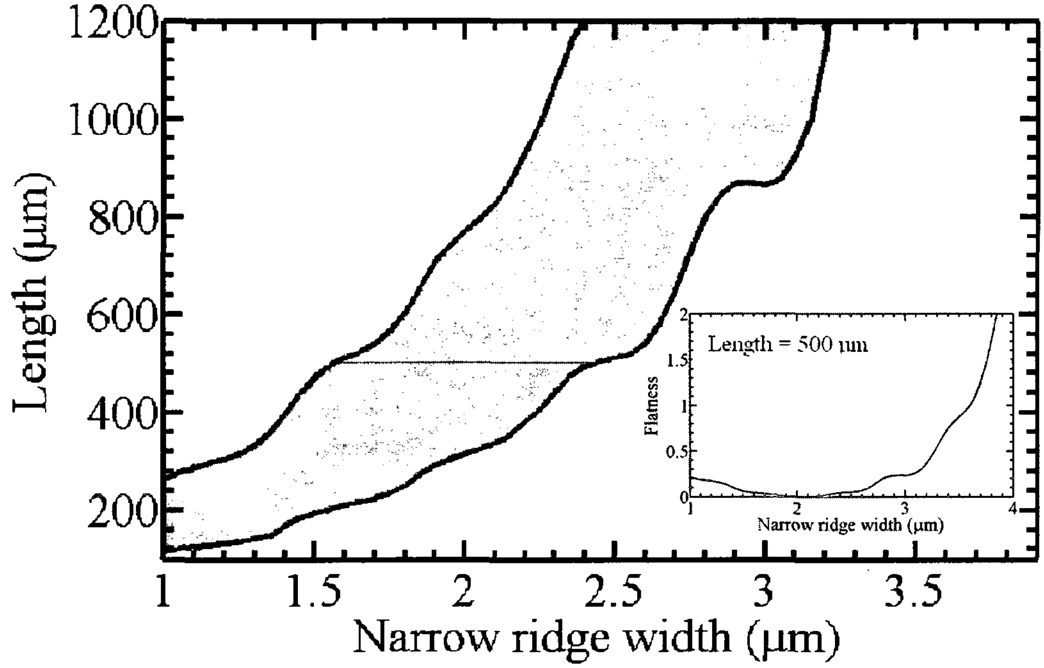

Figure 57. **Region satisfying the flatness criterion shaded in blue *vs.* cavity length and narrow rib width for a third-order grating with a wide rib width of 4 μm and duty cycle of 0.7. Inset shows cross-section at a length of 500 μm.**

it may be more desirable to minimize the flatness of the optical field, depending on the laser application. The inset shows a cross-section of this graph at a cavity length of 500 μm. The flatness forms a valley around $W_N = 2$ μm, and it is possible to achieve nearly zero flatness values near this value. This is true of all the regions satisfying the flatness criterion. In most cases, however, it is sufficient to satisfy the flatness criterion and not have a completely flat optical field.

6.1.2. λ/4 Phase-Shift

The addition of a λ/4 phase-shift is often employed in standard first-order DFB laser designs to remove the longitudinal mode degeneracy near threshold. The αL and δL values of the longitudinal mode solutions for an unshifted and phase-shifted first-order grating are illustrated in Figure 58a for facet reflectivities of r_1=r_2=0. As mentioned above, the unshifted grating has two longitudinal mode solutions with the same threshold gain, αL, on either side of the Bragg frequency, resulting in NGD=0. In practice, the facet reflectivities will not be identical, as assumed here. Even if both facets have

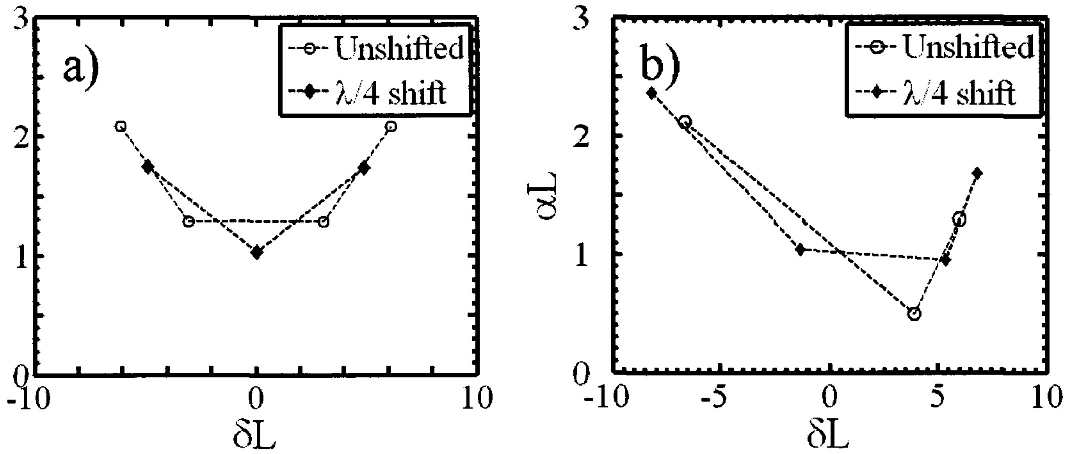

Figure 58. **Longitudinal mode solutions for a) first-order and b) third-order grating with a duty cycle of 0.8, with and without a λ/4 phase-shift**

identical reflectivity magnitudes, it is impossible to cleave the lasers into lengths that are accurate down to fractions of a grating period, and so the two facet phases will be random. These random facet phases will determine which mode will begin lasing first. This unpredictability greatly reduces the single-mode yield of the fabricated device if only a single laser wavelength is desired, as is usually the case. Two longitudinal modes with similar threshold gains can also encourage undesirable mode-hopping during laser operation. The addition of the phase-shift breaks the symmetry of the grating, resulting in a single longitudinal mode at the Bragg frequency with a lower threshold gain than the unshifted grating. This improves the single-mode yield, but often requires features smaller than the grating period to define the phase-shift.

Higher order gratings, in general, do not exhibit the longitudinal mode degeneracy of first-order index-coupled gratings, where NGD=0. The complex coupling coefficient will favour a single lowest threshold gain longitudinal mode solution, and the NGD > 0, as shown in Figure 52. This is also demonstrated in Figure 58b for a third-order grating with a duty cycle of 0.8. The shorter wavelength mode is now favoured in the unshifted grating solutions. Adding a λ/4 phase-shift will actually have a detrimental effect in this case. Although the shorter wavelength mode is still favoured, the threshold gains are now shifted upwards and NGD, i.e. longitudinal mode discrimination, is reduced. This will increase the probability of mode-hopping, and add uncertainty to the lasing wavelength.

How general is the reduced NGD with the addition of a phase-shift? A more comprehensive analysis for grating orders from first- to third-order of the minimum threshold gains, minimum Bragg frequency detuning, and NGD over a complete range of duty cycles from 0 to 1, a cavity length of 500 µm, and ideal reflectivities of $r_1 = r_2 = 0$ for both unshifted (solid lines) and phase-shifted (dashed lines) gratings is shown in Figure 59. These graphs are effectively cross-sections of the surface plots of Figure 50-52 at a cavity length of 500 µm, except now including phase-shifted solutions. This analysis reveals that while the addition of a phase-shift is helpful in all cases for a first-order grating, it is usually detrimental for higher order gratings.

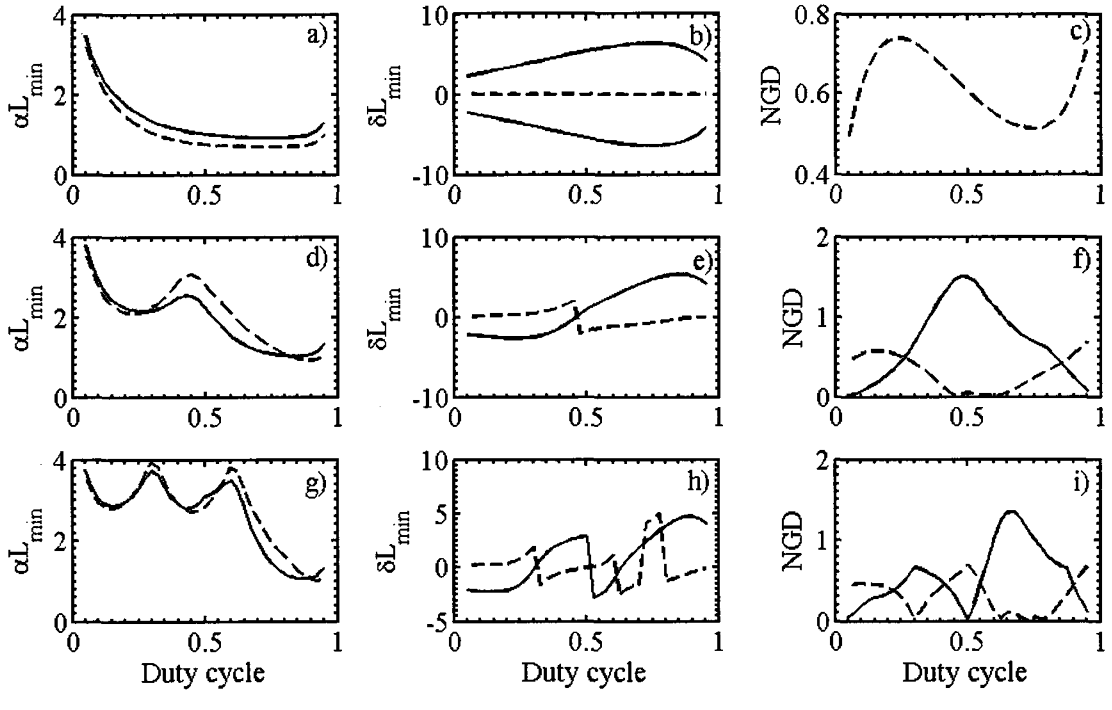

Figure 59. Normalized gain threshold (*αL*), normalized Bragg frequency deviation (*δL*) and normalized gain difference (NGD) vs. duty cycle for first- (a,b,c), second- (d,e,f) and third-order gratings (g,h,i), for a uniform grating (solid lines) and with a central λ/4 phase-shift (dashed lines).

First-order gratings have lower threshold gains and higher NGD values when the phase-shift is added. The lowest threshold gain of $(\alpha L)_{\min}$ = 0.69 occurs for the phase-shifted grating at a duty cycle of 0.75, for the unshifted grating the minimum of $(\alpha L)_{\min}$ = 0.91 also occurs at a duty cycle of 0.75. The wavelength detuning, shown in Figure 59b, has two modes that are symmetrical about the Bragg frequency for the unshifted grating, while the phase-shifted grating has a single mode at $(\delta L)_{\min} = 0$. For the first-order grating, the NGD is zero for the unshifted grating since there are two longitudinal modes with the same gain threshold. The addition of a phase shift is beneficial, yielding values of the NGD as great as 0.74 (Figure 59c, dashed line).

Phase-shifted gratings, and not unshifted gratings, also have the lowest $(\alpha L)_{\min}$ value over all duty cycles for second- and third-order gratings. These very low $(\alpha L)_{\min}$ values occur at very high duty cycles. The phase-shifted second-order grating had the lowest $(\alpha L)_{\min}$ of 0.92 at a duty cycle of 0.9, and the phase-shifted third-order grating had the lowest $(\alpha L)_{\min}$ of 0.99 at a duty cycle of 0.92. For higher grating orders, LC-DFB lasers with a phase-shifted grating generally show a higher threshold gain than the unshifted structures for most duty cycles, as shown in Figure 59d and g. In particular, for the duty cycles > 0.5, phase-shifted gratings have a lower threshold gain only when the duty cycle is > 0.9 in the second-order case and only for duty cycles < 0.55 and > 0.92 in the third-order case.

The wavelength detuning is very stable for an unshifted second-order grating DFB laser, shown by the solid line in Figure 59e, with a smooth variation over all duty cycles, as also observed in Figure 51. The wavelength changes from being longer than the Bragg wavelength for duty cycles < 0.5 to being shorter than the Bragg wavelength for duty cycles > 0.5. The phase-shifted laser (Figure 59e, dashed line), however, has an abrupt, highly undesirable, jump in detuning for a duty cycle of ~0.45. The situation is yet worse in a third-order grating. For the unshifted grating (Figure 59h, solid line), there is a single jump in longitudinal modes at a duty cycle of 0.5. There is a direct relationship between these wavelength detuning discontinuities and poor NGD values.

The wavelength detuning discontinuities occur at duty cycles when the NGD goes to zero, as seen in the NGD characteristics of the second-order (Figure 59f) and third-order (Figure 59i) cases. For higher order gratings, the addition of a phase-shift does not generally improve the NGD because additional mode discrimination is already provided through the radiation loss that occurs for non-negligible imaginary components of the coupling coefficient, reducing the need for a phase-shift. This was first noted by Kazarinov for second-order gratings [100]. The NGD values for these higher order gratings are greatly reduced near duty cycles where the wavelength jumps, observed in Figure 59e and Figure 59h, occur. This leads to the conclusion that, for most duty cycles of interest in higher order gratings, introducing a $\lambda/4$ phase-shift will worsen the longitudinal mode discrimination, and thus have precisely the opposite effect as intended.

6.1.3. Facet Reflectivity

The end facets of the laser cavity have so far been assumed to be perfectly anti-reflective, i.e. $r_1=r_2=0$. Although the fabricated lasers will ideally have perfect anti-reflection coatings at the end facets, in reality there will still be some finite facet reflection including a phase component. This phase component represents the additional distance traveled due to a partial grating period, a distance that, as mentioned earlier, cannot be consistently achieved when cleaving a laser. In DFB lasers with first-order gratings, this random facet phase determines which longitudinal mode will begin lasing at threshold. In lasers with higher order gratings, the generally complex coupling coefficient means that there is much more certainty as to which longitudinal mode will lase at the threshold.

To see the requirements on both the anti-reflection coatings and the NGD of the grating, variations in the facet reflectivities of both phase and magnitude are now examined. The different facet reflectivities are incorporated by changing the boundary conditions of the longitudinal mode equations, for example, in the error function of (4.64). The exact facet phase could be anything from 0 to π, so the longitudinal mode solutions are found over this range of phases for each facet reflectivity magnitude. From this range of solutions, the largest and smallest values of the threshold gain and Bragg frequency detuning are found, and their difference gives the worst-case deviation in the threshold gain and wavelength detuning due to unknown facet reflectivity phases for each facet reflectivity magnitude. The plot of this variation due to facet phases is shown in Figure 60 for different reflectivity magnitudes, assuming that the two facets are the same, and for the four lowest threshold gain longitudinal modes. As the magnitude of r becomes larger, the deviation in αL and δL will also grow. It is important to have as little reflection as

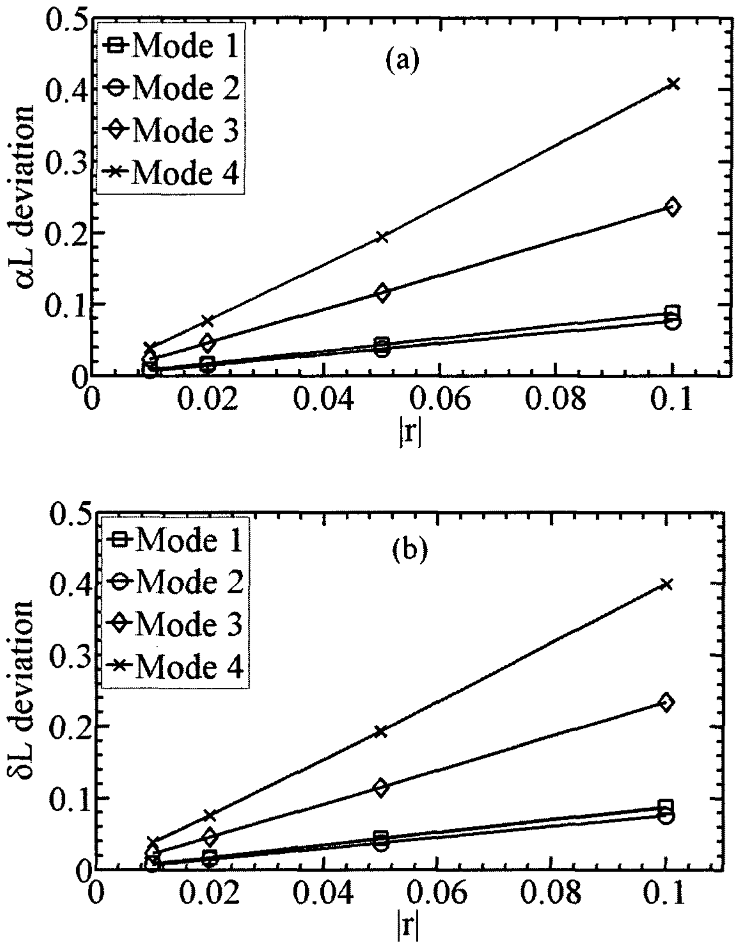

Figure 60. **Maximum deviation in (a) αL and (b) δL *vs.* magnitude of facet reflectivity for a random facet phase**

possible at the end facets, not only to prevent Fabry-Perot cavity modes from forming, but also to prevent instability in the longitudinal mode. For reflectivities of $|r| < 0.1$, such as those shown in Figure 60, a NGD value of > 0.2 will prevent any mode-hopping due to random facet phases for this geometry.

It is generally the case that one facet is highly-reflective and the other is anti-reflective. This results in most of the light exiting out of the single anti-reflective facet, rather than out of both as will be the case in our as-cleaved lasers. The effect of this on the standard grating parameters is illustrated in Figure 61, for a third-order grating with a cavity length of 500 μm and a duty cycle of 0.7. In this figure, the phase of both reflectivities is kept fixed at zero, while the magnitude of r_2 is increased from 0 to 1. The units of the minimum threshold gain, Bragg frequency deviation, and NGD are again normalized to be unitless by multiplying them by the cavity length. The minimum threshold gain decreases modestly as the magnitude of r_2 increases, and has a maximum of $(\alpha L)_{\min}$ = 1.92 at $|r_2| = 0$ and minimum of $(\alpha L)_{\min}$ = 1.76 at $|r_2|=1$. $(\delta L)_{\min}$ varies somewhat more

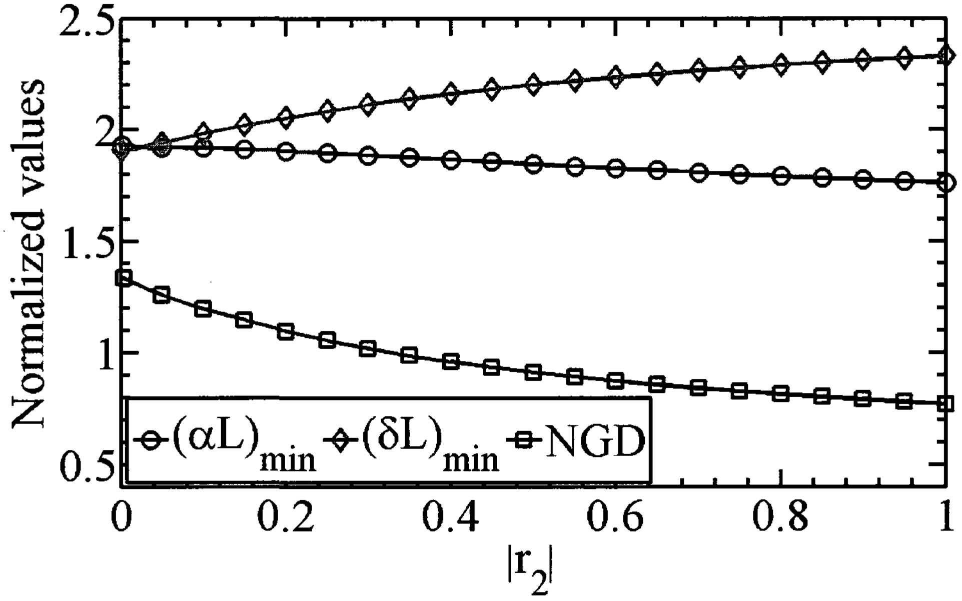

Figure 61. Variation of $(\alpha L)_{\min}$, $(\delta L)_{\min}$, and NGD *vs.* magnitude of r_2, for $r_1=0$, phase of $r_2=0$, a cavity length of 500 μm, and a third-order grating with W_N/W_W = 1.5/3 (μm) and a duty cycle of 0.7. Normalized values are unitless after multiplication with the cavity length, *L*.

significantly from a minimum of 1.9 to a maximum of 2.3 when $|r_2|$ goes from zero to one, respectively. The biggest effect is on the normalized gain difference, NGD, which decreases as $|r_2|$ increases, from 1.32 at $|r_2|=0$ to 0.77 at $|r_2|=1$. This decrease in NGD is in contrast to lasers with first-order gratings, which often use a single highly-reflecting end facet to lift the longitudinal mode degeneracy (i.e. increase the NGD so it is no longer nonzero) [101].

It would appear that having a highly reflective end facet has obvious benefits, lowering the threshold gain, producing a single-ended output facet, and still keeping NGD within the acceptable limits mentioned in Section 4.5 of NGD > 0.2. As seen from Figure 60, higher reflectivities leads to greater variation in the output parameters. This is confirmed by Figure 62, where $(\alpha L)_{\min}$, $(\delta L)_{\min}$, and NGD are plotted for a fixed r_2 magnitude of $|r_2|=0.95$, for a variation in the phase of r_2 from 0 to 2π. There is a large variation in all parameters as the phase is varied, particularly around a phase of $3\pi/2$ where there is a switch in longitudinal modes from negative to positive Bragg detuning values.

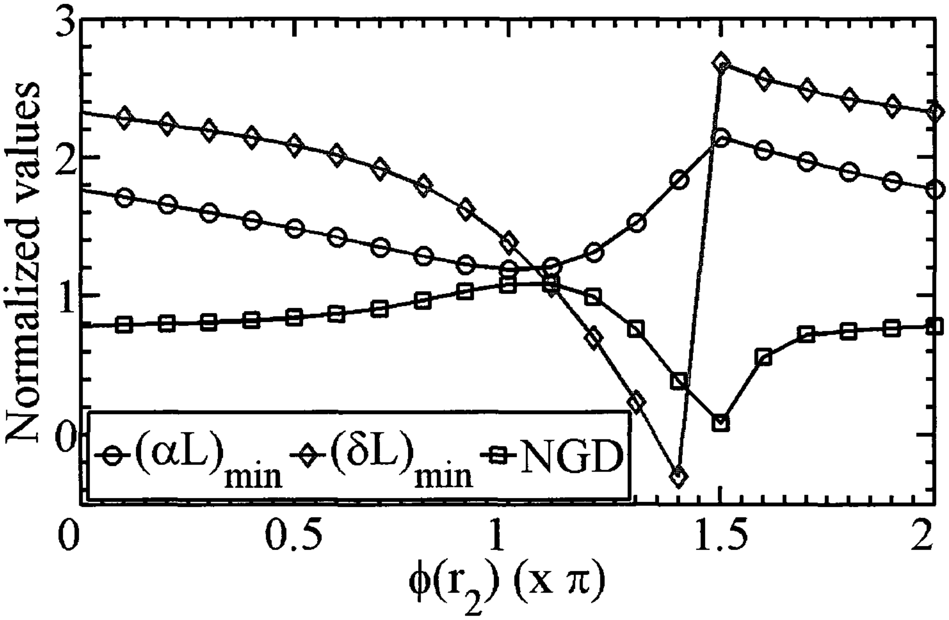

Figure 62. Variation of $(\alpha L)_{\min}$, $(\delta L)_{\min}$, and NGD *vs.* phase of r_2, for $r_1=0$, magnitude of $r_2 = 0.95$, a cavity length of 500 μm, and a third-order grating with $W_N/W_W = 1.5/3$ (μm) and a duty cycle of 0.7

6.2 Quasi-3D Static Laterally-Coupled Distributed Feedback Model

The simplified model described in Section 4.5 is useful for quick comparisons of the threshold characteristics of laterally-coupled distributed feedback lasers with different grating parameters. However, it neglects the spatial variation of the modal gain, carrier densities and effective refractive index along the laser cavity. The distribution of carriers, for example, can be very non-uniform along the laser cavity, particularly at higher powers where there is significant longitudinal spatial hole burning (LSHB). This leads in turn to a non-uniform gain profile, invalidating one of the assumptions of the simplified model. This work will use a quasi-3D model similar to the static model described by X. Li for DFB lasers [101], except now applied to modified coupled-mode coefficients calculated for LC-DFB lasers.

6.2.1 Solution Algorithm

This quasi-3D model divides the laser into two-dimensional slices along the longitudinal (z-) direction, similar to the simplified model described above, and follows the algorithm shown in Figure 63. The algorithm begins in step (1) by calculating the modified coupled-mode coefficients for a two-dimensional cross-section using the algorithm described in Section 4.4. A more accurate model would recalculate these coefficients for each two-dimensional slice according to the local variations in gain and refractive index, but this would require prohibitively long computational times. For a 50 section laser, a single iteration of such a model would require ~25 hours, and the calculation would have to be performed repeatedly to achieve a self-consistent result. Instead, the coefficients are calculated for the cross-section assuming a cold cavity, i.e. that there are no carriers present affecting the refractive index. The LAS2D simulations of Chapter 3 indicate that the refractive index changes in the MQW by ~0.25% from its cold cavity value when a moderate bias of 60 mA is applied. While this refractive index change would produce a slight change in the calculated coupling coefficients, this change will be neglected for the sake of a much more efficient model.

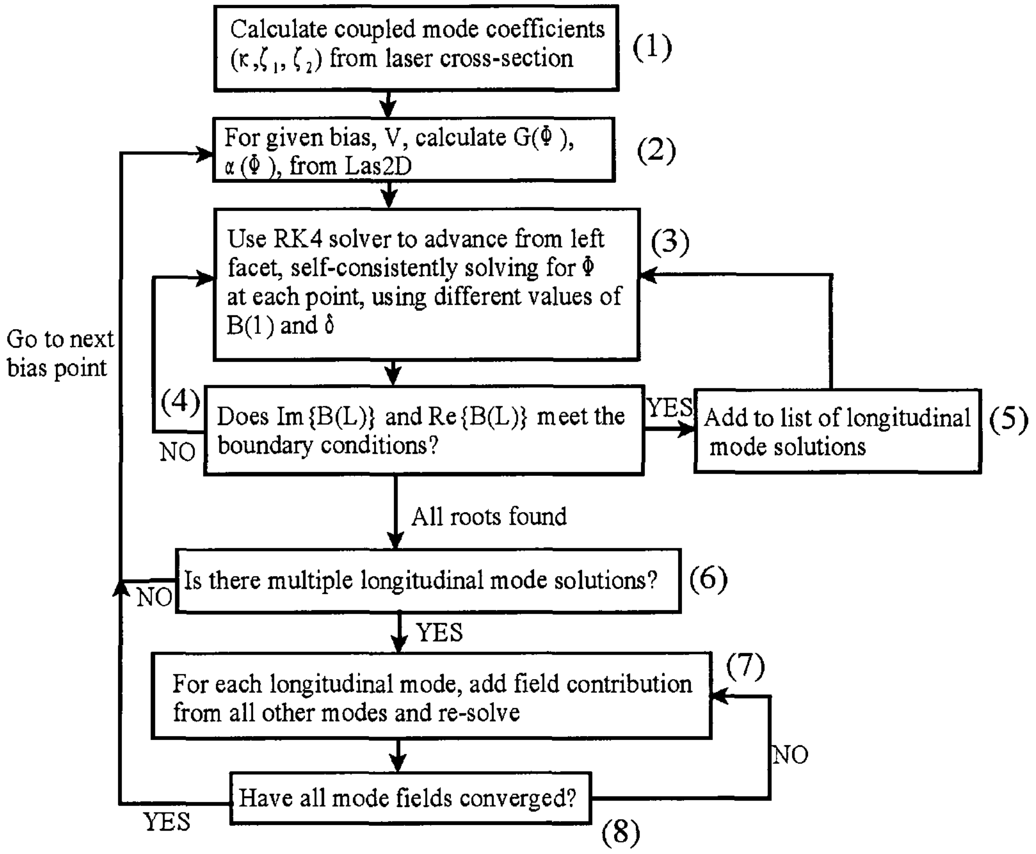

Figure 63. **Quasi-3D static model solution algorithm**

For a given laser cross-section and applied bias, LAS2D is then used in step (2) to calculate the modal gain/loss, spontaneous emission rate, carrier densities, and current density for a given range of photon flux density values, ϕ. This is a different calculation from the one for a standard FP laser in Chapter 3, and uses a solution mode of LAS2D that is normally used for semiconductor optical amplifier (SOA) simulations. These values are stored in a lookup table for the next stage of calculations. An example of the results of this stage for the modal gain and internal loss for an applied bias of 1.5 V is shown in Figure 64. This accurately takes into account the lower gain that results as the photon flux density increases. This saturation of the output power results from a lack of carriers able to supply gain as the photon flux density becomes very large. This nonlinear gain saturation will reduce the local modal gain in the regions of the laser cavity with a large optical intensity. Next, in step (3), the longitudinal mode solver starts with an

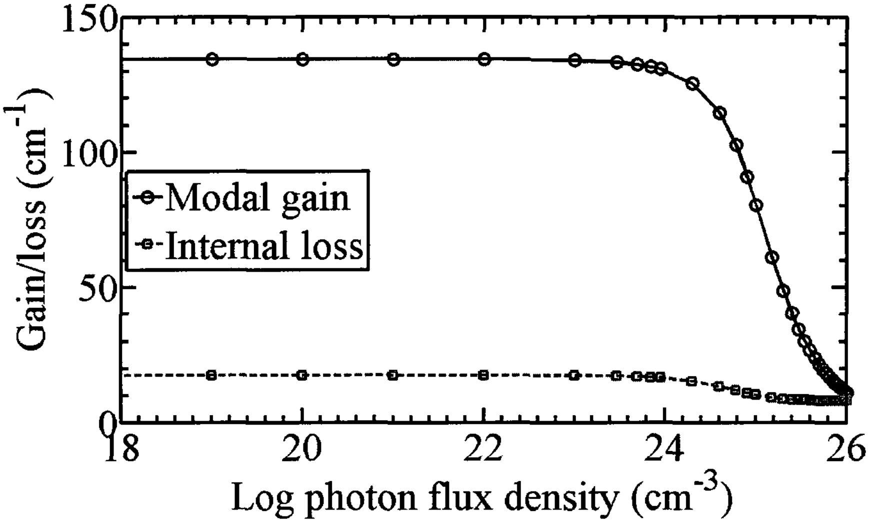

Figure 64. **Modal gain and internal loss *vs.* log of photon flux density for an applied voltage of 1.5 V**

initial guess for $B(1)$, the value of the backward-propagating field at the left facet, and δ, the Bragg detuning. It uses an RK4 solver, as described in Section 4.5, to integrate the coupled-mode fields along the length of the laser. Unlike in the simplified model, spontaneous emission is also included in this model, so that the modified coupled-mode equations are now:

$$\begin{aligned} \frac{dA}{dz}+\left(-\alpha(z)-j\delta-j\zeta_1-\frac{J_{sp}(z)}{|A|^2}\right)A=j\left(\kappa_p^*+\zeta_2\right)B \\ -\frac{dB}{dz}+\left(-\alpha(z)-j\delta-j\zeta_3-\frac{J_{sp}(z)}{|B|^2}\right)B=j\left(\kappa_p+\zeta_4\right)A \end{aligned} \qquad (6.1)$$

where a term representing the coupling of spontaneously emitted light, J_{sp}, has been added to both coupled-mode equations. In this model, the J_{sp} term is given by

$$J_{sp}=\beta R_{sp} \qquad (6.2)$$

where β represents the coupling of spontaneous emission into the lasing mode, and R_{sp} is the spontaneous emission rate, integrated over the laser cross-section. The value of R_{sp} is obtained from LAS2D, and $\beta_{sp} = 1 \text{ x } 10^{-4}$ is used for this model. Also different from the simplified model presented in Section 4.5 is that we now calculate the gain, $\alpha(z)$, self-consistently at the given bias point for each cross-section slice in the longitudinal direction. For each slice, the modal field amplitudes are first calculated assuming the value used for the modal gain/loss from the previous iteration. The field amplitudes are used to find the photon flux density, which is then used to recalculate the gain. This cycle is continued until the modal field amplitudes that are calculated in that section are consistent with the gain calculated with the photon flux density present. This continues for each cross-section until the right facet is reached, and the boundary conditions are checked in step (4). If the boundary conditions are satisfied, in step (5) a longitudinal mode solution has been found and added to a list. This continues until all δ values within a wide range have been checked. A similar two-dimensional NR root-finding algorithm to the one described in Chapter 4 is used again here, except with B(1) and δ, to find the exact longitudinal mode solutions.

There are generally multiple longitudinal mode solutions, so we must proceed to step (6) in the algorithm. We take the longitudinal mode solutions in step (7), starting with the one with the largest amplitude, and assume that they contribute to the photon flux according to their field amplitude at each point in the laser cavity. The other modes are then re-solved, beginning at step (3), with this background photon flux present. The longitudinal modes are continuously re-solved with the additional photon flux from the other modes present, until the mode fields and δ converge for all the longitudinal modes in step (8). In practice, for the laser that was simulated in the following section, a single longitudinal mode dominated for the range of bias currents that were studied, with a much weaker second mode appearing at higher biases. This greatly simplified the calculations compared to the general algorithm where there are many potential longitudinal modes that must converge.

6.2.2 Quasi-3D Static Model Results

The quasi-3D static model was compared with the experimental results of Li [101]. In his work, he develops a similar quasi-3D static model for a distributed feedback laser. Since he was able to match his simulated results to the experimental values, it is expected that our model should also provide reasonably close agreement to experiment. It is not the purpose of this thesis to compare the models directly. Rather, the intention is to use the detailed information on the experimental DFB laser in Li's work, including the epitaxial growth structure, to predict the LI curve. The data from Li's result was found from analyzing Figure 4.3 in [101] with ImageJ software to find the data points. The first attempt at matching the experimental data with the model predicted far higher output powers for a given bias point than the experimental points. This was particularly true at lower bias currents of < 50 mA. For instance, the model predicted an output power of 7.7 mW at a bias current of 45 mA, compared to the experimental value of 3.6 mW at this bias current.

It was found that the results could more closely match the experimental results if the loss factor was adjusted. If an additional loss of 1.4 cm^{-1} is added such that the error in the output power between the experimental and theoretical results at 100 mA is minimized, a more closely matching characteristic can be obtained, shown in Figure 65. There are still some significant deviations, particularly at lower bias currents. One major reason for this is that our LAS2D model parameters, given in Chapter 3, have not all been calibrated for Li's material system. While much information about the laser is provided by Li, ideally there would be FP test data that could be used for calibration of the model parameters of LAS2D outlined in Table 2. One of the tasks in any future work involving this model would be to properly calibrate the LAS2D parameters used against FP laser data. Our quasi-static 3D model also neglects amplified spontaneous emission at low bias currents below threshold, since we do not see lasing modes at this point. Although the quasi-3D model still requires fine-tuning, particularly of the LAS2D parameters that are used in step (2) of the algorithm, it is a considerable improvement over the simplified model,

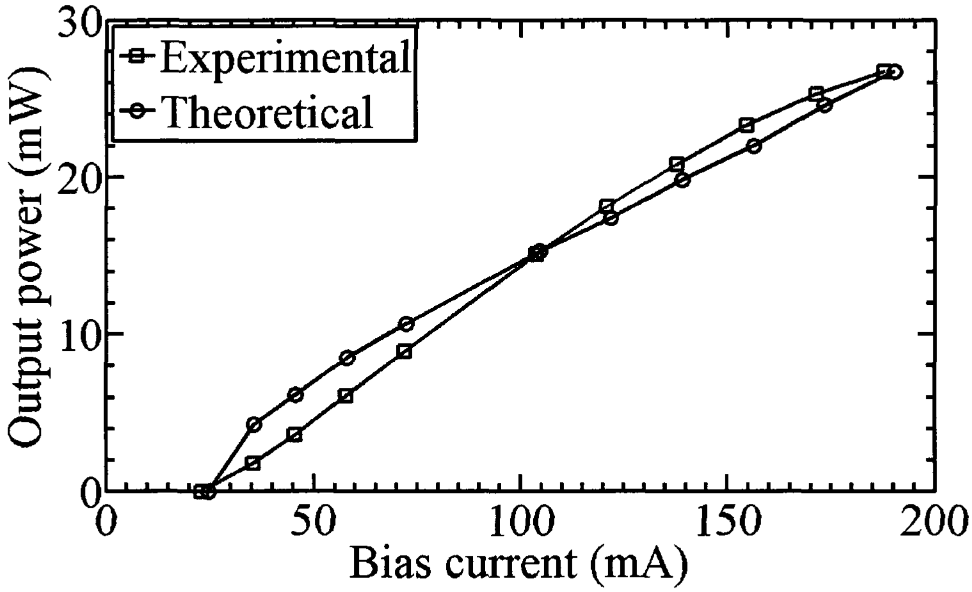

Figure 65. **Comparison of quasi-3D model results with work of X. Li [101]**

providing a better estimation of the laser performance. The model was applied to a 500 μm long LC-DFB laser with a grating of W_N / W_W=1.5/3 (μm) and a duty cycle of 0.7. The end facets were set to reflectivities of R_1 = R_2 = 0.3, consistent with an as-cleaved laser bar.

The LI curve for this laser is shown in Figure 66. The threshold current of the LC-DFB laser was calculated to be 10.5 mA from the intercept of the LI curve, excluding the zero power point at 12 mA. The maximum slope efficiency is 0.31 mW/mA. As a comparison, the LI curve generated for this laser is compared to that calculated by LAS2D for a Fabry-Perot laser of identical epitaxy with reflectivities of R_1 = R_2 = 0.3, and a ridge width of 3 μm. The FP laser has a threshold current of 9.15 mA and a maximum slope efficiency of 0.36 mW/mA. We thus have a reduction of 12% in the slope efficiency and a threshold current that is 15% higher when going from a FP laser to an LC-DFB laser with this grating configuration. The slightly worse numbers are not unexpected, since we are introducing additional loss with the grating, however, in return we obtain a high-quality frequency-selective DFB laser spectrum. The performance of the

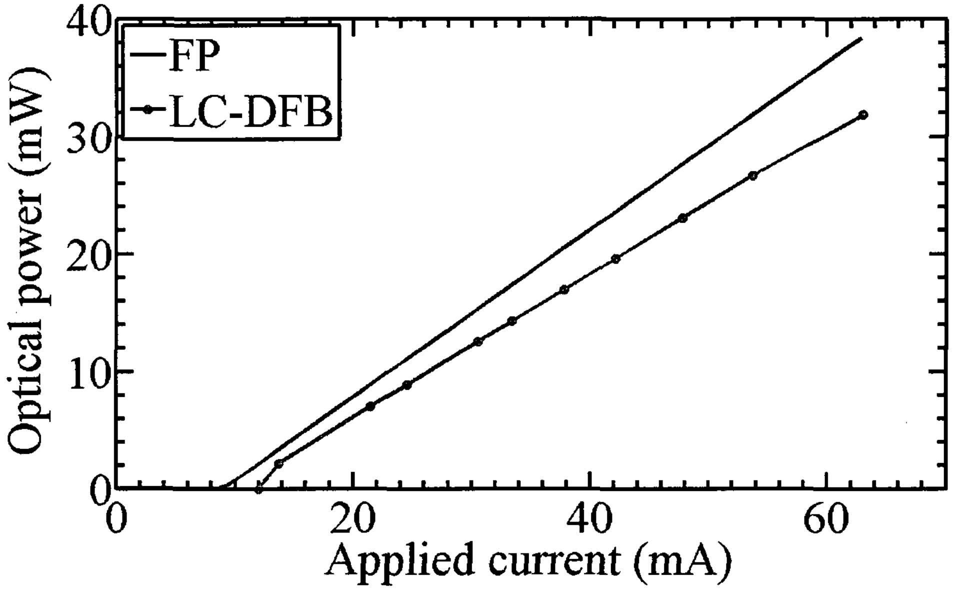

Figure 66. **Comparison of LC-DFB laser (ridge widths of W_N/W_w = 1.5/3 (μm), duty cycle of 0.7) quasi-static 3D LI curve and the LI curve of a Fabry-Perot laser with a ridge width of 3 μm calculated using LAS2D.**

LC-DFB laser could be improved by optimizing the duty cycle and length of the laser according to the analysis of Section 6.1.1, as third-order grating LC-DFB lasers with a length of 500 μm and duty cycle of 0.7 are not the lowest threshold gain design.

We can use this model to analyze spatial hole burning effects in a typical LC-DFB laser. In Figure 67, the average hole concentration in the first quantum well (closest to the ridge) is shown for an applied bias of a) 22 mA, and b) 63 mA. There is little change in the hole concentration in the longitudinal (*z*-) direction for both biases, indicating that longitudinal spatial hole burning (LSHB) is not a serious issue at these values of the applied bias. As we go to the higher applied bias, however, we begin to see some lateral spatial hole burning, as the holes in in the region under the ridge begin to be depleted, resulting in a local minimum at the centre of the ridge. Thus, for this particular laser geometry, we see that lateral, rather than longitudinal spatial hole burning is the dominant carrier depletion mechanism. Since the calculated flatness, *F*, at this cavity length and duty cycle is 0.035, this laser geometry satisfies the flatness criterion of $F < 0.05$, and so

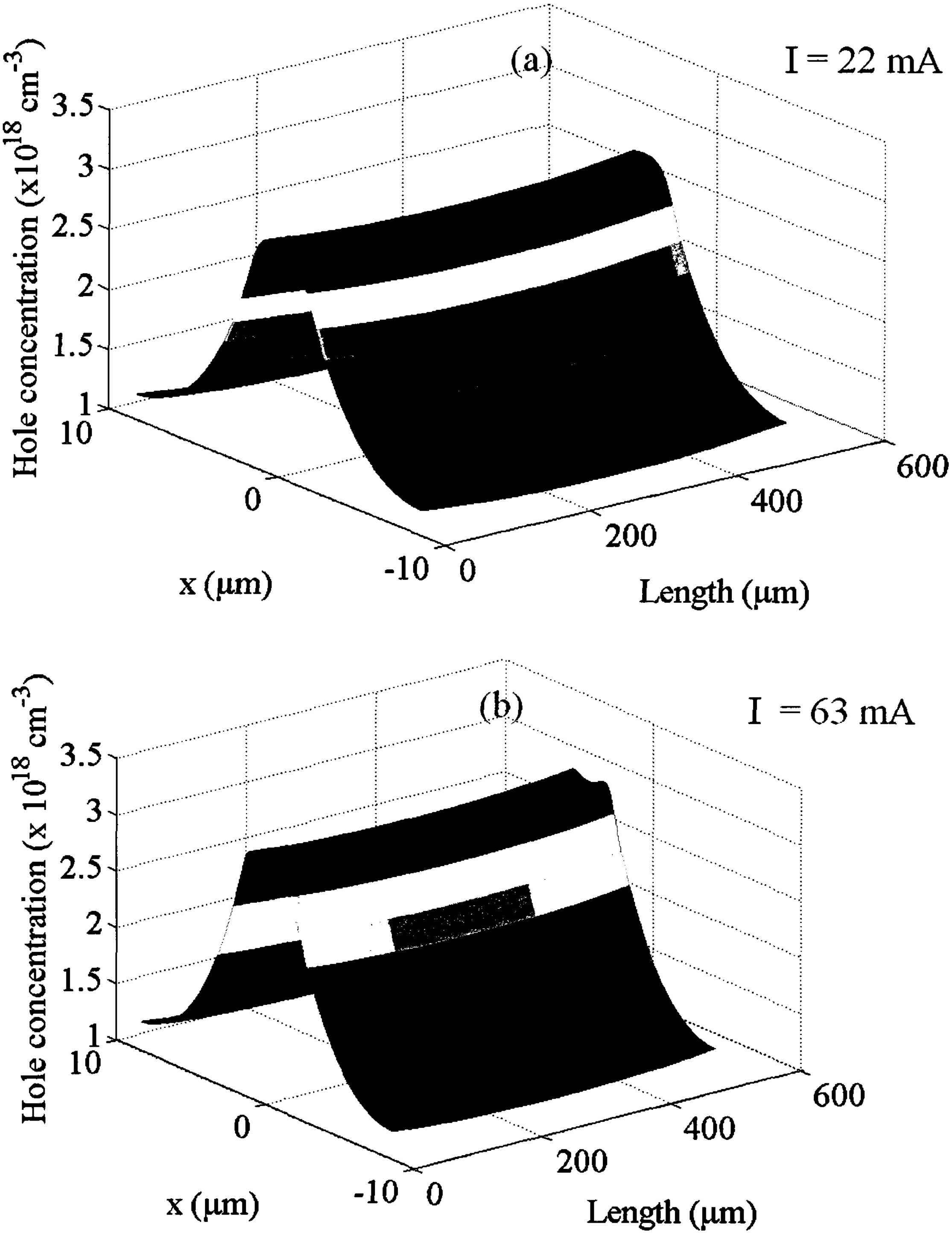

Figure 67. **Hole concentration in first quantum well *vs.* cavity length (*z*-direction) and *x*-direction for a) an applied bias of *I*=22 mA, and b) an applied bias of *I*=63 mA.**

low LSHB is to be expected. Other laser geometries with a greater *F* will likely demonstrate greater LSHB than is observed in this case.

A limitation on using LAS2D to generate the gain, loss, etc. *vs*. the photon density was revealed when attempting to find solutions at higher bias values. For bias voltages above 1.4 V the LAS2D solutions no longer converged. The LAS2D model that we are using was originally intended for SOAs that are operating in the linear gain region. It appears that when going to higher bias voltages where the gain begins to saturate, the model experiences convergence issues. This restricts our use of this model that relies on LAS2D to the linear part of the LI curve, unless this difficulty with convergence can be overcome. This is not necessarily a limit on the quasi-static model itself, however, and it could be possible to use another simulation tool or develop new software that could handle these higher bias values.

CHAPTER 7 - EXPERIMENTAL RESULTS

7.1 Mask Layout

The LC-DFB laser mask was designed to be compatible with a stepper lithography process, where a single stepper tile is repeatedly exposed along the wafer during processing. The size of the stepper tile used was 6 mm x 6 mm. Table 5 shows the design variations that were included on the mask. The different lasers are identified by the device label given in the first column. The next two columns are for the narrow and wide ridge widths, in microns. The narrow ridge widths have variations between 1.5 and 2.5 μm, and the wide ridge widths between 2.5 and 5 μm. The fourth column is for the grating order, which determines the period given in the next column, either 600 nm for the third-order or 800 nm for the fourth-order gratings, +/- 30 nm. There are two columns for the grating period since the mask includes some dual-wavelength designs, with different grating periods on either side of the mask, for possible use in the generation of microwave signals. There are also Fabry-Perot laser test structures and gratings with Bragg gratings detuned from 1310 nm to permit DFB lasing even if the material gain is not centered at the proper wavelength. Finally, the mask also includes some dual-wavelength designs, with different grating periods on either side of the ridge. These differences are smaller than the +/- 30 nm resolution limit on the lithography process, but it was decided to see if the average grating periods on either side of the ridge along the entire length of the laser cavity would provide the desired dual-wavelength operation, even if there was some variation in the individual grating periods.

The mask includes six layers: two dry-etching layers, an evaporated metal layer that includes the device labels shown in Table 5, a dielectric via layer, an InGaAs removal layer, and an electroplated metal layer. The processing steps are the same as those shown in Figure 5, with a few additional steps. The two dry-etching layers include one layer for

Device Label	W_N (um)	W_W (um)	Grating order	Period 1 (nm)	Period 2 (nm)	Duty cycle	Repeat	Description
L1,L23,L45	1.5	4	3	600	NA	0.5	3	Standard design
L2	1.5	4	3			0.6	1	Duty cycle var.
L3	1.5	4	3			0.7	1	
L4	1.5	4	3			0.8	1	
L5	1.5	4	3			0.9	1	
L7	1.5	2.5	3			0.5	1	3rd order ridge width variations
L8	1.5	3	3			0.5	1	
L9	1.5	3.5	3			0.5	1	
L10	1.5	4.5	3			0.5	1	
L11	1.5	5	3			0.5	1	
L12	2	3.5	3			0.5	1	
L13	2	4	3			0.5	1	
L14	2	4.5	3			0.5	1	
L15	2	5	3			0.5	1	
L16	2.5	4	3			0.5	1	
L17	2.5	4.5	3			0.5	1	
L18	2.5	5	3			0.5	1	
L28	1.5	2.5	4	800	NA	0.5	1	4th order ridge width variations
L29	1.5	3	4			0.5	1	
L30	1.5	3.5	4			0.5	1	
L31	1.5	4.5	4			0.5	1	
L32	1.5	5	4			0.5	1	
L33	2	3.5	4			0.5	1	
L34	2	4	4			0.5	1	
L35	2	4.5	4			0.5	1	
L36	2	5	4			0.5	1	
L37	2.5	4	4			0.5	1	
L38	2.5	4.5	4			0.5	1	
L39	2.5	5	4			0.5	1	
L6,L24,L44	1.5	4	3	600	NA	0.5	3	lambda/4 phase shift
L40	1.5	1.5	NA			NA	1	Fabry-Perot
L41	4	4	NA			NA	1	Fabry-Perot
L19,L20	1.5	4	3	607.9	608	0.5	2	0.2nm spaced dual WL
L21,L22	1.5	4	3	607.9	608	0.5	2	0.25nm spaced dual WL
L25,L26	1.5	4	3	607.5	608.4	0.5	2	2nm spaced dual WL
L27	1.5	4	3	606.8	609.1	0.5	1	5nm spaced dual WL
L42	1.5	4	3	594	NA	0.5	1	1280nm Bragg WL grating
L43	1.5	4	3	622	NA	0.5	1	1340nm Bragg WL grating

Table 5. LC-DFB mask design variations

the detailed etching around the ridge and one layer for the coarser etching of the trench around the ridge. The dielectric via will have sloped sidewalls (narrower near the ridge layer) to permit better coverage of the evaporated metal material, due to the highly directional nature of the metal evaporation process [102].

The mask also includes an InGaAs removal layer that defines regions where InGas is to be etched away. Removing InGaAs material will greatly reduce the amount of carriers

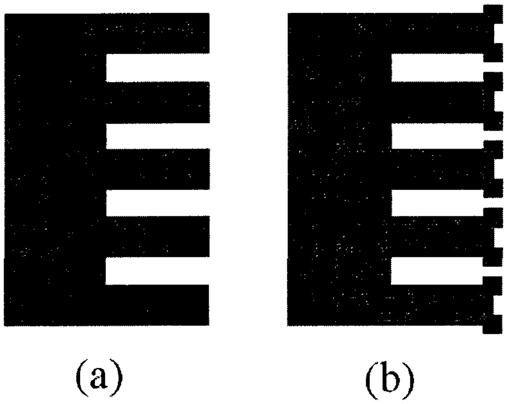

Figure 68. **a) Standard rectangular grating tooth definition, b) use of sub-resolution mask features to sharpen grating teeth.**

that will be injected in this region. This is done in the area of the grating teeth to reduce the amount of lateral current spreading. The evaporated metal contacts are the primary metal layer, however, if cracking of this layer occurs, the extra mask layer for electroplated metal contacts can be used. The use of sub-resolution features to sharpen the grating teeth was also attempted, as shown in Figure 68. These sub-resolution features were 100 nm x 100 nm squares placed at the end corners of the grating teeth. The intention was to reduce the rounding of the grating ends due to the resolution limits of the stepper lithography process.

The layout of these design variations on the mask is shown in Figure 69. The evaporated metal is used not only as a contact but also to create the device labels and cleaving marks. The device labels and cleave marks are spaced by 500 μm. The reader is referred to Figure 106 of Appendix A for more detailed labeling of the features here. The layout was created using dw-2000 v8.3 software from Design Workshop Technologies. One useful feature of this mask layout software is that it uses 'p-cells'. These are modules of code written in the GPE language that describe how to implement a repeated section of the layout. An example from this layout of such a repeated mask element is a standard LC-DFB laser. A single instance of this laser is generated for the layout when given a set of input parameters such as the ridge widths, duty cycle, laser length, etc. This allows for changes to be made to the mask in a fast and flexible manner. For instance, if it was

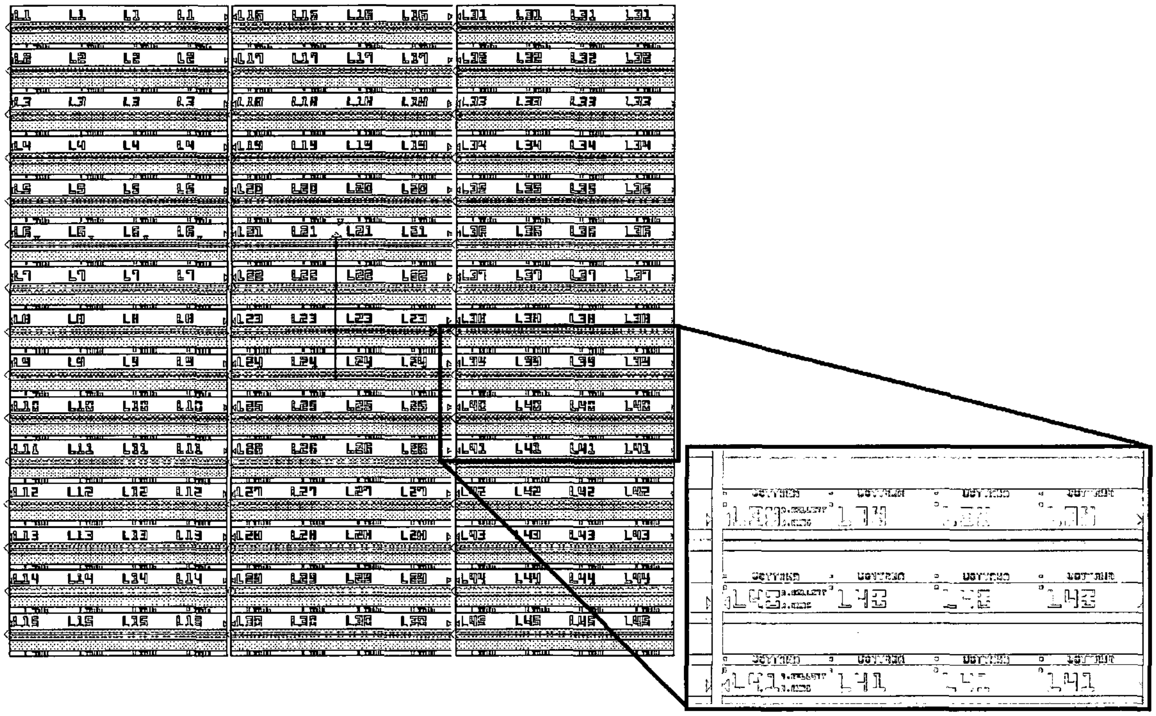

Figure 69. Layout of LC-DFB stepper tile with detail of lasers L39-L41.

decided to change the duty cycle of all devices in the next fabrication run, only the p-cell input corresponding to the duty cycle would need to be changed, instead of recoding the entire mask. The standard LC-DFB p-cell accepts as parameters the narrow and wide ridge width, grating period, duty cycle, etc. The script that lays out the entire mask creates an instance of each of these p-cells for each of the design variations described in Table 5. Those interested in more details on this method of mask layout can refer to Appendix A.

7.2 Device Fabrication

The LC-DFB lasers were fabricated at the Canadian Photonic Fabrication Centre (CPFC) in Ottawa, ON. The gratings were defined using i-line 5x stepper lithography, and etched using an inductively-coupled reactive ion etch (RIE) process [103] (for the fine grating features) and a wet chemical etch (for coarser features such as the trench surrounding the grating).

7.2.1 Scanning Electron Microscope Photos

Scanning electron microscope (SEM) photos were taken of the gratings by N. Kim of CPFC during the fabrication of the laser. The tilted view of a single standard grating (L1 referring to Table 5) at various magnifications in Figure 70 shows smooth, vertical, well-defined gratings. The grating periods are consistent over the length scale shown, with no missing or poorly defined grating teeth. The aspect ratio also remains consistent along the length of the grating. These photos indicate a stable, consistent manufacturing process. Measurements of the grating teeth across seven different wafers, taken at all points on the wafer, showed that the cross-wafer uniformity in the grating period was +/- 15 nm. Gratings were measured at the top, bottom, left, right and centre of each wafer, and no particular region of the wafer had greater non-uniformity than others. Omitting one of the wafers that had an unusually large grating period would result in a cross-wafer uniformity of the period of only +/- 6 nm. It is also important to note that the variations from the Bragg wavelength will tend to be consistent for a single grating, resulting in a consistent Bragg period for the laser.

The grating teeth are somewhat rounded, as observed in Figure 70 and confirmed in the detailed grating view of Figure 71. This rounding occurs despite the use of sub-resolution features in the mask as shown in Figure 68. As noted in Chapter 5, higher order gratings that are rounded are not necessarily detrimental compared to rectangular gratings. In this case, however, the rounded tooth shape differs from the shapes that have been studied earlier. The analysis in the next section, using exact measurements of the grating geometry taken from the SEM photos, will examine how this particular rounded grating shape influences the coupling coefficient.

Very fine grating features (near or below the stated resolution of the stepper lithography process) did not always turn out as intended. Such features tended to be 'washed-out' during the etching process. An example of this is the larger duty cycle grating that had

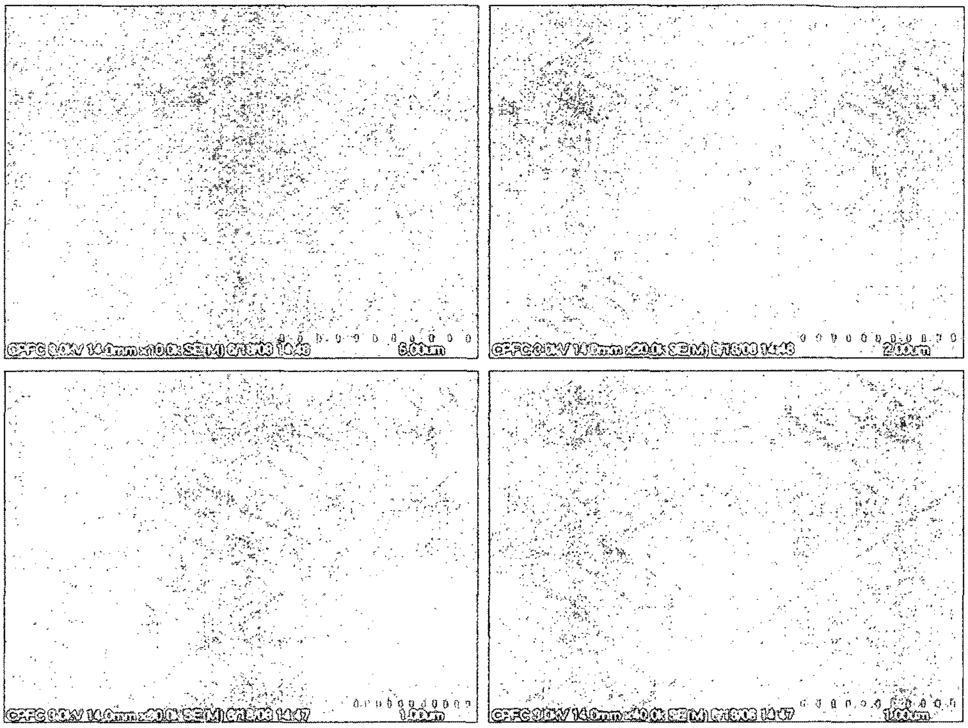

Figure 70. Tilted SEM view of a third-order grating with a duty cycle of 0.5 at various magnifications.

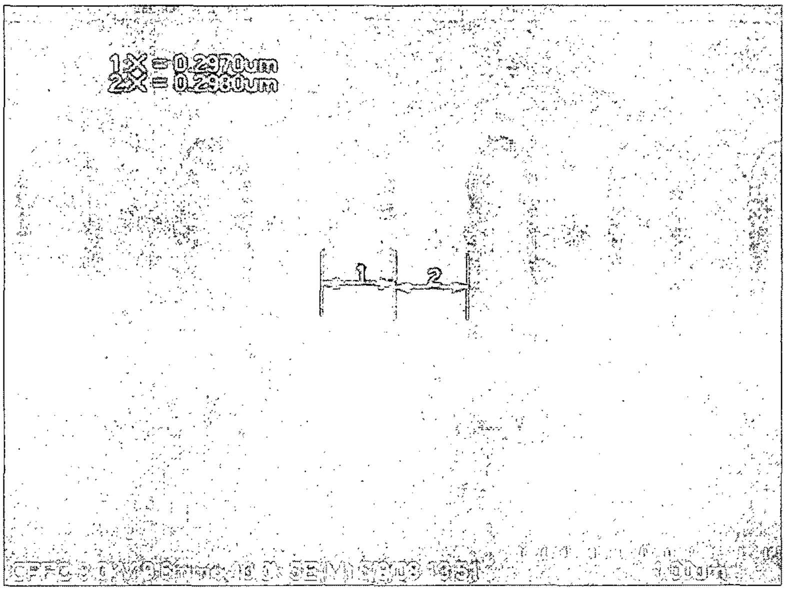

Figure 71. SEM detail of third-order grating with a duty cycle of 0.5

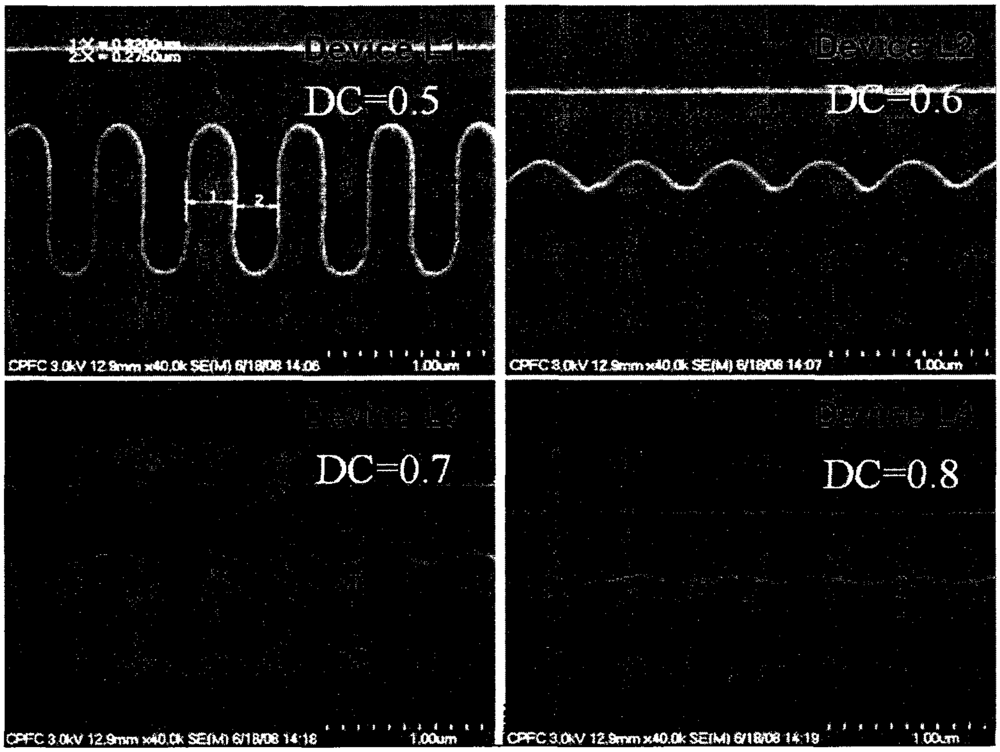

Figure 72. Top view of grating teeth for third-order gratings with increasing duty cycles

small gaps between the grating teeth. Instead of etching all the way through the grating teeth, the teeth are shallower and sinusoidally shaped, as shown in Figure 72. This indicates a catastrophic failure in the lithographic definition using stepper lithography at a duty cycle somewhere between 0.5 and 0.6. For a grating with a duty cycle of 0.8 the grating is almost completely washed out. The shallow, sinusoidal shape of the grating teeth at duty cycles > 0.5 will provide very little coupling, and thus the laser performance is expected to be more like an FP laser than a DFB laser for these devices.

A similar issue to the washing out of higher duty cycle gratings is seen in the phase-shifted gratings since they also require a small gap in the grating teeth in the $\lambda/4$ phase-shifted region. This gap is below the resolution of stepper lithography, and is completely washed out, as shown in the SEM photo of Figure 73. It is apparent that we have again reached the limits of our stepper lithography resolution, as with the higher duty cycle gratings. This will be less detrimental, however, than the entire gratings that were washed out while attempting higher duty cycles. The phase-shift, while not of the desired

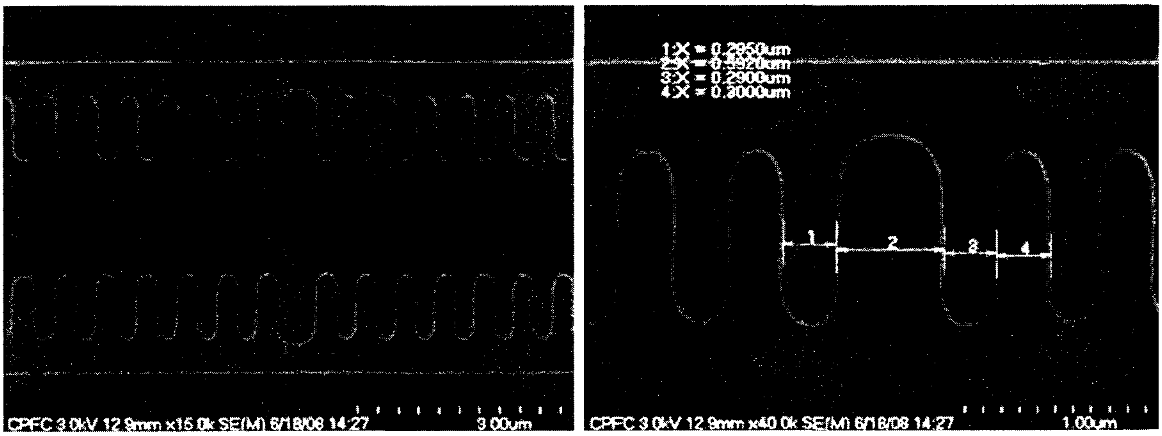

Figure 73. **λ/4 phase-shifted third-order grating**

$\lambda / 4$ length, will still break the symmetry of the grating. The measurements of this phase-shift feature show that it spans approximately half a period (i.e. an entire gap between grating teeth), or a distance of approximately 300 nm. This corresponds to a phase-shift of 0.23λ instead of the 0.25λ that was attempted. Although this is not the ideal case, it is still sufficient to produce a symmetry-breaking phase jump.

SEM photos of the ridge width variations reveal further fabrication imperfections that will impact the grating strength. Measurements from these photos, shown in Figure 74, show that the gratings intended to have $W_N = 1.5$ μm are instead broadened in the middle, so that $W_N \approx 1.75$ μm. In addition, the intended values of $W_W = 2.5$, 4.5, and 5 μm, have been shortened during fabrication to $W_W = 2.24$, 4.19, and 4.69 μm, respectively. Both of these variations will reduce the effective coupling coefficient, as demonstrated from Figure 35 and Figure 36. While only a single picture of these dimensions was provided, it is likely that these numbers are stable across the wafer, and that either a mask bias correction, or a design bias, could be used in future designs to improve these dimensions.

The side view of the gratings reveals some bowing in the sidewalls of the grating, resulting in non-uniform aspect ratios. The difference between the widest part of the gap, seen halfway up the grating, and the narrowest part of the gap, seen at the bottom of the gap, is 0.31 μm - 0.28 μm = 0.03 μm for the grating in Figure 75. This bowing of ~10%

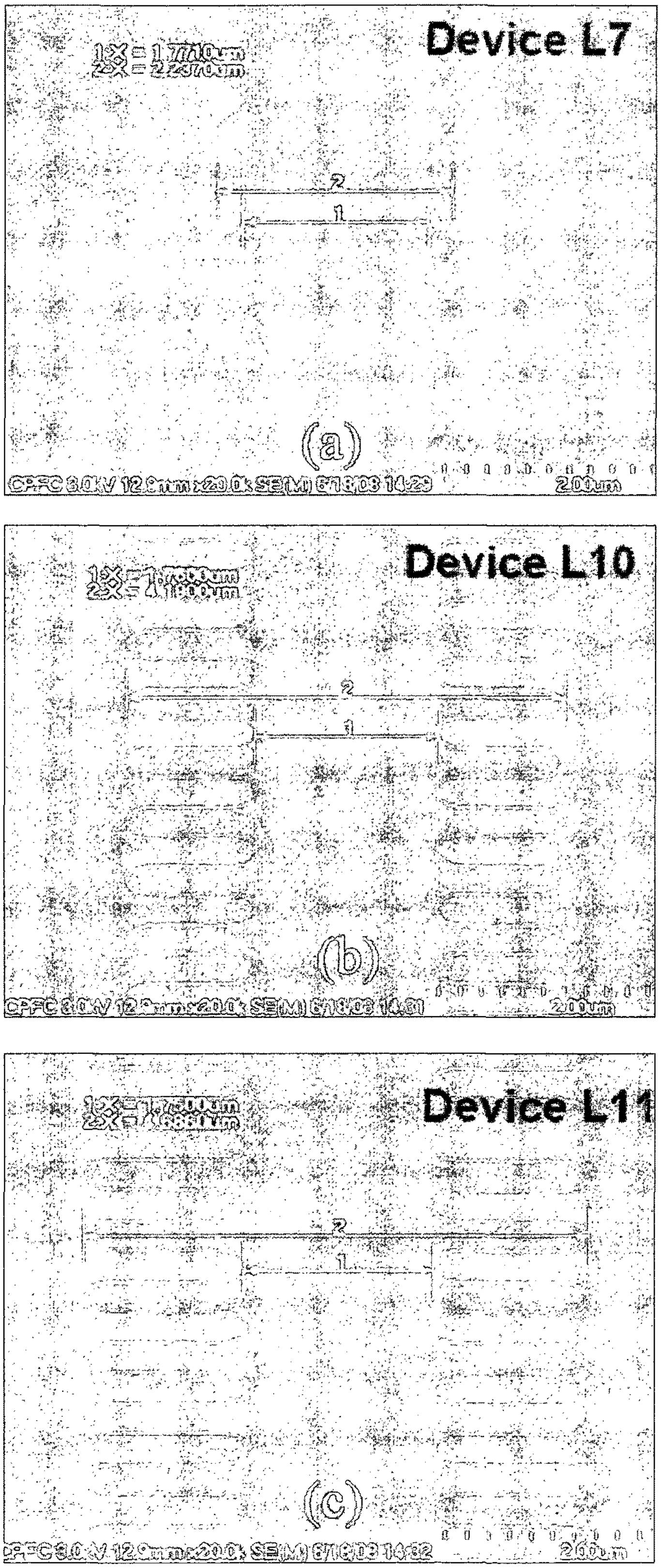

Figure 74. Top view SEM photos of third-order gratings with intended W_N/W_W values of a) 1.5/2.5, b) 1.5/4.5, and 1.5/5 (μm)

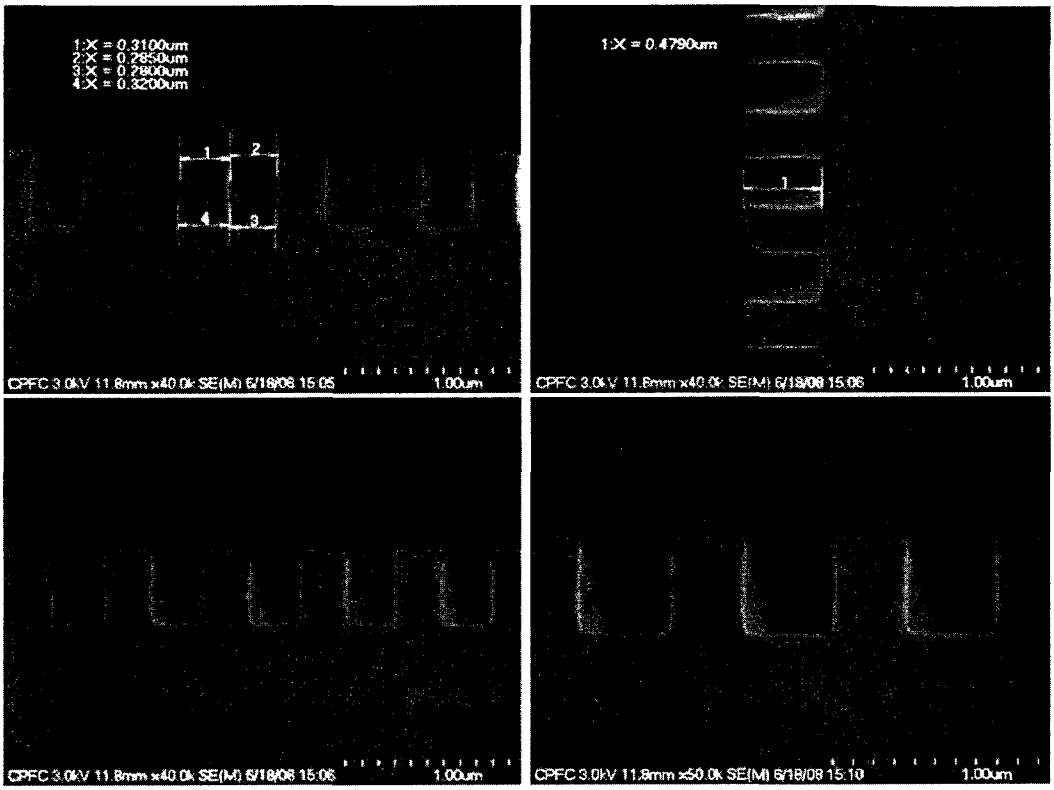

Figure 75. Side views of a third-order grating with a duty cycle of 0.5

will slightly decrease the coupling, but is expected to be a significantly smaller effect than the in-plane rounding of the grating teeth observed in the horizontal direction in Figure 71. The top and bottom surfaces of the grating etch are both nearly flat, with a slight tilt of ~1% with respect to each other observed in some cross-sections. Previous etch runs showed significant etch micro-loading that caused a much larger tilt in the bottom grating surface. Microloading is an aspect ratio dependent etch rate, and causes features with a high aspect ratio (such as the bottom of the grating teeth, where we have very fine features) to have more non-uniformity than features with a low aspect ratio. The etch target was adjusted accordingly in the final fabrication run to produce the much flatter gratings observed here. The laser chips were cleaved into device lengths of 500, 750, 1000, 1250, and 1500 microns. The laser bars were all tested with as-cleaved facets. Figure 76 shows the top view of a 1500 micron cavity length laser. The metal contacts show no noticeable lift-off, and the facet cleave is smooth and straight. Few of the lasers tested showed any visible evidence of cleave damage from above. The best way to see

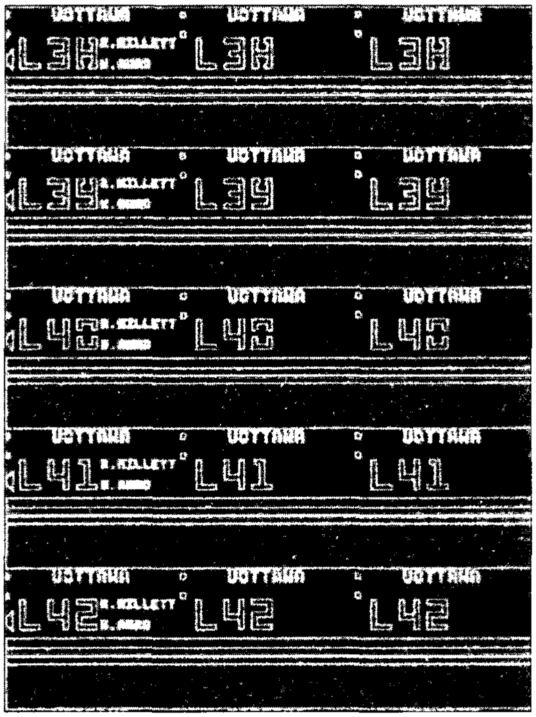

Figure 76. Top view of fabricated LC-DFB lasers L38-L42

the quality of the cleave, however, would be a facet inspection which was not performed for these lasers.

7.2.2 Revised Fourier Coefficients

The fabricated gratings revealed that the rectangular grating shape, assumed in the analysis of Chapter 5 is, in fact, rounded during the manufacturing process, as seen in Figure 71. This grating shape is more accurately modeled with a grating tooth that is elliptical at the grating ends. Using this model the rounded grating shape shown in Figure 77 is defined within a grating period by four parameters, h_1, h_2, h_3, and the duty cycle, γ. The length of an individual tooth is divided into three regions: the upper elliptical portion of length h_1, the middle straight section of length h_2, and the lower elliptical portion of length h_3. Using (4.47) and (4.48), the Fourier coefficients of this grating structure can be determined. The average refractive index will now be x- dependent, and is given by,

$$n_0^2(x)=\begin{cases} n_1^2(1-\gamma)\sqrt{1-\dfrac{(x-h_3)^2}{h_3^2}}+n_2^2\left[1-(1-\gamma)\sqrt{1-\dfrac{(x-h_3)^2}{h_3^2}}\right] & 0<x<h_3 \\ n_1^2(1-\gamma)+n_2^2\gamma & h_3\le x\le h_2+h_3 \\ n_1^2\left[1-\gamma\sqrt{1-\dfrac{(x-h_2-h_3)^2}{h_1^2}}\right]+n_2^2\gamma\sqrt{1-\dfrac{(x-h_2-h_3)^2}{h_1^2}} & h_2+h_3<x\le h_1+h_2+h_3 \end{cases} \tag{7.1}$$

In the limit where $h_1\to 0$ and $h_3\to 0$, $n_0^2(x)$ will reduce to the expression for a rectangular grating given by (4.57). The Fourier coefficients are

$$A_q(x)=\begin{cases} -\left(\dfrac{n_2^2-n_1^2}{\pi q}\right)\sin\left[\gamma\pi q\sqrt{1-\dfrac{(x-h_3)^2}{h_3^2}}\right] & 0<x<h_3 \\ -\left(\dfrac{n_2^2-n_1^2}{\pi q}\right)\sin\left[\gamma\pi q\right] & h_3\le x\le h_2+h_3 \\ -\left(\dfrac{n_2^2-n_1^2}{\pi q}\right)\sin\left[\gamma\pi q\sqrt{1-\dfrac{(x-h_2-h_3)^2}{h_1^2}}\right] & h_2+h_3<x\le h_1+h_2+h_3 \end{cases} \tag{7.2}$$

Once again, these equations reduce to those of the rectangular grating, (4.58), in the limit when $h_1\to 0$ and $h_3\to 0$.

The coupling coefficient for the rounded gratings will be smaller than those of rectangular gratings of the same duty cycle, as seen by comparison between Figure 32 and Figure 78. Similar to the triangular and sinusoidal grating shapes, the rounded grating shape has more optical confinement in the grating region compared to rectangular gratings due to larger n_0 values near the center of the mode. For a third-order grating with W_N/W_W = 1.5/4 (µm) and $\gamma=0.5$, the grating confinement is Γ_{grating} = 0.66% in the rounded grating, compared to Γ_{grating} = 0.36% for a rectangular grating. However, this confinement is smaller than comparable triangular or sinusoidal gratings, and the form of the rounded grating Fourier coefficient results in a lower overall coupling coefficient.

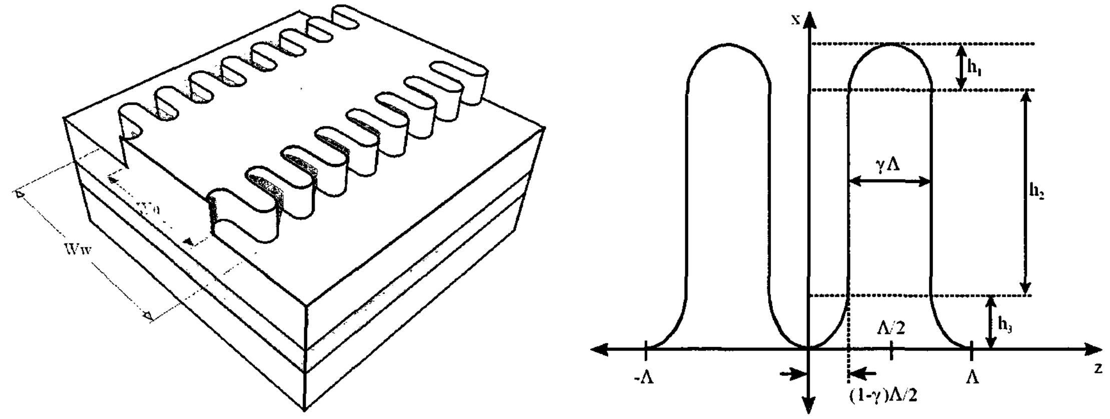

(a) (b)

Figure 77. **(a) Perspective view and (b) detailed tooth dimensions of rounded grating**

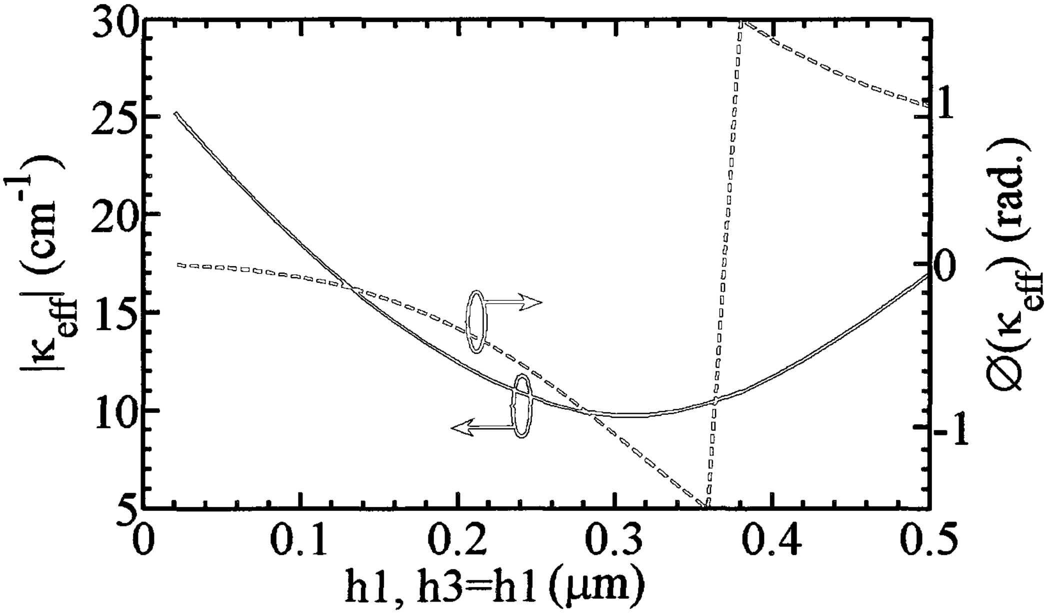

Figure 78. **Effective coupling coefficient *vs.* h_3 for a third-order rounded grating, with $h_1 = h_3$ and h_2 adjusted to maintain W_N/W_W = 1.5/4 μm, and a duty cycle of 0.5.**

The Fourier coefficients are integrated over the grating region, influencing κ_{eff} as previously discussed in Chapter 5. The third-order Fourier coefficients of different grating shapes, including the rounded grating, are shown in Figure 79. This comparison reveals that the most rapid variation from negative to positive values is for the rounded grating case. When these functions are multiplied by the electric field, $\varepsilon_0(x, y)$, which is a positive real value that falls off rapidly towards the lateral edge of the grating (i.e. as x

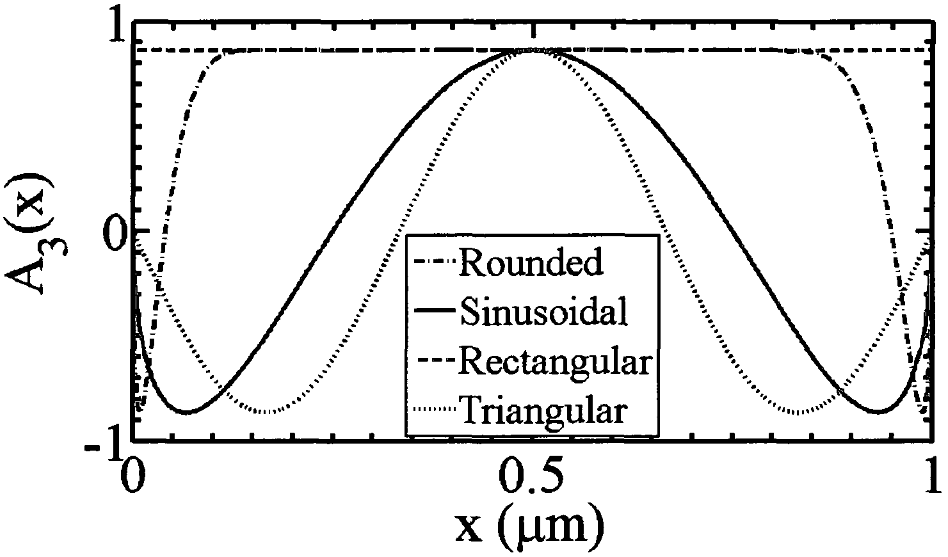

Figure 79. Fourier coefficient $A_3(x)$ for rounded, sinusoidal, rectangular, and triangular grating shapes

increases in this horizontal variation case), the quickly-varying Fourier coefficient of the rounded grating will result in a lower integrated value than for the other grating shapes. This lower integrated value, according to (4.38), results in a much lower κ_p. It is not unexpected then to see that of all the grating shapes examined to this point, triangular, sinusoidal, rectangular, and rounded, the rounded grating provides the weakest coupling. This weaker than expected coupling coefficient will impact the performance of these devices as we will see later in this Chapter.

In Figure 80, the effect of grating rounding on the longitudinal mode solutions is shown. Figure 80 shows the variation in a) $(\alpha L)_{\min}$, b) $(\delta L)_{\min}$, c) NGD, and d) flatness with grating rounding and length. From a), we see that there are minimum cavity lengths to reduce the amount of threshold gain required. When the grating rounding is small, i.e. $h_1 = h_3 \to 0$, and when the grating rounding is larger, i.e. more sinusoidally shaped, i.e. $h_1 = h_3 \to 0.5$, the threshold gain is minimized. In Figure 80b, we see that the Bragg frequency detuning decreases nearly linearly for all cavity lengths, from a maximum in the fully rounded case to a minimum in the rectangular grating case. From Figure 80c, we observe that the NGD increases for all cavity lengths as the grating rounding

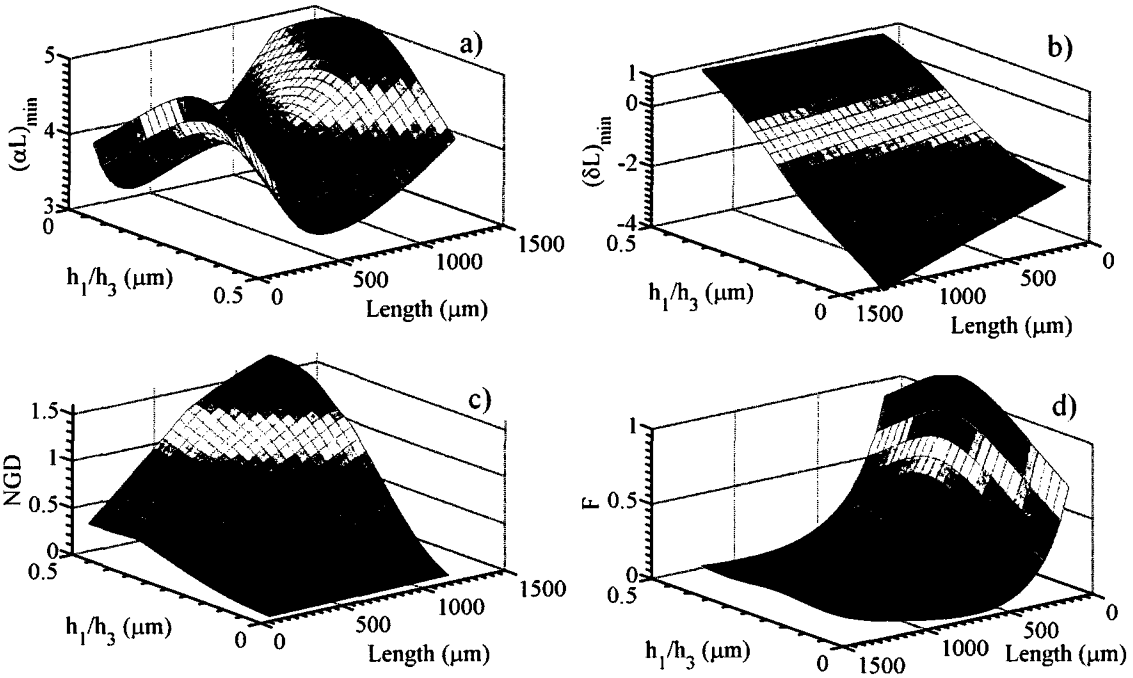

Figure 80. Characteristics of LC-DFB lasers with rounded gratings *vs.* grating rounding parameters h_1/h_3, where h_1=h_3, and cavity length: a) minimum threshold gain, b) Bragg deviation of minimum threshold gain, c) normalized gain difference, and d) optical field flatness.

increases. In Figure 80d, the flatness, *F*, is best at longer cavity lengths and for rectangular gratings with $h_1 = h_3 \to 0$ and rounded gratings with $h_1 = h_3 \to 0.5$.

For future design cycles, it may be desirable to use a lateral sinusoidal grating variation rather than attempt to fabricate a rectangular grating with perfectly sharp corners. The fabrication process seems to favor rounded rather than square grating shapes, so the sinusoidal shape may be easier to manufacture. In addition, it will have significantly better coupling than the rounded gratings, and even sharp rectangular gratings with half duty cycles.

The rounding of the grating was not the only process variation revealed by the SEM photos. To accurately assess the grating strength of the manufactured gratings, exact dimensions were taken from the available SEM photos. For the standard third-order grating, the measured rounding parameters from Figure 72 are h_1 = 0.2 μm, h_2 = 0.59 μm, and h_3 = 0.13 μm. It is assumed that the value of W_N was increased during fabrication from 1.5 to 1.75 μm. This dimension was measured from the SEM photos of Figure 74, but was not systematically measured for all gratings. In addition, the duty cycle was slightly increased from 0.5 to 0.53. The calculated effective coupling coefficient for this revised grating shape is $\kappa_{eff} = 12.2\angle -0.16$ cm^{-1}. This is a significant reduction from the expected value of $\kappa_{eff} = 26.5\angle 0\,\text{cm}^{-1}$ calculated for the standard grating in Chapter 5.

7.3 Measured Laser Parameters

While there are many tests that can be used to characterize semiconductor lasers, for this thesis we have relied on three basic measurements that provide a wealth of data on the laser properties: IV, LI, and optical spectrum. With nearly 1500 individual fabricated lasers, it would be difficult to perform all tests on each laser. Instead, the 750 or so devices that have been tested were heavily weighted to the design variations that had the best performance, such as the third-order grating structures. Only 16 representative devices were measured for a range of temperatures, due to the time-consuming nature of this test. The tests were performed by Kais Dridi and me at the University of Ottawa.

7.3.1 LI Characteristic

The fundamental laser measurement is the LI characteristic, or the optical output power for a given bias current. An example of an LI measurement, showing the relevant parameters to be extracted, is shown in Figure 81. The optical output power is negligible until the laser bias reaches the threshold current, I_{th}. At this point, the carrier injection into the active region is sufficiently high for the optical gain to be greater than the optical losses, and stimulated emission begins to dominate spontaneous emission. Above threshold, the optical power initially increases linearly with the bias current. The threshold current can be determined by the x-intercept of a linear fit of the LI curve just above threshold. The slope of the linear fit is known as the slope efficiency, $\Delta P / \Delta I$, and it is a useful measure of the efficiency of the laser diode. As the bias current increases, the carrier density increases. This results in greater spatial hole burning, and an increase

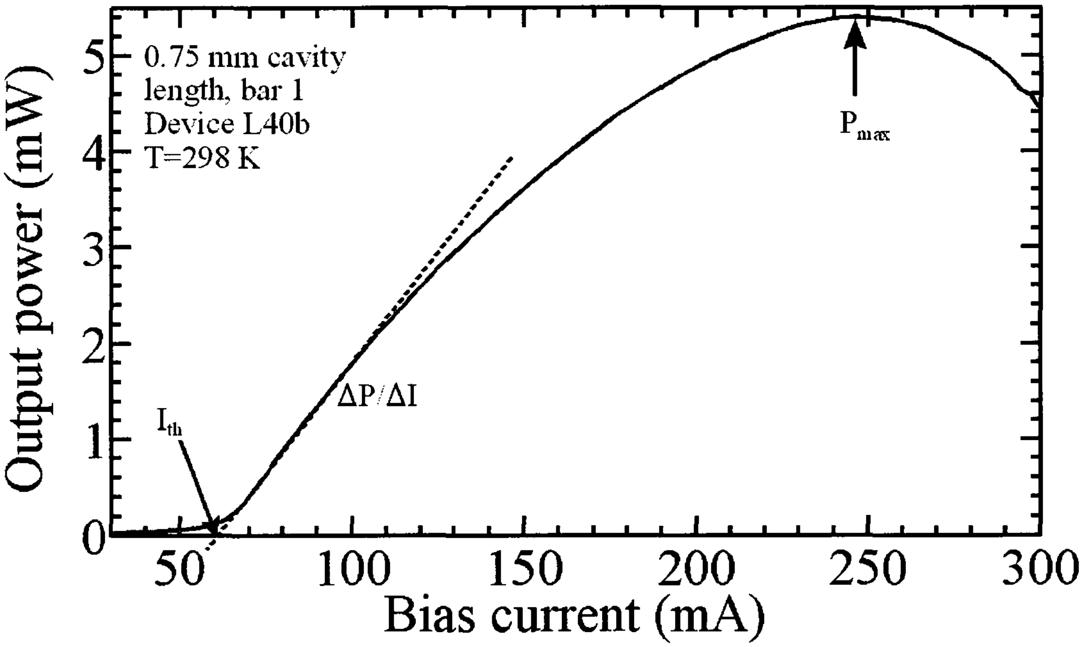

Figure 81. **Typical LI characteristic showing definitions maximum power, P_{max}, threshold current, I_{th}, and slope efficiency, ΔP/ΔI.**

in local temperature within the active region. Thermal roll-off begins to occur, and the slope of the LI characteristic begins to decrease, until finally the maximum output power, P_{max}, is reached. Beyond this point, the output power steadily decreases until catastrophic failure occurs at very high bias currents.

The LI curve of a laser provides a number of useful performance measures beyond the threshold current, slope efficiency, and maximum output power. It also provides information on the quantum efficiency, η, characteristic temperature, T_0, and approximate optical loss of the laser. The quantum efficiency of a laser diode is a measure of how efficiently the laser can convert electrons into photons via stimulated emission. The external quantum efficiency, η_d, can be obtained from the slope of the LI characteristic, $\Delta P / \Delta I$, using [104]

$$\eta_d = \frac{\Delta P}{\Delta I}\left(\frac{q\lambda}{hc}\right), \tag{7.3}$$

where λ is the free-space wavelength, (1.31 μm in this case), while the other constants are q=1.6022 x 10^{-19} C, the fundamental electronic charge, h=6.6262 x 10^{-34} J.s, Planck's constant, and c=2.99 x 10^{8} m/s, the vacuum speed of light.

The characteristic temperature, T_0, is derived from the threshold current as measured at different temperatures. T_0 is a measure of the temperature-dependence of the laser. A laser with a higher T_0 value has a lower dependence on temperature than a laser with a lower T_0 value. To obtain T_0, the threshold current *vs.* temperature characteristic is fitted to the exponential relation for a semiconductor diode given by

$$I_{th} = I_0 \exp\left(T / T_0\right), \tag{7.4}$$

where I_{th} is the threshold current, T is the temperature, and I_0 is the threshold current at 0 K. The I_0 term can be eliminated to obtain an expression for the characteristic temperature in terms of the change in the log of the threshold current, $\Delta ln(I_{th})$, and change in temperature, ΔT [104], as

$$T_0 = \frac{\Delta T}{\Delta \ln(I_{th})}. \tag{7.5}$$

The results of a characteristic temperature calculation are shown in Figure 82, where the natural logarithm of the threshold current has been plotted against the temperature. The error in threshold current of +/- 1 mA is slightly smaller than the size of the points. The data closely follows the linear fit of $\ln(I_{th})=0.025T$ - 3.3 mA, determined with MATLAB using the least-mean-squares (LMS) algorithm. The characteristic temperature, T_0, is the inverse of the slope of the linearly fitted line. For this device, T_0 = 40.05 K.

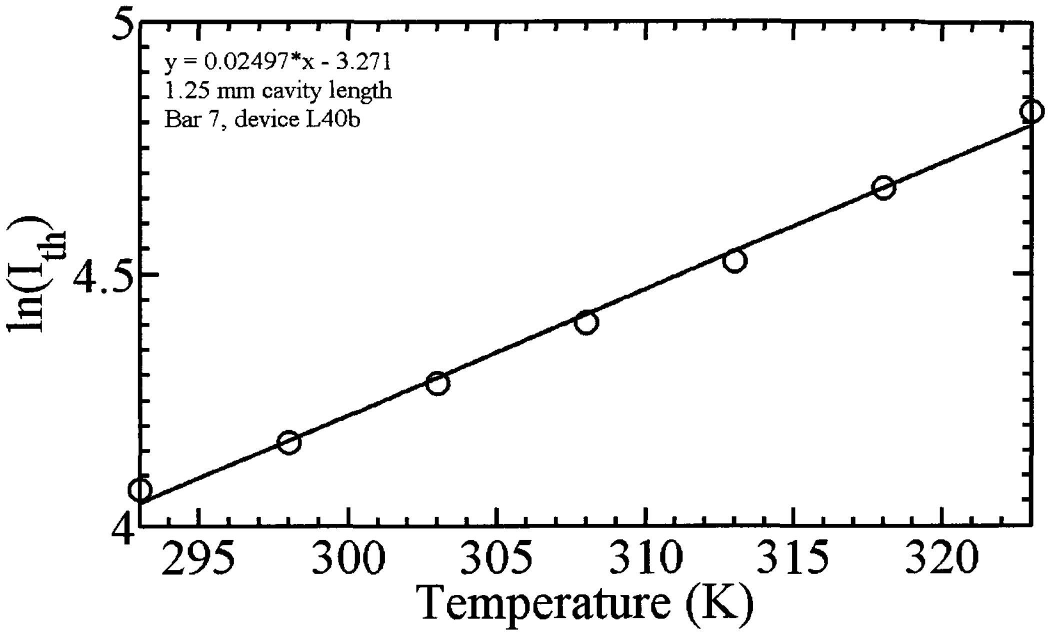

Figure 82. **Natural logarithm of threshold current *vs.* temperature for 1.25 mm cavity length device L40b. Linear fit to data is shown.**

To obtain the LI characteristic, the test setup shown in Figure 83 was used. The bars were placed on a custom-made brass and aluminum sample holder that was mounted on a thermoelectric cooler (TEC) to maintain a fixed operating temperature. There will be some variation between the set temperature of the TEC and the actual laser temperature, since the temperature used by the TEC controller (a Keithley 2510-AT autotuning TEC source meter) for setting the TEC is measured at the left of the holder, while the laser is placed at the right, approximately 5 cm away.

The sample holder was mounted above a Newport XYZ positioner. The light for the LI measurements was measured using a wide-area detector. The wide area detector was calibrated using a 1310 μm JDS Uniphase fixed laser source and a Newport 1830 power detector. The source-meter used was a Keithley 2400. The tests have all been fully automated using Labview software. Since the photodetector saturates at low output powers, a 10 dB attenuating Newport FSQ-ND10 neutral density filter was used.

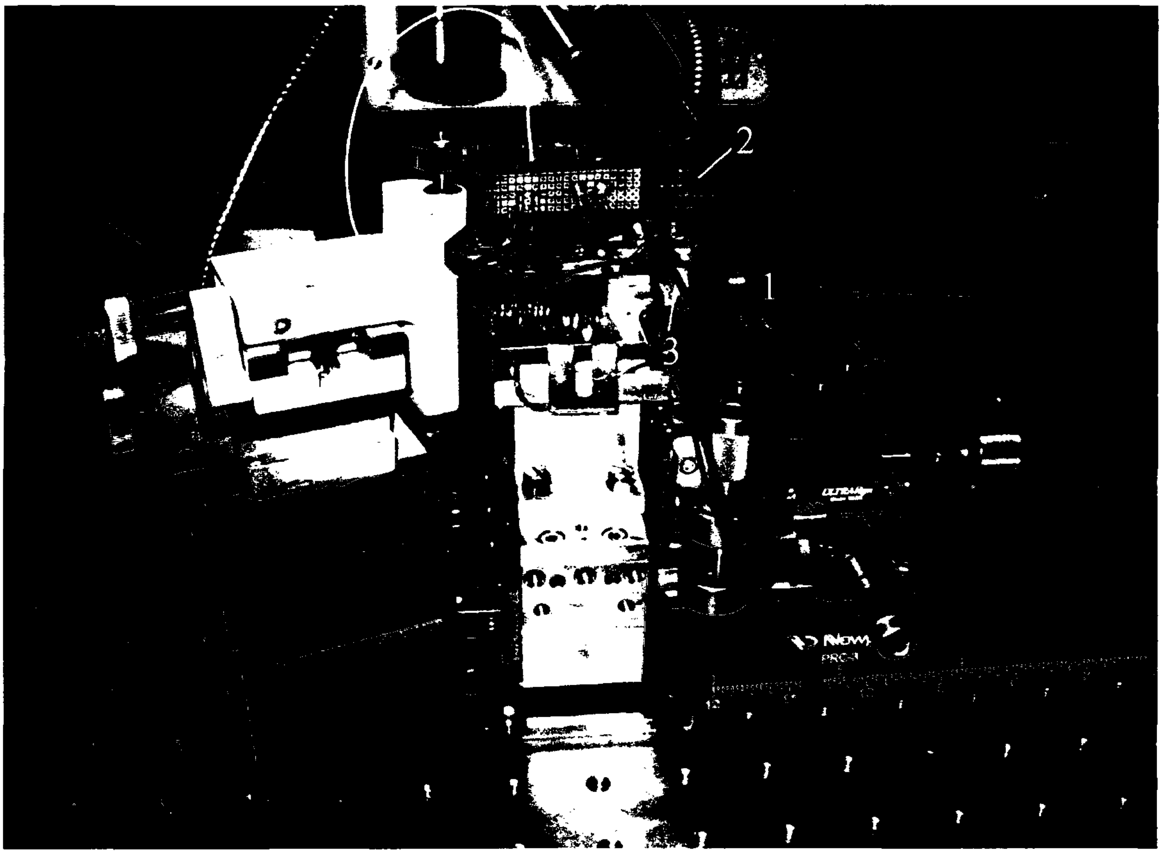

Figure 83. **Test setup for L-I measurements. 1) wide area detector, 2) attenuating lens, 3) bar under test.**

7.3.2 Optical Spectrum

The optical spectrum will clearly indicate successful DFB, rather than FP, lasing operation as the contrast between FP laser spectra and DFB laser spectra illustrated earlier in Figure 1 shows. The FP spectrum is broad, with many peaks and valleys due to the large number of Fabry-Perot modes that are supported. The ideal DFB spectrum, on the other hand, filters out all but a single longitudinal mode, producing a very sharp, spectrally pure peak. The peak wavelength of DFB lasing depends on the Bragg wavelength of the grating, which is independent of the material gain peak, although there must be some gain at the Bragg wavelength to permit lasing. In contrast, the peak wavelength of a FP laser will tend to occur near the material gain peak. Since the material gain is more sensitive to temperature than the Bragg wavelength of the grating, DFB lasers will tend to have a smaller dependence of the wavelength on the temperature and bias current. As mentioned in Section 2.2, the temperature dependence of the peak gain wavelength of a long-wavelength InGaAsP/InP laser is approximately $d\lambda_p / dT = 0.5$ nm/K, while for DFB lasers, the temperature dependence of the wavelength is dominated by the change in the Bragg wavelength, λ_b, due to a change of refractive index with temperature, which is approximately $d\lambda_b / dT$ = 0.1 nm/K [22]. There have been DFB lasers with stable single-mode operation over temperature ranges of > 100 K [21].

The important parameters to extract from the spectral measurements are the peak lasing wavelength, λ_{peak}, and the side-mode suppression ratio (SMSR), as defined in Figure 84. The side-mode suppression ratio is the difference between the power at the peak lasing wavelength and the next highest peak in the spectrum. Smaller SMSR values often indicate poor longitudinal mode discrimination, resulting in mode instability. The optical spectrum can also be used to determine the gain spectra for FP lasers using the Hakki-Paoli method, as will be discussed in Section 7.4. The full-width at half-maximum (FWHM) value is also shown in Figure 84, but the smallest resolution the HP4004 optical

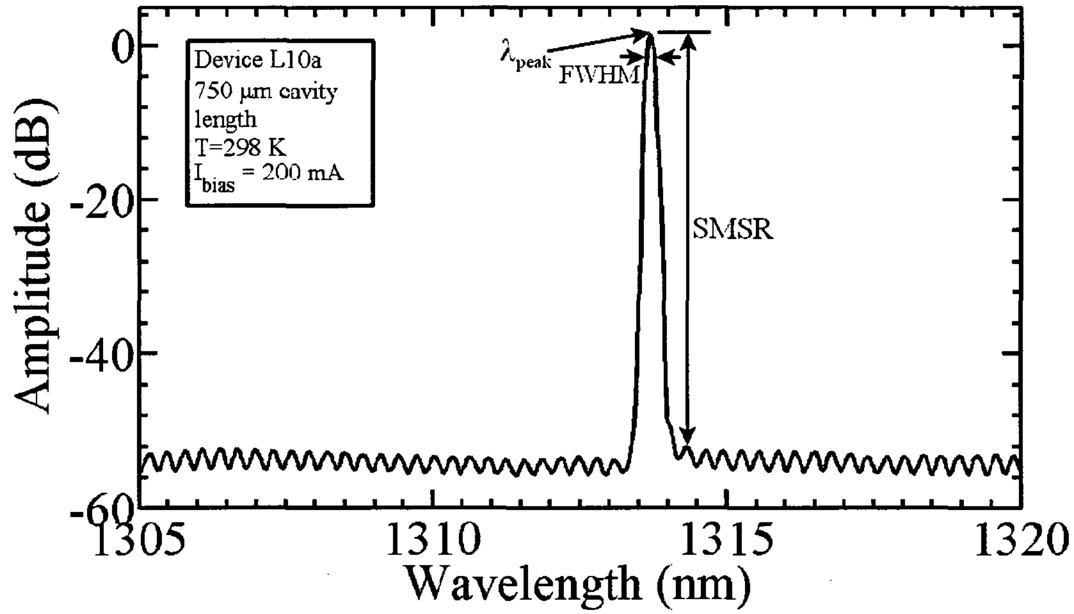

Figure 84. **Spectrum of 750 µm cavity length and W_N/W_W = 1.5/4.5 (µm) ridge width laser at an applied bias of 200 mA and temperature of 298 K, demonstrating peak wavelength, FWHM, and SMSR definitions.**

spectrum analyzer is capable of is 0.08 nm, a value that is too large to properly measure the small width of the FWHM of the DFB spectra.

The test setup for the spectral measurements uses the same custom bar holder as the LI (and IV) measurements. For the spectral measurements, the light is collected using a JDS Uniphase lensed fiber and input to a Hewlett-Packard 4004 optical spectrum analyzer. Due to the greater alignment sensitivity of the lensed fiber compared to the wide-area detector, the fiber is mounted on a Melles-Griot piezoelectric positioner that is capable of nanometer scale accuracy. The fiber is aligned using the piezoelectric controller before the the optical spectrum is captured using LabView software. The spectrum for a range of bias currents can also be captured using an automatic LabView routine to produce two-dimensional plots such as the representative ones in Figure 85. These plots give information on the bias-dependent stability of the DFB lasers. In Figure 85a, we see a non-functioning DFB laser. Only the amplified spontaneous emission spectrum

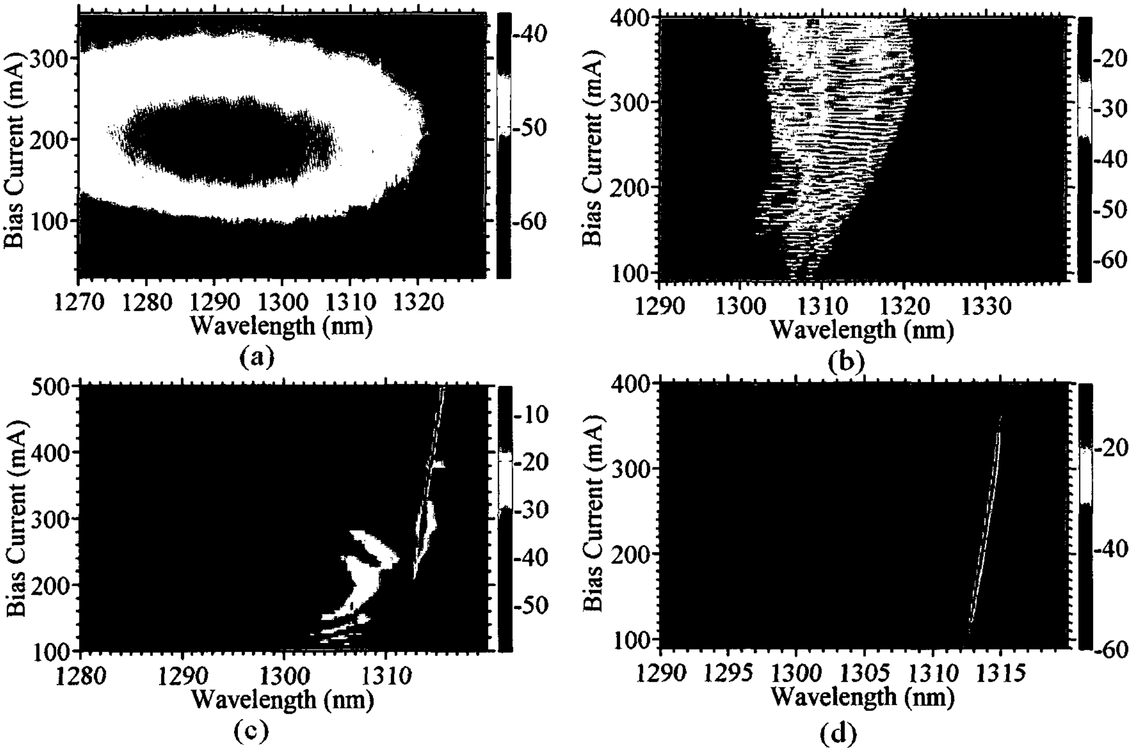

Figure 85. Examples of optical spectra for a range of bias currents. a) a damaged DFB laser, b) a Fabry-Perot laser, c) a conditionally-stable DFB laser, d) a stable DFB laser.

is observed, with some filtering near the Bragg wavelength showing that the grating is still operating as expected. Figure 85b shows a Fabry-Perot laser spectrum for comparison. Its broad spectrum becomes yet broader, and red-shifted, as the bias current increases. Figure 85c shows a conditionally stable DFB laser. In such lasers, DFB lasing occurs, but only at particular bias currents. In these lasers, the peak wavelength of the material gain is often too low to produce DFB lasing at the Bragg wavelength. The peak is red-shifted as the bias current increases until it overlaps sufficiently with the Bragg wavelength of the grating for DFB lasing to occur. Other DFB lasers showed stable DFB lasing for all bias points, such as the one shown in Figure 85d, although more than one longitudinal mode may occasionally be supported.

7.3.3 IV Characteristic

The current-voltage (or IV) characteristic of a laser diode provides an indication of the electrical quality of the p-i-n junction and metal contacts. An ideal laser diode will have all electrical carriers that are injected from the metal contacts collect in the active region, where they can contribute to the optical gain. In reality, some carriers will be trapped in other layers or be spread laterally into regions where the optical mode is vanishingly small, and hence will not contribute to the gain. The IV characteristic can help reveal how efficiently carriers are injected into the structure, but not whether all of these carriers necessarily going to the active region. Additional tests are required to measure the overall efficiency of a laser diode and the effects of additional carrier losses such as lateral current spreading.

A typical laser diode IV curve is shown in Figure 86. The current flowing through the p-i-n junction is negligible until the forward-biased turn-on voltage is reached. In the case of Figure 86, the turn on voltage is 0.9 V. Above the turn-on voltage, the current increases exponentially with voltage. The dynamic resistance of the laser diode is the slope of the IV curve, $R = \Delta V / \Delta I$. The laser diode in Figure 86 has a dynamic resistance of $R < 5$ ohms when the bias current is > 300 mA. A typical operating region

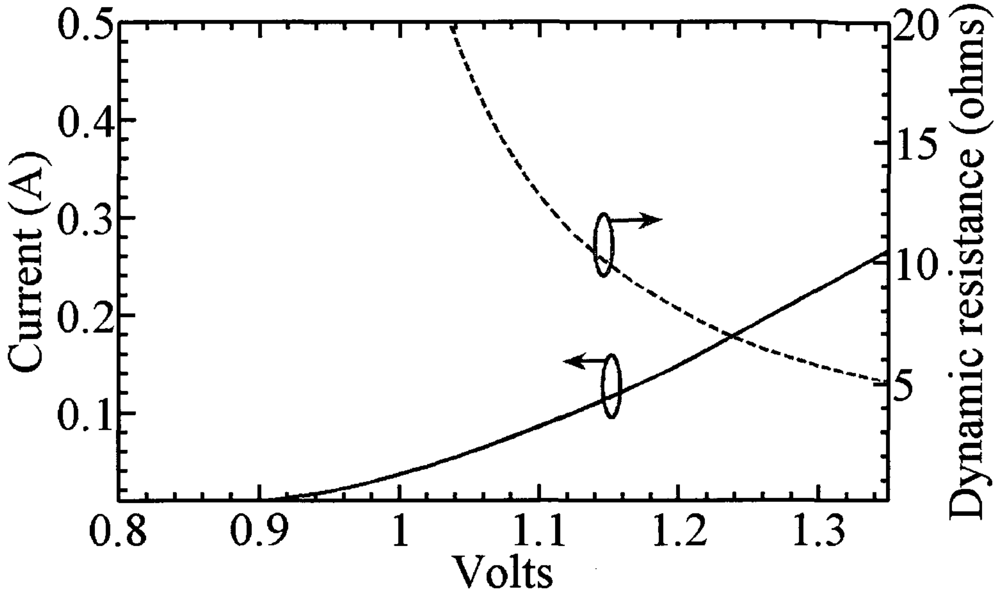

Figure 86. **Bias current and dynamic resistance *vs.* voltage for 1500 μm cavity length device L27 at a temperature of 298 K.**

for this laser is from 100 to 200 mA. In this region the dynamic resistance shown in Figure 86 varies from 12 ohms at 100 mA to 6 ohms at 200 mA. A laser diode with a low dynamic resistance will have less heating, and more overall carriers injected into the active region, resulting in a lower threshold current and better efficiency.

The IV characteristic is a simple measurement that requires only a source-meter. Either the test setup for the LI characteristic, or optical spectrum, discussed above, can be used to obtain the IV characteristic. The device is contacted with a needle probe on the upper p-contact, while the brass holder on which the device rests forms the n-contact since it is in contact with the metallized bottom surface of the laser. A Keithley 2400 SourceMeter was used for these measurements.

7.4 Fabry-Perot Lasers

There were two Fabry-Perot laser test structures defined on the mask - one with a ridge width of 1.5 μm, the other with a ridge width of 4 μm. These test structures are useful in determining the optical quality of the wafer through measurements of the gain, loss, characteristic temperature, and efficiency. The results for the FP laser measurements are tabulated in Table 6, and will be discussed in more detail in this section. As will be shown, there are several simple formulas that can be used to estimate the internal and external quantum efficiencies from the threshold current values of FP lasers of various lengths. The optical gain spectrum can also be extracted from the below-threshold amplified spontaneous emission spectrum, since in the DFB lasers the presence of the grating complicates these calculations. FP test structures can also be used to help calibrate future LAS2D calculations, and to define the extremes of the electrical properties of the DFB lasers. Compared to the DFB lasers, the narrow ridge FP laser is expected to have a higher dynamic resistance, and the wide ridge FP laser is expected to have a lower dynamic resistance. The lowest resistance in general was 5.6 ohms for a 1500 μm long Fabry-Perot laser with a ridge width of 4 μm. There were a total of 60 Fabry-Perot test structures, with both 1.5 and 4 μm ridge widths that were fabricated and cleaved, of these, 42 demonstrated lasing with reasonable output power.

The average threshold current densities of the Fabry-Perot lasers are plotted *vs.* the inverse cavity length in Figure 87. The error bars indicate the standard deviation of the data for each inverse cavity length. This characteristic has been fitted to a linear equation using the least-mean-squares algorithm. There is considerable variation from the linear fit in the threshold current density, particularly for the 1.5 μm ridge width lasers, where the norm of the residuals (i.e. the maximum deviation of the data points from the fitted line) is 1244. In comparison, the norm of the residuals is 264 for the 4 μm ridge width laser. The intercept of the fitted line with the J_{th} axis is the transparency current density, J_0, an indication of the quality of the semiconductor wafer that is independent of the laser geometry. The value of J_0 is 160 +/- 200 A/cm^2 as calculated from the 1.5 μm ridge

Cavity length/bar	Ridge width (μm)	Threshold current (mA)	Slope efficiency (mW/mA)	Maximum power (mW)
500/1	1.5	62	0.139	12.68
	4	68	0.185	19.3
500/11	1.5	55	0.100	5.44
	4	55	0.172	16.07
	4	74	0.081	5.81
500/12	1.5	56	0.084	5.19
	4	56	0.181	14.54
750/1	1.5	62	0.075	5.40
	1.5	39	0.230	39.99
	4	68	0.142	15.98
	4	60	0.146	12.28
750/6	1.5	51	0.192	18.38
	4	72	0.128	11.32
	4	84	0.124	12.34
1000/4	1.5	44	0.198	NA
	4	83	0.116	21.63
	4	85	0.121	NA
1000/6	1.5	43	0.191	NA
	4	82	0.110	NA
1000/12	1.5	45	0.216	46.30
	4	88	0.143	17.1
1000/16	1.5	45	0.219	43.50
	4	86	0.109	14.77
1250/1	4	129	0.086	12.48
1250/4	1.5	56	0.160	35.53
	4	110	0.101	16.58
	4	109	0.066	11.43
1250/7	1.5	54	0.171	46.90
	1.5	61	0.161	33.60
	4	104	0.103	15.63
	4	102	0.064	14.90
1250/10	1.5	55	0.147	35.20
	4	102	0.108	22.8
1500/3	1.5	61	0.144	38.99
	1.5	107	0.071	12.93
	4	116	0.070	13.40
1500/6	1.5	65	0.150	NA
	4	109	0.100	NA
1500/9	1.5	61	0.151	42.00
	1.5	80	0.106	19.33
	4	109	0.097	23.89
	4	108	0.124	21.59

Table 6. Summary of Fabry-Perot laser performance.

width characteristic, and 1300 +/- 50 A/cm^2 as calculated from the 4 μm ridge width characteristic. The deviation from linearity of these measurements is likely due to self-heating at higher threshold current densities. One way to check this, if the equipment is available, would be to redo these measurements using pulsed current sources. The short

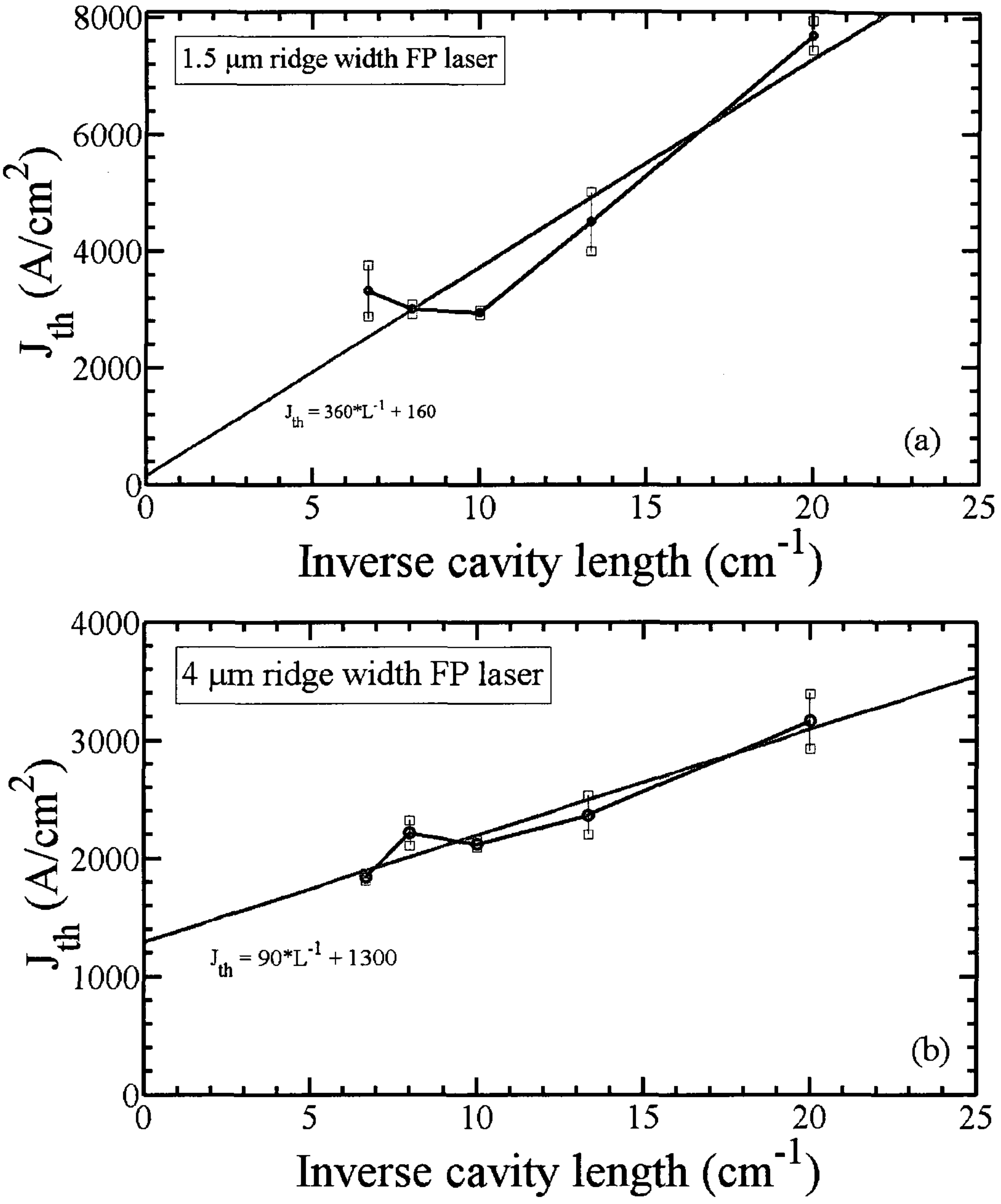

Figure 87. **Threshold current density *vs.* inverse cavity length for a) 1.5 μm ridge width, and b) 4 μm ridge width Fabry-Perot lasers, with linear fit.**

'on' timeframe of the current pulses would reduce the impact of self-heating on the results. Since the wider ridge width FP laser has half the current density of the 1.5 μm ridge width laser, the influence of self-heating is smaller, suggesting that the value of J_0 = 1300 A/cm^2 is more accurate. The deviations for longer cavity length lasers may also be due to these lasers being cleaved from near the edge of the wafer, resulting in a shifted

PL peak compared to other devices. This will be discussed in more detail later in this Chapter.

The threshold currents observed are significantly higher than expected from the LAS2D simulations of the 500 μm cavity length FP lasers of Chapter 3. These simulations predicted a threshold current of 8.3 mA for a 3 μm ridge width design, while the average experimental threshold current was 58 +/- 2 mA for the 1.5 μm ridge width lasers and 62 +/- 4 mA for the 4 μm ridge width lasers. A smaller ridge width was used for the original LAS2D calculations, so a direct comparison would require that these simulations be redone for a 1.5 and 4 μm ridge width laser. However, it is reasonable to suppose that the threshold current for a 3 μm ridge width would fall between the 1.5 and 4 μm ridge width value. The maximum slope efficiency, calculated by LAS2D as 0.33 mW/mA, has an average measured value of 0.094 mW/mA and 0.12 mW/mA for the 1.5 μm ridge width and 4 μm ridge width lasers, respectively.

Some discrepancy between the simulation and experimental results is to be expected, since many of the LAS2D parameters noted in Table 2 are empirical values that must be calibrated using experimental data. However, the large inconsistency between simulation and experiment suggests that more than fine-tuning of the model parameters is necessary. The marked discrepancy suggests a major source of optical loss or carrier recombination that is not properly accounted for in the LAS2D model. The most likely candidate for this unaccounted loss lies in the model that LAS2D uses for the metal contacts. In a standard Fabry-Perot laser design, ridge heights are at least 1 μm in height, making the overlap of the optical mode with the upper metal contact negligible. The grating etch depth was limited by the manufacturing process to < 0.5 μm. This results in an optical mode that is much closer to the upper metal contact layer, and the overlap of the mode with this layer is no longer negligible. Metal layers, as seen in Section 5.6, are very lossy, so any overlap with these contact layers can greatly increase the overall modal loss. LAS2D does not, by default, calculate the losses of the metal contacts, treating them only as ohmic contact boundaries in the electrical model. The value of optical loss calculated in Section 5.6 including the metal layers was $\alpha_i = 25\ \text{cm}^{-1}$, while LAS2D calculated only $\alpha_i = 7.5\ \text{cm}^{-1}$. While it is not within the scope of this thesis, when revisiting the LAS2D model to fit these experimental results, it will be necessary to account for this loss. This could be accomplished by either using a higher loss factor (i.e. by either changing the 'fap' or 'fgain' terms in the model, as defined in Table 2) due to the metal layer, or to construct a metal contact layer in the LAS2D simulation with an appropriate permittivity value. In either case, it is critical to account for the lossy metallic layers to accurately predict the performance of these lasers. In Section 7.9, we will also discuss an alternative LC-DFB laser design that can be used to minimize these metal contact losses.

We can provide very rough estimates of the optical losses of the FP lasers using the external quantum efficiency values calculated for several different cavity lengths. The inverse external quantum efficiency of the FP lasers for different cavity lengths is shown in Figure 88 for different cavity lengths. Fabry-Perot lasers follow the relation [104]

$$\frac{1}{\eta_d} = \frac{1}{\eta_i}\left[1 + \frac{\alpha_i}{\ln(1/R)} L\right], \tag{7.6}$$

where R is the facet reflectivity. If this relation is plotted as a $1/\eta_d$ *vs.* length characteristic, the intercept of this line with the $1/\eta_d$ axis in will give the inverse internal quantum efficiency, $1/\eta_i$, while the slope of this line is proportional to the optical loss, α_i.

The $1/\eta_d$ *vs.* length characteristic, shown in Figure 88a, is non-linear for the 1.5 μm ridge width laser, preventing an accurate fit to the data. It is often the case that this graph has high scattering of the data points due to microstructural differences in the lasers, and non-uniform injection in the longest cavity length lasers [104]. In addition, the self-

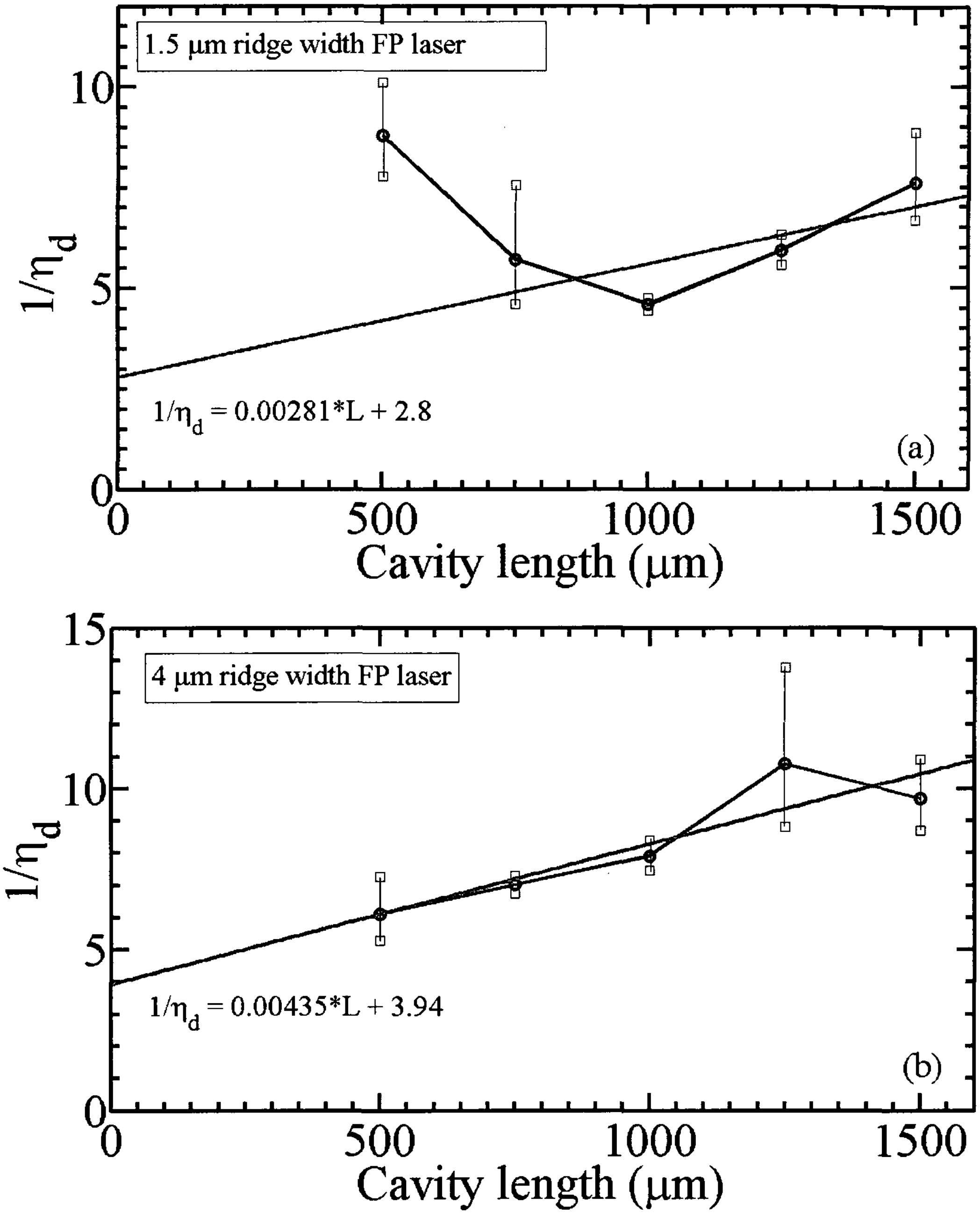

Figure 88. **Inverse external quantum efficiency *vs.* cavity length for a) 1.5 μm ridge width, and b) 4 μm ridge width Fabry-Perot lasers, with linear fit (red line).**

heating that occurs under continuous operation can have a detrimental effect on the measurements, with pulsed measurements being preferred. However, these measurements can still be used for very rough estimations of the loss and internal quantum efficiency. If the smallest cavity length values with the greatest self-heating effect, are neglected, the linear fit shown in Figure 88a is obtained. This linear fit indicates an internal efficiency of η_i = 0.357 +/- 0.14, still a highly uncertain result, even after neglecting the most non-linear values. The 4 μm ridge width FP laser has a much more linear $1/\eta_d$ *vs.* length characteristic, as seen in Figure 88b. The internal efficiency calculated using this laser is η_i = 0.254 +/- 0.07. These values indicate poor internal quantum efficiency, in other words, relatively few carriers are being converted into photons within the laser.

There is also a large difference in the slope of the linear fit between the two FP laser types, with the 1.5 μm ridge width laser having a significantly smaller slope of 0.0028 μm^{-1}compared to 0.0044 μm^{-1} for the 4 μm ridge width laser. It is assumed that the $\ln(1/R)$ term is the same for both lasers, with R = 0.3. Since both FP lasers were adjacent to each other on all of the bars, they should have nearly identical facet reflectivities. This results in a large difference in the calculated optical loss for the two lasers. The 1.5 μm laser had a calculated optical loss of α_i = 18.0 cm^{-1}, while the 4 μm laser had an optical loss of α_i = 37.3 cm^{-1}. This method relies on consistent lasers for different laser cavity lengths, however, there was considerable variation between bars of different cavity lengths. In particular, some of the longer cavity length bars were cleaved near the edge of the wafer, resulting in poorer quality MQW active regions with photoluminescence peaks near 1250 nm rather than 1310 nm. This may account for the larger variation in slope efficiencies at the longer cavity lengths, particularly for the 4 μm ridge width laser. In any case, despite the wide variation in the internal loss that was calculated, the value of 18.0 – 37.3 cm^{-1} is significantly higher than the value determined by LAS2D of α_i=7.5 cm^{-1} near threshold, but consistent with our calculated value of 25 cm^{-1} for the optical loss. This lends support to the hypothesis that additional loss mechanisms, such as the proximity of the metal contacts, are responsible for the anomalously large threshold currents observed.

The optical spectra for a 1 mm cavity length FP laser with a ridge width of 1.5 μm at three different temperatures for an applied current of 70 mA is shown in Figure 89. The optical spectrum was measured using the equipment mentioned in Section 7.3.2. These spectra show broad and numerous peaks due to the large number of Fabry-Perot modes supported by the laser cavity. At an applied current of 70 mA, the peak lasing wavelength of this FP laser changes from 1310.6 nm to 1326.6 nm when the temperature is increased from 298 to 323 K, a change of 0.65 nm/K. The red-shift in the gain peak with increasing temperature is due to bandgap shrinkage [105]. The spectrum also broadens as the temperature increases, as a result of the Fermi statistics of the injected carriers. The energy of an injected carrier is related to the temperature, *T*, through the Fermi distribution

$$\begin{aligned} f_n(E) &= \frac{1}{1+\exp\left[\left(E-F_n\right)/k_BT\right]} \\ f_p(E) &= \frac{1}{1+\exp\left[\left(F_p-E\right)/k_BT\right]} \end{aligned} \tag{7.7}$$

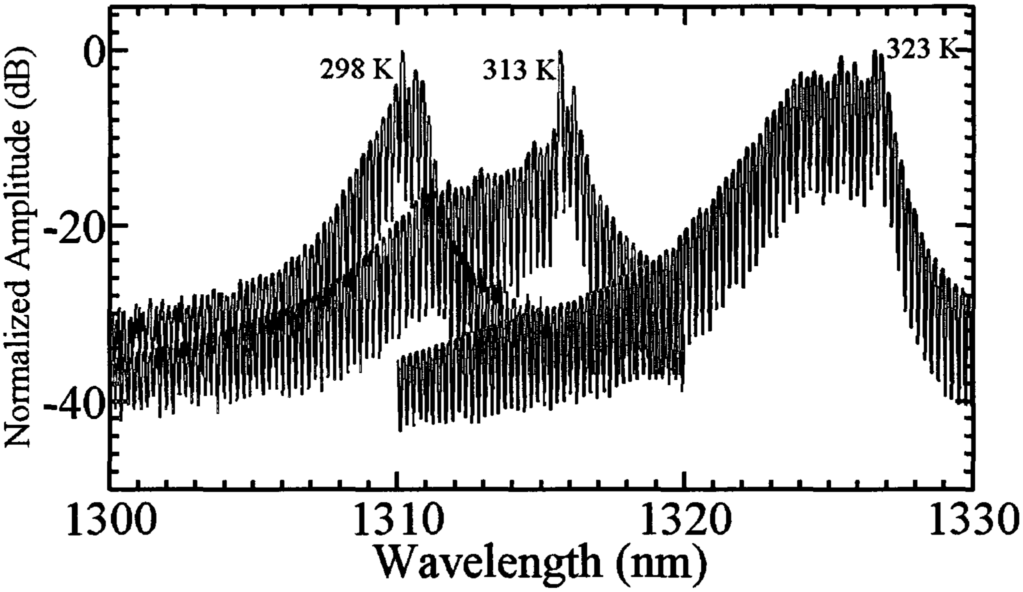

Figure 89. Spectrum of a) Fabry-Perot lasers with a ridge width of 1.5 μm and a cavity length of 1 mm at a bias current of 70 mA and temperatures of 298, 313, and 323 K.

where $F_{n\,(p)}$ is the electron (hole) quasi-Fermi level, and k_B is Boltzmann's constant. As the temperature increases, the carriers become more diffusely spread with energy, E. This allows a broader range of wavelengths to experience optical gain, resulting in the corresponding broadening of the optical spectrum in Figure 89 with higher temperatures.

The characteristic temperature of a narrow ridge Fabry-Perot laser was calculated using LI measurements in 5 K increments from 298 K to 323 K. The 1250 μm long laser with a ridge width of 1.5 μm that was tested had a T_0=40.05 K. As a comparison, this is slightly worse than a broad-area six QW compressively-strained InGaAsP laser analyzed by Piprek *et al.* [106], which had a measured T_0 = 55 K at room temperatures. The broader area of this laser, with a stripe width of 57 μm, will make it less sensitive to temperature, and so a lower T_0 compared to this laser is reasonable.

The optical gain spectrum of the epitaxial growth structure, $g(\lambda)$, can be determined from the below-threshold optical spectrum of the Fabry-Perot laser structures using the Hakki-Paoli method [107]. In this method, the modal gain is determined from the contrast ratio of the optical intensity peaks, I_{max}, and valleys, I_{min}, of the amplified spontaneous emission spectrum, using $r(\lambda)$, defined as

$$r(\lambda)=\frac{I_{\max}(\lambda)}{I_{\min}(\lambda)}, \tag{7.8}$$

according to the relation

$$g(\lambda)=\frac{1}{L}\ln\frac{\sqrt{r(\lambda)}-1}{\sqrt{r(\lambda)}+1}. \tag{7.9}$$

In Figure 90a, the amplified spontaneous gain spectrum for two below-threshold currents, 32 and 38 mA, is shown. The magnified view of these curves reveals the individual peaks and valleys of the gain spectrum that are used to calculate $r(\lambda)$. There are some noisy variations in the amplitude, particularly at powers below -70 dBm, near the limit of the sensitivity of the OSA. These variations become more apparent in the calculated modal gain spectra shown in Figure 90b, where at higher temperatures, or where the gain peak drops, the curves are noisier. The modal gain has a peak at 1311 nm at 25 C, with a 3 dB bandwidth of 24 nm. The gain is reduced as the temperature increases, since carriers are more spread out with energy according to Fermi statistics as the temperature increases. The gain is red-shifted as the temperature increases due to bandgap shrinkage, up to a gain peak of 1330 nm measured at 50 C. This shift of 0.76 nm/K demonstrates that the temperature dependence of the FP spectrum, measured above as 0.65 nm/K for a 1 mm long laser cavity, is dominated by the temperature dependence of the modal gain. The difference in the wavelength shift between the gain peak measurement and the lasing peak wavelength is likely due to the change in refractive index with temperature influencing the FP lasing modes, an effect that is not taken to account in these below-threshold ASE measurements.

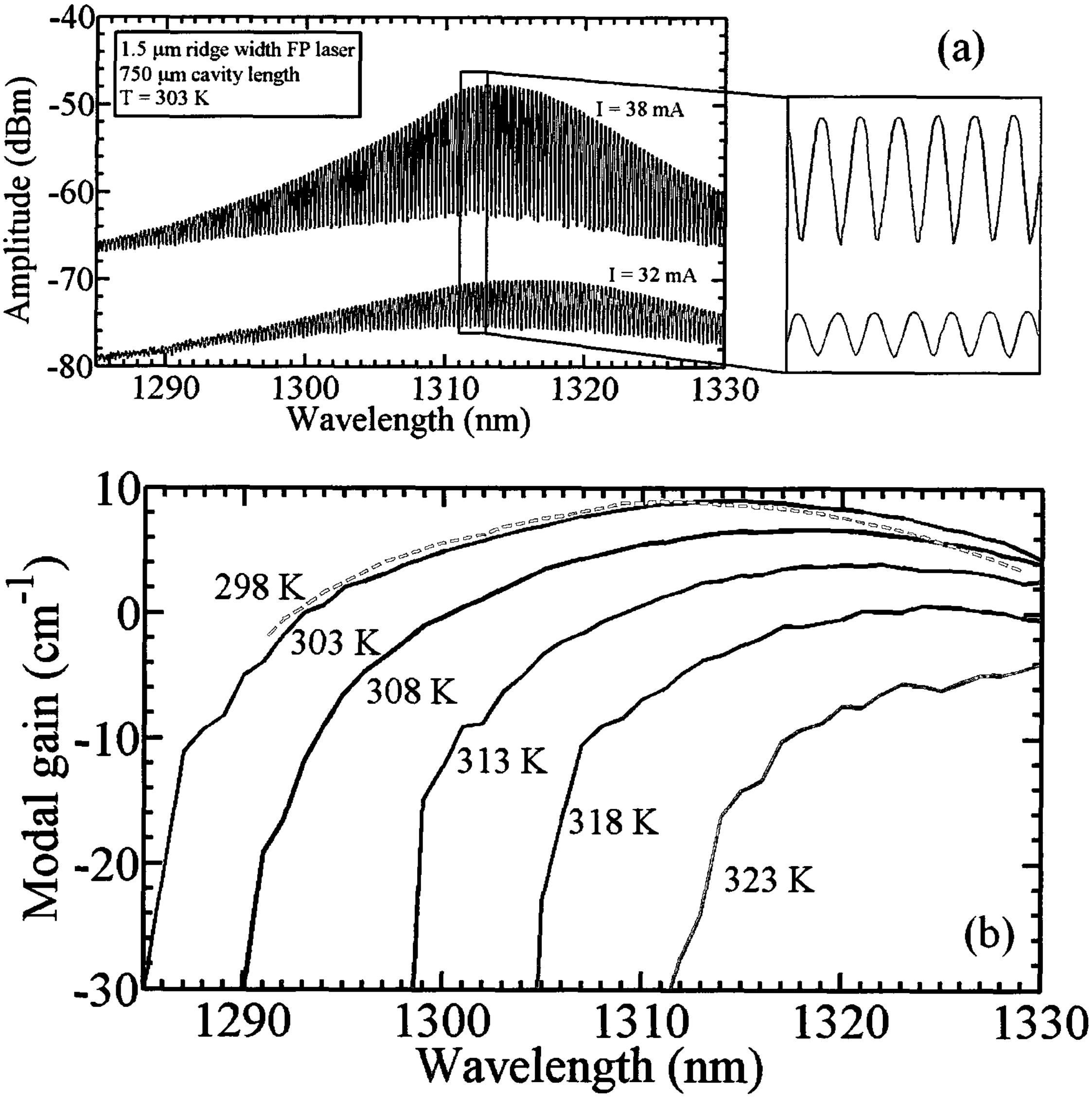

Figure 90. a) Sample of gain measurement using the Hakki-Paoli method; b) modal gain of 4 μm wide ridge Fabry-Perot laser with a cavity length of 750 μm, measured at 298 – 323 K, and a bias current of 38 mA (except for 298 K curve measured at 34 mA).

7.5 Third-Order Grating LC-DFB Lasers

7.5.1 Overall Performance

The third-order gratings are the lowest order that can be fabricated using the 5x i-line stepper at CPFC for a 1310 nm Bragg wavelength. Although we are pushing the limits of stepper lithography for these gratings, SEM photos showed that these gratings can be successfully fabricated, albeit with some rounding of sharp rectangular edges and ridge width variations. In Section 7.2.2 we demonstrated how this grating rounding can decrease the grating strength. This section, presenting the experimental results of the third-order grating LC-DFB lasers, will reveal how this rounding, and other fabrication variations, effects the LC-DFB laser performance. Since the third-order gratings were expected to have better performance than the fourth-order gratings, most of the design variations for the mask were for third-order gratings including the λ/4 phase-shift, duty cycle variation, dual-wavelength gratings, and LC-DFB gratings with different Bragg wavelengths.

A total of 532 of the LC-DFB lasers with third-order gratings were tested, excluding the dual-wavelength designs and those with shifted Bragg wavelength gratings. None of the higher duty cycle gratings showed DFB lasing, for reasons that will be explained in more detail below, so all of the results shown in this section are for half duty-cycle gratings. There was little variation in resistance observed between different devices. At a bias current of 200 mA, the average resistance measured for the third-order DFB devices was 6.4 ohms. The lowest measured resistance was 6.2 ohms for a 1250 μm long device with ridge widths of W_N/W_W = 1.5/5 (μm), while the highest resistance of 6.9 ohms was for a 500 μm long device with ridge widths of W_N/W_W = 1.5/4 (μm). Of the third-order lasers tested, 117 exhibited some DFB lasing, either stable or unstable. Out of these 117 lasers, a total of 82 showed stable DFB lasing for all bias currents, as shown in Figure 85d, for a total yield of stable DFB lasers of 15.4%.

There are two principal reasons for the poor yield of the LC-DFB lasers, both illustrated by, the distribution of all operational DFB lasers with cavity length shown in Figure 91. The first reason is the weakness of the gratings due to the grating rounding and variation in the ridge width. This would explain why the shortest cavity length lasers, 500 μm, have a particularly poor yield, with only five operational devices. Many of the non-operational 500 μm cavity length lasers showed Fabry-Perot-like lasing spectra, but did not have a sufficiently strong grating to produce DFB lasing. The second reason is that many of the bars were cleaved near the edge of the wafer. The edge of a multi-quantum-well wafer often shows unwanted process variations, and this wafer was no exception. Although it is not known where on the wafer the individual bars were cleaved, many of the bars with cavity lengths of 1250 μm and 1500 μm have a visibly rounded edge, indicating that they had come from the edge of the wafer. As a result, most of these longer cavity length lasers had gain peaks near a wavelength of 1250 nm or less, much too far from our desired Bragg wavelength of 1310 nm for any DFB lasing to occur. This issue was particularly prominent with the 1250 μm cavity length bars, where only a single bar showed a gain peak of ~1300 nm. The lower gain peak resulted in virtually a zero

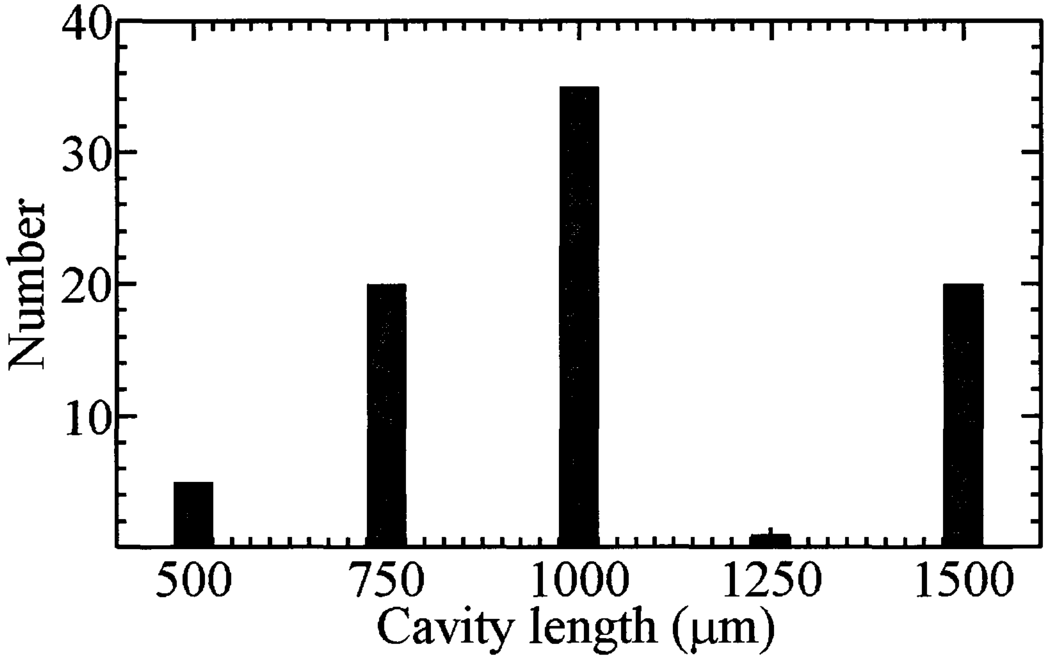

Figure 91. **Distribution of operational DFB lasers with cavity length.**

yield for this cavity length, and a poorer yield for the 1500 μm cavity length lasers than might otherwise be expected. If both of these lowest and highest cavity length lasers are excluded, the yield would be significantly higher. For instance, the yield of the third-order grating devices on 1 mm bars was 51%, with particular design variations showing even better individual yields. Therefore, we conclude that grating rounding and cross-wafer non-uniformity in the material properties, particularly near the wafer perimeter, are the major causes of the lower overall yield.

The threshold currents of the LC-DFB lasers were compared to the Fabry-Perot lasers for the highest yield cavity length of 1 mm. The distribution of threshold currents at this cavity length is plotted in Figure 92a along with the average threshold current of the 1 mm cavity length Fabry-Perot lasers with ridge widths of 1.5 μm (indicated by marker A) and 4 μm (indicated by marker B). The average threshold current of 45 +/- 0.5 mA for the narrow ridge width lasers is significantly smaller than the DFB threshold currents, most of which fall into the range between 85 and 95 mA, with an average of 95 mA. However, the wider ridge width laser is a much better comparison, since the LC-DFB lasers have wide ridge widths that vary from 2.5 to 5 μm. The average threshold current of the 4 μm ridge width FP laser is 85 +/- 1 mA. This is an encouraging comparison, as a significant number of LC-DFB lasers had a lower threshold current than the average FP laser current.

The slope efficiencies of 1 mm cavity length FP and LC-DFB lasers are compared in Figure 92b. The narrow ridge FP laser (indicated by marker A), with an average efficiency of 0.205 mW/mA, has nearly double the efficiency of the wide ridge FP laser (indicated by marker B) with an average efficiency of 0.12 mW/mA. Most of the DFB lasers have efficiencies in the 0.095 – 0.105 mW/mA range, with an average of 0.096 mW/mA. The additional grating loss is the main reason for the somewhat poorer efficiency of these lasers compared to complementary Fabry-Perot designs, and these results show reasonable agreement with the expected results from our quasi-static three-

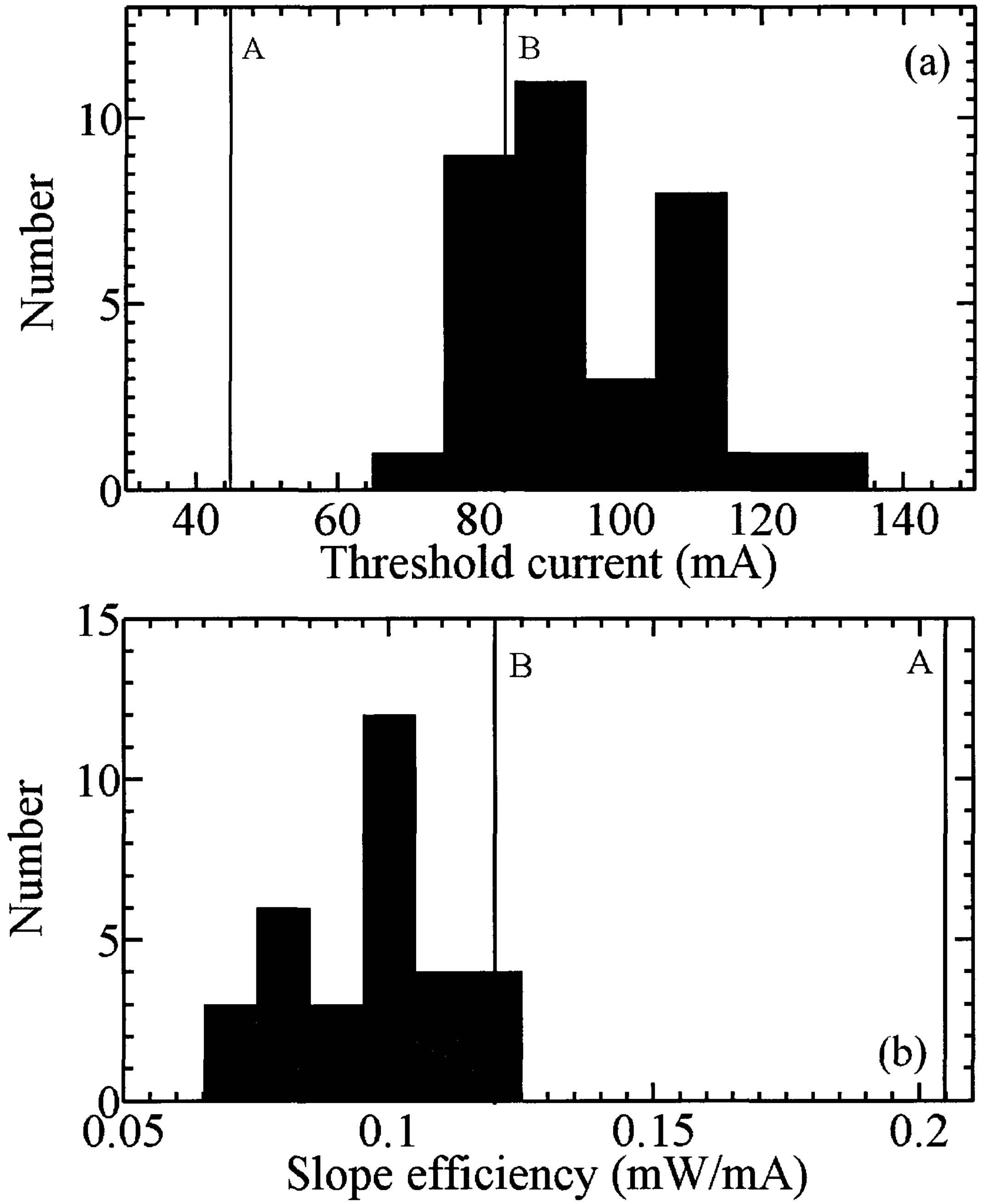

Figure 92. Distribution of a) threshold currents, and b) slope efficiencies for 1 mm cavity length LC-DFB lasers with third-order gratings; lines A and B indicate the average threshold current of the 1 mm cavity length Fabry-Perot lasers with ridge widths of 1.5 and 4 μm, respectively.

dimensional model shown in Figure 66. With only a 20% poorer average slope efficiency, and 12% higher average threshold current, compared to the wide ridge Fabry-Perot laser, the penalty for the additional grating loss is very modest, particularly for the benefit of having a high side-mode suppression ratio. The SMSR values are excellent for the operational DFB lasers, as shown in Figure 93. Nearly all have greater than 40 or even 50 dB of SMSR, even without any additional facet coatings to produce an AR/HR laser cavity.

Overall, the LC-DFB lasers performed well, with an average threshold of 95 mA compared to 85 mA for a 4 μm ridge width FP laser. The threshold currents are higher than expected from the LAS2D simulations due to additional losses, likely because of the proximity of the optical mode to the metal contacts. The LC-DFB lasers had a lower than expected yield due to cross-wafer non-uniformities and rounding of the grating teeth resulting in a weaker grating. The operational lasers demonstrated excellent side-mode suppression ratios of > 50 dB, a value better than many commercially-available DFB

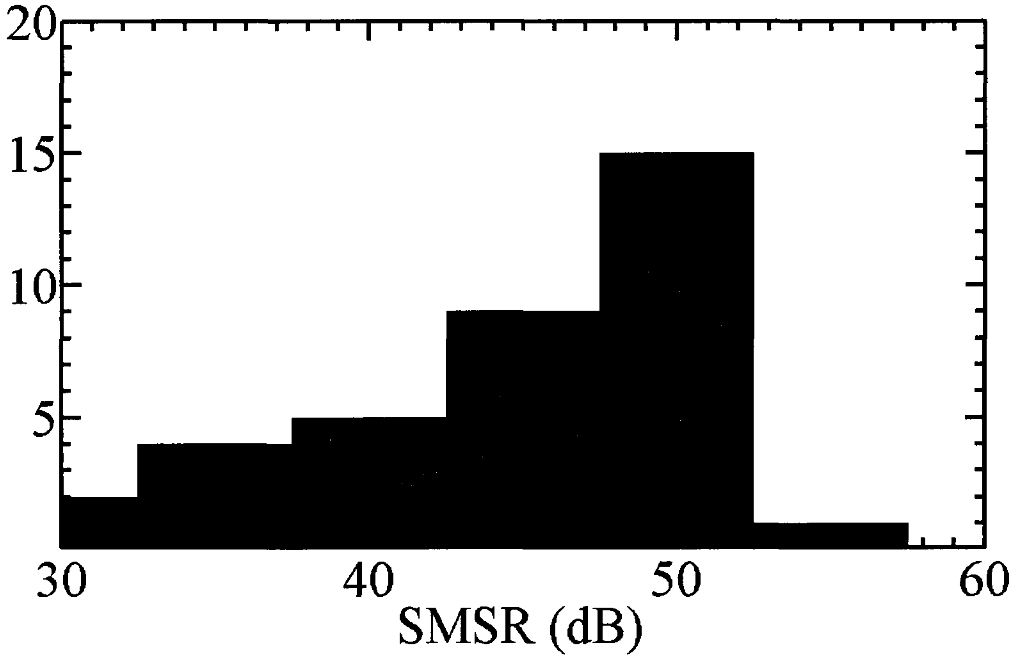

Figure 93. **Distribution of side-mode suppression ratio of operational LC-DFB lasers with third-order gratings**

lasers. In the rest of this section, the performance of specific third-order grating variants will be examined, beginning with the standard grating structure used as a baseline for the other grating variations.

7.5.2 Results for Standard Grating Devices

The standard third-order grating is designed with a narrow ridge width of 1.5 μm and a wide ridge width of 4 μm. It is placed at three different locations on the stepper tile (devices L1, L23, and L45), so there will be a standard grating structure on every cleaved bar. There are a total of 93 standard grating structure lasers that were fabricated. 16 out of the 93 devices showed DFB lasing, for a yield of 17%.

The effects of the weaker than expected grating are apparent from the fact that there was no DFB lasing observed for the shortest cavity length (500 μm) bars. While the LI curves of the shorter cavity length bars do show that they are lasing, it is apparent from the measured optical spectrum that the gratings are not strong enough to produce DFB lasing characteristics. For cavity lengths greater than 750 μm, DFB lasing is clearly observed, with most operational standard grating devices having cavity lengths of 1 mm. The best lasers showed SMSR values of > 50 dB. The average threshold current of the operational devices with a cavity length of 1 mm was 102 +/- 8 mA, 20% higher than the 4 μm ridge width FP laser. Figure 94, showing the LI characteristic and optical spectrum of a 1 mm long standard grating devices, demonstrates the potential of these devices. Not only does this laser have an SMSR = 52 dB, but it also has a threshold current of only 84 mA, lower than the average FP laser.

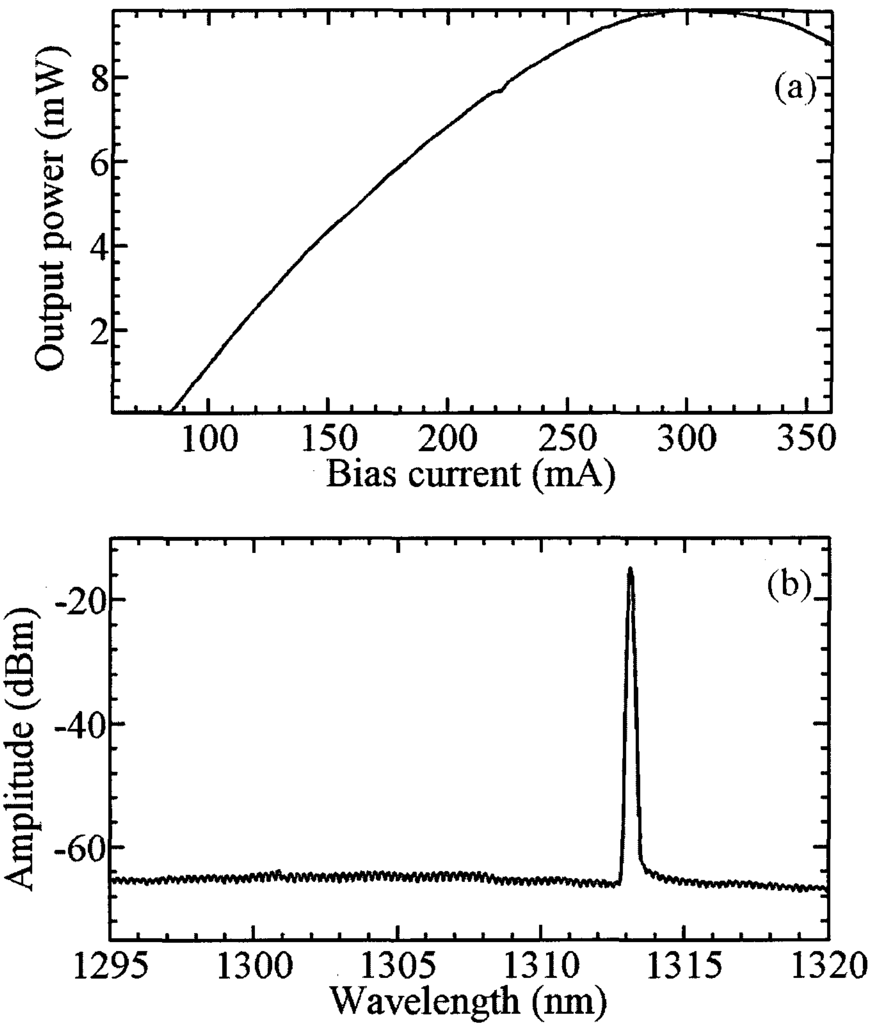

Figure 94. **Example of a standard grating a) LI characteristic and b) spectrum at I_{th} = 150 mA, for a 1 mm cavity length at T=25°C**

7.5.3 Results for λ/4 Phase-Shifted Grating Devices

As with the standard grating structure (devices L1, L23, and L45), a λ/4 phase-shifted grating is present on every laser bar (devices L6,L24, and L44). The phase-shifted gratings that were fabricated are not precisely λ/4 phase-shifted, as seen earlier in Figure 73, but this phase-shift should still have the desired effect. While we found in our theoretical investigation that, in general, higher order phase-shifted gratings will perform worse than unshifted higher order gratings, in this special case of a third-order grating with a duty cycle of 0.5, the longitudinal mode discrimination should be better for the phase-shifted grating, as seen in Figure 58. However, as noted above, the rounded grating has resulted in a weaker grating with an imaginary component even at a duty cycle of 0.5, blurring the differences between the phase-shifted and unshifted gratings in the fabricated lasers. Using the coupling coefficients calculated for the standard grating, the longitudinal mode solutions are $(\alpha L)_{\min} = 2.7$, $(\delta L)_{\min} = -4.1$, and NGD=0.25. When a phase-shift is added, the longitudinal mode solutions are $(\alpha L)_{\min} = 2.8$, $(\delta L)_{\min} = -5.9$, and NGD = 0.1. The phase-shifted gratings are thus expected to have slightly worse performance than the standard grating for this case.

The standard grating lasers had a better yield than the phase-shifted grating lasers. At the 1 mm cavity length, there were seven working standard grating devices, compared to three working phase-shifted devices. The performance of the standard grating lasers was also superior, with an average threshold current of 102 +/- 8 mA and an average SMSR of 47.3 +/- 2.4 dB compared to an average threshold current of 116 +/- 6 mA and an average SMSR of 40.7 +/- 2.1 dB for the phase-shifted lasers. These results confirm the expected poorer performance for these gratings, a result that has also been observed by researchers working on similar lasers at Tampere University in Finland [108]. This is in contrast to standard first-order gratings that have better performance, in particular higher SMSR values, when a phase-shift is added.

7.5.4 Impact of Duty Cycle Variation

The duty cycle variations for the third-order gratings were pushing the limits of the stepper lithography resolution. The standard grating had a duty cycle of 0.5, with an expected grating tooth gap of ~300 nm. The higher duty cycles that were attempted, 0.6, 0.7 and 0.8, had grating tooth gaps of 240, 180, and 120 nm, respectively. As Figure 72 shows, the fabrication of the gratings with duty cycles > 0.5 was unsuccessful. The smaller grating spacing of the higher duty cycle gratings has been washed out, and instead a sinusoidal pattern with a very weak grating strength emerges. The result of these very weak gratings is that none of the higher duty cycle gratings showed DFB

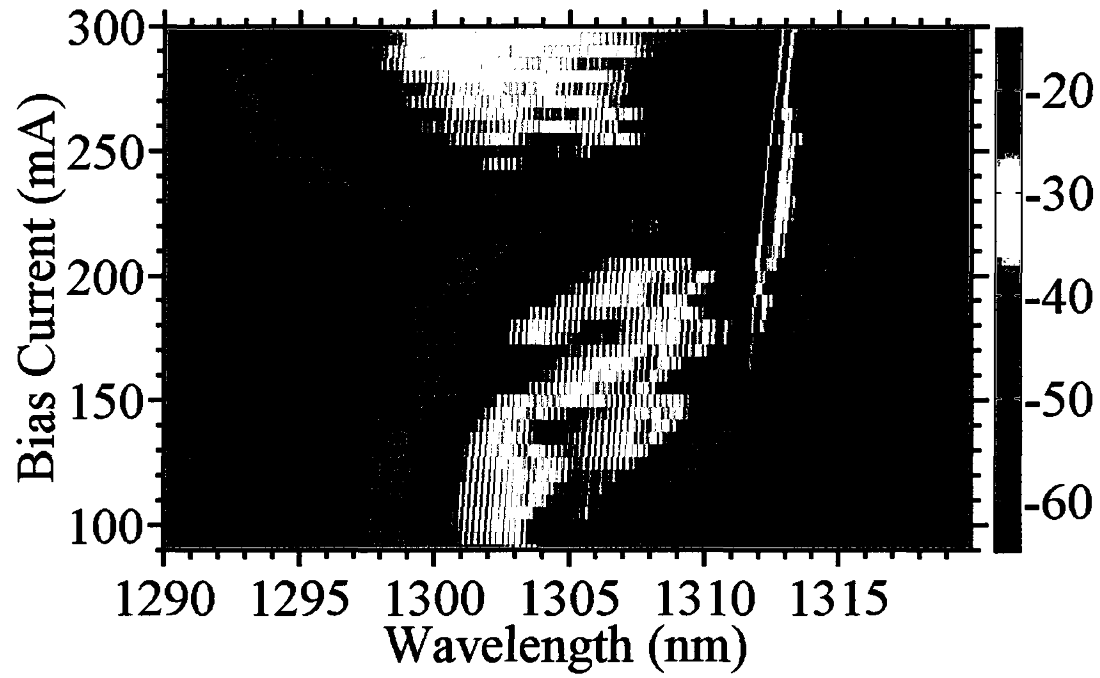

Figure 95. **Example of higher duty cycle spectrum (1 mm bar 5, intended duty cycle = 0.6)**

lasing characteristics. A sample spectrum, shown in Figure 95, demonstrates that these lasers are more like Fabry-Perot than DFB lasers. Instead of a single strong DFB lasing peak, there is conditionally-stable DFB lasing in the range of 200-250 mA, with a maximum SMSR of 27 dB, considerably poorer than the SMSR > 50 dB observed for the half duty-cycle grating devices. A more precise fabrication method than i-line stepper lithography will be required to create the narrow spacing between the grating teeth required for 1310 nm gratings with duty cycles > 0.5.

7.5.5 Impact of Ridge Width Variations

The mask layout included 13 variations on the ridge width including the standard design, with narrow ridge widths ranging from 1.5 to 2.5 μm and wide ridge widths ranging from 2.5 to 5 μm. Of all the variations on the mask, those of different ridge widths had the best single-mode DFB lasing yield, and had excellent characteristics including the highest SMSR of 53.6 dB for a 750 μm long laser with ridge widths of W_N/W_W = 1.5/4.5 (μm). There are 37 instances of the devices labeled from L7 to L15, with W_N = 1.5 and 2.0 μm (see Table 5 in Section 7.1), and 30 instances of the devices labeled from L16 to L18, with W_N = 2.5 μm. These are divided roughly equally between the different cavity lengths. Most of these devices were tested since they had the best yields.

The distribution of operational lasers at a cavity length of 1 mm for different ridge widths is shown in Figure 96 for a) W_N = 1.5 μm, b) W_N = 2.0 μm, and c) W_N = 2.5 μm. The largest number of operational devices was for the standard grating design where W_N/W_W = 1.5/4 (μm). This does not indicate a higher yield for this design, since there were at least twice as many lasers with the standard grating that were fabricated compared to the other designs, with twelve devices tested at a 1 mm cavity length. The best yielding design was for W_N/W_W = 1.5/3.5 (μm), with five operational designs out of the six devices tested at this 1 mm cavity length. Although all ridge width variations had some operational lasers, the poorest designs had only a single operational device at this cavity length. These designs were those with ridge widths of W_N/W_W = 1.5/2.5, 1.5/5, 2/4.5, 2/5, 2.5/4, and 2.5/4.5 (μm). From Figure 72a, we see that the W_N/W_W = 1.5/2.5 grating is nearly washed out, which will result in a weaker grating and poorer yield. The lasers with the widest narrow ridge width of W_N = 2.5 μm had very poor yields. This could be due to the lower coupling coefficient with wider narrow ridge widths that was predicted in Figure 35. Since our coupling coefficient is already degraded due to rounding of the grating, the additional widening of the narrow ridge width is likely to weaken the grating too much for DFB lasing to occur. At the W_N=1.5 and 2.0 μm ridge widths, the widest ridge widths have the poorest yield. Although we predict from Figure 36 gradually improving coupling coefficients as the wide ridge width increases, this may be counteracted by increased diffusion of carriers into the teeth of the grating as the wide ridge width increases. These carriers contribute to a larger lateral leakage current, reducing the injection efficiency and decreasing the amount of gain that is possible for lasing operation.

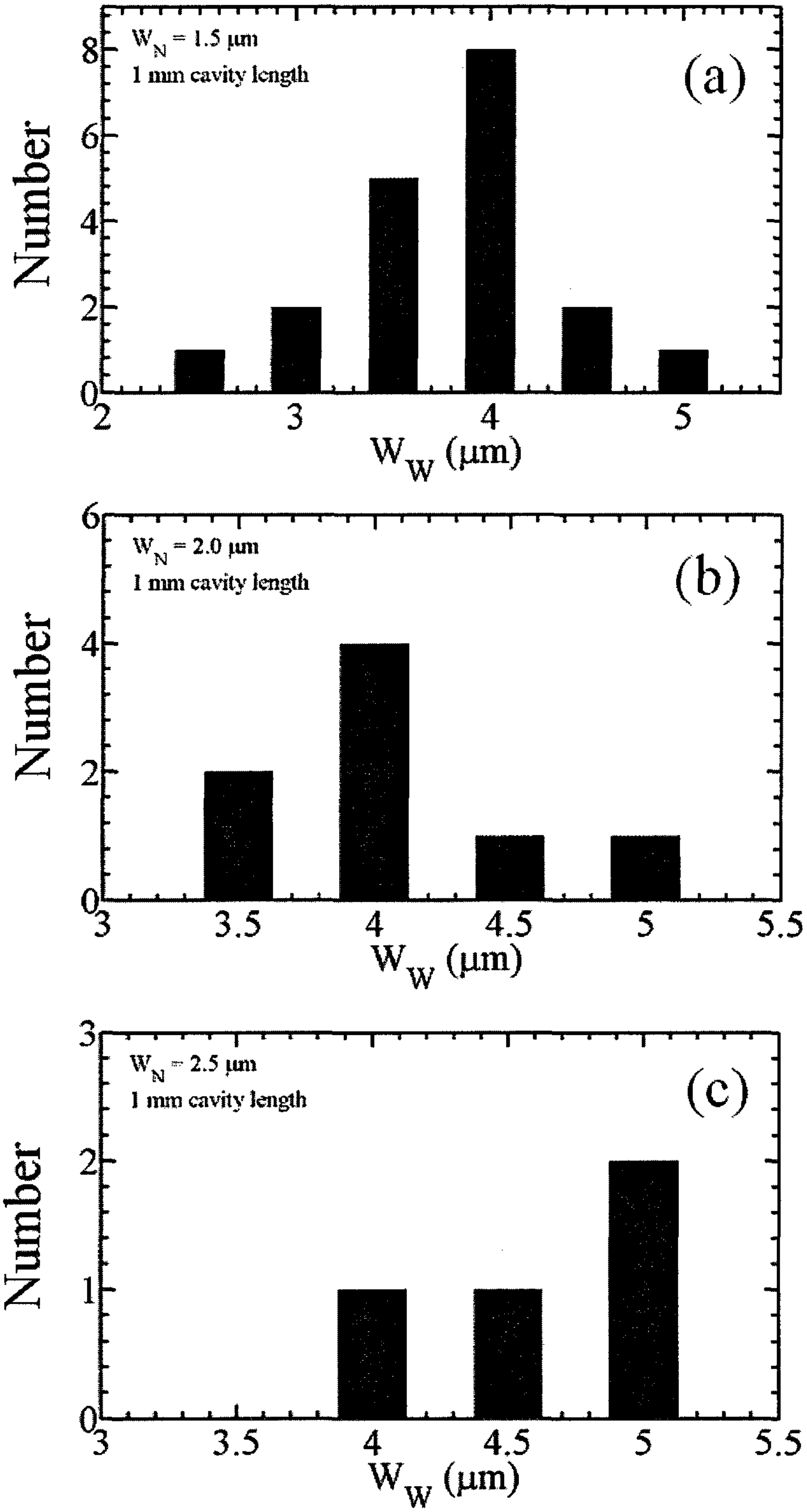

Figure 96. Distribution of operational LC-DFB lasers *vs.* wide ridge width for a) 1.5 μm, b) 2.0 μm, and c) 2.5 μm narrow ridge widths and a cavity length of 1 mm

The average threshold currents of the different ridge widths are shown in Figure 97a. The cavity length of all the lasers is 1 mm. There are too few operational lasers with W_N = 2 and 2.5 μm to confidently predict trends, but the lasers with W_N = 1.5 μm show that the threshold current grows larger as the wide ridge width increases. This supports the hypothesis that there are additional carrier losses at wider ridge widths due to diffusion into the wider grating teeth. This trend is confirmed in the plot of the average slope efficiency *vs.* wide ridge width plot for the same lasers shown in Figure 97b. In this plot, the W_N = 1.5 and 2.0 μm lasers have generally reduced slope efficiency as the wide ridge width increases. The W_N = 2.5 μm lasers, however, have an opposite characteristic. The results for these lasers are less reliable, however, since only 1-2 lasers were operational at this narrow ridge width. The uncertainties in the measurements, and the small number of operational lasers at ridge widths of 2 and 2.5 μm make any conclusions comparing the performance of different narrow ridge width gratings doubtful, but it should be noted that the W_N = 2 μm narrow ridge width lasers showed lower threshold currents and higher slope efficiencies, in general, than the other two narrow ridge widths. At this cavity length of 1 mm, one of the best designs in terms of slope efficiency and threshold current is the W_N/W_W = 2/4 (μm) design, with an average threshold current of 86 +/- 3 mA and an average slope efficiency of 0.104 +/- 0.005 mW/mA. In addition, this design had a good yield, with four of the six tested lasers with this ridge width at a cavity length of 1 mm demonstrating stable DFB behaviour (and one of the inoperational devices near the edge of a damaged bar). At this narrow ridge width, we have a balance between a strong grating and good electrical injection.

In our earlier, purely optical, analysis of the grating for different ridge widths in Section 5.4, we would expect that the threshold current would decrease as the narrow ridge width decreased and the wide ridge width increased. It is likely that electrical effects, such as larger current spreading at wider ridge widths, have played a role in the deviation from the expected results observed in Figure 97. It should also be emphasized that the grating calculations in the earlier chapters assumed sharp, rectangular gratings. The rounded gratings that were actually fabricated will likely have somewhat different trends

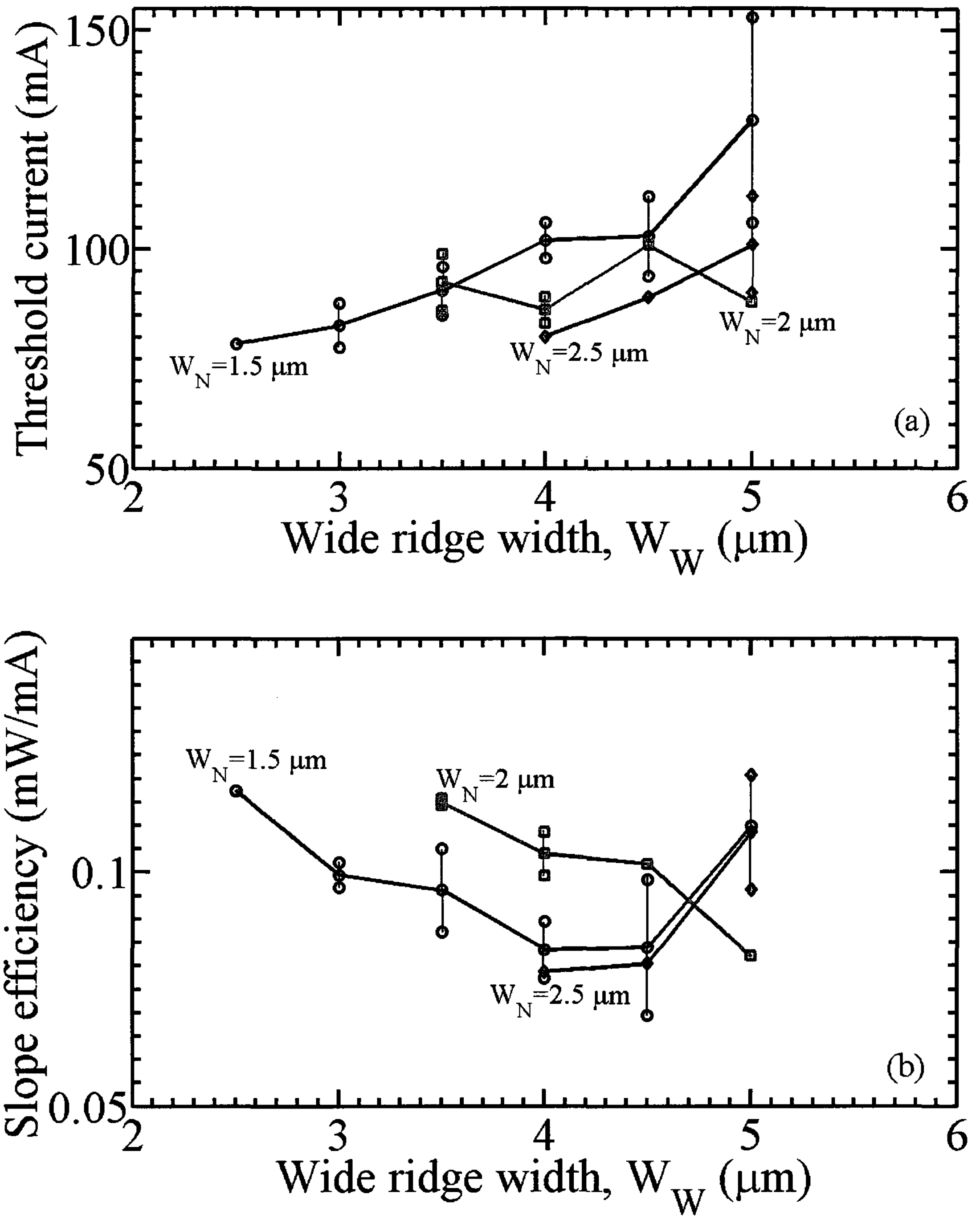

Figure 97. a) Average threshold current, and b) average slope efficiency of third-order grating LC-DFB lasers with different wide and narrow ridge widths.

compared to the rectangular gratings. Only SEM photographs of a few gratings with ridge width variations were taken, as shown in Figure 74, so there could be significant deviations for the other gratings as well. In particular, the high contrast (low W_N and high W_W) gratings may not have been defined properly, or experienced even more grating rounding than for the standard design.

7.5.6 Results for Dual-Wavelength Devices

The dual-wavelength designs feature wavelength spacings from 0.2 to 5 nm. There were a total of 210 dual-wavelength devices of all cavity lengths that were fabricated, though only approximately 40 of these have been tested. Many of the dual-wavelength designs showed multi-mode spectral characteristics, and only a few showed DFB lasing. Sixteen devices showed good dual-wavelength operation at particular bias currents, but the spectral spacing did not match the designed spacing. Instead, the wavelengths were separated by 1.9 – 5 nm. The power is not balanced at both lasing wavelengths, but instead one lasing peak tends to be dominant, often being 30 dB higher than the other. A typical example is shown in Figure 98, for a 1 mm long device with an intended wavelength spacing of 0.2 nm. The spacing between the two peaks is instead 3.5 nm, from 1309.3 to 1312.8 nm, and the power imbalance between the two peaks is 27 dB.

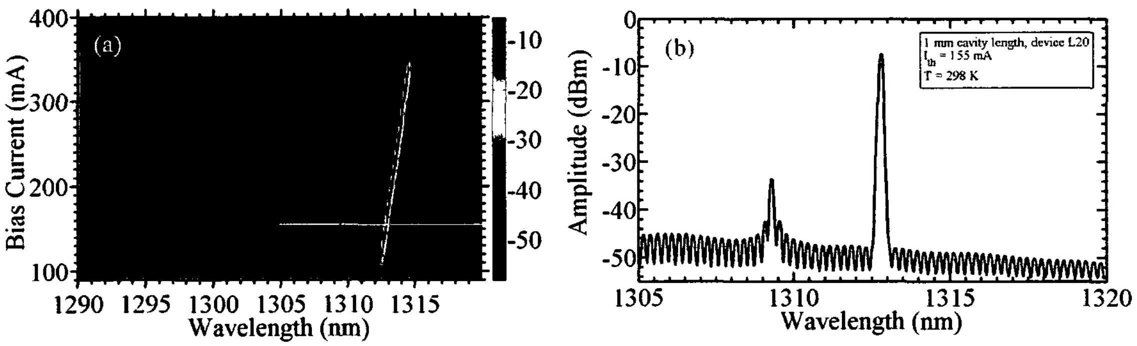

Figure 98. **Typical dual-wavelength spectrum, 1mm device L20 for a) a range of bias currents, and indicated by the yellow line, b) at I_{th} = 155 mA.**

The best dual-wavelength result, shown in Figure 99, is for a 1 mm long device with an intended wavelength separation of 0.25 nm. The actual wavelength separation is 3.7 nm, from 1310.1 to 1313.8 nm, and the power imbalance between the two peaks at a bias current of 156 mA is only 1.7 dB. The wavelength separation, however, is still too large for typical RF applications. Wavelength separations of 0.2 nm would provide a 40 GHz frequency separation, while the separation here of 3.7 nm corresponds to a frequency separation of 640 GHz. Even the smallest wavelength separation of 1.9 nm corresponds to a frequency separation of 330.3 GHz. The dual-wavelength lasers attempted on this mask had period differences of 0.1 – 2.2 nm, so it is not unexpected that they would not all work when fabricated with stepper lithography, which as an uncertainty of 15 nm in the grating period. It was hoped that the variations in the individual grating periods would average out to the desired separation on either side of the grating over the length of the laser cavity. However, the inherent process variations may be too large, or the cavity lengths too short, to average out the Bragg wavelength differences on either side of grating in this way. A more thorough analysis of this would be useful for future design iterations. Nevertheless, the demonstration of some dual-wavelength lasing is encouraging, and could be greatly improved with more precise fabrication techniques.

7.5.7 Temperature Dependence

The temperature dependence of the lasers was determined from two experimentally measured parameters: the shift of the gain peak with temperature, and the characteristic

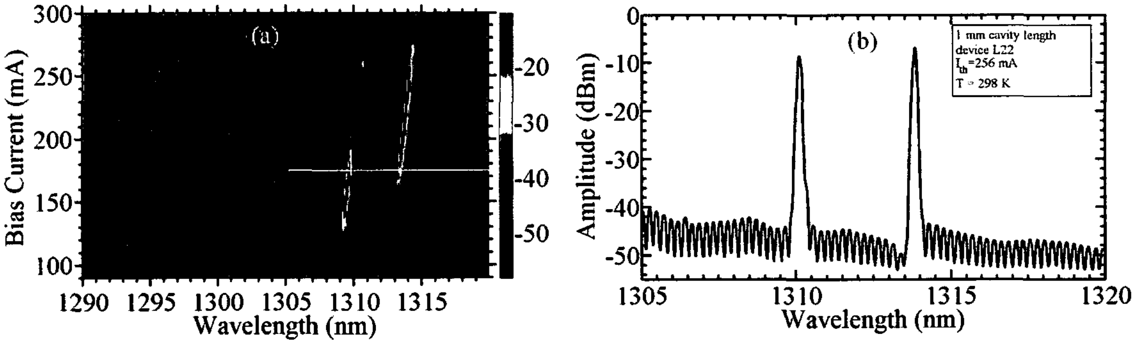

Figure 99. **Best dual-wavelength spectrum, 1mm device L22 for a) a range of bias currents, and indicated by the yellow line, b) at I_{th} = 156 mA.**

temperature, defined in Section 7.3.1. The DFB lasing spectrum is shown in Figure 100 for a range of temperatures measured for a 1 mm device with $W_N/W_W = 2/3.5$ (μm) at a bias current of 200 mA. The red-shift in the lasing peak was only 0.06 nm/K, much less than the 0.65 nm/K measured for the Fabry-Perot devices. In DFB lasers, the wavelength is dependent on the properties of the Bragg grating, rather than simply the material/modal gain, as with FP lasers. Since Bragg wavelength shifts are primarily due to refractive index changes with temperature, they are much less than the shift in material gain wavelength with temperature. This produces the much smaller temperature dependence of the lasing wavelength, as discussed earlier in Section 7.3.2.

Characteristic temperatures were measured for a wide range of cavity and ridge width sizes; the results are summarized in Table 7. The DFB lasers had an average characteristic temperature, T_0, of 303.2 K, with values ranging from a low of 300.3 for a 750 μm long laser to a high off 309.2 for a 1000 μm laser. This agrees with the Fabry-Perot laser results, with a measured T_0 = 313 K for a 1250 μm device. This indicates that the LC-DFB lasers do not have a significantly greater threshold current sensitivity to temperature compared to FP lasers.

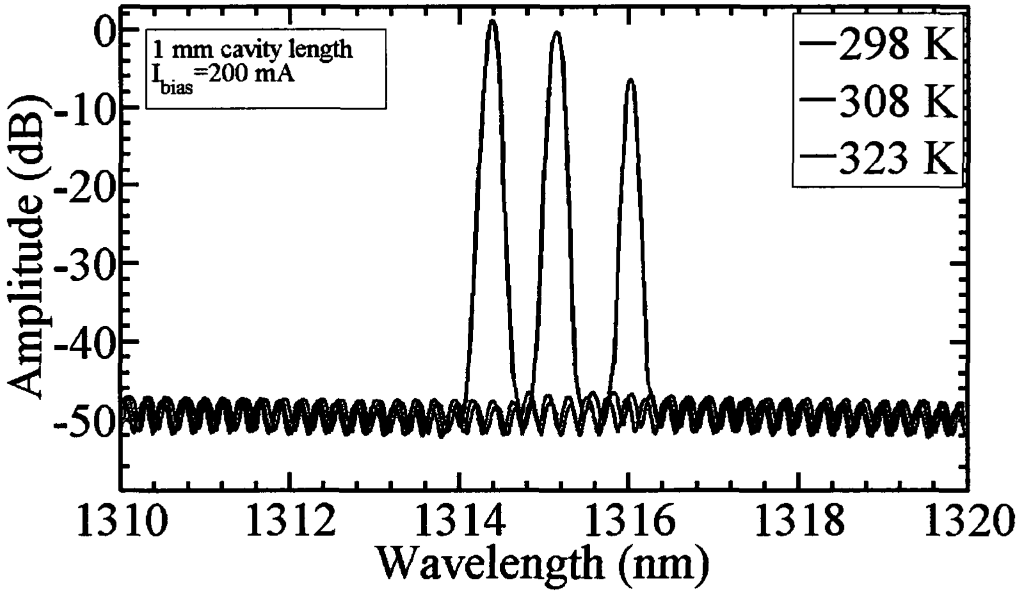

Figure 100. **Spectrum of a 1 mm cavity length device L12 at a bias current of 200 mA and temperatures of 298, 308, and 323 K.**

Cavity Length (μm)	**W_N/W_W (μm)**	**T_0 (K)**
500	1.5/2.5	302.9
	1.5/2.5	303.6
750	1.5/2.5	28.69
	1.5/3	301.7
	1.5/3	300.5
	1.5/3.5	300.3
	1.5/4.5	303.4
	1.5/5	302.4
	2/3.5	307.1
	2/4	305.1
1000	2/3.5	301.8
	1.5/4.5	308.3
	1.5/2.5	301.6
	2/4.5	309.2
1250	Fabry-Perot	313
	2.5/4.5	300.2

Table 7. Characteristic temperature summary

In conclusion, the LC-DFB lasers have a similar temperature dependence of the threshold current as FP lasers, but a significantly lower lasing wavelength sensitivity. The LC-DFB lasers do not depend on the modal gain sensitivity to temperature, but instead the refractive index sensitivity to temperature, which is comparatively lower. This makes these lasers ideal for stable operation over a range of operating temperatures, or possibly uncooled operation.

7.5.8 Bragg Wavelength

The distribution of peak wavelengths at the maximum SMSR bias current for the operational DFB lasers is shown in Figure 101. This distribution indicates a wavelength

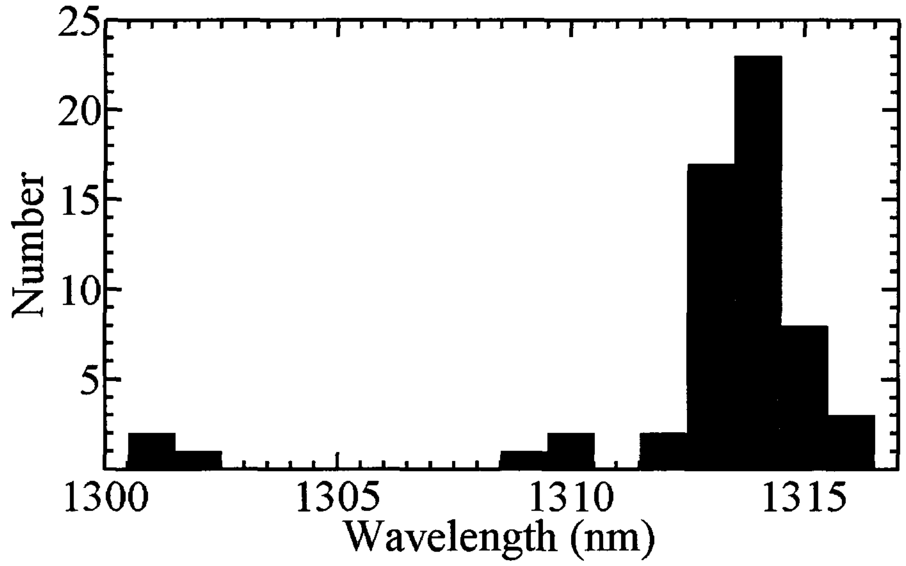

Figure 101. **Distribution of peak wavelength at highest SMSR value for third-order lasers**

range of approximately 10-13 nm for these DFB lasers. There is a definite bias towards wavelengths longer than the the Bragg wavelength of 1310 nm. There are a few factors that contribute to this longer wavelength. First, the Bragg frequency detuning was found to be negative in the rounded grating solutions of Figure 80, meaning the actual lasing wavelength will be red-shifted compared to the Bragg wavelength. The scale of the detuning is small, however, and accounts for ~ 0.2 nm of red-shift. More likely is that at these high SMSR values, the laser is sufficiently forward-biased that there is some temperature elevation, resulting in a temperature dependent shift in the refractive index, and hence the lasing wavelength. A difference in the effective refractive index of 3.24 +/- 0.007 is enough to produce changes in the Bragg wavelength of 1310 +/- 2.9 nm. This change in the refractive index of ~0.2% is well within the uncertainties of our calculations of the effective refractive index in Chapter 3.

7.6 Fourth-Order Grating LC-DFB Lasers

The fourth-order gratings exhibited poor DFB characteristics, such as the example shown in Figure 102. A very faint streak reveals some feedback near 1315 nm, but it is far too weak to produce a DFB characteristic. Instead, a Fabry-Perot spectral characteristic is observed, with hopping between a few broad peaks at different bias currents. This spectrum also demonstrates lasing peaks near 1300 nm rather than 1310 nm, an example of the cross-wafer non-uniformity in the gain peak. However, none of the fourth-order LC-DFB lasers exhibited good DFB spectral characteristics, and the most likely reason is that the gratings were too weak. A useful exercise would be to take SEM photos of the fourth-order gratings to provide a clue as to what went wrong with these lasers. The larger grating spacing should have made the fabrication easier, and the simulations of Chapter 5 indicated that fourth-order gratings should have comparable coupling coefficients. It is possible that the fourth-order design is more sensitive to fabrication

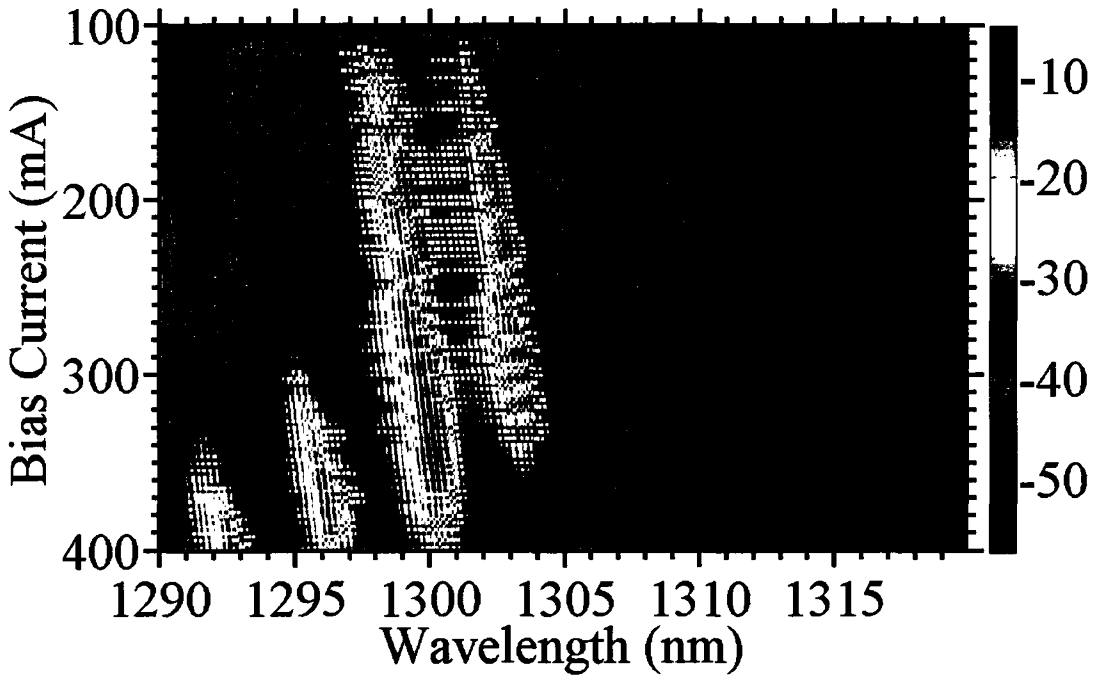

Figure 102. Representative sample of the spectrum of a fourth-order grating LC-DFB laser - 1 mm bar 4, W_N/W_W = 2.5/4.5 (μm).

variances, such as grating rounding, than the third-order designs, or that the longitudinal mode occurs at higher wavelengths (1315 nm and above) compared to the third-order grating lasers.

7.7 Extraction of Modified Coupled-Mode Coefficients

The most challenging data analysis task is the extraction of the modified coupled-mode coefficients from the experimental data. The extraction of these coefficients will provide experimental data for comparison with the two-dimensional simulations outlined in this thesis. Due to the time-consuming nature of this data extraction, it was done for only the standard grating. In particular, we wish to show how well the rounded grating coefficients calculated in Figure 78 agree with the experimental data. The generally accepted method of extracting these coefficients is to use the below-threshold spontaneous emission spectrum. We will use a variation of this technique using the Green's function method described by Wenzel [79] specifically for gain- or loss-coupled lasers with complex coupling coefficients. Green's functions were described earlier in this thesis in Section 4.1.4.

To implement this model, we first express the modified coupled-mode equations for a laser below threshold at an optical wavelength of λ in the matrix equation

$$\mathbf{E}_\lambda(z)\boldsymbol{\Psi}(z)=\mathbf{F}_\lambda(z) \tag{7.10}$$

where the matrix operator $\mathbf{E}_\lambda(z)$ is formulated from the modified coupled-mode equations as

$$\mathbf{E}_\lambda(z)=\begin{bmatrix} \frac{\partial}{\partial z}+(-\alpha-j\delta-j\zeta_1) & j(\kappa_p^*+\zeta_2) \\ j(\kappa_p+\zeta_4) & -\frac{\partial}{\partial z}+(-\alpha-j\delta-j\zeta_3) \end{bmatrix}. \tag{7.11}$$

$\mathbf{\Psi}(z)$ are the longitudinally-varying field amplitudes,

$$\mathbf{\Psi} = \begin{bmatrix} A(z) \\ B(z) \end{bmatrix}, \tag{7.12}$$

and $\mathbf{F}_\omega$ is the vector of Langevin noise functions that model the randomly distributed spontaneous emission events

$$\mathbf{F}_\lambda = \begin{bmatrix} f_\lambda^+ \\ f_\lambda^- \end{bmatrix}. \tag{7.13}$$

The Langevin noise functions, $f_\lambda^{+,-}$ are random variables that have an ensemble average of zero:

$$\left\langle f_\lambda^\pm(z) \right\rangle = 0 \tag{7.14}$$

and a cross-correlation over wavelength and distance, z, of

$$\left\langle f_\lambda^+(z), f_{\lambda'}^{+*}(z') \right\rangle = 2D_\lambda(z)\delta(z-z')\delta(\lambda-\lambda'), \tag{7.15}$$

where D_ω is a diffusion coefficient, and δ is the Dirac delta function.

The diffusion coefficient, $D_\lambda(z)$, is obtained from the gain coefficient, g, and spontaneous emission factor, n_{sp}, using the relation

$$D_\lambda(z) = \frac{hc}{\lambda} g(\lambda, z) n_{sp}(\lambda, z). \tag{7.16}$$

To evaluate the diffusion coefficients, the spontaneous emission spectrum is assumed to take the form of a Lorentzian with a full width at half maximum of $\Delta\lambda_{sp}$ and a center wavelength of λ_{sp}. This Lorentzian, and hence the spontaneous emission spectrum, is assumed to be invariant along the laser cavity. Since the MQW active region, from which most of the spontaneous emission in this wavelength range will be emitted, is invariant along the laser cavity, this assumption should be valid. The coefficient, D_λ, thus reduces to:

$$D_\lambda = f_{sp}\frac{\lambda_0}{\lambda}\frac{\left(\Delta\lambda_{sp}/2\right)^2}{\left(\Delta\lambda_{sp}\right)^2+\left(\lambda_{sp}-\lambda\right)^2}, \tag{7.17}$$

where f_{sp} is a term governing the degree of spontaneous emission.

Equation (7.10) can be solved using Green's functions, yielding a $\mathbf{\Psi}$ of the form:

$$\mathbf{\Psi} = \begin{bmatrix} \left\langle \mathbf{G}_{1,\lambda}(z,z'),\mathbf{F}_\lambda(z')\right\rangle \\ \left\langle \mathbf{G}_{2,\lambda}(z,z'),\mathbf{F}_\lambda(z')\right\rangle \end{bmatrix} \tag{7.18}$$

where $\mathbf{G}_{1(2),\lambda}(z,z')$ are the wavelength-dependent Green's functions, and the inner product is defined as

$$\langle G,F\rangle = \int_0^L \left[G^+(z)F^-(z)+G^-(z)F^+(z)\right]dz. \tag{7.19}$$

The Green's function vectors of (7.18) are given by

$$\mathbf{G}_{1(2),\lambda}(z,z') = \begin{bmatrix} g^+_{1(2),\lambda}(z,z') \\ g^-_{1(2),\lambda}(z,z') \end{bmatrix}. \tag{7.20}$$

where $g^{\pm}_{1(2),\lambda}(z,z')$ are the individual Green's functions in the forward (positive) and backward (negative) directions. These functions satisfy the inhomogeneous coupled wave equation with a δ source term

$$\mathbf{E}_{\lambda}(z)\mathbf{G}_{1,\lambda}(z,z')=\begin{bmatrix}0\\ \delta(z-z')\end{bmatrix}, \tag{7.21}$$

and

$$\mathbf{E}_{\lambda}(z)\mathbf{G}_{2,\lambda}(z,z')=\begin{bmatrix}\delta(z-z')\\ 0\end{bmatrix}. \tag{7.22}$$

The Green's functions can be calculated by solving the homogeneous coupled wave equation,

$$\mathbf{E}_{\lambda}\mathbf{G}_{2,\lambda}(z,0)=0 \tag{7.23}$$

subject to the inhomogeneous boundary condition at $z = 0$ [79]

$$g^{+}_{2,\lambda}(0,0)-r_0 g^{-}_{2,\lambda}(0,0)=1, \tag{7.24}$$

where r_0 is the reflectivity of the facet at z=0. Once $g^{\pm}_{2,\lambda}$ has been calculated, it can be used to obtain the power spectral density at the z=0 facet through the relation

$$S^{-}_{\lambda}(0^{-})=\left(1-|r_0|^2\right)\left\{\int_0^L\left[\left|g^{+}_{2,\lambda}(0,z)\right|^2+\left|g^{-}_{2,\lambda}(0,z)\right|^2\right]2D_{\lambda}dz\right\}. \tag{7.25}$$

Note that we neglect the term for gain-coupled lasers that is present in Wenzel's original formulation since it is not required here.

The form of $\mathbf{E}_\lambda$ permits the self-coupling terms, $\left(-\alpha - j\delta - j\zeta_{1,3}\right)$, to be simplified in terms of polynomial functions with respect to the wavelength. The two imaginary terms are combined, and are considered to be inversely proportional to the wavelength and proportional to a group index n_g. The spectrum of α, the gain/loss term, is considered to be approximately parabolic. Our measurement of the gain spectrum of a FP laser in Figure 90 shows the parabolic form of this spectrum. The self-coupling terms thus reduce to

$$\begin{aligned} j\left(-\alpha - j\delta - j\zeta_{1,3}\right) = \frac{2\pi}{\lambda_0}\left\{n_g(z)\left[\frac{\lambda_0}{\lambda}-1\right]+\Delta n(z)\right\} \\ +\frac{j}{2}\left\{g_p(z)-g_c(z)\left[\lambda-\lambda_p(z)\right]^2\right\} \end{aligned} \tag{7.26}$$

where λ_0 is the reference wavelength, Δn is the refractive index variation, g_p is the peak value of the imaginary part of the self-coupling term at a wavelength λ_p, and g_c is the curvature of the wavelength dependence of this term. The fitting terms are thus changed from the modified coupling coefficients to those outlined in (7.26): $n_g, \Delta n, g_p, g_c,$ and λ_p. These terms can be used to obtain the self-coupling term, but not the exact values of α, δ, and $\zeta_{1,3}$. The real part of $\zeta_{1,3}$ will have an identical effect on the spectrum as the δ term, and the imaginary part of $\zeta_{1,3}$ will have an identical effect on the spectrum as the α term, so they cannot be separated using this method. Similarly, the effective coupling coefficient can be extracted, but not the individual κ_p and $\zeta_{2,4}$ terms. In other words, this method is able to extract the real and imaginary parts of the self-coupling and cross-coupling terms, but not the individual components of the real and imaginary portions of these terms.

A fitting procedure with the N-point logarithmic below-threshold spontaneous emission spectrum, $S(\lambda) = S_\lambda^-\left(0^-\right)$, is used to minimize the error function, $\sigma^2(\mathbf{p})$

$$\sigma^2(\mathbf{p}) = \frac{1}{N}\sum_{i=1}^{N}\left(\log S(\lambda_i,\mathbf{p}) - \log S(\lambda_i)\right)^2 \tag{7.27}$$

where $S(\lambda_i,\mathbf{p})$ are the theoretical values, $S(\lambda_i)$ are the experimental values, and **p** is the vector of the parameters that must be fitted. There were ten parameters that were fitted in the final implementation of this algorithm. Obviously, an ten-dimensional constrained nonlinear optimization problem is not trivial. To reduce the solution time, the spectrum was roughly optimized manually to provide a good starting point for the fitting algorithm. The simplex algorithm was used to obtain the best fit, the details of which can be found in [109]. This algorithm is not constrained, so the results require careful analysis to ensure that they are physical (e.g. no negative facet reflectivities, etc.). Despite the good initial fit, it was still a lengthy calculation to find the best fit solution, requiring approximately 7000 function evaluations.

The spectrum to be fitted came from a 1 mm long standard-grating LC-DFB laser with ridge widths of W_N/W_W = 1.5/4 (μm). The threshold current of this laser is 83 mA, and the spectrum was taken at a bias current of 70 mA to ensure that only the amplified spontaneous emission spectrum was measured. The best fit solution for this laser is

Parameter name	**Value**
Right facet reflectivity, R_0	0.3
Left facet reflectivity, R_L	0.3
Right facet phase, φ_0	**-0.87 rad.**
Left facet phase, φ_L	**-0.68 rad.**
Effective coupling coefficient, κ_{eff}	**12.5∠1.38 cm^{-1}**
Length, L	1 mm
Gain peak, g_p	**-17.5 cm^{-1}**
Curvature of gain wavelength, g_c	**0.013 cm^{-1} nm^{-2}**
Gain peak wavelength, λ_p	1312 nm
Gain reference wavelength, λ_0	**1312.4 nm**
Group index, n_g	**3.78**
Index change, Δn	**1.31 x 10^{-6}**
Spontaneous emission strength, f_{sp}	**7.955 x 10^{-7}**
Spontaneous emission linewidth, $\Delta\lambda_{sp}$	50 nm
Spontaneous emission centre wavelength, λ_{sp}	1312 nm

Table 8. Fitted parameters to amplified spontaneous emission spectrum

summarized in Table 8, with the fitted parameters in bold.

The fitted spectrum for this laser is shown in Figure 103, and it agrees reasonably well with the measured data points, with a maximum deviation of 26% and an average deviation of 7.5%. The parameter of most interest is the effective coupling coefficient, which according to the fitted results is $\kappa_{eff} = 12.5\angle 1.38$ +/- $1.4\angle 0.05$ cm^{-1}. The complex nature of κ_{eff} is also confirmed, underscoring the need for the extended Streifer model of these higher order LC-DFB lasers. We compare this value with that of the rounded grating, calculated in Section 7.2.2, to ensure a more accurate comparison of the experimental data with the actual fabricated grating coupling coefficients. If we compare this to the calculated value of the standard grating in Figure 72 of $12.2\angle -0.16\,\text{cm}^{-1}$, we see excellent agreement in the magnitudes, but not in the phase of the coupling coefficient. The difference in the coupling coefficient can be explained by the variations in the rounded grating parameters. As shown in Figure 78, the phase of κ_{eff} can vary considerably depending on the exact amount of grating rounding. For example, a rough

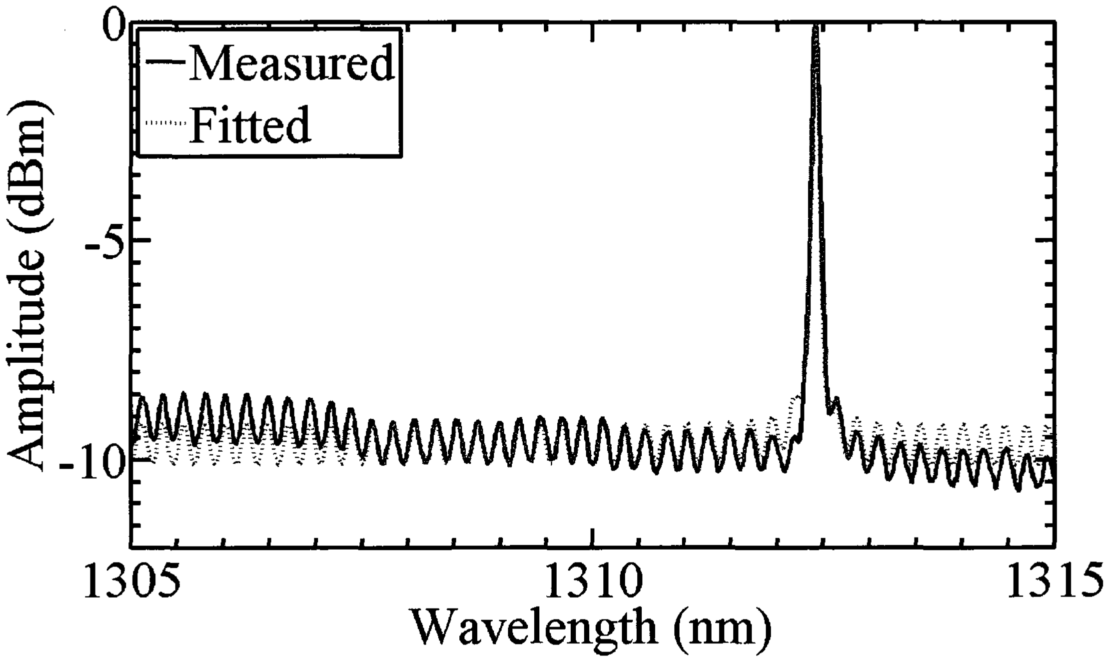

Figure 103. Measured and fitted amplified spontaneous emission spectrum of 1 mm cavity length laser with W_N/W_W = 1.5/4 (μm) ridge widths at T=298 K and I_{th} = 70 mA.

first-pass approximation of the parameters that match the measured coupling coefficient are W_N = 1.68 μm, γ=0.48, h_1 = 0.17 μm, h_2=0.54 μm, and h_3 = 0.25 μm. These fitting parameters actually match quite well with the SEM photo of the standard grating taken in Figure 71, rather than the standard grating pictured in Figure 72, as the overlay of the SEM photo and the theoretical grating with the parameters given above in Figure 104 demonstrates. The effective coupling coefficient calculated for this rounded grating is $\kappa_{eff} = 12.3\angle 1.41$ cm^{-1}, a difference of 2% from the measured coupling coefficient, well within the tolerance of this measurement. This measurement of the coupling coefficient provides validation for the theoretical calculations of the coupling coefficient that have been performed in this thesis.

7.8 Performance Comparison

The 1 mm long LC-DFB lasers had average threshold currents of 95 mA and efficiencies of 0.096 mW/mA. The best design of a third-order grating with W_N / W_W = 2/4 (μm) had a threshold current of 85 mA and a slope efficiency of 0.104 mW/mA. These threshold

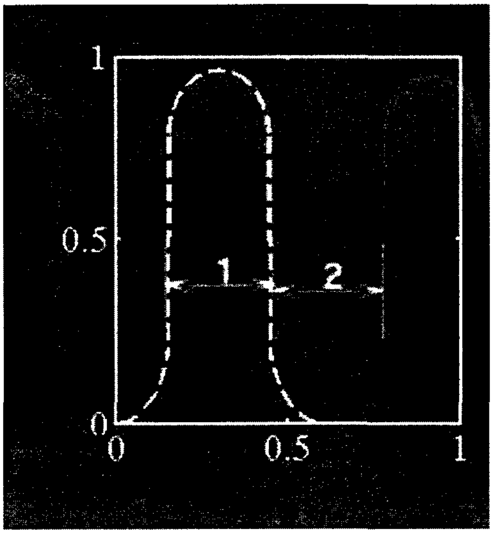

Figure 104. **Comparison of standard third-order grating SEM photo and a rounded grating, outlined in yellow, with h_1=0.17 μm, h_2 = 0.54 μm, h_3=0.25 μm, and γ=0.48. Scale on axes is in μm.**

currents are higher than most other designs reported in Table 1, however, the threshold currents could easily be improved with some reworking of the design, as will be described below. The side-mode suppression ratio of the LC-DFB lasers of > 50 dB is exceptionally good, outperforming all designs but that of Reid *et al.* [50]. In fact, these side-mode suppression ratios are better than a range of commercially available 1310 nm DFB lasers, including designs such as the NEC NDL7673P laser with an SMSR of 30 dB, the Ortel/Emcore 1611A-104-10 with an SMSR of 35 dB, and the Agere D372-20AS, including isolator, with an SMSR of 40 dB. This favorable performance on the first fabrication run, and the fact that the threshold currents can likely be reduced in future designs, indicate that these lasers could potentially be commercially feasible.

7.9 Improved Design

The additional losses measured for all of the lasers due to the metal contact losses suggest that the laser geometry must be improved. Figure 105 is the most obvious solution to minimize these additional losses. The shallow etch that is required for the fabrication of the gratings is kept while the central ridge in this design is increased in height so that the

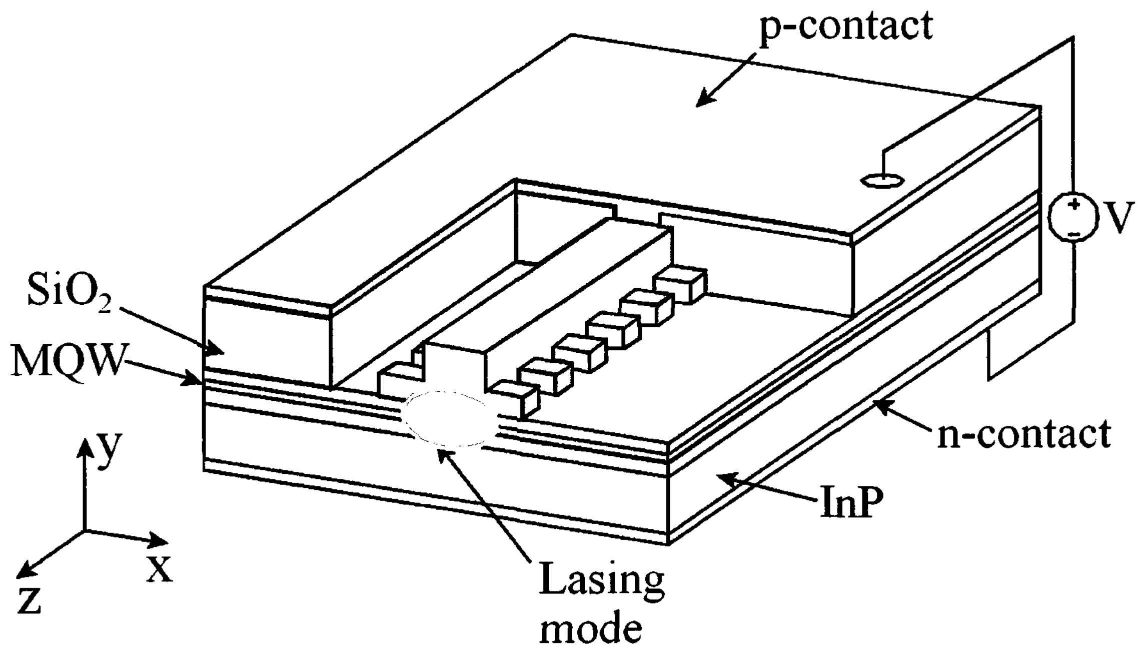

Figure 105. **Improved LC-DFB laser design to reduce metal contact losses**

distance between the metal contact and the optical mode permits minimal mode overlap. This design could be checked using the simulation techniques described in this thesis for the optical properties, and LAS2D simulations could be used to ensure good electrical properties. However, it would require an additional etch step to fabricate that will complicate the manufacturing of the laser. The higher central ridge may also interfere with the deposition of the silica mask over the gratings. Ultimately, these factors would have to be quantified to determine whether or not this improved design is feasible.

CHAPTER 8 – CONCLUSIONS

This thesis has described the detailed design considerations, experimental results, and applications of a distributed feedback laser with a higher order laterally-coupled grating. An extension of Streifer's modified coupled-mode theory to two dimensions enabled a comprehensive analysis of the impact of the grating properties on the LC-DFB laser performance. This model has provided fundamental design insights, allowing a better understanding of how the laser parameters affect the device operation. These design insights can provide a guide for the optimization of advanced designs using any fabrication and material constraints. The successful fabrication of LC-DFB lasers with higher order gratings using stepper lithography was also demonstrated. The lasers had excellent yields for a first fabrication attempt, and the performance was quite good given the range of fabrication variations. With some further maturation of the design these LC-DFB lasers could have commercial potential, perhaps integrated with other optoelectronic devices. Extraction of the effective coupling coefficient for the standard grating design showed good agreement with the expected theoretical results. In the appendices, a the mask design, and an example of a 4x4 optical switch that could be monolithically integrated with these lasers, are described.

8.1 Modeling Summary

The epitaxial growth structure of this laser was first modeled and optimized using LAS2D simulation software. The grating properties were then described by extending a modified coupled-mode analysis to a two-dimensional cross-section. This was applied to the LC-DFB laser to obtain modified coupled-mode coefficients for different ridge geometries. The effective coupling coefficient often differs substantially in both magnitude and phase compared to the simple coupling coefficient, proving the need for this extended treatment.

The effective coupling coefficient, κ_{eff}, depends significantly on duty cycle as shown in Figure 28, with N maxima occurring in the $|\kappa_{eff}|$ *vs.* γ characteristic, and N-1 phase jumps occurring in the $\phi(\kappa_{eff})$ *vs.* γ characteristic for a grating of order N. Larger duty cycles generally produce stronger gratings. It is often useful to have a higher order grating with a large duty cycle rather than a lower order grating for a given minimum manufacturing resolution, since this can provide higher κ_{eff} values according to Figure 30. The grating coupling can be strengthened by using a smaller W_N or wider W_W, but these values must also be determined with the electrical properties of the laser in mind. The grating height produces periodic resonances in the partial wave terms as shown in Figure 32, producing a corresponding resonance in the magnitude and phase κ_{eff}. These resonances also occur in the κ_{eff} *vs.* ridge width characteristics, shown in Figure 35 for the narrow ridge width and Figure 36 for the wide ridge width, but are not as pronounced. In Section 5.5, we showed how the use of different grating shapes can produce coupling coefficients as strong, or stronger, as a rectangular grating, particularly at higher grating orders, and may be simpler to fabricate. Longitudinal modeling demonstrated that the minimum normalized threshold gain, $(\alpha L)_{\min}$, closely follows the κ_{eff} characteristic. For a given grating geometry, there will be a cavity length that produces the smallest minimum threshold gain. This cavity length balances the increased coupling of a longer cavity length with a lower waveguide loss of a shorter length. There will also be particular duty cycles to be avoided where the Bragg detuning changes abruptly and the lasing mode wavelength will not be as stable. The normalized gain difference, or NGD, will increase with $\phi(\kappa_{eff})$. Extending the analysis to a quasi-3D model more accurately shows the longitudinal characteristics of the laser. This model matches well with previously published experimental results, but was too time-consuming to apply to the numerous grating variations considered here. To extract the coupling coefficients from the optical spectrum, a Green's function approach, outlined in Section 7.7, was used.

This model was used with a 10-dimensional simplex algorithm to find the best fit of the model parameters to the experimental data.

Appendix B describes further modeling that was performed for a quantum well intermixed SOA-based 4x4 optical switch that could potentially be integrated with the LC-DFB lasers described here. In particular, the amount of blueshift in the absorption spectrum with different quantum well compositions, strains, and thicknesses was calculated using Fick's model for diffusion and Chuang's strain model. In addition, a compact 1x4 MMI design for use in this switch is described, and modeled using the beam-propagation method. The proposed 4x4 non-blocking switch layout has a footprint of only 5.3 mm x 3.4 mm, and has an estimated insertion loss of 22.8 dB. This loss would be compensated by the SOA regions of the switch.

8.2 Experimental Summary

SEM photos of the fabricated gratings showed that they were within 15 nm of the target period, with smooth and vertical sidewalls. The SEM photos also showed rounding of the rectangular grating teeth. Analysis of this rounding revealed that it resulted in a significant drop in the magnitude of the calculated coupling coefficient from 26 cm^{-1} to 12 cm^{-1} for the standard third-order grating design. IV measurements of the lasers showed good metal contacts, with resistances of < 5 ohms for bias currents of up to 300 mA.

The Fabry-Perot lasers were useful test structures, providing basic information on the quality of the MQW wafer. The threshold currents of these lasers was much higher than those calculated using LAS2D. While LAS2D estimated threshold currents of 8.5 mA for the 500 μm long laser with a 4 μm wide ridge, the average measured threshold current was 62 +/- 4 mA, with a lowest measured value of 55 mA. The value of J_0 was determined from the threshold currents of these lasers to be 1240-1380 A/cm^2, large values that are consistent with the additional loss. Using a rough estimation of the optical loss from the external quantum efficiency, the internal modal loss was found to be 18.0 – 37.3 cm^{-1}. This is much larger than the value of 7.5 cm^{-1} calculated by LAS2D, suggesting that a significant source of loss is neglected by LAS2D. A likely source of the additional losses is an excessive overlap of the optical mode with the metal contact layers. Our simulations in Chapter 5 that included this effect calculated a loss of 25 cm^{-1}, providing additional proof that the metal contact layers are the dominant source of the additional loss. Fabrication constraints prevented etching the ridge any deeper than 0.4 μm, though ridge depths of 1-1.5 μm are more typical for FP lasers. This additional loss must be considered in any future improvements to this design. One suggestion to avoid this is to simply do a two-step etch, one for a higher central ridge, and one for the grating region, as shown in Figure 105. The gain spectrum of a 1 mm long 1.5 μm ridge width FP laser, calculated using the Hakki-Paoli method, shows a gain peak at a wavelength of 1311 nm at a temperature of 298 K, with a 3 dB bandwidth of 24 nm. The gain is red-shifted as the temperature increases, up to a gain peak of 1330 nm measured at 323 K. This represents a shift with temperature of 0.76 nm/K for the material gain.

The fabricated lasers with third-order gratings and longer cavity lengths all demonstrated DFB lasing, with SMSR values of up to 54 dB. The reduced coupling coefficient due to grating rounding is likely the reason why we failed to observe DFB lasing for the 500 μm cavity length lasers, with $\kappa L = 0.6$. The fourth-order gratings did not show DFB lasing. It would be useful to obtain SEM photos of the fourth-order gratings to help determine the cause of their failure. The operational third-order DFB lasers were heavily weighted to the 1 mm cavity length, with 51% of the lasers at this cavity length showing single-mode operation. This is much higher than the overall DFB yield of 15% for third-order lasers of all cavity lengths, and an extremely good yield for a first attempt at a semiconductor chip design. This is due to two main reasons: 1) the weak grating preventing DFB lasing at shorter cavity lengths, and 2) the longer cavity length bars having been cleaved near the wafer edge where, due to cross-wafer non-uniformities, the PL peak of the quantum well active region is closer to 1250 nm than 1310 nm.

The functional third-order DFB lasers showed average threshold currents ranging from 80 – 129 mA for the 1 mm long laser cavity length, and average slope efficiencies from 0.078 – 0.117 mW/mA. The best overall design had a cavity length of 1 mm and ridge widths of W_N/W_W = 2/4 (μm), with a threshold current of 86 +/- 3 mA and a slope efficiency of 0.104 +/- 0.005 mW/mA. This is comparable to the average threshold current of 84 +/- 1 mA for the 4 μm ridge width. Despite the additional source of loss due to the higher order grating, this design shows threshold currents comparable to the Fabry-Perot design. The slope efficiency of the best DFB laser design is still less than for both the FP lasers, with 0.2 mW/mA for the 1.5 μm ridge width and 0.12 mW/mA for the 4 μm ridge width.

The LC-DFB lasers had a low temperature dependence, as expected, with a spectral shift of the lasing peak of 0.06 nm/K compared to 0.65 nm/K for the Fabry-Perot device measured. The average T_0 for the measured DFB lasers was 303.2 K, with values ranging from a minimum of 300.3 for a 750 μm long laser to a maximum of 308.3 K for a 1 mm laser. The characteristic temperatures were all smaller, but not significantly, than the single FP laser which had $T_0 = 313$ K.

The final, and most complicated analysis, was the extraction of the modified coupled mode coefficients from the amplified spontaneous emission spectrum. This required a ten-dimensional non-linear fitting procedure using the simplex algorithm. The unconstrained fit was accurate to within an average deviation of 7.5%, giving a $\kappa_{eff} = 12.5\angle 1.38$ +/- $1.4\angle 0.05$ cm^{-1}. This showed a significant deviation in phase compared to an expected theoretical value of $\kappa_{eff} = 12.2\angle -0.16$ cm^{-1} calculated from the SEM photo of Figure 72, but a rough calculation showed that this experimental value agrees well with a grating closely matching the standard grating shown in Figure 71 that has a calculated $\kappa_{eff} = 12.3\angle 1.41$. Within the observed fabrication variations, this measurement of the effective coupling coefficient showed good agreement with our theoretical analysis.

In conclusion, this thesis has presented a complete, self-consistent model of LC-DFB lasers, including suggested optimal design parameters, mask design, laser fabrication, test and measurement, and analysis of the experimental results. This comprehensive portrait of these lasers has revealed many positive qualities that should provide encouragement for those who will continue research on this laser.

8.3 Future Work

I have been fortunate to have a thesis topic that has provided a wealth of interesting results. Like all good thesis topics, it has also offers abundant opportunities for future work, including both new applications and theoretical investigations. The grating shape analysis of Chapter 5 has suggested a counter-intuitive method of improving the grating strength by using other shapes such as triangular, sinusoidal or trapezoidal. It is still an open question whether these different shapes could be easily and reliably manufactured. However, the unintentional rounding of the grating teeth that was observed in the fabricated gratings seems to suggest that curved grating teeth can be manufactured, perhaps by using sub-resolution mask features. A full investigation of different grating shapes, perhaps using e-beam lithography for more accurate patterning, would provide experimental validation of the theoretical predictions made here. It would also be helpful to simulate the impact that variations in the grating period will have on the performance of the laser.

The high threshold currents observed in the fabricated lasers suggest that the lossy metal contact layers are too close to the optical mode. These losses could be mitigated by increasing the height of the central ridge, while keeping the adjacent grating layers at a height convenient for manufacturing, as shown by Figure 105. If this geometry is to be used, it should be modeled using the simulation tools developed in this thesis. In addition, the losses could be reduced by using some of the low threshold gain grating geometries demonstrated in Chapter 5, particularly larger duty cycles. Unfortunately the larger duty cycle gratings could not be successfully fabricated since we were pushing the limits of the stepper lithography resolution. The laser design could also be readily adapted to other wavelengths. Of particular interest is the telecommunications C-band around 1550 nm, where there is minimal loss in a standard optical fiber. Using larger Bragg wavelengths would allow longer grating periods to be used, easing the fabrication tolerances.

These laterally-coupled gratings are also not limited to laser applications. In addition, the gratings could be used in photonic integrated circuits as wavelength filters, or to reflect light at particular points. These gratings could also be used to provide a high degree of optical isolation where desired on a photonic circuit. Bragg gratings have numerous uses in photonic systems, and any of these could be developed using these laterally-coupled gratings.

Packaging the LC-DFB laser would allow it to be tested in a fiber-optic communication system. Packaging optoelectronic components is not a trivial problem, and numerous compromises between cost and performance must be made. A properly designed package must not only protect the laser chip from the environment, but also provide thermal heat sinking, allow stable and efficient coupling to an output fiber, and provide the proper electrical connections for DC, or high-speed RF current if needed. The package may also include monitoring of the laser output using a built-in photodiode. Particularly for high-speed operation, minimizing the parasitic capacitances and inductances of the laser package is critical and requires extensive modeling of these effects. A spot size converter would improve the efficiency of coupling from the optical waveguide mode to a more circular fiber optic mode. Placing the laser chip on a carrier, and then wire-bonding the electrical leads is a standard practice that would improve the robustness, and hence the lifetime, of the laser.

The LC-DFB laser design holds promise as a dual-wavelength source for the generation of microwave signals. In this fabrication run, dual-wavelength sources were included on the LC-DFB mask, but did not perform well. Fabricating precise grating periods out of either side of the ridge using e-beam lithography may be necessary to improve the results of the dual-wavelength gratings. There has been very little theoretical work on dual-wavelength LC-DFB designs up until now, and proper modeling of the dual-wavelength lasers would be a useful next step.

APPENDIX A – AUTOMATED MASK LAYOUT WITH DW-2000

The mask layout for the LC-DFB lasers described in this thesis was created using an automated layout algorithm implemented with DW-2000 software. Rather than creating a layout algorithm that only places the exact elements needed for a particular mask, this algorithm uses 'p-cells' to allow the dimensions of similar devices in the layout to be quickly and easily changed without requiring a complete rewrite of the mask script.

The idea behind the use of p-cells is to avoid rigidly coding individual device dimensions (in our case, a laser), instead using a general layout function to create an instance of each device given arbitrary input parameters. For instance, rather than encoding separately LC-DFB lasers with grating periods of 300, 400, 500 and 600 nm, a general code is written that will create a laser for any given grating period. Instead of rewriting, or copy and pasting the code for a specific laser repeatedly, the code is called with a single parameter, in this case the period, varying for each device.

The layout described in Chapter 7 used four different types of p-cells to create all of the LC-DFB design variations: a standard LC-DFB laser, a FP laser, a dual-wavelength laser, and a phase-shifted DFB laser. This is a somewhat arbitrary choice, as it was possible to create every design variation on the mask using a single, all-purpose p-cell. The more modular approach used here, however, made it simpler to encode the mask and to eliminate unnecessary code for future masks. For example, future masks are unlikely to include lasers with phase-shifted gratings, since these devices exhibited poorer performance. The parameters used for the standard DFB p-cell are shown in Table 9, the parameter names are defined in a diagram of a standard p-cell shown in Figure 106.

Parameter name	Default Value (µm)
WRidgeW	4
NRidgeW	1.5
Period	0.608
Duty_cycle	0.5
LaserLen	2000
TrenchW	20
MetalW	200
OutlineW	400

Table 9. Standard DFB laser p-cell parameters

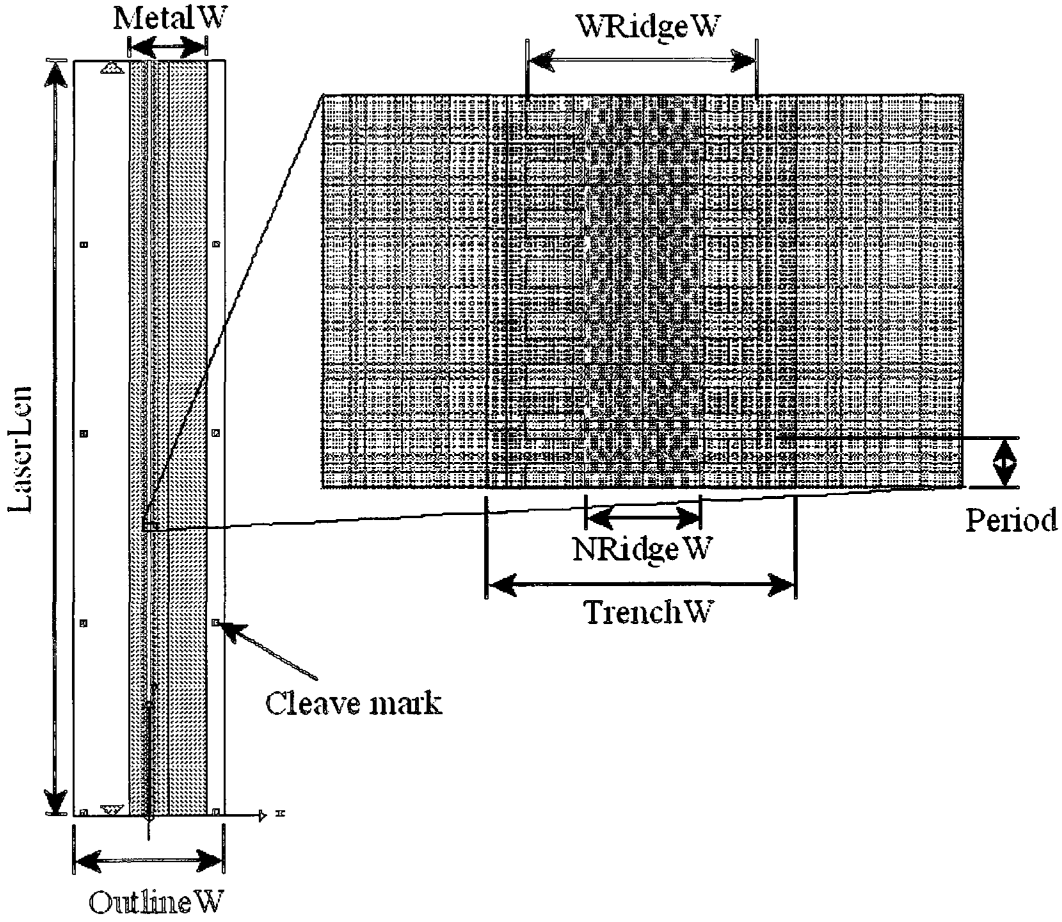

Figure 106. Standard p-cell with grating detail

APPENDIX B – APPLICATION TO OPTICAL SWITCHING

One of the motivations for the LC-DFB laser is that it can be readily integrated with other photonic components. This Appendix describes one such example of an integrated optical device, a 4x4 non-blocking optical switch. This monolithically-integrated switch can be readily combined with the lasers described above to produce a multifunctional photonic integrated circuit. For instance, the lasers could act as sources for the add ports of a reconfigurable add-drop multiplexer (ROADM) module. This chapter begins with a brief introduction to monolithically-integrated optical switches and using quantum well intermixing (QWI) as a monolithic integration method. The motivation for pursuing 4x4 SOA-based switches is described. Next, QWI is discussed in more detail, and a simulation of intermixing in strained quantum wells is outlined. Particular emphasis is placed on intermixing of tensile-strained quantum wells, as the SOA-based switch will use tensile strain in the multi-quantum well active region to reduce the polarization dependent gain. The use of tensile strain will also introduce TE and TM polarization to the laser, complicating the analysis above. The reconsideration of the laser model to include TM polarization is beyond the scope of this thesis. It is also possible to use compressively-strained quantum wells to implement the switch. This may be the preferred option if the laser is integrated on the same chip, since the polarization of the generated light will be overwhelmingly TE, eliminating the need for low PDL switching using tensile-strained quantum wells. The next section of this Appendix features the design of a 1x4 MMI splitter/combiner that is a critical part of the overall 4x4 optical switch. This device has low insertion loss, excellent output uniformity, and a compact size. Finally, in the final section, the overall 4x4 integrated switch design is presented.

B.1 Introduction

The development of next-generation fiber-optic networks will require fast and flexible routing of high-volume traffic through many optical channels. High-speed multiple-channel optical switches are a necessary enabler. Numerous approaches have been proposed, including using Mach-Zehnders [110], total-internal reflection [111], and ring resonators [112]. Switches based on semiconductor optical amplifiers (SOAs) offer minimal insertion loss due to gain compensation in forward-bias, have low crosstalk due to high attenuation in reverse-bias, and can switch at high speeds due to the nanometer-scale switching time of SOAs [113], [114].

SOA-based switches can be realized in disparate monolithic integration modalities, such vertical coupling [115], selective-area regrowth [116], or quantum well intermixing (QWI) [117]. We implement a 4x4 optical switch using QWI, a process that has demonstrated good results for other monolithically-integrated devices such as lasers [118], [119]. Various implementations of QWI exist, including ion-implantation [120], impurity-free vacancy disordering [121], sputtered silica-induced intermixing [122], pulsed laser irradiation induced intermixing [123], and inductively-coupled plasma-enhancement [124]. We use the inductively-coupled plasma process, but our design it is not restricted by it.

Most earlier work has focused on 2x2 switches, for example, the SOA-based optical switches fabricated using QWI in [117]. Integrated 4x4 SOA switches with a low polarization dependence and insertion loss have been demonstrated using regrown passive waveguides [116]. Using integrated 4x4 switches as building blocks for large-scale ROADMs in place of 2x2 switches reduces alignment issues and the number of assembly steps in manufacturing. It also potentially reduces the number of separate temperature control devices that may be required.

We will use a non-blocking tree architecture, shown in Figure 107, for our integrated 4x4 switch. It requires eight 1x4 splitters, eight 1x4 combiners, and 16 SOAs. This 4x4 architecture has an intrinsically higher splitting/combining loss (12 dB, or 6 dB for each 1x4 splitting/combining operation) than a 2x2 switch (6 dB, or 3 dB for each 1x2 splitting/combining operation). However, if we wish to implement a 4x4 switch using

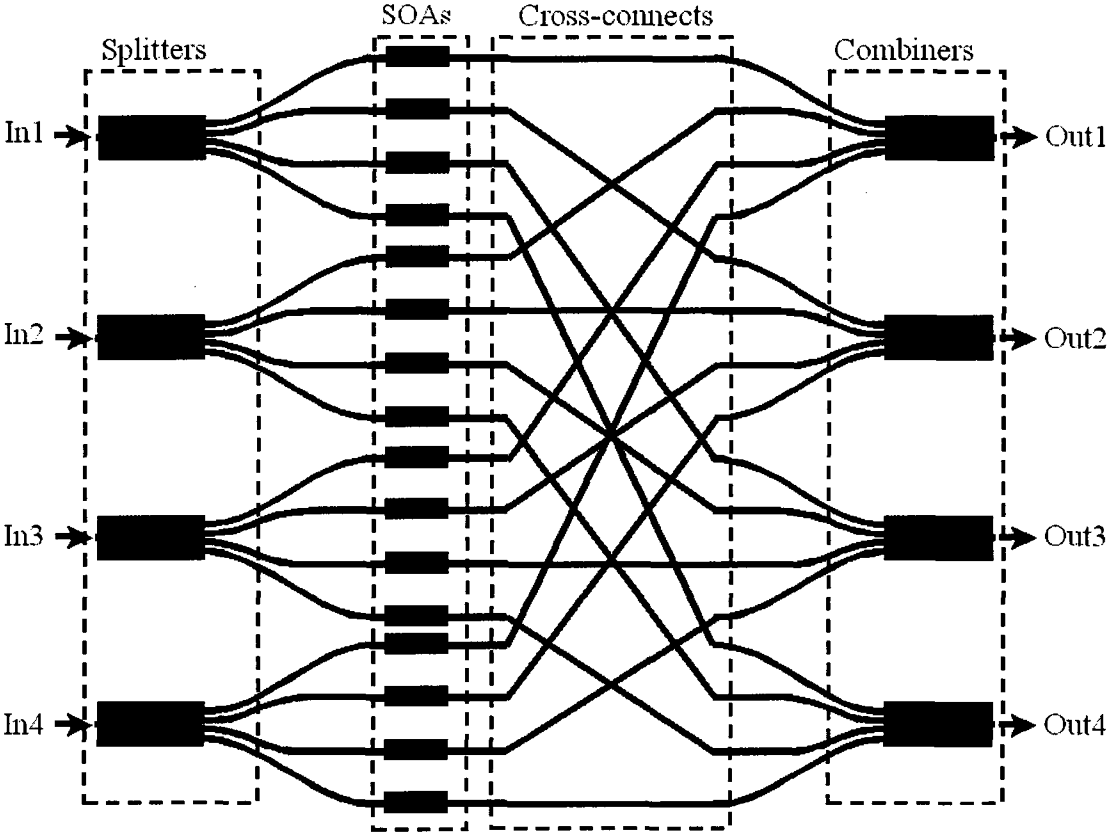

Figure 107. **Tree architecture for a non-blocking 4x4 SOA switch**

2x2 building blocks, a nonblocking configuration such as a Clos network [125] requires 6 discrete 2x2 switches, with three 2x2 switches in each path, for total splitting/combining losses of 18 dB per channel. The fully integrated switch can provide lower losses without even considering the additional coupling losses that would occur between discrete switching elements. To keep the integrated switch loss to a minimum, it is necessary to keep excess losses as low as possible. To realize such low excess losses for our non-blocking integrated 4x4 switch, we report the detailed design of our multi-quantum well (MQW) active region and our 1x4 splitters/combiners.

B.2 Quantum Well Intermixing

The fabrication of quantum wells requires thin layers of different material compositions to be deposited on a substrate. The natural response of adjacent materials with a concentration gradient is to have the materials flow into each other, i.e. intermix, from the layers of high concentration to layers of low concentration. The basic mathematical formulation of this diffusion of materials is known as Fick's laws. At low temperatures the crystal lattice of InP quantum wells is stable and negligible intermixing occurs. Only at very high temperatures, typically around 600°C depending on the exact epitaxial layer structure and growth technique used [126] does natural intermixing occur in as-grown InP-InGaAsP wells. The goal of QWI techniques is to modify the quantum wells in the desired passive sections such that these regions will begin to intermix at temperatures lower than the as-grown quantum wells. The wafer is then annealed at this lower temperature, causing intermixing in the passive regions and leaving the rest of the quantum wells unaffected. This intermixing causes a blue-shift in the absorption spectrum of the quantum wells that greatly reduces optical loss in the passive regions. The tailoring of multiple bandgaps can thus be achieved with the same nominal MQW epitaxial growth structure. To best realize polarization independence in SOA regions, tensile-strained quantum well active regions are needed. However, to achieve the same transition energies, these require larger quantum well thicknesses than do unstrained quantum wells. Since thicker quantum wells do not intermix as easily, our analysis below considers the impact of tensile strain on the blue-shifting induced by the quantum well intermixing process.

B.2.1 Theory

The in-plane strain, ε, of an interdiffused $In_{1-x}Ga_xAs_yP_{1-y}$ quantum well grown along the z-axis is given at each point by the local lattice constants using (3.7). This in turn can be used to determine the local bandgap shifts according to (3.10), (3.11), and (3.14), as described earlier in Section 3.1.

The bandgap shifts and strains depend in turn on the local composition of the intermixed quantum well. The diffusion of atoms from the intermixing process can be modeled by a one-dimensional diffusion equation, also known as Fick's first law:

$$J = -D\frac{\partial C}{\partial z}, \tag{B.1}$$

where J is the atomic flux, D is the diffusion coefficient, and C is the atomic concentration. The concentration at any given time, assuming mass balance and a constant diffusion coefficient, is described by Fick's second law as

$$\frac{\partial C}{\partial t} = D\frac{\partial^2 C}{\partial z^2}. \tag{B.2}$$

A reasonable approximation to a quantum well embedded in barrier material is given by a layer of negligible thickness with initial atomic species concentration C_0 and surrounded by infinitely thick layers. In this case, solving (B.2) reveals that the diffusant concentration takes the familiar Gaussian profile in time:

$$C(z,t) = \frac{C_0}{2\sqrt{\pi D t}}\exp\left(-\frac{z^2}{4Dt}\right). \tag{B.3}$$

For a material of finite thickness *h*, the solution to (B.2) is given in term of the error function, *erf*, as

$$C(z,t) = \frac{C_0}{2}\left(erf\left(\frac{h/2+z}{2L_d}\right) + erf\left(\frac{h/2-z}{2L_d}\right)\right), \tag{B.4}$$

where the degree of diffusion is characterized by the interdiffusion length

$$L_d = \sqrt{Dt}\,. \tag{B.5}$$

In general, the diffusion lengths of the semiconductor group III and V species that comprise the sub-lattices are different, $L_{d,III} \neq L_{d,V}$. An additional parameter, known as the interdiffusion ratio, *k*, is needed to fully characterize diffusion:

$$k = \frac{L_{d,V}}{L_{d,III}} \tag{B.6}$$

The faster diffusion of group V materials in $In_{1-x}Ga_xAs_yP_{1-y}$ results in $k > 1$, with typical values being $1.5 < k < 2$. A value of $k = 1.7$ has been experimentally demonstrated [127],[128], and will be used here. To determine blueshift, the concentration of the group III and V elements after interdiffusion, $C_{\mathrm{III(V)}}$, is first calculated separately at each point, *z*, as

$$C_{III(V)} = C_{B,III(V)} + \frac{C_{QW,III(V)} - C_{B,III(V)}}{2}\left[erf\left(\frac{L_{QW}/2+z}{2L_{d,III(V)}}\right) + erf\left(\frac{L_{QW}/2-z}{2L_{d,III(V)}}\right)\right], \tag{B.7}$$

where the initial concentrations in QW and barrier (B) are $C_{QW,\mathrm{III(V)}}$ and $C_{B,\mathrm{III(V)}}$, respectively, for the species in either group III or group V.

The bandgap of the $In_{1-x}Ga_xAs_yP_{1-y}$ material at each location is calculated from (3.15), while the strain and effective masses of electrons and light- and heavy-holes are determined at each location through interpolation. The strain and bandgap are used to determine the local band edge shifts. An example of the band profile for a diffusion length of 0.8 nm is shown in Figure 108 for a 13 nm thick quantum well with 0.5% tensile strain.

Quantum well conformation being known, the one-dimensional Schrödinger's equation (3.1) may be solved for the conduction and valence bands energy levels. The finite square well approximation used in Section 3.1 is no longer valid, so the answer must be found using a numerical differential equation solver. We find the numerical solution using finite-element analysis with COMSOL software [85]. As before, the differences between the conduction band and the light- and heavy-hole energy levels provide the transition energies of the intermixed quantum well. The blue-shift due to the intermixing process can be calculated by comparison with the as-grown (unintermixed, square) quantum wells. Since we are using tensile strain, the light-hole valence band is shifted upwards, so the conduction band to light-hole valence band transition has the lowest energy and is therefore dominant, as shown earlier in Figure 10. The conduction band to light-hole valence band transition provides a more balanced gain for both TE and TM polarizations, so the polarization-dependent gain (PDG) of tensile-strained quantum wells is reduced compared to unstrained or compressively-strained quantum wells.

B.2.2 Quantum Well Intermixing Analysis Results

In this analysis, all quantum wells were embedded in 12 nm thick $In_{0.93}Ga_{0.07}As_{0.15}P_{0.85}$ barrier material that is lightly (~0.01%) compressively strained. Quantum wells of

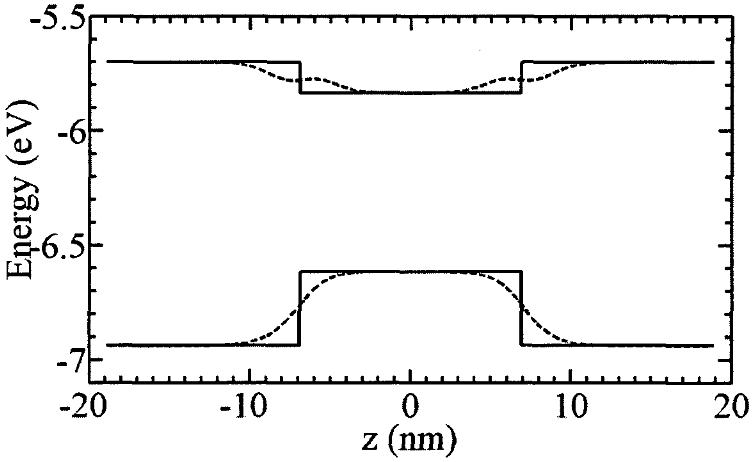

Figure 108. Conduction band and light-hole valence band of 0.5% tensile-strained 13 nm InGaAs quantum well in 0.01% compressive-strained InGaAsP barrier material. Solid lines are for the unintermixed quantum well, dashed lines are for the quantum well intermixed with a group III diffusion length of 0.8 nm and *k*=1.7.

specific tensile strain were achieved by varying the quaternary concentrations while adjusting the quantum well thickness to maintain a constant conduction band to light hole transition energy of 0.81 eV (1530.7 nm) in the unintermixed quantum well. The greater the tensile strain, the thicker the quantum well needed to maintain a transition energy of 0.81 eV in the unintermixed quantum well. The MQW active region is embedded in a double heterostructure whose growth structure is given in Table 10. This p-i-n SCH structure has been chosen to provide good electrical and optical confinement in the SOA regions. The doping is minimal to reduce the intervalence band absorption in the passive waveguide regions after the intermixing process. To provide horizontal confinement, a 4 μm wide ridge waveguide is used.

The quantum well thicknesses required for 0.3%, 0.5%, and 0.7% tensile-strained quantum wells were 11.2, 12.2, and 13.8 nm, respectively. As shown in Figure 109, when thicker quantum wells are intermixed, they have smaller blue-shifts for the same diffusion length value than thinner, less strained quantum well structures. These data were obtained from the finite-element solution of Schrödinger's equation as noted above.

Layer	Material	Thickness (μm)	Doping (cm-3)
11 – P cap	InGaAs	0.1	Zn: 1 x 1019
10 – P cap	$Ga_{0.19}In_{0.81}As_{0.41}P_{0.59}$	0.02	Zn: 1 x 1018
9 – Ridge	InP	0.6	Zn: 3 x1017
7 – Upper clad	$Ga_{0.31}In_{0.69}As_{0.66}P_{0.34}$	0.2	Zn: 1 x 1017
6 – Barrier (repeat 4)	$Ga_{0.35}\ In_{0.65}As_{0.77}P_{0.23}$	0.012	Undoped
5 – QW (repeat 5)	$Ga_{0.54}\ In_{0.46}As$	0.0122	Undoped
4 – Barrier	$Ga_{0.35}\ In_{0.65}As_{0.77}P_{0.23}$	0.012	Undoped
3 – Lower clad 2	$Ga_{0.31}In_{0.69}As_{0.66}P_{0.34}$	0.2	Si: 1 x 1017
2 – Lower clad 1	InP	0.04	Si: 5 x 1017
1 – Buffer	InP	2	Si: 1 x 1018
0 – Substrate	InP	130	Si: 4 x 1018

Table 10. Epitaxial growth structure for a quantum-well intermixed SOA switch

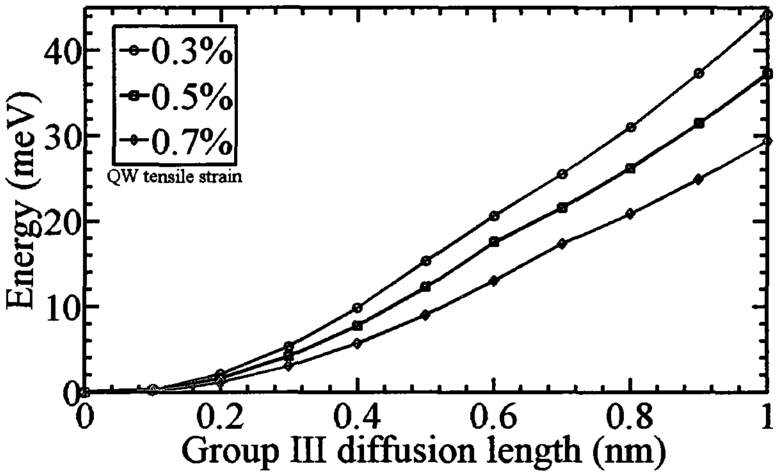

Figure 109. **Blue-shift of conduction band to light-hole band transition energy *vs.* group III diffusion length for quantum wells with an unintermixed transition energy of 0.81 eV and tensile strains of 0.3, 0.5 and 0.7%. *k*=1.7 in this calculations.**

The blueshift is expected to saturate beyond diffusion lengths of 1 nm as the neighboring quantum wells in the MQW stack begin to diffuse into each other.

For our intended intermixing of 0.3% tensile-strained quantum wells, we thus reasonably anticipate blueshifts approaching 44 meV. Such blueshifts are less than the 100 meV or more that have been demonstrated for other quantum well compositions [129]. Compared to the results of [130] where a 60 meV blueshift resulted in a passive waveguide loss of 2.98 cm^{-1} our waveguide losses will be larger. Selecting a 0.5% tensile-strained quantum well will give a better polarization dependent gain than 0.3% tensile-strained quantum wells, but its maximum blueshift is less than that of the lower strained system. This smaller blueshift will result in higher waveguide losses that should be determined experimentally.

B.3 1x4 Integrated Optical Splitter/Combiner

The coupler/splitter is a critical component of our 4x4 switch design. In the non-blocking tree configuration used here, a total of eight 1x4 MMI couplers and splitters are used, with two in each input/output path. The couplers and splitters must have a low insertion loss, low wavelength and polarization sensitivity, and good fabrication tolerance. While Y-branch and total internal reflection splitters/combiners have shown promise [131], the excellent performance and fabrication tolerance of multimode interference (MMI) devices have made them a popular choice for monolithically-integrated splitter/combiners, and they are the technology that will be used here.

The length of the multimode interference region for a 1xN splitter is determined, using an effective index method analysis according to [132], as

$$L = \left(\frac{3L_\pi}{4N} \right). \tag{B.8}$$

L_π is the beat length of the two lowest-order modes of the MMI region, whose propagation constants are β_0 and β_1. It can be estimated as

$$L_\pi = \frac{\pi}{\beta_1 - \beta_0} \approx \frac{4 n_r W_e^2}{3\lambda_0}, \tag{B.9}$$

where n_r is the effective ridge refractive index and λ_0 is the free-space wavelength; W_e is an effective width given by

$$W_e = W_M + \left(\frac{\lambda_0}{\pi} \right) \left(\frac{n_c}{n_r} \right)^{2\sigma} \left(n_r^2 - n_c^2 \right)^{-1/2}, \tag{B.10}$$

where W_M is the actual waveguide width and n_c is the effective refractive index of the cladding. We wish to separate the output waveguides of the MMI splitter/coupler by 50 μm to ensure minimal interference between neighboring waveguides, and to have sufficient isolation between adjacent SOA contacts. The effective width of the MMI region determines the spacing of the output waveguides. The beat length has a quadratic dependence on W_e, so the length of the MMI scales rapidly as the spacing required between output waveguides increases. For an output spacing between the four output waveguides of 10 μm, an MMI width of at least W_M = 40 μm is required, leading to a total MMI length of 954 μm. To reach the 50 μm waveguide separation using the weakly-guided ridge waveguides would require a set of four long bends. In particular, the uppermost and lowermost waveguides would have to bend nearly 100 μm to achieve the required separation. BPM simulations of this waveguide have shown that a 100 μm waveguide bend requires a length of 1500 μm to avoid extensive losses. With the addition of such a bend the total device length would be nearly 2500 μm.

A more spatially compact 1x4 splitter/combiner is obtainable using two-stage cascade of 1x2 MMI splitters, as shown in Figure 110. Each 1x2 MMI splitter requires an MMI section with a length of 147 μm. The first MMI splitter provides two waveguides, whose separation from each other is governed by their fourth-order polynomial layouts. At an optimal distance, a second MMI splitter terminates each waveguide at the same tilt angle. Note that, due to the optimized position of the second MMI the two inner waveguides are already separated by about 40 μm when they leave the second splitting stage. The layouts of the resulting four waveguides are then further optimized to yield the desired waveguide separations over with the shortest possible length. The total 1x4 MMI splitter/combiner length, after separating all four waveguides by 50 μm, is 1600 μm. Due to these considerations, using two cascaded 1x2 MMI splitters rather than a single 1x4 MMI splitter improved the compactness of the design by approximately 900 μm.

The 1x4 splitter was simulated via the beam-propagation method using OptiBPM 6.1 software [133]. The two-dimensional simulation was performed using the effective index method to approximate the waveguide of Table 10 in the lateral direction. The BPM simulation used the (1,1) Padé approximation with perfectly-matched layer boundary conditions. The step size used was 0.05 μm in the z-direction, and 0.04 μm in the x-direction. The splitter/combiner had an excess loss of only 1.53 dB for TE polarized light and 1.54 dB for TM, with an output uniformity of < 0.01 dB. The contour plot of the optical field in the splitter, shown in Figure 111, shows minimal scattering, with most

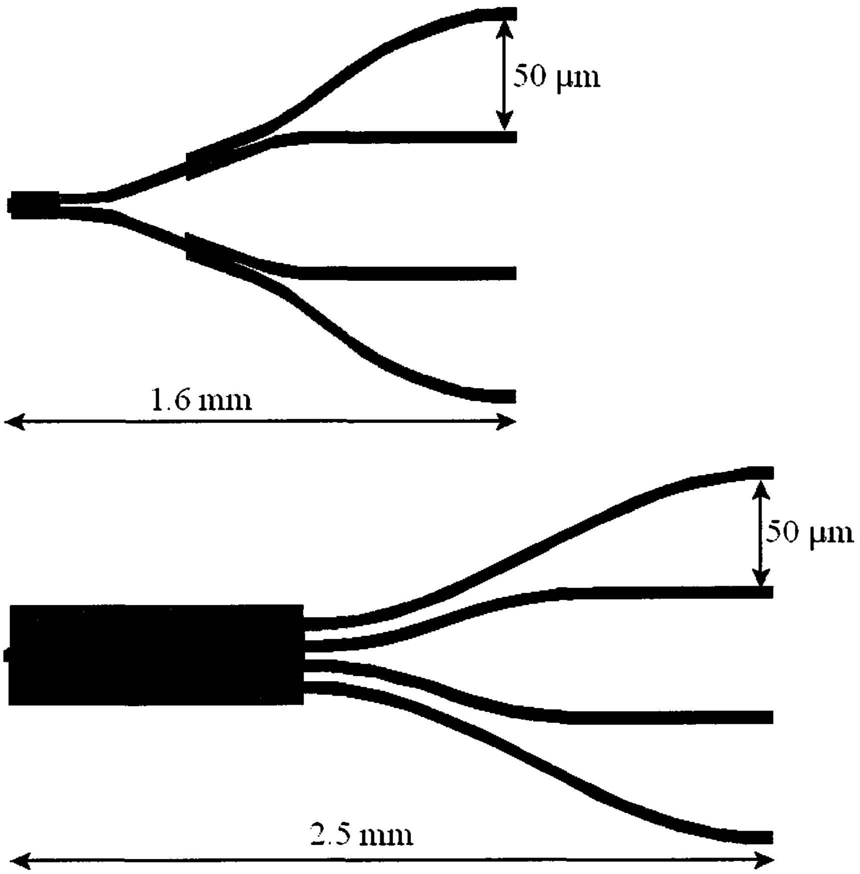

Figure 110. Size comparison of 1x4 MMI splitter using cascaded 1x2 splitters (top), and a single 1x4 splitter (bottom).

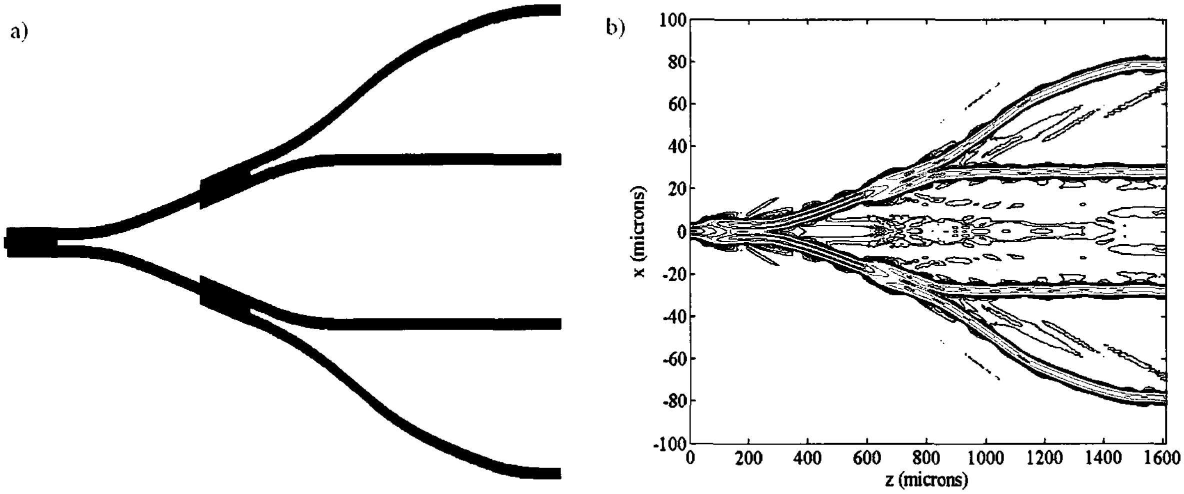

Figure 111. 1 x 4 multimode interference coupler/splitter. a) Layout of coupler/splitter, b) beam-propagation method simulation of splitter with 2 dB contours from 0 to 30 dB.

of the stray light along the central axis.

B.4 Overall Design

The overall layout of the switch is shown in Figure 112. The nonblocking tree architecture requires 16 SOAs and 8 1x4 MMI splitters/combiners. The SOAs are in two blocks of 8, each SOA being 1 mm long and separated by 50 μm from its neighbor. To improve compactness, total internal reflection turning mirrors are created by placing a 45 degree angle etch at appropriate waveguide bends. The excess mirror loss was minimized using two-dimensional finite-element simulations, shown in the inset of Figure 112. However, fabrication limitations, such as surface roughness, will add further losses to the TIR mirrors, and experimental results will be required to fully estimate the losses of the mirror design. Previous TIR mirrors have proven to be capable of 1 dB or less of excess loss [134]. The total footprint of this design is 5.33 mm x 3.44 mm.

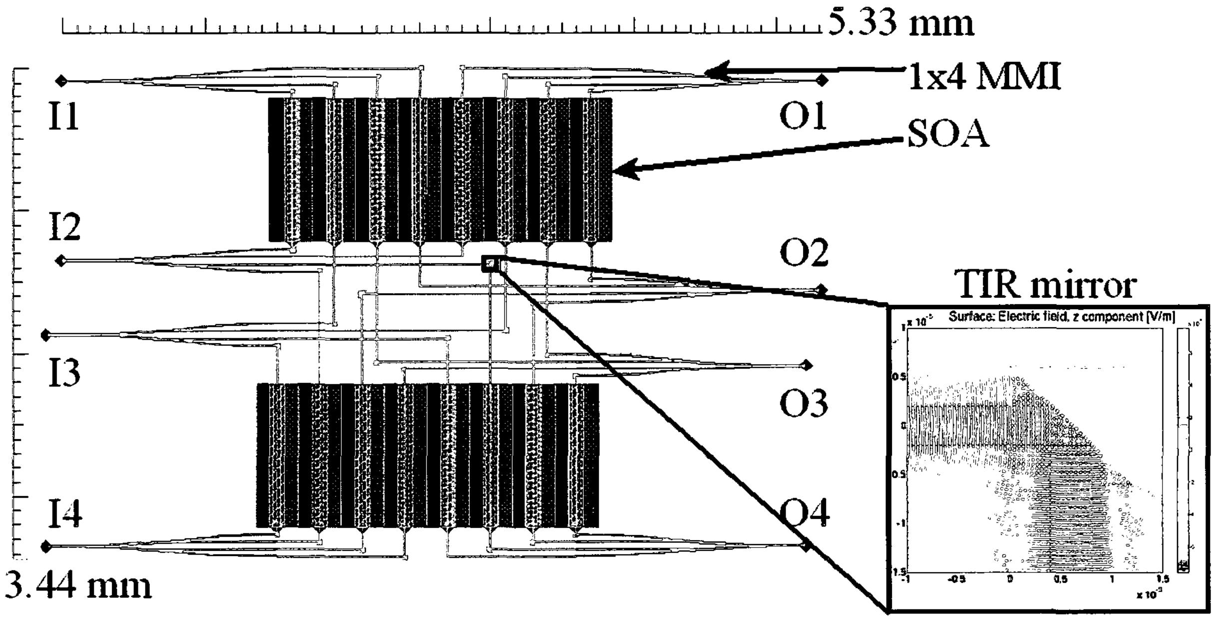

Figure 112. **Layout of 4x4 non-blocking SOA switch architecture with finite-element simulation of TIR mirror (insert).**

The total on-chip losses of the 4x4 optical switch can now be estimated. The loss per path will be due to waveguide losses, splitter/combiner losses, scattering at the turning mirrors, and fiber coupling losses. The longest path in the 4x4 splitter, as shown in Figure 4, is 3 mm in length. We use an estimated modal loss of 6 cm^{-1} for the intermixed waveguides, assuming that for these quantum wells of 38 meV blueshift, the loss will be at least double the 2.98 cm^{-1} loss observed when the blueshift was 60 meV [130]. This results in an estimated 1.8 dB total waveguide loss. The turning mirrors are each assessed a 1.5 dB loss, incorporating an estimated loss due to fabrication imperfections such as surface roughness. Since each path includes two turning mirrors, this will result in 3 dB of turning mirror loss. The splitters/combiners will add 12 dB of loss since there will be one 1x4 splitter and one 4x1 combiner in each path. In addition, each splitter/combiner, as demonstrated in Section 2, introduces 1.5 dB of excess loss, for a total of 3 dB. The combined contribution of all these losses, with approximately 3 dB of fiber coupling loss, is a total loss of 22.8 dB. This total loss is to be compensated by the gain in the SOA region of the device.

REFERENCES

[1] Einstein, *Z. Deutsch Phy.*, 1916.

[2] J. von Neumann, "Notes on the Photon-Disequilibrium-Amplification Scheme, September 16, 1953," *IEEE J. Quantum Electron.*, vol. QE-23, pp. 659-673, June 1987.

[3] A.L. Schawlow and C.H. Townes, "Infrared and Optical Masers," *Phys. Rev.*, vol. 112, pp. 1940-1949, Dec. 1958.

[4] T. Maiman, "Stimulated Optical Radiation in Ruby," *Nature,* vol. 187, pp. 493-494, Aug. 1960.

[5] R. Dupuis, "An Introduction to the Development of the Semiconductor Laser," *J. Quantum Electron.*, vol. QE-23, pp. 651-657, June 1987.

[6] M. Nathan, "Invention of the Injection Laser at IBM," *IEEE J. Quantum Electron.*, vol. QE-23, pp. 679-683, June 1987.

[7] N. Holonyak, "Semiconductor alloy lasers – 1962," *IEEE J. Quantum Electron.*, vol. QE-23, pp. 684-691, June 1987.

[8] R. Rediker, "Research at the Lincoln Laboratory Leading up to the Development of the Injection Laser in 1962," *IEEE J. Quantum Electron.*, vol. QE-23, pp. 692-695, June 1987.

[9] R. N. Hall, G.E. Fenner, J.D. Kingsley, T.J. Soltys, and R.O. Carlson, "Coherent light emission from GaAs junctions," *Phys. Rev. Lett.*, vol. 9, pp. 366-368, 1962.

[10] M.I. Nathan, W.P. Dumke, G. Burns, F.H. Dill, and G. Lasher, "Stimulated emission of radiation from GaAs p-n junctions," *Appl. Phys. Lett.*, vol. 1, pp. 62-64, 1962.

[11] T.M. Quist, R.H. Rediker, R.J. Keyes, W.E. Krag, B. Lax, *Appl. Phys. Lett.*, vol. 1, pp. 91-92, 1962.

[12] N. Holonyak, and S.F. Bevacqua, "Coherent visible light emission from GaAsP junctions," *Appl. Phys. Lett.*, vol. 1, pp. 82-84, 1962.

[13] I. Hayashi, M.B. Panish, and P.W. Foy, "A low threshold room temperature injection laser," *IEEE J. Quantum Electron.*, vol. 5, pp. 211-212, 1969.

[14] I. Hayashi and M.B. Panish, "GaAs $Ga_xAl_{1-x}As$ heterojunction injection lasers which exhibit low threshold room temperature operation," *J. Appl. Phys.*, vol. 41, pp. 150-163, 1970.

[15] H. Kressel, and N. Nelson, "Close confinement gallium arsenide PN junction laser with reduced optical loss at room temperature," *RCA Rev.*, vol. 30, pp. 106-113, 1969.

[16] Zh. I. Alferov, V.M. Andreev, E.L. Portnoi, and D.N. Tretyakov, "Injection properties of n-$Al_xGa_{1-x}As$ p-GaAs heterojunctions," *Sov. Phys. Semicond.*, vol. 2, pp. 843-845, 1969.

[17] J.P. van der Ziel, R. Dingle, R.C. Miller, W. Wiegmann, and W.A. Nordland, Jr., "Laser oscillation from quantum states in very thin GaAs-$Al_{0.2}Ga_{0.8}As$ multilayer structures," *Appl. Phys. Lett.*, vol. 26, pp. 463-465, Apr. 1975.

[18] R.C. Miller, R. Dingle, A.C. Gossard, R.A. Logan, W.A. Nordland, Jr., and W. Wiegmann, "Laser oscillation with optically pumped very thin GaAs-$Al_xGa_{1-x}As$ multilayer structures and conventional double heterostructures," *J. Appl. Phys.*, vol. 47, pp. 4509-4517, Oct. 1976.

[19] N. Kirstaedter, N.N. Ledentsov, M. Grundmann, D. Bimberg, V.M. Ustivov, S.S Ruvimov, M.V. Maximov, P.S. Kop'ev, Zh.I. Alferov, U. Richter, P. Werner, U. Gösele, and J. Heydenreich, "Low threshold, large T_0 injection laser emission from (InGa)As quantum dots," *Electron. Lett.*, vol. 30, pp. 1416-1417, Aug. 1994.

[20] J. Carroll, J. Whiteaway, and D. Plumb, *Distributed feedback semiconductor lasers*, SPIE Press, London, UK, 1998.

[21] Y. Suematsu, K. Kishino, S. Arai, and F. Koyama, "Dynamic single-mode semiconductor lasers with a distributed reflector," Chapter 4 in R.K. Willardson and A.C. Beer, eds., *Semiconductors and Semimetals*, vol. 22, Academic Press, San Diego, 1985.

[22] S.L. Chuang, *Physics of Optoelectronic Devices*, Wiley-Interscience, New York, NY, 1995.

[23] W.H. Bragg and W.L. Bragg, *X-rays and crystal structure*, G. Bell, London, UK, 1915.

[24] S. Li, G. Witjaksono, S. Macomber, and D. Botez, "Analysis of surface-emitting second-order distributed feedback lasers with a central grating phaseshift," *IEEE J. Quantum Electron.*, vol. 9, pp. 1153-1165, Sept./Oct. 2003.

[25] H. Kogelnik and C.V. Shank, "Stimulated Emission in a Periodic Structure," *Appl. Phys. Lett.*, vol. 18 pp. 152-154, Feb. 1971.

[26] H. Kogelnik and C.V. Shank, "Coupled-Wave Theory of Distributed Feedback Lasers," *J. Appl. Phys.*, vol. 43, pp. 2327-2335, May 1972.

[27] M. Nakamura, H.W. Yen, A. Yariv, E. Garmire, S. Somekh, and H.L. Garvin, "Laser oscillation in epitaxial GaAs waveguides with corrugation feedback," *Appl. Phys. Lett.*, vol. 25, pp. 224-225, 1973.

[28] M. Nakamura, K. Aiki, J. Umeda, A. Katzir, A. Yariv, and H.W. Yen, "GaAs-GaAlAs Double-Heterostructure Injection Lasers with Distributed Feedback," *IEEE J. Quantum Electron.*, vol. QE-11, pp. 436-439, July 1975.

[29] D.R. Scifres, R.D. Burnham and W. Streifer, "Distributed feedback single heterojunction diode laser," *Appl. Phys. Lett.*, vol. 25, pp. 203-204, Aug. 1974.

[30] H.C. Casey, S. Somekh, and M. Ilegems, "Room temperature operation of low-threshold separate confinement distributed feedback diode lasers," *Appl. Phys. Lett.*, vol. 27, pp. 487-489, Aug. 1975.

[31] Y. Uematsu, H. Okuda, and J. Kinoshita, "Room-temperature cw operation of 1.3-μm distributed-feedback InGaAsP/InP lasers ," *Electron. Lett.*, vol. 18, pp. 857-858, 1982.

[32] K. Utaka, S. Akiba, K. Sakai, and Y. Matsushima, "Room-temperature cw operation of distributed-feedback buried heterostructure InGaAsP-InP lasers emitting at 1.57 μm," *Electron. Lett.*, vol. 17, pp. 961-963, 1981.

[33] B.Fay, "Advanced optical lithography development, from UV to EUV," *Microel. Eng.*, vol. 61-62, pp. 11-24, July 2002.

[34] L.M. Miller, J.T. Verdeyen, J.J. Coleman, R.P. Bryan, J.J. Alwan, K.J. Beernink, J.S. Hughes, and T.M. Cockerill, "A Distributed Feedback Ridge Waveguide Quantum Well Heterostructure Laser," *IEEE Photon. Tech. Lett.,* vol. 3, pp. 6-8, Jan. 1991.

[35] V.V. Wong, W.-Y. Choi, J.M. Carter, C.G. Fonstad, H.I. Smith, Y. Chung, and N. Dagli, "Ridge-waveguide sidewall-grating distributed feedback structures fabricated by x-ray lithography," *J. Vac. Sci. Technol. B*, vol. 11, pp. 2621-2624, Nov/Dec 1993.

[36] R.D. Martin, S. Forouhar, S. Keo, R. J. Lang, R.G. Hunsperger, R. Tiberio, and P.F. Chapman, "InGaAs-GaAs-AlGaAs laterally-coupled distributed feedback (LC-DFB) ridge laser diode," *Electron. Lett.*, vol. 30, pp. 1058-1060, June 1994.

[37] R.C. Tiberio, P.F. Chapman, R.D. Martin, S. Forouhar, and R.J. Lang, "Laterally coupled distributed feedback laser fabricated with electron-beam lithography and chemically assisted ion-beam etching," *J. Vac. Sci. Technol. B,* vol. 12, pp. 3746-3749, June 1994.

[38] R.D. Martin, S. Forouhar, S. Keo, R.J. Lang, R.G. Hunsperger, R.C. Tiberio, and P.F. Chapman, "CW Performance of an InGaAs-GaAs-AlGaAs Laterally-Coupled Distributed Feedback (LC-DFB) Ridge Laser Diode," *IEEE Photon. Tech. Lett.,* vol. 7, pp. 244-246, 1995.

[39] Y. Watanabe, N. Chen, K. Takei, K. Chikuma, N. Futakuchi, and Y. Nakano, "Laterally Coupled Strained MQW Ridge Waveguide Distributed-Feedback Laser Diode Fabricated by Wet-Dry Hybrid Etching Process," *IEEE Photon. Tech. Lett.,* vol. 10, pp. 1688-1690, 1998.

[40] N. Chen, Y. Watanabe, K. Takei, and K. Chikuma, "InGaAsP/InP laterally coupled distributed feedback laser," *Jpn. J. Appl. Phys.,* vol. 39, pp. 1508-1511, 2000.

[41] J.T. Hastings, M. H. Lim, J.G. Goodberlet, and H. I. Smith, "Optical waveguides with apodized sidewall gratings via spatial-phase-locked electron-beam lithography," *J. Vac. Sci. Technol. B.*, vol. 20, pp. 2753-2757, Nov/Dec. 2002.

[42] J.T. Hastings, M. H. Lim, H.I. Smith, "Optical Waveguide with Non-Uniform Sidewall Gratings," *Intl. Patent No. WO 03/102646 A2*, May 30, 2002.

[43] M. Müller, M. Kamp, A. Forchel, and J.-L. Gentner, "Wide-range-tunable laterally coupled distributed feedback lasers based on InGaAsP-InP," *Appl. Phys. Lett.,* vol. 79, pp. 2684-2686, 2001.

[44] M. Müller, F. Klopf, M. Kamp, J.P. Reithmaier, and A. Forchel, "Wide Range Tunable Laterally Coupled Distributed-Feedback Lasers Based on InGaAs-GaAs Quantum Dots," *IEEE Photon. Technol. Lett.,* vol. 14, no. 9, pp. 1246-1248, 2002.

[45] F. Gerschütz, M. Fischer, J. Koeth, I. Krestnikov, A. Kovsh, and A. Forchel, "Temperature insensitive 1305 nm InGaAs/GaAs quantum dot distributed feedback lasers," *Conference on Lasers and Electro-optics*, CThHH4, May 4-9, 2008.

[46] J. Wiedmann, H.-C. Kim, K. Ebihara, B. Chen, M. Ohta, S. Tamura, J.-I. Shim, and S. Arai, "GaInAsP/InP Distributed Reflector Lasers Consisting of Deeply Etched Vertical Gratings," *Jpn. J. Appl. Phys.*, vol. 40, pp. 6845-6851, Dec. 2001.

[47] L. Bach, S. Rennon, J.P. Reithmaier, A. Forchel, J.L. Gentner, and L. Goldstein, "Laterally Coupled DBR Laser Emitting at 1.55 μm Fabricated by Focused Ion Beam Lithography," *IEEE Photon. Tech. Lett.*, vol. 14, pp. 1037-1039, July 2002.

[48] L. Bach, W. Kaiser, J.P. Reithmaier, A. Forchel, M. Gioannini, V. Feies, and I. Montrosset, "22-GHz Modulation Bandwidth of Long Cavity DBR Laser by Using a Weakly Laterally-Coupled Grating Fabricated by Focused Ion Beam Lithography," *IEEE Photon. Technol. Lett.,* vol. 16, no. 1, pp. 18-20, 2004.

[49] R. Schreiner, P. Nagele, M. Korbl, A. Groning, J.L. Gentner, and H. Schweizer, "Monolithically Integrated Tunable Laterally Coupled Distributed-Feedback Lasers," *IEEE Photon. Tech. Lett.,* vol. 13, pp. 1277-1279, 2001.

[50] B. Reid, M. Poirier, S.R. Das, D. Ducharme, R. Dowlatshahi, S. Langstaff, N.S. Kim, R. Kuchibhatia, and S. Djavani-Tabrizi, "Narrow Linewidth and High Power Distributed Feedback Lasers Fabricated without a Regrowth Step," *ECOC 2003.*

[51] B. Reid, "Weakly Guiding Ridge Waveguides with Vertical Gratings," *Intl. Patent No. WO 2005/011076 A1*, July 31, 2003.

[52] P.K. Das, M. Uemukai, T. Suhara, "InGaAs/AlGaAs Quantum Well Laterally-Coupled Distributed Feedback Laser," *Jpn. J. Appl. Phy.,* vol. 43, pp. 2549-2550, 2004.

[53] J. Wang, J.-B. Tian, P.-F. Cai, B. Xiong, Chang-Zheng Sun, and Yi Luo, "1.55 μm AlGaInAs-InP Laterally Coupled Distributed Feedback Laser," *IEEE Photon. Tech. Lett.,* vol. 17, pp. 1372-1374, 2005.

[54] S. Golka, C. Pflügl, W. Schrenk, and G. Strasser, "Quantum cascade lasers with lateral double-sided distributed feedback grating," *Appl. Phys. Lett.*, vol. 86, 2005.

[55] F. Pozzi, R.M. De La Rue, M. Sorel, "Dual-wavelength InAlGaAs-InP laterally coupled distributed feedback laser," *IEEE Photonics Technol. Lett.*, vol. 18, pp. 2563-2265, Dec. 2006.

[56] A. Laakso, M. Dumitrescu, J. Viheriälä, J. Karinen, M. Suominen, and M. Pessa, "Optical modeling of laterally-corrugated ridge-waveguide gratings," *J. Optical Quantum Electron.*, DOI 10.1007/s11082-009-9292-3, April 2009.

[57] P. Anandarajah, L.P. Barry, and A. Kaszubowska, "Performance Issues Associated with WDM Optical Systems using Self-Seeded Gain Switched Pulse Sources Due to Mode Partition Noise Effects," *IEEE Photon. Technol. Lett.*, vol. 14, pp. 1202-1204, Aug. 2002.

[58] S.L. Chuang, "Efficient band-structure calculations of strained quantum wells," *Phys. Rev. B.*, vol. 43, pp. 9649-9661, 1991.

[59] M. Ogasawara, H. Sugiura, M. Mitsuhara, M. Yamamoto, and M. Nakao, "Influence of net strain, strain type, and temperature on the critical thickness of In(Ga)AsP-strained multi quantum wells," *J. Appl. Phys.*, vol. 84, pp. 4775-4780, Nov. 1998.

[60] G. Letal, "Integrated Distributed Feedback Lasers and Electroabsorption Modulators Fabricated Using Helium-Plasma-Assisted InP Defect Induced Quantum Well Intermixing," *Ph.D. thesis*, McMaster University, 2000.

[61] P.J.A. Thijs, L.F. Tiemeijer, J.J.M. Binsma, and T. van Dongen, "Progress in Long-Wavelength Strained-Layer InGaAs(P) Quantum-Well Semiconductor

Lasers and Amplifiers," *IEEE J. Quantum Elecron.*, vol. 30, pp. 477-499, Feb. 1994.

[62] J.J. Coleman, "Strained-Layer InGaAs Quantum-Well Heterostructure Lasers," *IEEE J. Sel. Topics Quantum Electron.*, vol. 6, pp. 1008-1013, Nov./Dec. 2000.

[63] M. Yamamoto, N. Yamamoto, and J. Nakano, "MOVPE Growth of Strained InAsP/InGaAsP Quantum-Well Structures for Low-Threshold 1.3 μm Lasers," *IEEE J. Quantum Electron.*, vol. 30, pp. 554-561.

[64] LAS2D, Laboratoire d'Optoélectronique, École Polytechnique de Montréal, Montréal, QC, Canada.

[65] A. Champagne and R. Maciejko, *LAS2D Users Guide*, Laboratoire d'Optoélectronique, École Polytechnique de Montréal, Montréal, QC, Canada, January 2006.

[66] M. Asada, A. Kameyama, and Y. Suematsu, "Gain and intervalence band absorption in quantum-well lasers," *IEEE J. Quantum Electron.*, vol. 20, pp. 745-753, 1984.

[67] J. Piprek, J.K. White, A.J. Springthorpe, "What Limits the Maximum Output Power of Long-Wavelength AlGaInAs/InP Laser Diodes?" *IEEE J. Quantum Electron.*, vol. 38, pp. 1253-1259, 2002.

[68] A.M. Shams-Zadeh-Amiri, J.Hong, X. Li, and W.-P. Huang, "Second- and Higher Order Resonant Gratings with Gain or Loss-Part I: Green's Function Analysis," *IEEE J. Quantum Electron.*, vol. 36, pp. 1421-1430, 2000.

[69] J.E.A. Whiteaway, G.H.B. Thompson, A.J. Collar, and C.J. Armistead, "The Design and Assessment of $\lambda/4$ Phase-Shifted DFB Laser Structures," *IEEE J. Quantum Electron.*, vol. 25, pp. 1261-1279, June 1989.

[70] T. Makino, "Threshold Condition of DFB Semiconductor Lasers by the Local-Normal-Mode Transfer Matrix Method: Correspondence to the Coupled-Wave Method," *J. Lightwave Technol.*, vol. 12, pp. 2092-2099, Dec. 1994.

[71] T. Rozzi, F. Chiaraluce, and M. Lanari, "A Rigorous Anlysis of DFB Lasers with Large and Aperiodic Corrugations," *IEEE J. Quantum Electron.*, vol. 27, pp. 212-223, Feb. 1991.

[72] A.J. Lowery, "Transmission-line modeling of semiconductor lasers: The transmission-line laser model," *Int. J. Numerical Model.*, vol. 2, pp. 249-265, 1989.

[73] A.J. Lowery, "Dynamic Modelling of Distributed-Feedback Lasers Using Scattering Matrices," *Electron. Lett.*, vol. 25, pp. 1307-1308, Sept. 1989.

[74] VPIphotonics, Inc., http://www.vpiphotonics.com/photonics_home.php.

[75] B. Reid, I. Woods, J.K. White, K. Hinzer, M. Vitic, D. Robinson, and A. Grabham, "Simulations of statistical parameter distributions in distributed-feedback lasers using a transmission-line laser model," *Photonics North 2004*, Ottawa, ON, 2004.

[76] W. D'Oosterlinck, G. Morthier, R. Baets, and T. Erneux, "Optical Bistability in a Traveling-Wave SOA Connected to a DFB Laser Diode: Theory and Experiment," *IEEE J. Quantum Electron.*, vol. 42, pp. 739-746, Aug. 2006.

[77] S. J. Farlow, *Partial Differential Equations for Scientists and Engineers*, Dover Publications, Inc., New York, NY, 1993.

[78] J.D. Freeze, M.A. Jensen and R.H. Selfridge, "A Unified Green's Function Analysis of Complicated DFB Lasers," *IEEE J. Quantum Electron.*, vol. 33, pp. 1253-1259- Aug. 1997.

[79] H. Wenzel, "Green's Function Based Simulation of the Optical Spectrum of Multisection Lasers," *IEEE J. Sel. Top. Quantum Electron.*, vol. 9, pp. 865-871, May/June 2003.

[80] A. Yariv and A. Gover, "Equivalence of the Coupled Mode and Floquet-Bloch formalisms in periodic optical waveguides," *Appl. Phys. Lett.*, vol. 26, no. 9, pp. 537-539, May 1975.

[81] W. Streifer, D.R. Scifres, and R. Burnham, "Analysis of grating-coupled radiation in GaAs:GaAlAs lasers and waveguides," *IEEE J. Quantum Electron.*, vol. QE-12, pp. 422-428, July 1976.

[82] W. Streifer, D.R. Scifres, and R.D. Burnham, "Coupled wave analysis of DFB and DBR lasers," *IEEE J. Quantum Electron.*, vol. QE-13, pp. 134-141, Apr. 1977.

[83] W.-Y. Choi, J.C. Chen, and C.G. Fonstad, "Evaluation of coupling coefficients for laterally-coupled distributed feedback lasers," *Jpn. J. Appl. Phys.*, vol. 35, pp. 4654-4459, Sept. 1996.

[84] C.H. Chen, L.H. Chen, and Q.M. Wang, "Coupling coefficients of gain-coupled distributed feedback lasers with absorptive grating," *Electron. Lett.*, vol. 32, pp. 1288-1290, Jul. 1996.

[85] *www.comsol.com*, COMSOL Multiphysics 3.4, COMSOL Corporation.

[86] W. Streifer, D. Scifres, and R.D. Burnham, "Coupling Coefficients for Distributed Feedback Single- and Double-Heterostructure Diode Lasers," *IEEE J. Quantum Electron.*, vol. QE-11, pp. 867-873, Nov. 1975.

[87] W. Streifer, R. Burnham, and D. Scifres, "Analysis of Grating-Coupled Radiation in GaAs:GaAlAs Lasers and Waveguides – II: Blazing Effects," *IEEE J. Quantum Electron.*, vol. QE-12, pp. 494-499, Aug. 1976.

[88] W.H. Press, S.A. Teukolsky, W.T. Vetterling, B.P. Flannery, *Numerical Recipes in C++: The Art of Scientific Computing, 2nd ed.*, Cambridge University Press, New York, NY, 2005.

[89] J. Kinoshita and K. Matsumoto, "Yield analysis of SLM DFB lasrs with an axially-flattened internal field," *IEEE J. Quantum Electron.*, vol. 25, pp. 1324-1332, June 1989.

[90] C. F. Fernandes, "Single Phase-Shifted DFB Laser Diodes," *Microw. Opt. Technol. Lett.*, vol. 17, pp. 398-402, Apr. 1998.

[91] Y. Zhong, X. Zhu, G. Song, Y. Huan, and L. Chen, "Effect of metal contact's reflection on the effective coupling coefficient of second-order DFB laser diodes," *Microw. Opt. Technol. Lett.*, vol. 42, pp. 339-342, Aug. 2004.

[92] Y. Zhong, X. Zhu, G. Song, Y. Huang, and L. Chen, "Two-dimensional simulation of high-order laterally-coupled GaAs-AlGaAs DFB laser diodes," *Semicond. Sci. Technol.*, vol. 19, pp. 971-974, 2004.

[93] J. Kinoshita, "Analysis of Radiation Mode Effects on Oscillating Properties of DFB Lasers," *IEEE J. Quantum Electron.*, vol. 35, pp. 1569-1583, Nov. 1999.

[94] P. Correc, "Coupling Coefficients for Trapezoidal Gratings," *IEEE J. Quantum Electron.*, vol. QE-24, pp. 8-10, Jan. 1988.

[95] S.-C. Cho, B.-G. Kim, and N. Dagli, "Extended Additional Layer Method of Calculating the Coupling Coefficient of Arbitrarily Shaped Gratings," *Microw. Opt. Technol. Lett.*, vol. 16, pp. 143-145, Oct. 1997.

[96] M. A. Ordal, L.L, Long, R.J. Bell, S.E. Bell, R.R. Bell, R.W. Alexander, Jr., and C.A. Ward, "Optical properties of the metals Al, Co, Cu, Au, Fe, Pb, Ni, Pd, Pt, Ag, Ti, and W in the infrared and far infrared," *Appl. Opt.*, vol. 22, pp. 1099-1120, Apr. 1983.

[97] G.M. Smith, D.V. Forbes, R.M. Lammert, and J.J. Coleman, "Metallization to asymmetric cladding separate confinement heterostructure lasers," *Appl. Phys. Lett.*, vol. 67, pp. 3847-3849, Dec. 1995.

[98] P.B. Johnson and R.W. Christy, "Optical constants of transition metals: Ti, V, Cr, Mn, Fe, Co, Ni, and Pd," *Phys. Rev. B*, vol. 9, pp. 5056-5070, June 1974.

[99] J.H. Weaver, "Optical properties of Rh, Pd, Ir, and Pt," *Phys. Rev. B*, vol. 11, pp.1416-1425, Feb. 1975.

[100] R. Kazarinov, and C. Henry, "Second-order distributed feedback lasers with mode selection provided by first-order radiation losses," *IEEE J. Quantum Electron.,* vol. QE-21, pp. 144-150, Feb. 1985.

[101] X. Li, "Distributed Feedback Lasers: Quasi-3D Static and Dynamic Laser Model," in J. Piprek (ed.) , *Optoelectronic Devices*, pp. 87-119, Springer, New York, NY, 2005.

[102] R.R. Tummala, E.J. Rymaszewski, and A.G. Klopfenstein, *Microelectronics Packaging Handbook: Semiconductor Packaging*, Chapman & Hall, 1996.

[103] K. Williams, A. Hayes, S. DiStefano, O. Huang, and E. Ostan, "Reactive ion beam etching of ferroelectric materials using an RF inductively coupled ion beam source," *Proc. 10th IEEE Symp. Appl. Ferroelectrics*, vol. 2, pp. 783-786, Aug. 1996.

[104] K.S. Mobarhan, "Test and Characterization of Laser Diodes: Determination of Principal Parameters," *Newport Photonics Instrumentation and Measurement Application Note No. 1*, http://www.newport.com/servicesupport/PDF_Files/APPNOTE1.pdf.

[105] J. Piprek, *Semiconductor Optoelectronic Devices: Introduction to Physics and Simulation*, Academic Press, San Diego, CA, 2003.

[106] J. Piprek, P. Abraham, and J.E. Bowers, "Self-Consistent Analysis of High-Temperature Effects on Strained-Layer Multiquantum-Well InGaAsP-InP Lasers," *IEEE J. Quantum Electron.*, vol. 36, pp. 366-374, Mar. 2000.

[107] B.W. Hakki and T.L. Paoli, "Gain spectra in GaAs double-heterojunction injection lasers," *J. Appl. Phys.*, vol. 46, pp. 1299-1306, 1975.

[108] J. Viheriälä, *Private communication*, May 2008.

[109] J.C. Lagarias, J.A. Reeds, M.H. Wright, and P.E. Wright, "Convergence Properties of the Nelder-Mead Simplex Method in Low Dimensions," *SIAM Journal of Optimization*, vol. 9, pp. 112-147, 1998.

[110] K. Suzuki, T. Yamada, M. Ishii, T. Shibata, and S. Mino, "High-Speed Optical 1 x 4 Switch Based on Generalized Mach-Zehnder Interferometer With Hybrid

Configuration of Silica-Based PLC and Lithium Niobate Phase-Shifter Array," *IEEE Photon. Technol. Lett.*, pp. 674-676, 2007.

[111] J. Yang, Q. Zhou, and R.T. Chen, "Polyimide-waveguide-based thermal optical switch using total-internal-reflection effect," *Appl. Phys. Lett.*, vol. 81, pp. 2947-2949, 2002.

[112] Y. Goebuchi, T. Kato, and Y. Kokubun, "Fast and stable wavelength-selective switch using double-series coupled dielectric microring resonator," *Phot. Technol. Lett.*, vol. 18, pp. 538-540, 2006.

[113] M. Renaud, M. Bachmann, and M. Erman, "Semiconductor Optical Space Switches," *IEEE J. Sel. Topics in Quantum Electron.*, vol. 2, pp. 277-288, 1996.

[114] K.A. Williams, G.F. Roberts, T. Lin, R.V. Penty, I.H. White, M. Glick, and D. McAuley, "Integrated Optical 2x2 Switch For Wavelength Multiplexed Interconnects," *J. Sel. Topics Quantum Electron.*, vol. 11, pp. 78-85, 2005.

[115] S. Yu, S.-C. Lee, O. Ansell, and R. Varrazza, "Lossless Optical Packet Multicast Using Active Vertical Coupler Based Optical Crosspoint Switch Matrix," *J. Lightwave Technol.*, vol. 23, pp. 2984-2992, 2005.

[116] W. van Berlo, M. Janson, L. Lundgren, A.-C. Mörner, J. Terlecki, M. Gustavsson, P. Granestrand, and P. Svendsson, "Polarization-Insensitive, Monolithic 4 x 4 InGaAsP-InP Laser Amplifier Gate Switch Matrix," *IEEE Photon. Technol. Lett.*, vol. 7, pp. 1291-1293, 1995.

[117] B. Qiu, X.F. Liu, M.L. Ke, H.K. Lee, A.C. Bryce, J.S. Aitchison, J.H. Marsh, "Monolithic Fabrication of 2x2 Crosspoint Switches in InGaAs-InAlGaAs Multiple Quantum Wells Using Quantum-Well Intermixing," *IEEE Photon. Technol. Lett.*, vol 13, pp. 1292-1294, 2001.

[118] D. A. Thompson, J. F. Haxell, A.S. W. Lee, T. Yin. G.J. Letal, B.J. Robinson, N. Bertsch, and J.G. Simmons, "New methods of defect-enhanced quantum well intermixing and demonstrated integrated distributed feedback laser-modulator," *Proc. SPIE*, vol. 4078, pp. 148-161, 2000.

[119] Y. Huang, F. Xia, V. Menon, S. Forrest, and M. Gokhale, "Reduction of Absorption Loss in Asymmetric Twin Waveguide Laser Tapers Using Argon Plasma-Enhanced Quantum-Well Intermixing," *IEEE Photon. Technol. Lett.*, vol. 16, pp. 2221-2223, 2004.

[120] S. Charbonneau, E.S. Koteles, P.J.Poole, J.J. He, G.C. Aers, H. Haysom, M. Buchanan, Y. Feng, A. Delage, F. Yang, M. Davies, R.D. Goldberg, P.G. Piva, and I.V. Mitchell, "Photonic integrated circuits fabricated using ion implantation," *IEEE J. Sel. Topics Quantum Electron.*, vol. 4, pp. 772-793, 1998.

[121] B.S. Ooi, K. McIlvaney, M.W. Street, A.S. Helmy, S.G. Ayling, A.C. Bryce, J.H. Marsh, and J.S. Roberts, "Selective quantum-well intermixing in GaAs-AlGaAs structures using impurity-free vacancy diffusion," *IEEE J. Quantum Electron.*, vol. 33, pp. 1784-1793, 1997.

[122] S.P. McDougall, O.P. Kowalski, C.J. Hamilton, F. Camacho, B. Qiu, M. Kee, R.M. De La Rue, A.C. Bryce, and J.H. Marsh, "Monolithic integration via a universal damage enhanced quantum well intermixing technique," *IEEE J. Sel. Topics Quantum Electron.*, vol. 4, pp. 636-646, 1998.

[123] B.S. Ooi, T.K. Ong, and O. Gunawan, "Multiple-wavelength, integration in InGaAs-InGaAsP structures using pulsed laser irradiation induced quantum well intermixing," *IEEE J. Quantum Electron.*, vol. 40, pp. 481-490, 2004.

[124] J. Arokiaraj, H. S. Djie, and T. Mei, "Investigations on the blue-shift phenomena in argon plasma intermixed GaAs/InGaAsP quantum well structures," *Appl. Surf. Sci.* , vol. 237, pp. 256-260, 2004.

[125] C. Clos, "A Study of Non-Blocking Switching Networks," *Bell. Sys. Tech. J.*, 406-424 (1953).

[126] J. H. Haysom, "Quantum Well Intermixing In InP/InGaAs(P) Heterostructures," *Ph.D. thesis, University of Ottawa*, 2001.

[127] H.S. Djie, S.L. Ng, O. Gunawan, P. Dowd, V. Aimaz, J. Beauvais, and J. Beerens, "Analysis of strain-induced polarization-insensitive integrated waveguides fabricated using ion-implantation-induced intermixing," *IEE Proc. Optoelectronics*, vol. 149, pp. 138-144, 2002.

[128] H. Chen, R.M. Feenstra, P.G. Piva, R.D. Goldberg, I.V. Mitchell, G.C. Aers, P.J. Poole, and S. Charbonneau, "Enhanced group-V intermixing in InGaAs/InP quantum wells studied by cross-sectional scanning tunneling microscopy," *Appl. Phys. Lett.*, vol. 75, pp. 79-81, 1999.

[129] A. McKee, C.J. McLean, G. Lullo, A.C. Bryce, R.M. De La Rue, J.H. Marsh, C.C. Button, "Monolithic integration in InGaAs-InGaAsP multiple-quantum-well structures using laser intermixing," *IEEE J. Quantum Electron.*, vol. 33, pp. 45-55, 1997.

[130] H.S. Djie, C. Sookdhis, T. Mei, and J. Arokiaraj, "Photonic integration using inductively coupled argon plasma enhanced quantum well intermixing," *Electron. Lett.*, vol. 38, pp.1672-1673, 2002.

[131] R. Millett, H. Schriemer, and X. Zhang, "Irrelevance of bending angle in simple Y-branch power splitter design," *Proc. SPIE*, vol. 5577, pp. 503-510, 2004.

[132] L.B. Soldano and E.C.M. Pennings, "Optical multi-mode interference devices based on self-imaging: principles and applications," *J. Lightwave Technol.*, vol. 13, pp. 615-627, 1995.

[133] *www.optiwave.com*, Optiwave, 7 Capella Court, Ottawa, ON, Canada, K2E 7X1.

[134] D.G. Kim, C. Ozturk, J. H. Shin, J.C. Yi and N. Dagli, "Self-aligned total internal reflection mirrors with very low loss," *Conf. Integ. Photon. Research*, IThG5, 2004.